The University Of Sheffield.

Department Of Mechanical Engineering.

Thesis

Investigating the effects of cryogenic processing on the wear performance and microstructure of engineering materials

Author: **Robert William Thornton**

Supervisors: **Dr. Tom Slatter**

Prof. Roger Lewis

Date: **August 2014**

Thesis submitted to The University of Sheffield in partial fulfilment of the requirements for the degree of Doctor of Philosophy

Abstract

Cryogenic processing (or cryogenic treatment or 'cryotreatment') includes a range of batch heat treatment processes conducted at temperatures below 193K (-80°C). These processes have been industrially applied since the first half of the Twentieth Century and commercially available for around forty years in the United States and Europe. During this time remarkable improvements (of up to 1257%) in the wear resistance of tool steels have been reported, along with smaller but significant improvements in hardness and other mechanical properties.

While martensitic tool steels have been the focus of the bulk of published research in this field, substantial effects have also been reported in other important engineering materials. However, coherent findings backed up by sound experimental results, analyses and appropriate metallurgical investigations have so far proved elusive. Currently, a significant portion of cryogenic treatment services are applied to automotive brake rotors and industrial cutting tools. Therefore a range of materials used in these applications were subjected to a combination of tribological testing and microstructural analyses to evaluate the effects of deep cryogenic treatment (93K).

Deep cryogenic treatment (DCT) was determined to improve the sliding wear resistance of EN10083 C50R pearlitic carbon steel, and AISI A2, D6 and M2 austenitic (as-cast) tool steels. Qualitative observations suggested that improvements in these tool steels were due to an increase in <100nm carbides following DCT. In the case of pearlitic carbon steel, however, no such observations were made, even following further characterisation of the material. It was theorised that the precipitation of nano carbides, along grain boundaries that were unable to be thoroughly investigated, were instead responsible. Mixed changes in the wear resistance of SAE J431 G10 grey cast iron are reported, thought to be as a result of the degradation of graphite flakes, but with similar beneficial changes as theorised to occur in C50R steel thought likely.

Furthermore, DCT was determined to have improved the abrasive wear resistance of SHM H13A cobalt-bonded tungsten carbide (WC-Co) turning inserts, when used to machine AISI 1045 steel, although indications of reduced toughness were also observed. DCT was determined to primarily effect the Co-binder phase, resulting in greater resistance to WC grain removal, but greater vulnerability to crack propagation.

In discussing these results, methodologies necessary for understanding the effects of cryogenic treatments are reviewed from an industrial or 'applications-based' and a scientific or 'materials-based' perspective. Finally, the significance of these findings was critically assessed, with a range of improvements to methodologies suggested.

Acknowledgements

The author wishes to express his deepest gratitude to his supervisors for their guidance, advice and support throughout his studies:

- Dr. Tom Slatter
- Prof. Roger Lewis

And to thank his industrial sponsor, not simply for making some bits of metal really cold for him, but for his advice and insight:

- Andy Priscott, Owner, Cryogenic Treatment Services Ltd.

The author would also like to acknowledge the invaluable advice and assistance of the other co-authors of his papers during this period:

- Dr. Hywel Jones, Sheffield Hallam University
- Dr. Hassan Ghadbeigi, The University of Sheffield

And some others worthy of particular mention, for their assistance in the murky world of materials science…

- (Soon-to-be-Dr.) Alfonce Chamisa, The University of Sheffield – Fresh out of finishing his own PhD, for his assistance in preparing thin foils for and gathering data from transmission electron microscopy and electron diffraction.
- Dr. Hassan Ghadbeigi (again), The University of Sheffield – For voluntarily taking on the 'much coveted' role of 'additional thesis reader'.
- Alan Jarvis, The University of Sheffield – For willing (borderline worryingly eager) discussions around metallurgy and crystallography, shared professional lamentations, and for the unprompted sourcing of numerous additional references for this thesis.
- Dr. Nik Reeves-McLaren, The University of Sheffield – Providing expertise and insight into the practicalities of X-ray diffraction and crystallography.
- (Soon-to-be-Dr.) Panos Efthymiadis , The University of Sheffield – For generously providing the opportunity to conduct (and then conducting) an electron back-scatter diffraction experiment and Ioannis Violatos for processing the data collected, and agreeing to allow me to use the results to validate other findings from X-ray diffraction experiments.

- Dr. David Asquith, Sheffield Hallam University – For entertaining crazy theories in a way that only a materials physicist can.
- Dr. Mahmoud Mostafavi, The University of Sheffield – Not only for good-natured support, but also for discussing aspects of metallurgy that we both 'love' so much, and an introduction to Dr. David Collins, The University of Oxford, for yet more gratefully received discussions about crystallography, X-ray and neutron diffraction data.

Numerous others have contributed to this research, either with their own expertise, by providing crucial industrial understanding, or through their own projects investigating the effects of cryogenic treatments on the tribological performance of engineering materials:

Dave Butcher	Technical support	Masoud Al-Amri	BEng Final Year Project 2009-10
Steve Weston, Sandvik Coromant	Industrial advice; tungsten carbide specimens	Andy Hindle Ross Preston	MEng Final Year Project 2009-10 MEng Final Year Project 2010-11
Dr. Aiden Lockwood, Sandvik Coromant	Industrial advice	Kareem Al-Ashri	MSc Research Project 2011-12

The research presented here was conducted with the support of:

- Engineering and Physical Sciences Research Council – for providing funding through the Doctoral Training Partnership / Account scheme of 2009.
- Cryogenic Treatment Services Ltd. – for the provision of deep cryogenic treatment of all specimens used.
- Sandvik Coromant UK – for the provision of the 20 SHM H13A (SCMT 120408 – KM) turning inserts and CoroTurn 107 (SSBCR 2020K 12) tool holder used for the tool wear development study presented here.
- Materials Engineering Research Institute, Sheffield Hallam University – for the use of an Alicona InfiniteFocus Microscope to produce wear scar micrographs from tool steel specimens.

Abbreviations and acronyms

AFM	*Atomic-force microscopy*	*HIP*	*Hot isostatic pressing*
AISI	*American Iron and Steel Institute*	*HSM*	*High-speed machining*
ASTM	*American Society for Testing and Materials*	*HSS*	*High-speed steel*
BS	*British Standard*	*ICDD*	*International Centre for Diffraction Data*
BUE	*Built-up edge*	*ISO*	*International Standards Organization*
C/C	*Carbon-carbon (composite)*	*LGV*	*Light goods vehicle*
CBN	*Cubic boron nitride*	*MMC*	*Metal-matrix composite*
CGI	*Compacted graphite iron*	*P/M*	*Powder metallurgy*
CHT	*Conventional heat treatment*	*PCBN*	*Polycrystalline cubic boron nitride*
CMC	*Ceramic matrix composite*	*PDF*	*Powder diffraction file*
CT	*Cold treatment*	*PVD*	*Plasma vapour deposition*
CVD	*Chemical vapour deposition*	*SAE*	*Society of Automotive Engineers*
DCT	*Deep cryogenic treatment*	*SCT*	*Shallow cryogenic treatment*
DLC	*Diamond-like coating*	*SEM*	*Scanning electron microscopy*
EBSD	*Electron back-scatter diffraction*	*SHM*	*Sandvik Hard Materials*
ED(X)S	*Energy-dispersive (X-ray) spectroscopy*	*SME*	*Small and medium-sized enterprises*
EN	*Euronorm*	*TEM*	*Transmission electron microscopy*
FEG	*Field-emission gun*	*TTT*	*Time-temperature transformation*
GCI	*Grey cast iron*	*WDS*	*Wavelength-dispersive spectroscopy*
GFRP	*Glass-fibre reinforced plastic*	*XRD*	*X-ray diffraction*

Nomenclature

a	Contact half-width	μm
a	Lattice parameter	nm
d_{hkl}	Lattice plane spacing	nm
E	Elastic modulus	GPa
f	Feed rate	mm/rev
G_x	Diffracted intensity with depth from surface	-
h	Indentation depth	nm
h, k, l	Miller indices	-
k_x	Gradient in x	-
KT	Crater depth	μm
L	Camera length	mm
HR-	Rockwell hardness (- scale)	-
HV_x	Vickers hardness under x Newton load	MPa
N	Number of samples	-
p_0	Peak contact pressure	MPa
P	Indentation load	μN
r	Radius	mm
R	Electron diffraction spot separation	mm
R	Goniometer radius	mm
r_ε	Nose radius	mm
R_a	Arithmetic mean roughness	μm
R_q	Root mean square (rms) roughness	μm
t	X-ray penetration depth	μm
t_s	(Cryogenic) soaking time	hr
T_s	(Cryogenic) soaking temperature	K
u	Uncertainty	$Contextual$
$VB_{B/N}$	Flank/notch wear extent	μm
V_c	Cutting speed	m/min
WR	Wear rate	$Various$
x	Depth from XRD specimen surface	μm
x, y, z	Cartesian coordinates	$Various$
Z	Atomic number	-

α_n	*Clearance angle*	^{o}
Δh	*Specimen height*	mm
$\Delta z_{c,x}$	*Crater depth correction*	μm
$\varepsilon(x)$	*Error in x*	*Contextual*
θ	*X-ray / electron diffraction angle*	^{o}
κ_r	*Lead angle*	^{o}
λ	*X-ray / electron wavelength*	nm
λ_s	*Cutting inclination*	^{o}
μ	*Coefficient of friction*	-
μ	*Linear absorption coefficient*	cm^{-1}
ν	*Poisson's ratio*	-
σ	*Standard deviation*	*Contextual*
σ_r	*Radial stress*	*MPa*
σ_t	*Tensile stress*	*MPa*
σ_{uts}	*Ultimate tensile stress*	*MPa*
σ_y	*Yield stress*	*MPa*
σ_z	*Axial stress*	*MPa*
σ_θ	*Tangential stress*	*MPa*
τ_y	*Shear yield strength*	*MPa*
τ_1	*Principal shear stress*	*MPa*

Contents

1. Introduction

The term 'cryogenic' pertains to something at or causing the creation of very low temperatures, typically <193K (-80°C) and has a wide variety of uses in medical devices, electrical components as well as superconductors used in fields such as quantum physics. Additionally 'cryogenic' is associated with cooling fluids in high-output industrial machining processes, and can also be found referring to materials engineering and heat treatment technologies. While low temperatures are indeed involved in both instances, the term 'cryogenic' should not be used when referring to the field of 'cryonics', which is of course to do with the preservation of living creatures beyond the help of contemporary medicine.

Perhaps unsurprisingly, the mechanical engineering and tribology based research presented here concerns the use of the term 'cryogenic' in relation to 'cryogenic processing' – a technique whereby materials and components are subjected to low temperature treatments with the aim of enhancing their performance by causing permanent microstructural changes. Cryogenic processing is therefore a low-temperature batch heat treatment technique, discussed here in the context of its effects on the mechanical properties, tribological performance and microstructure of engineering materials.

In this first chapter, a brief background of the technique is given, highlighting its origins and early uses. The scientific and commercial motivations for the studies conducted are explained and the application areas of interest outlined. Following an overview of the modern cryogenic processing industry, the aim and objectives of the research presented here are given, along with the outline structure of this thesis.

1.1. The history of cryogenic processing

The earliest examples of sub-zero temperature processing come from Swiss watch-makers. In the mid-nineteenth century, they used to leave delicate gears and the materials for watch parts buried in snow in mountain caves over the winter, having noticed that this would make gears more durable, and allow parts to be made with more precision as the materials deformed less during machining. This enabled them to produce more reliable and longer lasting timepieces [1]. During the first half of the Twentieth Century tool and die-makers began freezing their tooling as they realised they could machine more parts per cutting edge than before. Some aero-engine components and even cutlery started to be treated as well.

During the Second World War cryogenic processing was widely utilised to enhance the wear resistance of mechanical parts in machinery and vehicles, although serious

research into its effects were effectively suspended until the 1960s when NASA engineers noticed that spacecraft parts exhibited different properties after returning from space. Shortly afterwards, in the 1970s and 1980s Dr. Randall Barron [2, 3], along with Charles Mulhern [4], conducted what are considered the first contemporary research projects into the effects of deep cryogenic processing. In studies using lathe tools and abrasive wear experiments on a range of ferrous alloys, Barron recorded significant increases in wear resistance in some materials (up to 718% in the case of AISI D2 steel) whereas in others (AISI A2, A6 and T2 steels) cryogenic processing appeared to have no effect.

Cryogenic processing or cryogenic treatment, often simply referred to as 'cryotreatment', affects the entire cross-section of materials and components and is often considered as a single additional stage to a conventional heat treatment cycle (although, as is discussed in Section 1.3.2, for many tools and components cryotreatment is already a part of the 'conventional' process). Cryotreatment involves lowering the material to temperatures below 193K and holding or 'soaking' for a defined period of time before raising the material back to ambient temperature. The objective of cryotreatment is therefore to cause permanent changes to the microstructure of a material that enhances desired properties, with minimal or insignificant adverse effects.

1.2. Motivation for research project

Cryogenic processing has become a widely used heat treatment technique for a number of products, including industrial cutting tools, automotive brake and engine system components, as well as specialist products including pressure transducers for space applications and even sports equipment. However, since its introduction as an industrial treatment process in the 1930s and the initiation of concerted research efforts in the 1970s [2] and 1980s [3, 4], reviews [5-7] have consistently highlighted the lack of cohesion and consistency in reported changes in the properties and performance of cryotreated materials.

Although a wide range of laboratory-based and applications-based testing has been carried out, few studies have linked the results of mechanical testing, tribological bench testing and realistic in-service testing with the microstructural examinations necessary to explain the performance changes seen in cryotreated materials and components. This lack of coherence and fundamental understanding prevents further exploitation of this technology, for instance in the treatment of raw materials as opposed to finished components, or in identifying and designing optimised materials for cryotreatment, therefore preventing the greatest possible enhancements in properties such as hardness and wear resistance to be achieved.

The range of potential applications for cryotreatment is vast, meaning significant financial savings could be realised by manufacturers and consumers in using cryotreated products with greater performance and longevity, while the cryogenic processing industry could benefit from being able to offer treatment services to a broader range of clients.

Cryogenic treatment companies currently treat a wide range of parts and components, but of all of these there are two groups of products that are mentioned most frequently in company promotional literature: automotive brake rotors, and industrial cutting tools. Common materials used in the manufacture of these components therefore form the focus of this work.

1.2.1. Brake rotors

1.2.1.1. Brake rotor materials

Brake rotors form part of a critical system in all road-going vehicles, with differing demands and performance expectations depending on whether they are to be fitted to passenger light goods vehicles (LGVs), sports cars or used in motor racing. While the materials brake rotors are manufactured from vary widely, there are a number of fundamental requirements that all must meet. Brake rotor performance must be resilient to large changes in temperature, with a consistent braking response and predictable wear development provided throughout their service life [8].

Brake rotor manufacturers therefore have to optimise the strength, mass, wear resistance and thermal performance of brake rotor materials against cost and service life. The work presented here concerns economy brake materials, which primarily consist of grey cast irons and low-carbon steels; their manufacturability and low cost being important factors in their widespread use for passenger LGVs and lightweight, low-cost sports cars. With relatively simple chemical compositions, the phases of these materials are acceptably reflected using a standard iron-carbon (Fe-C), or more precisely an iron-cementite (Fe-Fe_3C), binary phase diagram, which is presented in Figure 1. The carbon contents typically considered for steels and cast irons range from 0.03 – 1.5wt% and 2 – 4wt% respectively [9], although some flexibility exists depending on the complexity of the alloy.

Pearlitic, lamellar graphite or 'grey' cast iron (GCI) is a common material in the manufacture of brake rotors for passenger LGVs, with a number of alloying elements added to enhance desirable properties. Thermal conductivity is enhanced by the presence of these graphite flakes, while their large thermal storage capacity means GCI brake rotors are less likely to overheat and suffer from brake fade during use. In studies on graphite flake morphology, Hecht et al. [10] demonstrated their importance

in the thermal diffusivity of SAE J431 G3000 (now G10) grey cast iron. In their study they determined that a 50% increase in thermal diffusivity was related to a fourfold increase in the size of graphite flakes, when testing grey cast irons with identical chemical compositions. The interlocking nature of these graphite flakes enhances the thermal conductivity of grey cast iron [11]. Although graphite flakes may be observed to be independent from one another and separated when commonly viewed in section, local clusters of graphite flakes are typically connected at a centre from which they first nucleated, during cooling from the liquid phase, as a single eutectic cell [12].

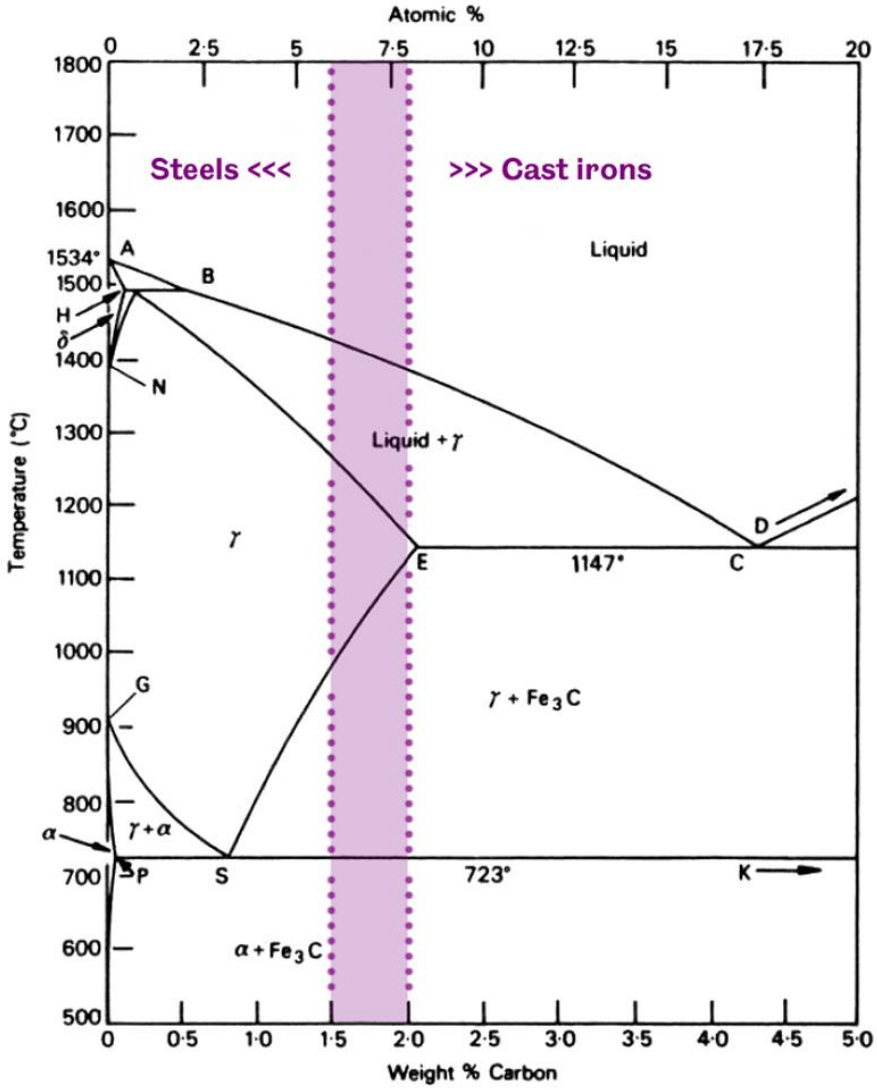

Figure 1 - Binary phase diagram for the Fe-Fe_3C (iron-cementite) system (adapted from Bhadeshia et al. [9]) illustrating distinction between steels and cast irons based on carbon content.

In common with grey cast irons, in pearlitic steels additives such as chromium and molybdenum give greater resistance to abrasion and improved heat cracking behaviour [8]. Chromium and molybdenum harden ferrite by means of substitutional solid solution strengthening (the replacement of iron atoms by alloy atoms in the body-centred cubic crystal lattice), while chromium restricts the development of face-centred cubic austenite (Figure 2 (a) and (c) respectively). Manganese is added to

refine the grain size and increase the hardenability of the pearlite matrix while acting as a de-oxidising agent along with silicon. Silicon additionally acts as a graphite stabiliser in grey cast irons and prevents the formation of iron carbides [11, 13].

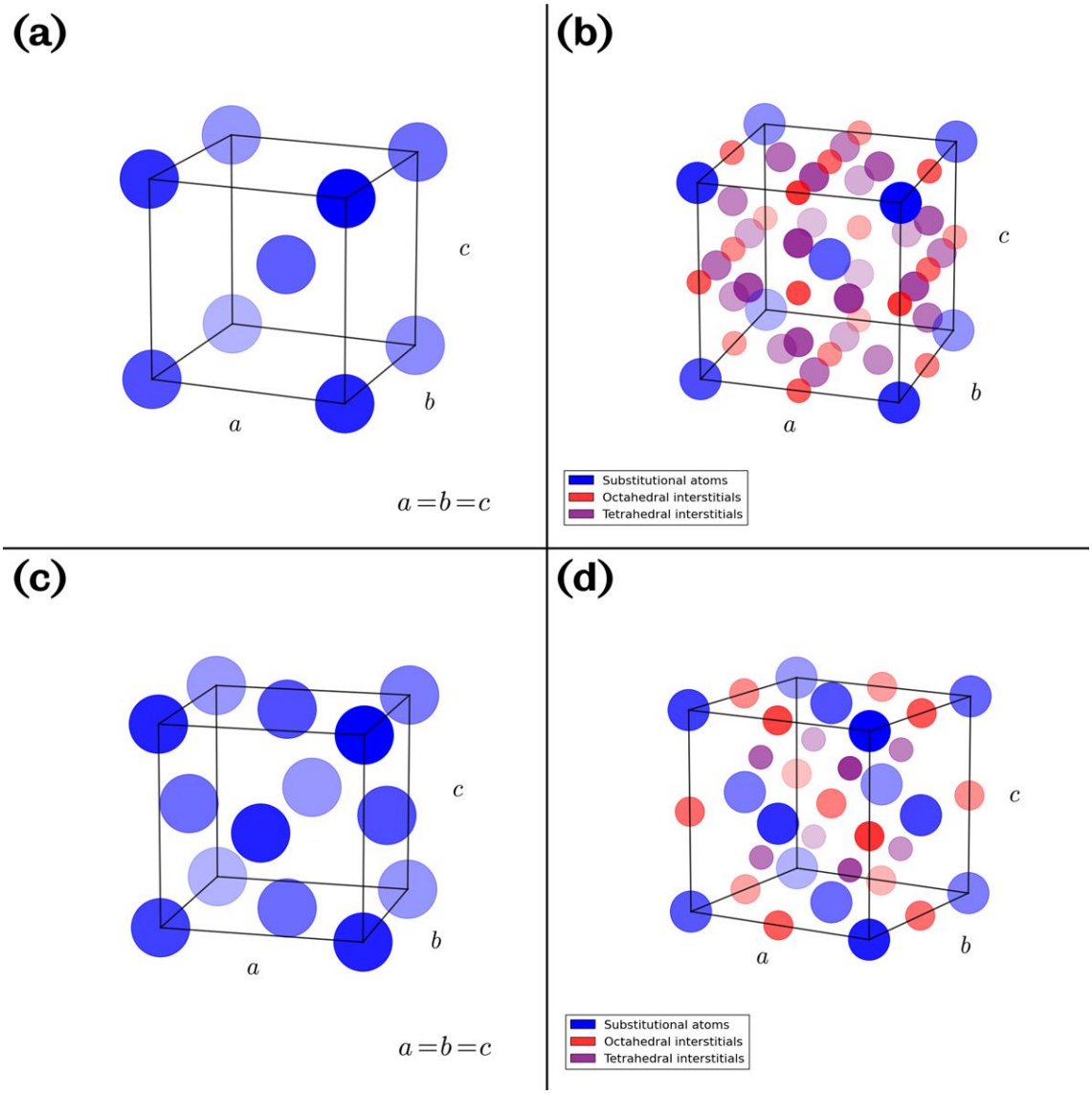

Figure 2 – Diagramatic representation of the primary substitutional atoms in (a) body-centred cubic and (c) face-centred cubic unit cells and (b, d) their respective interstitial sites.

The properties of pearlitic materials are inherently linked to their interlamellar spacing – the distance between cementite lamellae in a ferrite matrix. Typically characterised by their mean free ferrite path (MFFP), it has been shown that the strength and hardness vary inversely to the square root of the distance that a crack may propagate through ferrite before encountering a hard cementite boundary [13]. While these ferrite-cementite interfaces also allow for the easy initiation of cracks, the short allowable propagation distances mean that a significant amount of energy is absorbed by the pearlite structure.

Controlling the interlamellar spacing through heat treatment is therefore crucial. As pearlite is formed by the nucleation and growth of cementite and ferrite from

austenite, the parameters of the resulting structure are diffusion dependent. Therefore at lower transformation temperatures (considered a large 'undercooling' from the eutectoid temperature), carbon diffuses over shorter distances, leading to more numerous but finer cementite lamellae. To achieve this, cooling rates must initially be relatively high to ensure the formation of cementite is limited until the optimum transformation temperature is reached. In the case of a eutectoid carbon steel, (a time-temperature transformation (TTT) diagram for which is shown in Figure 3), fine pearlite will be formed if steel is cooled from the eutectoid temperature at an average of around 150K/s for one second, before being held at around 823K (550°C) for several minutes to allow the pearlite to form (Figure 3 (a)). By means of comparison the formation of 100% martensite requires continuous cooling rates averaging >5K/s (although generally much higher rates are used to produce much finer martensite; Figure 3 (b) indicates a typical cooling rate of approximately 850K/s). As this would require quenching into a cryogenic fluid (and therefore impractical on an industrial scale), cryogenic treatment can theoretically be applied to plain carbon steels sometime later to complete the martensite transformation. However, the reality of applying cryogenic treatments is much more complex – further discussion is provided in Section 2.2.3.

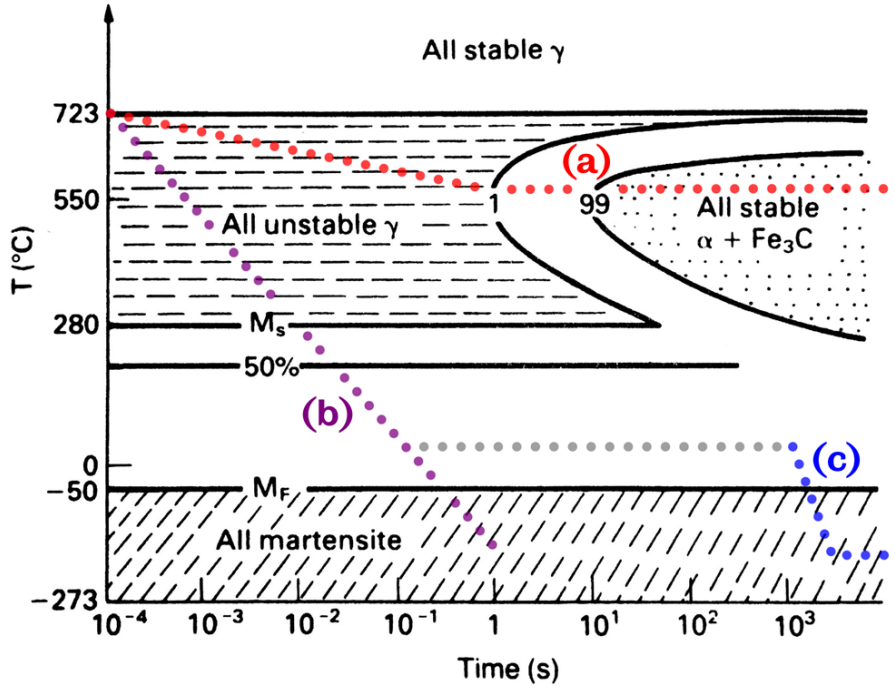

Figure 3 - Time-temperature transformation diagram for a 0.8% carbon steel (adapted from Ashby et al. [14]) showing cooling curves for: (a) pearlite; (b) 100% quenched martensite; (c) 100% martensite using cryogenic treatment.

Both grey cast irons and carbon steels offer a high thermal storage capacity and a high level of manufacturability, although they both result in large and heavy brake rotors with relatively poor corrosion resistance. Grey cast irons additionally offer good thermal conductivity and therefore resistance to brake fade during prolonged use, making these materials preferred for the passenger vehicle market.

In recent years alternatives to these materials have been considered. In pin-on-disc testing involving compacted graphite iron (CGI), Cueva et al. [15] determined that lower contact pressures were required to achieve the same friction force, temperature and similar wear rates, using CGI as compared to GCI. Materials having previously been used exclusively in high-performance vehicles are also being considered for passenger LGVs as manufacturing costs fall. These include metal-matrix composites (MMC), carbon-carbon (C/C) composites, ceramic matrix composites (CMC) as well as titanium alloys.

The majority of MMCs suggested for wider use in brake rotors are those based on aluminium, as Al-MMCs offer the benefits of significant weight savings while giving similar friction and wear characteristics. Their one major drawback is a low melting point, which limits their applications [16]. In more demanding applications, such as those experienced in motor racing or in aircraft braking systems, C/C composites are often used, as they have significantly greater resistance to high temperatures while having very low densities. However, the braking performance of C/C composites at low temperatures is poor, while manufacturing costs currently prohibit their wider use [17]. By contrast CMCs offer substantial weight savings over ferrous alloys, and thermal stability up to 1300°C [18]. For example C-SiC rotors (carbon fibre reinforced ceramics with a matrix containing silicon carbide) have superior abrasion and corrosion resistance and service lives of up to 300,000km, with typical masses around 33% of equivalent rotors made from cast iron. However, their manufacture is complex and therefore inherently expensive, prohibiting their widespread use.

Titanium alloys and titanium MMCs have also been considered candidates for brake disc materials. Observing friction and temperature data from commercial titanium alloys, Ti-MMCs and a thermally spray-coated titanium alloy sliding against commercial lining materials, Blau et al. [19] determined that Ti-MMCs exhibited inferior wear performance to the reference cast iron used, but superior wear performance to those of the commercial titanium alloys. Having demonstrated the lowest wear rate, the thermally spray-coated alloy was recommended for further testing and analysis.

While these lightweight alternatives clearly offer a number of benefits, due to factors such as their cost, complexity and because they do not offer significantly improved braking performance for domestic and commercial vehicles, it is considered that cast iron and steel will remain the primary brake rotor materials for passenger LGVs [8]. Environmental concerns, such as the creation of fine particulates during the manufacture of composite materials, have also yet to be resolved [20].

1.2.1.2. Brake rotor wear

Brake rotors form part of a complex tribosystem; being forced into contact with composite brake pads containing additives to enhance their thermal properties, that are held together by a phenolic resin binder [21]. Severe contact conditions exist between brake rotors and pads, with contact pressures between 500kPa and (in extreme circumstances) 2400kPa [8], although for common brake friction pairs a maximum of 1200kPa may be reached. Sliding speeds between rotors and pads are typically around 50% of the speed of the vehicle [22]. Under these conditions, temperatures in the friction ring are capable of reaching 700°C with prolonged use on typical passenger LGVs. As the brake rotors may absorb as much as 90% of the kinetic energy of the vehicle as heat, it is desirable that they are able to rapidly dissipate this energy [8].

The temperature rise of the brake rotors is directly related to the kinetic energy and therefore the mass of the vehicle on which they are mounted, as well as their own mass and the specific heat capacity of the brake rotor material from which they are manufactured. Larger brake rotors are therefore less susceptible to 'brake fade' – the reduction of the coefficient of friction between the brake rotors and pads as the temperature of each material rises [8]. However, as larger brake rotors inevitably increase the mass of the vehicle, there is also a drive towards finding lower density alternatives to traditional brake materials, to maximise fuel efficiency.

Common wear mechanisms for brake friction materials include abrasion, adhesion, oxidation and ablation of binding agents [8] (translated from Oehl and Paul [23]). During the running-in process for brake friction pairs, debris from brake rotors will become embedded in the pad material, under certain circumstances resulting in significant abrasive wear of the rotor [8] (translated from Severin and Musiol [24]). During this time the coefficient of friction will also increase, as the disc and pad surfaces wear to create conformal contacts [22]. Both second and third body abrasive wear mechanisms are therefore important, as a result of the contact between the brake friction materials, their debris and particles from other sources, such as the road surface material and other naturally occurring contaminants. Some of these features are illustrated by the electron micrographs shown in Figure 4, where the grooved machined surface of a grey cast iron brake disc is replaced by a smoother topography as a result of the transfer film that has built up between the brake rotor and pad materials. Signs of surface fatigue can also be seen.

Whereas it is often the objective for tribological pairs to achieve the minimum amount of wear with the minimum level of friction, in the case of brake friction materials it is the objective to achieve the minimum amount of wear with the maximum amount of

friction. For this reason lubrication is an important consideration; not in the context of reducing the friction of the contact (i.e., with oils or greases), but in increasing pad and rotor lifespans by minimising internal wear processes and adhesion of wear particles with the friction materials [8].

The life of a brake rotor is largely determined by the material from which it is made and how it is utilised. In the case of grey cast iron rotors under regular use on public roads, abrasive wear which gradually reduces their cross-section and thermal capacity is of importance, whereas for extremely hard brake materials such as C-SiC, abrasion is much less of a consideration. Similarly high braking loads can lead to large temperature variations in grey cast iron discs, which may cause thermal cracking. C-SiC rotors have a much greater resilience to thermal shock, although unlike grey cast iron they can suffer from corrosion (of their carbon fibres) at high temperatures instead. However, high braking loads can also reduce the rate of wear of grey cast iron rotors as a result of the softening of the brake pads [8].

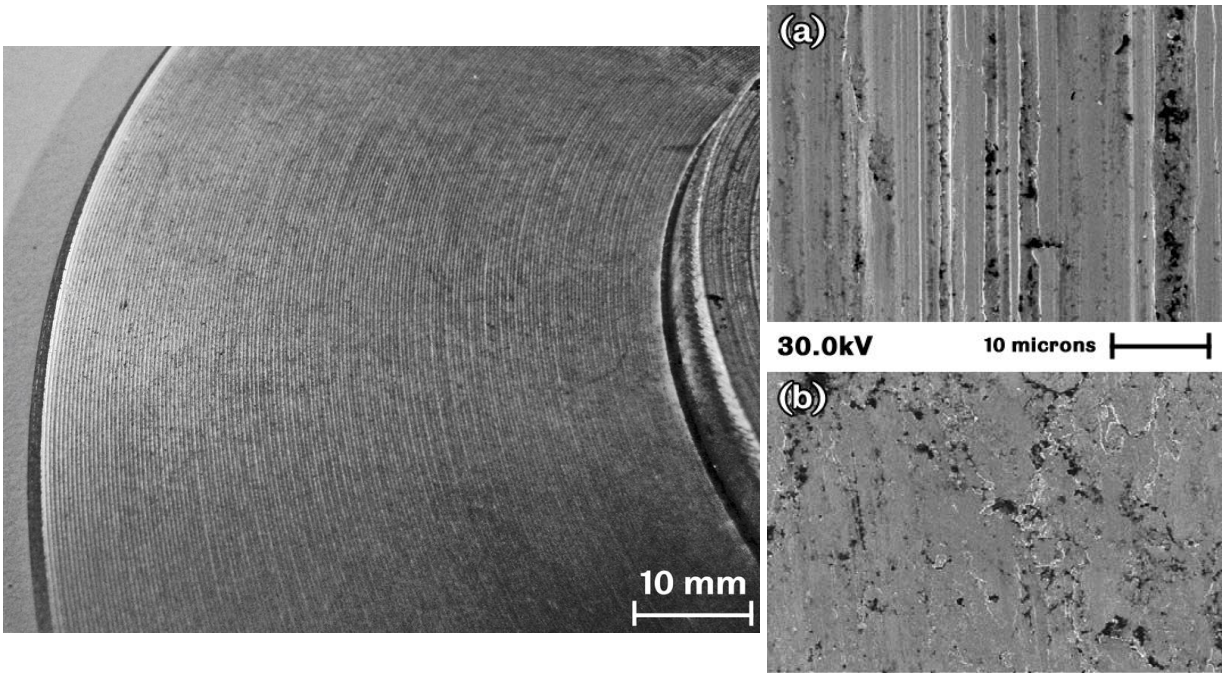

Figure 4 - Photograph of the machined surface of a SAE J431 G10 grey cast iron brake rotor (from present studies) and electron micrographs taken by Österle et al. [25] of EN-GJL-250 grey cast iron brake rotor (a) machined surface and (b) worn surface with transfer layer after multiple braking cycles.

Due to their current prevalence in mainstream automotive applications, the research presented here includes studies on the effects of cryogenic treatment on the tribological performance and metallurgical structure of lamellar graphite cast iron and carbon steel brake rotor materials. These studies are presented in Chapters 4 and 7.

1.2.2. Cutting tools

Solid cutting tools, bits and inserts are required for the machining of a wide range of materials including woods, polymers, light alloys, cast irons and steels, hard metals and

superalloys. The properties of the material to be machined, the desired surface finish and production rates all impact on the specific properties and performance required of cutting tool materials. As such the variety of materials used in the manufacture of cutting tools is extensive; however their required properties fall into a number of common categories: strength, hardness, wear resistance and thermal stability.

In simple terms, tool materials must be stronger and harder than the materials they are intended to cut. These properties must be maintained at the elevated temperatures they experience during use. The challenge that these requirements represent becomes clear when considering that, in conventional machining operations, sliding speeds at the tool-workpiece interface may reach 600m/min, temperatures may rise to 1000°C and the cutting edge may experience contact pressures of up to 2GPa [26, 27].

High-speed machining (HSM) has become increasingly common over the last two decades, as it offers higher cutting speeds and feed rates than can be achieved by conventional machining processes [28]. The boundaries between conventional machining and HSM for a range of workpiece materials are shown in Figure 5.

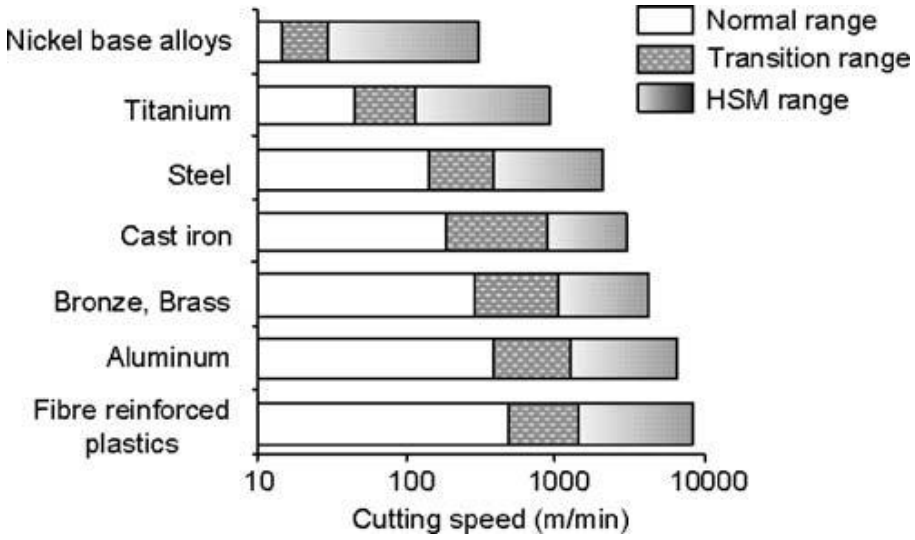

Figure 5 - Conventional and high-speed machining (HSM) regimes for a range of common engineering materials suggested by Schulz et al. [29] (redrawn by Iqbal et al. [28]).

While lower cutting forces, the potential for improved surface finish and, most importantly, increased productivity are cited as benefits of HSM [30], the high speeds result in a nearly adiabatic cutting process that cause high localised temperatures as heat cannot be conducted away from the cutting zone. In machining AISI 4140 high strength alloy steel with uncoated cemented carbide inserts at 925m/min, Abukhshim et al. [31] reported temperatures of up to 1150°C at the tool-chip interface by using infrared thermography.

1.2.2.1. Tool wear

The severe conditions experienced at the tool surface are not trivial to analyse, in part because of the variation in conditions experienced by different cutting zones (Figure 6). Tool materials are subjected to high stresses (tool tip and primary shear zone), abrasion and heating (rake face within the secondary shear zone) and rubbing (between the flank face and the workpiece) [32].

Wear processes commonly considered in relation to cutting tools (and where they are found) therefore include abrasive wear (flank face), crater wear (rake face), notch wear and chipping (cutting edge), as well as diffusion wear (flank and rake faces). For reference to these areas and to see an overview of tool wear processes see Figure 7. In their thorough review of these processes, Robinson et al. [33] highlight the influence of cutting parameters (cutting speed, depth of cut and feed rate) on the stresses and temperatures experienced by cutting tools.

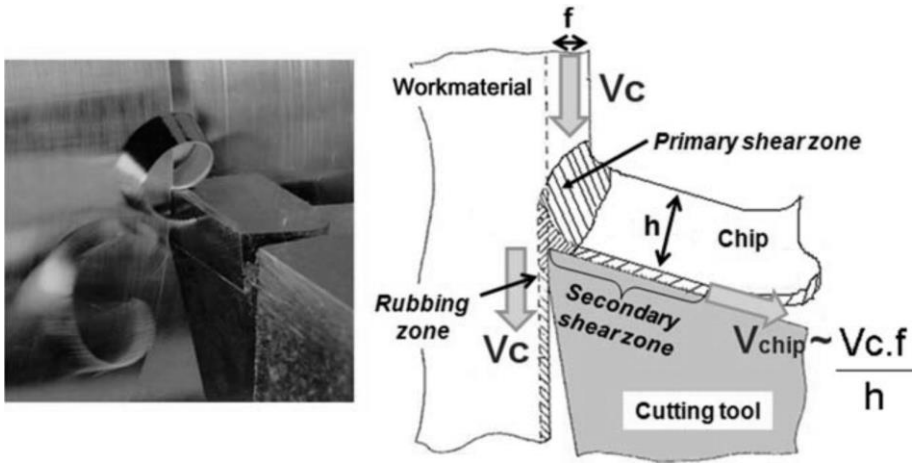

Figure 6 - Standard orthogonal cutting model with different contact zones identified [32].

The continued development of any of these wear processes will eventually cause the 'failure' of the tool; where failure can be defined in terms of characteristics of the tool or workpiece, or by changes in the cutting forces and power requirements of the machine tool. While the criteria used in different industrial environments vary, all are inextricably linked to the state of wear on the tool. Figure 8 illustrates common tool wear features and failure modes.

The causes of these examples of tool wear arguably fall into two categories: misuse or overuse of the tool, and normal wear development. The wear features and failure modes illustrated in Figure 8 are categorised in this manner in Table 1.

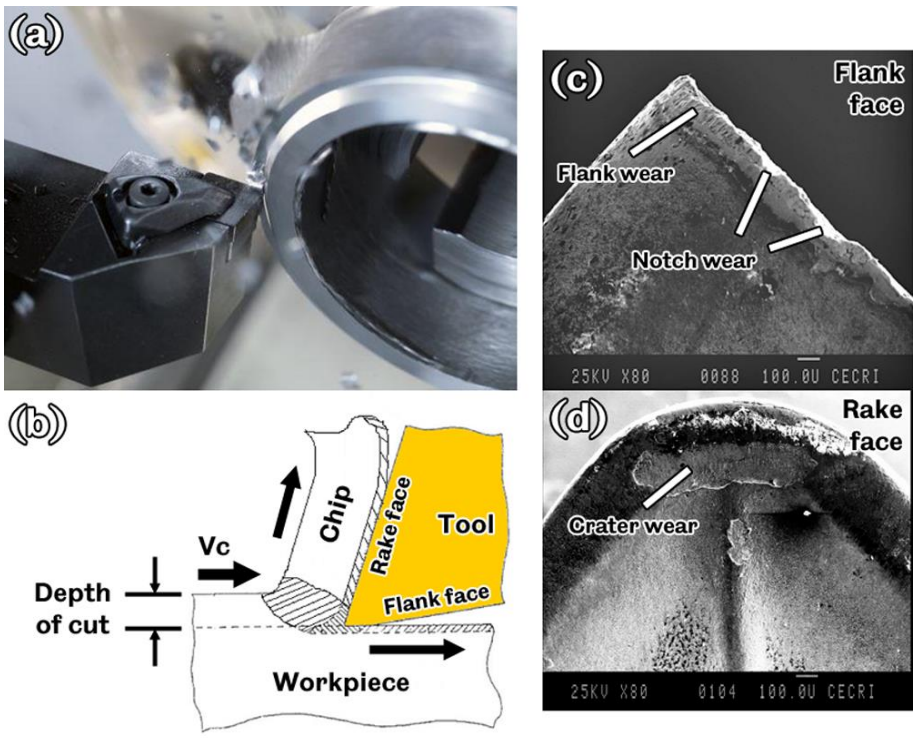

Figure 7 - Overview of common tool wear processes: (a) Insert used in turning operation (Sandvik Turning Guide); (b) Orthogonal cutting model adapted from Rech et al. [34]; (c) and (d) Electron micrographs taken by Vadivel et al. [35] showing wear on flank and rake faces of tool inserts.

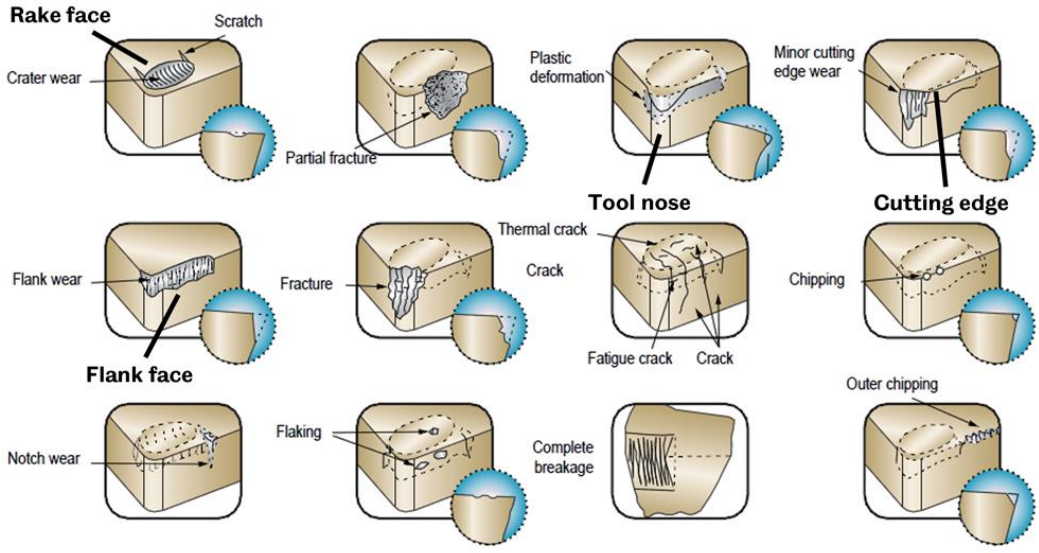

Figure 8 - Summary of common tool wear mechanisms (adapted from Sowa Turning Guide).

Table 1 - Categorised tool wear features and failure modes.

Tool misuse / overuse	Normal wear development
Fracture	Crater wear
Plastic deformation	Flank wear
Thermal cracking	Cutting edge wear
Breakage	Chipping

Although cutting conditions vary significantly between machining operations, it is beyond the scope of this research to consider in detail the complexities caused by the combination of cutting dynamics, chip formation, temperature and the interaction of different wear mechanisms, on the wear development of cutting tools. While failure

modes typically associated with the misuse or the severe use of cutting tools are beyond the remit of this research, normal forms of tool wear commonly used in defining tool-life are briefly discussed.

In his assessment of flank wear in cutting tools, Astakhov [36] explains its use as a popular industrial measure of tool wear as it determines the diametric accuracy of machining, and therefore the achievable tolerances in the machined workpiece. Due to the complexities of the processes occurring at the tool-workpiece interface (high sliding friction between, and plastic deformation of the tool and machined surface), the 'effective' coefficient of friction does not match that predicted by standard mechanical testing. Astakhov highlights that although abrasive, adhesive, diffusive and oxidative types of wear are commonly measured by investigators, the predominant failure mechanism, when machining difficult to machine materials or in high-speed machining, is due to the plastic deformation of the cutting wedge (between the rake and flank faces of the tool) as a result of high temperature creep of the material. In conclusion, Astakhov suggests that metrics such as flank wear cannot be used to compare the performance of different tools; instead proposing a 'resource' of the cutting tool, which is defined as the limiting amount of energy that can be transmitted through the cutting wedge until it fails. While these conclusions may be valid with regard to 'benchmarking' different types of cutting tools, materials and coatings against one another, it is suggested that simpler metrics of tool wear, such as those defined by relevant testing standards and commonly used in industry today, remain valid for the comparative testing of cryogenically treated and non-cryogenically treated cutting tools of the same grade, as presented as part of this research. Astakhov rationally suggests that the dimensional accuracy and surface finish of the workpiece should be the preferred tool failure criterion, as this is the most objective estimate of tool wear, although this does not in itself provide any information as to the causes of tool failure, as tool wear mechanisms do.

Crater wear depth is more commonly used as a failure criterion for carbide tools [37], as opposed to high-speed steel or ceramic tools. Although it is typically considered simply as the removal of material from the rake face of a tool near the cutting edge, there are both mechanical and chemical wear mechanisms responsible. In high-speed machining of AISI 1045 steel using a cemented tungsten carbide tool, Subramanian et al. [38] quantified the contributions made to crater wear by mechanical and dissolution mechanisms using neutron activation analysis. They found that as cutting speed (and therefore tool temperature) increased, so did the proportion of dissolution wear occurring; increasing from 66% at 150m/min to 93% at 240m/min. The rate of dissolution of tungsten in the chip increased substantially over this range, while the rate of mechanical wear remained almost constant.

1.2.2.2. Tool coatings

A number of tool coatings have been developed to mitigate both mechanical and chemical wear mechanisms in cutting processes. In their review of physical-vapour deposition (PVD) coatings, Van Stappen et al. [39] highlight that titanium-nitride (TiN) coatings are often effective in reducing adhesive wear between some tool and workpiece materials, while titanium-aluminium-nitride ((Ti,Al)N) coatings can be used when greater oxidation resistance is required, and titanium-carbon-nitride (Ti(C,N)) coatings are typically superior in the machining of tough materials where greater abrasive wear resistance is needed. For increased corrosion resistance, it is suggested that chromium-nitride (CrN) or Ti_2N (plasma nitriding followed by PVD TiN coating) type coatings can be used. It should be noted however, that coatings such as these may still react significantly with workpiece materials at the high tool-workpiece interface temperatures caused by high-speed machining regimes.

More recently diamond and diamond-like coatings (DLCs) have become popular, as their high hardness and abrasion resistance make them ideal for cutting hard metals and difficult-to-machine materials, such as a number of composites and aluminium-silicon (AlSi) alloys which create extremely abrasive particles. In a comparative study, Zhang et al. [40] conducted turning tests using cobalt-bonded tungsten carbide (WC-Co) tools to machine a glass-fibre reinforced plastic (GFRP) composite material. They demonstrated that diamond and diamond-like coatings reduced the flank wear rate of the WC-Co tools by factors of 12 and 3 respectively, although in friction tests against silicon nitride (Si_3N_4), tungsten carbide (WC-Co) and ball-bearing steel counterfaces, diamond coatings were found to have a coefficient of friction 3-4 times that of diamond-like coatings. This was in part explained by the diamond coating process producing a greater surface roughness, suggesting that the coefficient of friction could be reduced with more careful process control.

1.2.2.3. Tool materials

There is a wide range of materials from which cutting tools are manufactured, typically by conventional melting and subsequent machining processes, or by powder metallurgy. Of all these materials, tool steels probably represent the broadest category and the greatest number of tools produced by volume. These complex iron-carbon alloys with silicon, manganese, chromium, molybdenum, vanadium and tungsten can be formed and treated to achieve a wide range of properties including hardness up to around 8000MPa and thermal stability to 1000°C [41]. In common with the brake materials discussed in Section 1.2.1, silicon and manganese act primarily as de-oxidising agents in tool steels, while chromium promotes the formation of carbides and gives greater abrasion resistance. Molybdenum and vanadium are strong carbide

formers; promoting secondary hardening (the precipitation of fine carbides at elevated temperatures during use or the tempering process) which strengthens and hardens the material rather than allowing it to soften. Molybdenum additionally promotes toughness and tensile strength, while tungsten is added primarily to improve wear resistance and hardness, which is retained at high temperatures. It is for these reasons that high-speed steels contain greater proportions of molybdenum and tungsten than other tool steels. Carbides formed with tungsten are extremely hard, while in high-speed steel tungsten produces a matrix that does not appreciably soften during tempering [11].

The finished properties of tool steels are greatly affected by their heat treatment during manufacture as well as their alloy composition. This is typically achieved by austenitising treatment followed by quenching (hardening) and tempering. In the first of these steps the material is heated above its eutectoid temperature, such that a solid solution of γ-austenite containing dissolved or partially dissolved alloying elements is present. Effective austenitising requires considerable periods of time (often hours, depending on cross-section), to ensure that the metallic alloying elements are able to dissolve and become homogeneously distributed throughout the material [14]. This is because solid state diffusion processes follow a standard Arrhenius relationship (Equation 1.1). This relationship indicates that the diffusivity of a given element X (D_X) is dependent on its frequency factor (D_0, which can be considered as the theoretical rate of diffusion at infinite temperature), activation energy (Q_X) and temperature (T) [13].

$$D_X = D_0 e^{-\frac{Q_X}{RT}} (cm^2 s^{-1}) \quad (1.1)$$

Using data collated by Honeycombe [13] and using the relationship given by Equation 1.1, it can be seen from Figure 9 that the diffusivity of common metallic alloying elements in iron, such as chromium, nickel and tungsten, are orders of magnitudes slower than those of the interstitial solution formers such as carbon and nitrogen at similar temperatures. In order for the metallic alloying elements to achieve the same diffusivity that carbon or nitrogen possess at room temperature, the temperature of iron ferrite must be raised to around 700°C. Above the eutectoid temperature, when the iron has transformed to austenite, these diffusivities fall as a result of the transition to the close-packed fcc structure.

Heating steels into the austenite region is essential for conventional heat treatments, due to its substantially greater solution capacity than ferrite. However, the close-packed nature of its face-centred cubic structure decreases diffusion rates even further, as greater amounts of energy are required to enable the movement of atoms in the lattice to allow for the diffusion of alloying elements through it [13].

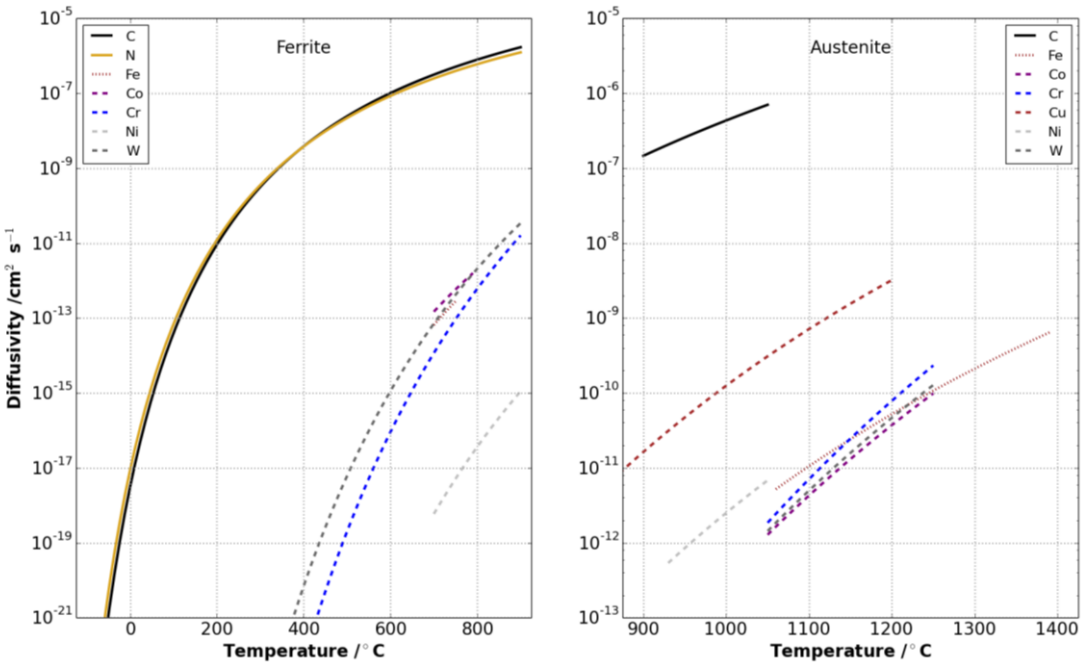

Figure 9 - Graphs showing the temperature dependence of the diffusivity of interstitial (solid lines) and substitutional (dotted lines) alloying elements in ferrite and austenite.

Following austenitising, the second step involves rapid cooling (by water, oil or gas) to transform as much of the material as possible into martensite. The austenite to martensite transformation occurs by a diffusionless shear reaction at high cooling rates, resulting in a supersaturated interstitial solid solution of carbon in α'-ferrite with a body-centred tetragonal structure. The newly formed martensite is strong but brittle, and the material may still contain small amounts of retained austenite even if the martensite finish (M_f) temperature has been passed. This is particularly true with high alloy contents that typically stabilise the austenite phase and slow its rate of transformation.

Not only does this retained austenite act to weaken the material overall, but during subsequent tempering it may decompose into ferrite and thin films of cementite which surround other nearby grains. This leaves long paths along grain boundaries where cracks may easily propagate, resulting in the embrittlement of the material [13]. Similar grain boundary cementite films are found in pearlitic materials, which are illustrated in Figure 10 surrounding ferrite grains in plain carbon steel. To avoid the formation of such films in tool steels it is desirable to reduce or eliminate retained austenite from the structure before subsequent tempering steps.

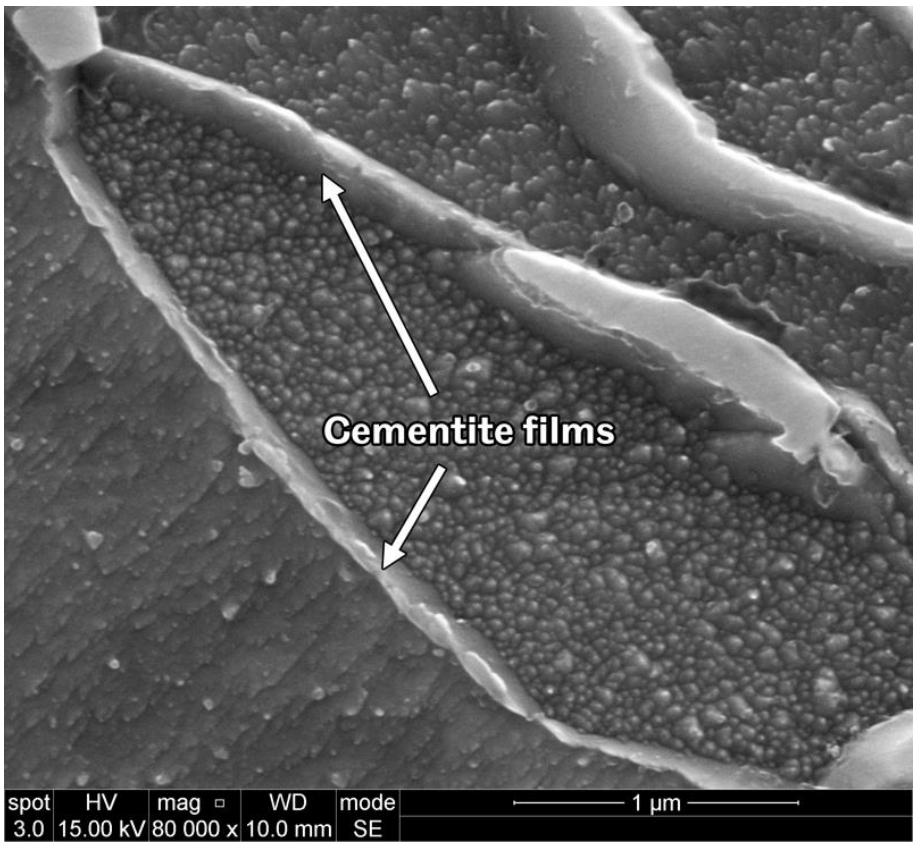

Figure 10 - Electron micrograph of cementite films along ferrite grain boundaries in a pearlitic carbon steel.

During the third step, the material is tempered at low to intermediate temperatures between room temperature and the eutectoid temperature. One of the consequences of this process is that carbon, which is rejected from the newly formed martensite, forms a dispersion of carbides which further hardens the material. While these carbides may initially precipitate as ε-carbide, which has a hexagonal close-packed structure, they typically grow into cementite and other alloy carbides, which may spheroidise at higher tempering temperatures and durations. Due to the further rejection of carbon from the supersaturated solid solution, the body-centred cubic structure of α-ferrite may return with further tempering [13].

By altering the chemical composition and heat treatments of tool steels it is possible to create materials with a wide range of desirable properties. Table 2 gives a summary of the different groups of tool steels and their characteristics as defined by the AISI system. Of course with any tool steel there is a solubility limit for these alloying elements, which inevitably means that trade-offs must be made. For instance high tungsten contents may produce very hard cutting tools at the cost of reduced toughness, whereas high molybdenum contents will give greater toughness, but reduced hot hardness. The intended use of a cutting tool (dry or wet machining, tough or hard workpiece material, continuous or interrupted cutting etc.) to a large extent therefore dictates the tool material used. Consideration also has to be given to the ease and economy of manufacturing tool bits and inserts. As can be seen from Table 3,

some of the most wear resistant tool steels (M-, T- and D-type) also have poor machinability, even in their annealed condition. This is an inevitable effect of the high percentage of alloying elements in these materials, which leads to the precipitation of hard carbides throughout the matrix.

Table 2 - General descriptions of AISI tool steel groups [41].

Type	Group	Description
W	Water-hardening tool steels	Lowest alloy content, low hardenability and shallow depth of hardening.
S	Shock-resisting tool steels	High toughness and fracture resistance, high strength and wear resistance to resist impact loading.
O	Oil-hardening tool steels	Very high wear resistance for cold-working conditions.
A	Air-hardening tool steels	High wear resistance under cold-working conditions, with varied hardness and toughness.
D	High carbon, high chromium cold-work tool steels	Extremely high wear and abrasion resistance. Excellent hardenability, but difficult to machine and grind.
P	Mold steels	Low carbon contents and hardness compared to other steels; enhanced by carburising.
H	Hot-work tool steels (Cr, W, Mo)	Cr: high-temperature impact loading resistance, thermal stability and thermal fatigue resistance. W: greater resistance to high-temperature softening. Mo: alternative to tungsten; provides resistance to high-temperature softening.
T	Tungsten high-speed tool steels	High hardenability, excellent wear resistance and red hardness.
M	Molybdenum high-speed tool steels	Similar characteristics to T-type steels, however will more readily decarburise so hardening must be done carefully.

Table 3 - Hardness and rankings (1 = best, 5 = worst) for characteristics of AISI tool steel groups (adapted from [41]).

Type	Hardness	Machinability	Toughness	Thermal stability	Wear resistance
M	60 – 70 HRC	4	5	1	2
T	60 – 68 HRC	4	5	1	2
D	54 – 61 HRC	5	5	3	2
A	35 – 67 HRC	4	4	3	3
H	34 – 60 HRC	4	3	3	4
O	57 – 64 HRC	3	4	5	4
P	28 – 64 HRC	4	3	5	4
S	40 – 60 HRC	4	2	5	5
W	50 – 64 HRC	1	3	5	5

Hardmetals offer a number of advantages over cast tool steels. With the hardness of typical hardmetal tool materials being twice that of the hardest tool steels and offering greater thermal stability and wear resistance, these materials are typically used for high volume manufacturing operations, where continuous and aggressive machining parameters are employed. Cutting tool materials such as tungsten carbides are commonly produced by liquid phase sintering and hot isostatic pressing (HIP). This process uses carbide and metallic powders produced by ball milling, which are mixed, pressed (along with a temporary 'wax' binder) and then sintered at temperatures close to the melting points of the metallic binder. As stoichiometric tungsten carbide

(WC) has a much higher melting point (in fact first decomposing into liquid W and solid C at 2780°C; see top of red highlighted region in Figure 11 (left)) than typical binders such as cobalt and nickel, it remains in solid solution during this process.

During a typical sintering cycle (shown in Figure 12) the press lubricant or 'wax' is removed during initial heating, before the furnace is evacuated and the temperature raised to facilitate oxide reduction. Below the eutectic temperature, solid state sintering occurs, during which the carbide phases begin to dissolve in the metallic binder. Further dissolution and precipitation of new phases (depending on composition, the high-temperature W_2C phase (see Figure 11 (left)), or cobalt-tungsten-carbides $Co_xW_yC_z$ or graphite [42]; typically due to excess tungsten or carbon respectively) occurs above the eutectic temperature, and porosity is nearly completely eliminated during liquid phase sintering [43]. The binder will wet, adhere to and engulf the other particles [44]. A metal matrix composite is formed in which hard carbides are 'cemented' in a metallic binder. Cobalt-tungsten-carbides (sometimes referred to as η-phase) and graphite should be avoided for cutting tool applications, as they may embrittle [45] or weaken the material respectively [42].

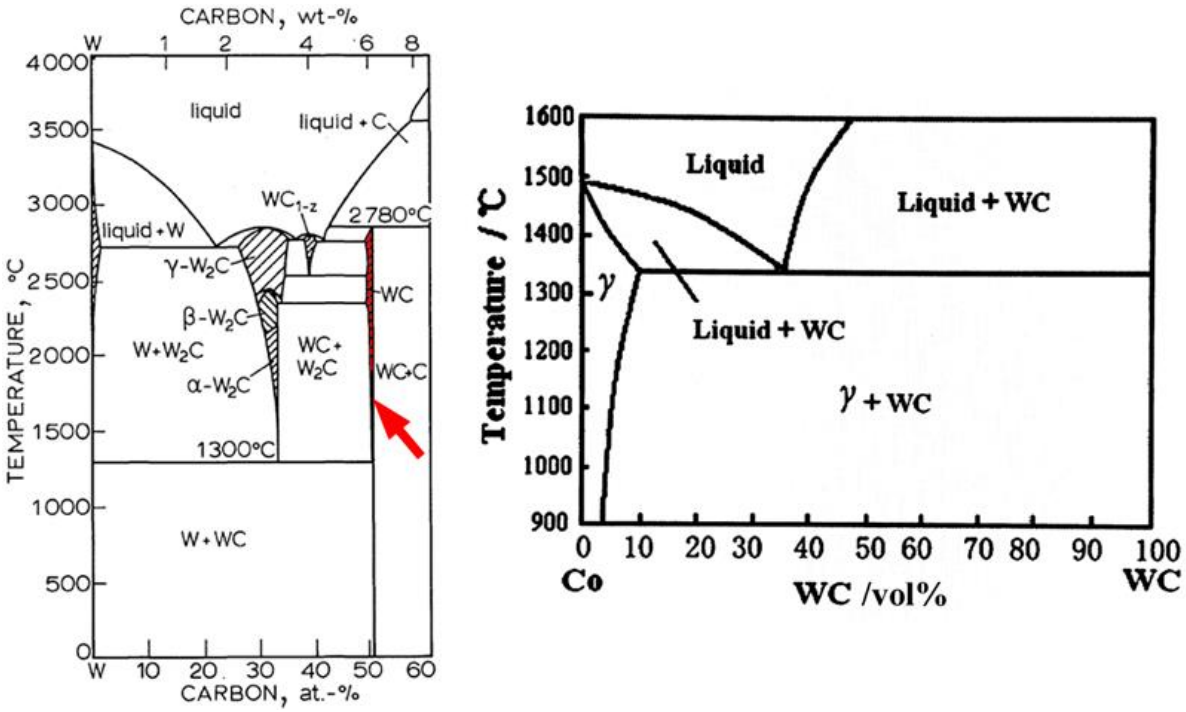

Figure 11 - Phase diagrams for (left) W-C system with WC phase region highlighted (adapted from Exner[46]) and (right) pseudo-binary WC-Co system (adapted from Sun et al. [47]).

Cobalt is the most commonly used binder for tungsten carbide cutting tools. The main reasons for this lie in its favourable wetting and adhesion characteristics, as well as good mechanical properties. Although pure cobalt has a hexagonal close-packed (hcp) structure at room temperature (transforming to face-centred cubic (fcc) at 417°C), the diffusion of W, C into cobalt stabilises the fcc phase down to room temperature (with W and C going into substitutional and interstitial solid solution with Co

respectively). This fcc phase is then stable through annealing [46]. As can be seen from the pseudo-binary diagram presented in Figure 11 (right), the dissolution of W, C into Co also has the effect of reducing the melting temperature of the binder phase to around 1300°C. Sintering temperatures are therefore generally just above this, between 1300 – 1400°C, to ensure good wetting of the carbide grains occurs [48].

The fine grain sizes (<5μm) and uniform microstructures of sintered carbides are what give them substantially greater hardness and wear resistance than cast tool steels. Diffusion of the carbide phase in the binder is critical in grain growth, therefore rapid sintering processes at lower temperatures should promote the finest grain sizes and most desirable mechanical properties [47]. However, this presents a particular challenge in the creation of ultrafine carbides (grain sizes <0.5μm) as the diffusivity and solubility of W, C in fcc Co are quite high near the eutectic temperature, and higher still in the Co liquid phase [49]. Interestingly, while carbide grains are typically quite fine, recent investigations using electron back-scatter diffraction (EBSD) by Mingard et al. [50] have demonstrated that the cobalt binder forms an irregular three-dimensional 'skeleton' through the material, with large regions (100 – 200μm across) possessing the same crystallographic orientation. Although it would be tempting to assume these massive regions represented individual cobalt grains, the authors stress that further investigations are needed to properly characterise their perimeters and properties.

The use of sintering and processes such as hot isostatic pressing allows superior cutting materials to be produced than by other methods. As a result of HIP P/M materials can be produced with near 100% density and, because of the uniform pressure applied from all directions, isotropic properties as well. The resulting material is extremely strong and wear resistant (as seen by comparing e.g. hardness values of tool steels and cemented carbides in Table 4) as, on a microstructural level, HIP creates grains of nearly uniform size and distribution; a feature which is very difficult to achieve by casting or forging [44].

In the manufacture of cutting tools, the WC-Co system is often enhanced through the addition of cubic carbides, to give WC-MC-Co systems (where M = Ti, Ta, Nb, Hf, V) [43]. These cubic carbides can substantially improve wear resistance and hardness, as highlighted by the properties given in Table 4, where it can be seen that the hardness of WC-5.8%Co-0.2%VC-0.2%TaC is approximately 20% greater than that of the more basic WC-6%Co material, although with some loss of compressive strength.

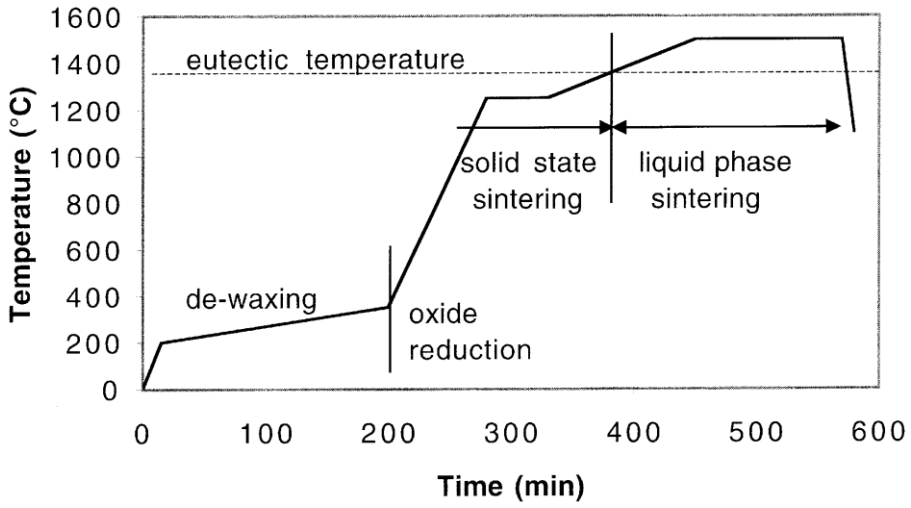

Figure 12 - A typical heat treatment cycle for sintering of cemented carbides [43].

Cubic boron nitride (CBN) is now commonly used in hard turning operations on steel. Its high hardness and wear resistance, as well as lack of chemical affinity for iron (unlike diamond) make it suitable for machining hardened steel parts. This reduces the number of operations required, for instance by removing the need for grinding that can cause significant temperature gradients near the surface of the workpiece that can cause thermal deformation and phase transformations, thereby removing the need for separate heat treatment (annealing and hardening) steps. In a review on the use of polycrystalline cubic boron nitride (PCBN) tools, Dogra et al. [51] identify the different characteristics of PCBN tools dependent on the binder present. High CBN content tools have the greatest toughness, but suffer from adhesion with the workpiece due to the presence of metallic binders. Low CBN content tools with ceramic phases have greater chemical stability and high temperature diffusion resistance, making them more suitable for continuous cutting operations, while binder-less CBN tools have superior thermal properties and abrasion resistance.

Table 4 - A summary of the features and properties of common industrial cutting materials [39, 52, 53].

Material category	Description	Hardness /MPa	Compressive strength /MPa
Hard coatings	Diamond	78480 – 98100	-
	Diamond-like coatings (DLC)	39240 – 58860	
	CBN thin films	44145	
	Ti_2N, TiN, Ti(C,N), (Ti,Al)N, CrN	17658 – 31392	
Soft, self-lubricating coatings	MoS_2	<981	-
Cubic boron nitride	Polycrystalline product that can be formed with ceramic or metallic binders, or pure.	45000 – 55000	-
Cemented carbides	Metal matrix composites with carbide aggregates in metallic binders. Aggregates include WC, TiC, SiC and TaC.	17069 (WC-5.8Co-0.2VC-0.2TaC)	3350
		14175 (WC-6Co)	3538
Tool steels	Complex Fe-C alloys with Si, Mn, Cr, Mo, V, W.	3924 – 7848	1500 – 4000

Tool steels and cemented carbides are important materials in low-cost, mass production as well as some high-end machining operations. Studies on the effects of deep cryogenic treatment on the tribological performance, tool wear and metallurgical structures of these materials are presented in Chapters 4 (tool steels) and 5 (tungsten carbide).

1.3. The cryogenic processing industry

While cryogenic processing has been used as an industrial technique for over 80 years, arguably a cryogenic processing industry has only existed for around 40 years, as awareness and understanding of cryogenic treatment has grown. While the majority of established companies can be found in the USA and the EU (primarily in the UK), interest in cryogenic treatment is growing in rapidly developing, heavily industrial economies such as India and China.

1.3.1. The state of the industry today

A range of cryogenic treatment companies can be found around the world. Although the majority of these reside in the United States, there are notable others in Europe and Australasia. The oldest of these, 300° Below Cryogenic Tempering Services, Inc. was established in 1966 (as CryoTech), however, the majority of cryogenic treatment companies have started up in the past thirty years. The industry is therefore dominated by small- and medium-sized enterprises (SMEs).

Cryogenic treatment companies offer a range of services, including cryogenic nitrogen and helium treatments, thermal cycling, as well as pre- and post-cryotreatment tempering of finished parts and raw materials. A number of these companies additionally supply cryogenic processing equipment, both to industry and research institutions. Table 5 summarises the services offered by some of these companies, indicating typical soaking temperatures (T_s), times (t_s), treatment types, liquid helium (LHe_2) processing capabilities and an overview of the equipment they offer.

It is interesting to note that the range of services offered by these companies reflects the variety of results highlighted in the published literature in Section 1.2. In fact it is possible to relate most of the differences between treatment parameters offered by these companies with the microstructural changes of martensitic ferrous alloys, which are discussed in Section 2.2.3, by association with their temperature- or time-dependence. These changes have been summarised in Table 6 for reference.

Table 5 - Examples of cryotreatment companies and their advertised service capabilities.

Company (location)	$T_{s,min}$ /K	t_s /hr	Treatment types	LHe_2?	Equipment supplied
300° Below Cryogenic Tempering Services, Inc. (Illinois, USA) Est. 1966	88	72 (total process)	N_2 atmosphere.	N	Model 921 processor: Electrical and nitrogen cooling, 682kg capacity, 2.5kW.
Controlled Thermal Processing, Inc. (Illinois, USA) Est. 1980	88	n/a	Air cooled by heat exchange with LN_2.	Y	Applied Cryogenics, Inc processors: 0.2-1.2m^3 capacity, post-cryo tempering, 4.4-11kW.
CryoPlus, Inc. (Ohio, USA) Est. 1994	88	10	Pre-cryo temper; LN_2 spray (vaporises).	N	n/a
Cryogenic Institute of New England, Inc. (Massachusetts, USA) Est. 2002	88	24	LN_2 immersion.	Y	Batch and continuous cryogenic treatment equipment: 88-878K range.
Cryogenic Treatment Services Ltd. (Nottinghamshire, UK) Est. 2004	78	24	N_2 atmosphere; Post-cryo temper.	N	n/a
Cryogenics International (Arizona, USA) Est. 1986	78	24-62	N_2 atmosphere	N	Treatment systems up to 0.8m^3 capacity.
Frozen Solid (Cambridgeshire, UK) Est. 1998	78	Material dependent	N_2 atmosphere; Post-cryo multi-stage tempering.	Y	n/a

Whereas the elimination of retained austenite is theoretically achieved once a material passes the martensite finish (M_f) temperature, the development of smaller secondary carbides and nano-carbides is also time-dependent, meaning both lower treatment temperatures and longer soak times may have beneficial effects. In fact, as is subsequently discussed in Section 2.2.3, both these changes have not only shown to be time-dependent, but intrinsically linked. The issue of pre- or post-cryotreatment tempering is material-dependent and related to the initial phase composition of any treated material.

Table 6 - Summary of the dependence of microstructural changes due to cryogenic treatment in ferrous alloys.

Microstructural change	Parameter dependence
Conversion of retained austenite to martensite	Temperature only (theoretically)
Precipitation of nano carbides	Time, temperature
Dispersion and refinement of secondary carbides	Time, temperature

As a result of these factors no cryogenic treatment company should offer a single, 'one-size-fits-all' cryotreatment service. Cryotreatment parameters should be varied to suit the material and degree of microstructural change or performance required. For large and repeated batches of materials or parts to be treated, an optimised cryotreatment cycle may represent a significant saving in terms of overheads and

reduction in the quantity of cryogenic coolant required. Indeed, for the cryogenic processing industry, it is in this optimisation of processes where commercial advantage and valuable intellectual property may lie. However, the extensive materials characterisation facilities and high-level of expertise required to determine the parameters of these optimal processes have so far prevented acknowledged leaders in commercial cryogenic treatment services from emerging.

1.3.2. Current uses of cryotreatment processes

Cryogenic treatment companies (such as those mentioned in Section 1.3.1) are involved in a combination of commercial processing and after-market treatments, with the former becoming increasingly more significant. Although initially cryotreatment services were applied almost exclusively to products in their finished forms, it has increasingly become part of larger manufacturing chains; an example of this being the treatment of cutting tool inserts prior to coatings being applied, as cryotreatment has been shown to have adverse effects on coatings such as TiN [54]. However, products such as brake discs, sports equipment and audio cabling are often still treated in their finished forms or after partial disassembly.

Research-led and commercial cryotreatment practices differ significantly, as highlighted in Table 7. Likely due to the basis of many cryotreatment operations on purely anecdotal evidence rather than rigorous analysis, there are a number of examples of 'bad practice' within the commercial cryogenic processing industry, from the point of view of the research community. These include the restriction of cryogenic treatment parameters (as discussed in Section 1.3.1), the use of anything other than nitrogen atmosphere cooling, and the almost exclusive use of cryogenic treatment as an 'after-market' process.

Table 7 - Summary of differences between research-led and commercial cryotreatment practices.

Research	Commercial
Varied cryotreatment parameters.	Restricted treatment parameters, often only one fixed cycle offered.
Wide consensus around use of N_2 atmospheric cooling for best results.	Varied cooling practices (LN_2 immersion, LN_2 spray, N_2 atmosphere, LN_2 heat exchange with air).
Recognition of need to understand cryotreatment holistically within heat treatment cycles.	Cryotreatment typically applied as an 'after-market' process.
Small batch sizes.	Large batch sizes.

1.3.3. The future of cryotreatment and its applications

Although ferrous-based alloys and cobalt-bonded tungsten carbides feature in the bulk of cryogenic processing research and constitute a significant portion of commercial

cryotreatment service requirements, a number of other materials have also been shown to benefit from cryogenic treatment.

Aerospace materials such as aluminium and magnesium alloys represent a developing area for cryogenic treatment. In a study by Lulay et al. [55] it was determined that DCT at -196°C (77K) caused a significant (12%) increase in the impact energy of 7075-T651 aluminium alloy, without any significant change in strength or hardness. It is interesting to note that specimens held at their soak temperature for 2hrs showed no significant improvement, whilst those treated for 48hrs did, indicating a time-dependent microstructural change is likely responsible. In a study on the effects of cryogenic treatment on AZ91 magnesium alloy (which is typically used in castings), Asl et al. [56] observed improved wear resistance and creep behaviour after DCT at -196°C (77K). The improved creep behaviour was attributed to morphological changes which prevented grain boundary sliding at high temperatures.

For space applications, alloys of titanium and magnesium have been tested at cryogenic temperatures, usually by direct immersion in liquid nitrogen. Sun et al. [57] performed mechanical tests on Ti-2.5Cu alloy at temperatures of 77K obtained by this method, finding that both the ductility and low-cycle fatigue life of the alloy was improved. They conclude that nano-scale precipitates hinder the movement of dislocations, thereby preventing crack formation. Similar tests were performed by Xiong et al. [58] to determine the tensile properties of an extruded MgGdYZr(Mn) alloy at cryogenic temperatures. Their results showed a significant increase in tensile strength, yield strength and elongation before fracture, which they attribute to the precipitation of a large number of "rod-like, tree-like and chrysanthemum-like" features within the microstructure. While direct immersion in liquid nitrogen, or cryo-quenching may lead to thermal shock and brittleness of materials, these investigations seem to show that the microstructural changes due to DCT may have a more significant effect on the performance of a material.

Cryogenic processing has also been shown to have beneficial effects on non-metallic composite materials, such as the PTFE/Kevlar hybrid fabric tested by Zhang et al. [59]. Typically used as bearing liner materials due to their tribological properties, PTFE and Kevlar exhibit poor adhesion to the resin binder due to their chemically inert nature. Cryogenic treatment was shown to improve the wear resistance of the hybrid material, with the improvement suggested to be as a result of increased mechanical interlocking of the phenolic resin used, as a result of the fabric roughening at cryogenic temperatures.

1.4. Aim and objectives

The aim of this work was to address the deficiency in scientific and industrial understanding as to the effects and applications of cryogenic processing, in a range of common engineering materials, through a combination of physical testing and microstructural analysis techniques.

The following objectives were set in order to meet the aim of the project:

1. Review the current state of the art in cryogenic processing technologies and techniques, its effects on industrially important materials and the focus of current research efforts, to identify areas in which knowledge is deficient and therefore facilitate investigations to be undertaken of value to industry and the research community.
2. Conduct laboratory-based tribological tests to provide comparative data indicating the relative performance of a range of ferrous alloys including a grey cast iron, a non-alloy steel and three tool steels following deep cryogenic treatment.
3. Conduct workshop-based tool wear development tests to provide indicative data on the relative performance of sintered tungsten carbide tools during typical machining operations following deep cryogenic treatment.
4. Conduct microstructural examinations of a range of important engineering materials. Ferrous alloys and a sintered tungsten carbide material will be analysed to form a comparative study of the effects of deep cryogenic treatment on a range of engineering materials.
5. Further characterise the microstructures of materials showing the most significant performance changes observed during laboratory-based or applications-based testing, identifying the changes responsible for modifying wear behaviour in cryogenically treated materials, and suggesting what metallurgical mechanisms are active, in the materials studied, during cryogenic treatment.

1.5. Thesis structure

The research presented here is structured to match the objectives laid out in Section 1.4. A thorough review of cryogenic treatment technology, processes and effects is conducted before experimental methodologies are explained and the results from tribological laboratory testing and tool wear testing are presented. A discussion follows to highlight the relationships between experimental results, published

research and the fundamental mechanisms at work before the conclusions of the research presented here are summarised. Table 8 summarises this structure.

Table 8 - Summaries of chapter contents.

Chapter	Summary of content
1	History of cryogenic treatments; motivations for research; background literature studies; aim and objectives of this research.
2	Studies on the technology and processes of cryogenic treatment, and reported changes in material properties and microstructures as a result.
3	Overview, rationale, explanation and limitations of experimental methodologies selected.
4	Results and analyses from pin-on-disc and reciprocating sliding tests performed on brake rotor (SAE J431 G10, EN10083 C50R) and tool steel (AISI A2, D6, M2) materials respectively.
5	Microstructural characterisation of EN10083 C50R steel by high-resolution scanning electron microscopy, transmission electron microscopy, X-ray diffraction, electron back-scatter diffraction and electron diffraction.
6	Results and analyses from tool wear development tests performed on tungsten carbide turning inserts (SHM H13A).
7	Discussion linking results, literature and mechanisms responsible for changes in material properties and performance due to cryogenic treatments.
8	Summary of conclusions and list of publications arising from this work.
9	References of cited works and sources.
10	Appendices corresponding to Chapters 1-4 – i.e. Appendix 10.x relates to Chapter x.

1.6. Summary

Cryogenic processing (alternatively known as cryogenic treatment or 'cryotreatment') refers to a range of sub-zero heat treatments that are currently applied to batches of materials and components, predominantly by specialist companies offering after-market services. It involves cooling materials to temperatures below 193K (-80°C) with the objective of permanently or semi-permanently altering their microstructures in such ways as to offer performance improvements, increased wear resistance and ultimately increased service life of components and tools.

Widely available published research in this field extends back to 1973 (although it is likely a significant body of research exists in now defunct publications from the former Soviet Union dating from up to two decades previously), with the majority of studies focusing on the effects of cryogenic treatment on tool steels, although the past decade has seen a number of publications relating to tungsten carbide tool materials as well. Minor areas of research include valve steels, light alloys and composite materials.

Commercial cryogenic processing companies are mainly found in the USA and the EU, although there is strong interest from major economies such as India and China. Most of these companies exist as small and medium-sized enterprises (SMEs) who, due to the lack of coherence in the published literature as to the fundamental mechanisms at work during cryogenic treatments, offer a range of treatment parameters and

processes; some of which are inherently flawed and most of which are not optimised to achieve the maximum benefits with minimum consumption of materials (such as liquid nitrogen) and with the minimum processing times.

As the bulk of cryogenic treatment services are applied to automotive brake rotors and industrial cutting tools, common materials from these groups were selected for study. While a large body of research exists on the effects of cryogenic treatments on hardened martensitic tool steels (as discussed in Chapter 2), there is minimal scientific literature concerning its effects on grey cast irons and plain carbon steel brake rotor materials, which are nonetheless commonly cryogenically treated. The use of cryogenic treatments as part of an alternative processing route to conventional heat treatments (e.g. of tool steels) has yet to be explored, while their application to tungsten carbide tool materials represents a growing area of research.

The research presented here comprises a mixture of experimental testing and microstructural analyses. By comparing the results of these analyses with published results and theories, the research presented seeks to address some of the deficiencies in scientific and industrial understanding as to the effects of cryogenic treatments on the range of important engineering materials highlighted, which includes grey cast iron, plain carbon steel, tool steels and cobalt-bonded tungsten carbides.

2. A review of cryogenic processing technology, treatments and effects

While sub-zero treatments of materials have arguably been possible for centuries through the exploitation of naturally occurring environmental conditions, cryogenic treatments have only been practically possible since the liquefaction of a number of important gases (notably nitrogen and helium) was achieved in the late 19th Century. Following the industrialisation of these processes in the first half of the 20th Century cryogenic treatment started to be used on a significant scale in manufacturing. Since then advances in insulation, temperature sensors and digital controllers have allowed the development of the efficient cryogenic processors used commercially today.

In this chapter the state-of-the-art of cryogenic treatment is presented, starting with an overview of cryogenic treatment processes and commonly discussed parameters. A literature survey follows in which current published understanding is discussed, with areas of disagreement, confusion and opportunity being highlighted. It is these areas of opportunity that provide the focus for the research presented.

2.1. Cryotreatment technology and processes

Cryotreatment commonly involves a supply of liquid nitrogen into a thermally insulated tank containing the parts or materials to be treated, although specialist treatments are also available using liquid helium. The cryogenic fluid can be used in one of three ways: for direct immersion of parts to perform a 'cryo-quench'; as a working fluid to cool air within the tank; or as a gas that that is circulated by fans, thereby creating a 'dry' atmosphere.

Cryo-quenching risks causing thermal shock [60], where damaging thermal stresses are established by large temperature gradients between the surface and bulk of a material, while cryogenic cooling of air can lead to the build-up of vapour ice on the surfaces of components, unless all moisture can be removed beforehand. Using gaseous nitrogen or helium creates a largely inert atmosphere within the tank and has neither of these drawbacks [61], while allowing for the controlled cooling of parts and materials. Cryogenic treatments using liquid nitrogen and liquid helium are theoretically able to reach 77K (-196°C) and 5K (-268°C) respectively; the temperatures at which they boil. Due to its abundance (making up 78% of the Earth's atmosphere) nitrogen is commonly used in cryotreatment, whereas helium is reserved for extremely specialised use.

Figure 13 illustrates the difference between cryotreatment cycles involving cryo-quenching (CQ) by liquid nitrogen (LN_2) and cooling or cryotreatment (CT) by gaseous nitrogen (N_2) following on from a regular heat treatment cycle in a typical quench-hardened carbon steel, and preceding a post-treatment tempering cycle. As cryogenic treatments are typically offered as an after-market service, parts and materials are subjected to an indefinite 'transition' period between regular heat treatment and cryotreatment. In reality, tempering may have been performed prior to cryogenic treatment, which at best represents wasted process time and in the worst case inhibits the effective application of cryogenic treatment; such as when tempering may cause the decomposition of retained austenite into cementite and ferrite (as previously discussed in Section 1.2.2.3).

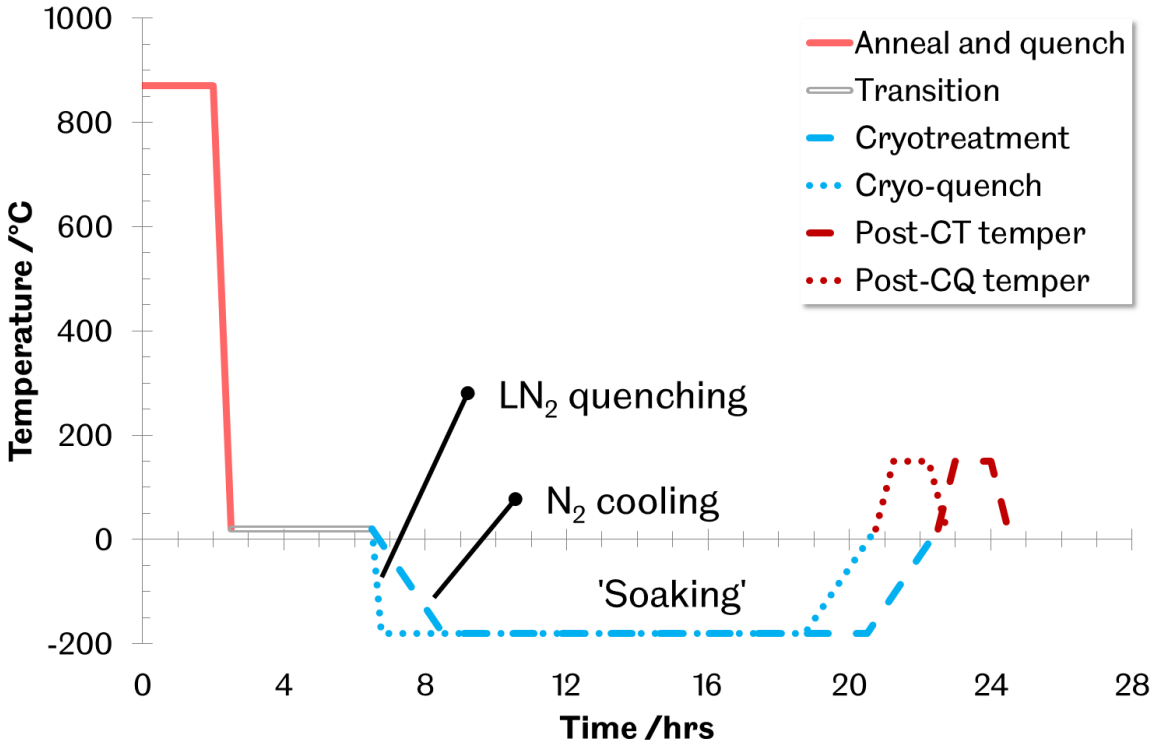

Figure 13 - Cryotreatment cycles illustrating liquid nitrogen quenching and gaseous nitrogen cooling. The 'Transition' line indicates an indefinite period of time for transport and storage prior to cryotreatment.

The most common practice is to carry out cryotreatment using gaseous nitrogen as the cooling medium. Figure 14 shows a schematic diagram for such a setup in which liquid nitrogen is held in an external tank or reservoir, before being vaporised, pumped into an insulated chamber and blown around the parts to be treated by fans. The flow of nitrogen is controlled by the temperature inside the chamber which is measured by thermocouples. To avoid the thermal shock associated with cryo-quenching, cooling and heating rates in the chamber typically fall within the range of 0.1 – 2.0K/min.

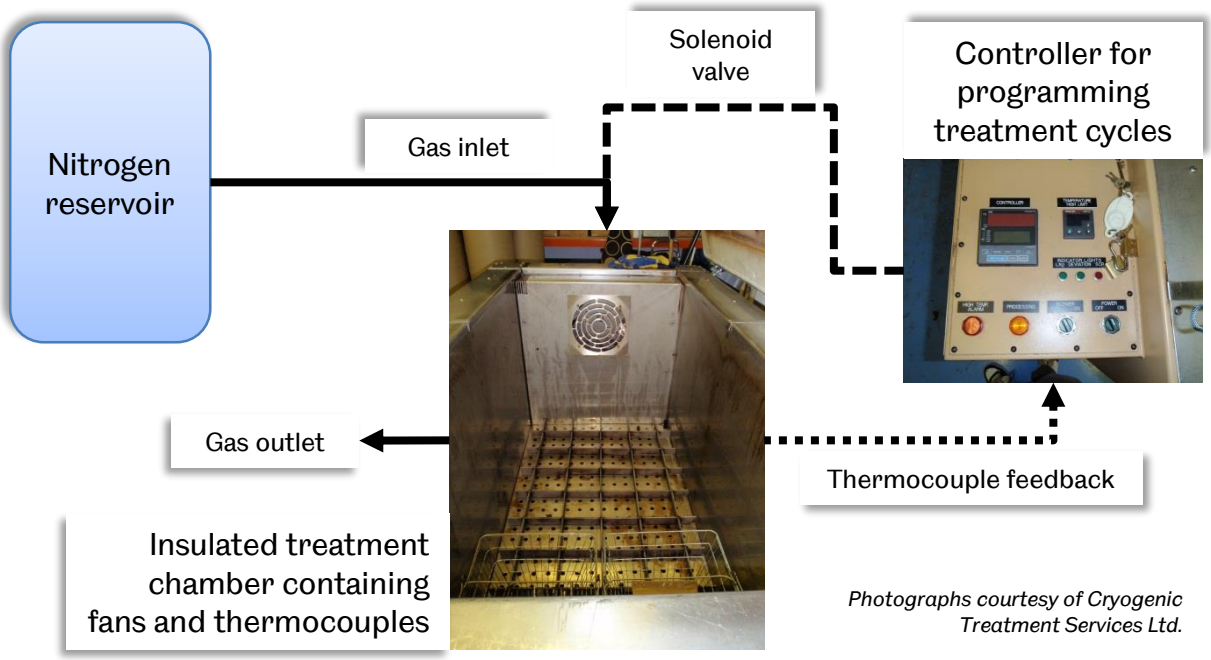

Figure 14 - Schematic of equipment for cryotreatment using gaseous nitrogen cooling.

The parameters that are typically controlled and varied during cryotreatment are: cooling rate, soaking temperature, soaking time, heating rate and the position of the cryotreatment within the overall treatment cycle in cases where materials or components are to be tempered. In their early study on AISI T8 and AISI 1045 steels, Barron and Mulhern [4] determined that the greatest increase in wear resistance for these materials could be achieved by using a low cooling rate (6K/min), a long soaking time (24h) and a low temperature (77K) soak. More recently, Darwin et al. [62] utilised Taguchi Design of Experiment methods, to determine the significance of parameters in maximising the wear resistance of a high-chromium martensitic steel through deep cryogenic treatment. They determined that the significance of parameters was as follows: (1) soaking temperature, 72%; (2) soaking time, 24%; (3) rate of cooling, 10%; (4) tempering temperature, 2%; and that the tempering period was statistically insignificant.

The on-going development of cooling agents has led to the establishment of different classifications of sub-zero treatments. By soaking temperature these are either cold treatments which can be achieved with dry ice (CT: 273-193K), shallow cryogenic treatments (SCT: 193-113K) or deep cryogenic treatments (DCT: 113-77K) which both require liquid nitrogen [63].

One of the key commercial factors supporting the adoption of cryotreatment is its relatively low cost, both in terms of the equipment required and running costs per treatment cycle. Although a number of companies treat small batches of finished components for the automotive, aerospace and manufacturing industries, as well as treating more novel items such as sports equipment, cryotreatment is not yet a widely

used industrial process despite reported evidence indicating substantial improvements in wear resistance, hardness and fatigue scatter reduction. The reasons for this lie in the lack of any cohesive understanding of the physical effects of cryotreatment on the microstructure and composition of treated materials, although a number of substantial studies have been carried out [5].

2.2. Current understanding of the effects of cryotreatment

Research into the effects of cryotreatment on materials has largely been confined to commonly used tool steels and manufacturing applications. This is understandable due to the benefits that have been seen in machining processes since tooling began to be cryotreated as far back as the 1930s. More recent studies have considered its application to other tool materials, such as sintered tungsten carbides, as well as common aerospace and automotive materials, such as the investigation by Lulay et al. [55] on the effects of cryotreatment on the mechanical properties of 7075 aluminium alloy, and that of Asl et al. [56] on how cryotreatment effects the microstructure, creep and wear behaviours of AZ91 magnesium alloy. However, as the research presented here concerns ferrous alloys and sintered tungsten carbides, other materials are omitted from this review.

With the exception of the early works of Barron and Mulhern [3, 4], often lacking in the literature are studies on some of the most basic or commonly used alloys, with most preferring to investigate complex alloys used in demanding applications. This makes it difficult to draw conclusions as to how the composition of the material and its heat treatment history benefits or inhibits cryotreatment, and therefore allow the most suitable alloys for cryotreatment to be identified.

2.2.1. Mechanical properties

In some of his early research on the effect of cryotreatment on tool wear during turning operations, Barron [2] performed Rockwell-C hardness and Charpy impact tests on two high-speed steel tool alloys. Treating the alloys using a LN_2 quench and soaking method, he determined that cryotreatment had no effect on the hardness of the materials, but reduced their impact strengths by up to 65% depending on the soaking time allowed. This supports the suggestion by Preciado [60] that cryo-quenching techniques can lead to thermal shock and brittleness in treated materials.

Investigating the effect of altering the order of treatment processes (whether tempering is conducted before or after cryogenic treatments), Yan et al. [64] demonstrated that the hardness of a high speed steel (W9Mo3Cr4V) could be improved by approximately 2 HRC if deep cryogenic treatment was followed by tempering. It was similarly shown that the impact toughness of the material could be

increased from 0.34 MJ/m^2 to 0.45 MJ/m^2 using this processing route, whereas only marginal improvements were seen when conducting tempering before cryogenic treatments.

Molinari et al. [65] investigated the effects of DCT on the properties of high-speed steel (HSS) tools. They determined that DCT had a noticeable effect on the micro-hardness of some materials: in their investigation the hardness of an ASP 60 spline forming tool increased from 9350±196 to 12100±226MPa $HV_{0.4905}$ (+29.5%) whereas the hardness of an AISI M2 drill showed no change from 8730MPa $HV_{0.981}$. They noted, however, that the standard deviation of hardness on its cross-section decreased from 628 to 216MPa. Interestingly, they were able to show during dry sliding wear testing of AISI M2 steel that the wear rate was significantly reduced due to DCT and was directly related to an increase in macro-hardness from 8100MPa to a maximum of 8770MPa $HV_{294.3}$ (+8.2%) after quenching and two tempering cycles followed by DCT. Using V-notched Charpy specimens they also showed that the impact energy of the material remained the same after DCT at 2J. As Molinari et al. employed the gaseous nitrogen cooling technique rather than cryo-quenching, they avoided the extreme brittle behaviour seen by Barron.

Alongside their work on HSS tools, Molinari et al. conducted tests on AISI H13 hot work tool steel; measuring hardness, impact energy and fracture toughness. They determined that DCT had no significant effect on hardness or impact energy but increased fracture toughness from 42.8 N/mm$^{3/2}$ to 49.1 N/mm$^{3/2}$ (+14.7%, although the units appear to be erroneous – the same values in MPa m$^{1/2}$ would seem appropriate), again after two tempering cycles and DCT. More recently Koneshlou et al. [66] conducted a range of tests on AISI H13 tool steel using similar treatment cycles to those employed by Molinari et al. that are summarised in Table 9. As can be seen, the most significant differences are the soaking times during cryotreatment, and the order in which tempering and cryotreatment cycles were carried out. Koneshlou et al. found that DCT increased the ultimate tensile strength of H13 tool steel from 1580MPa up to a maximum of 1720MPa (+8.9%), its hardness from 49 HRC to a maximum of 59 HRC (+20.4%) and its impact energy from 15.4J to 18.2J (+18.2%). The greatest improvements were found when the material was quenched, tempered, cryotreated and tempered again.

Table 9 - Heat treatment parameters for AISI H13 tool steel applied by Molinari and Koneshlou.

	Molinari et al. [65]	Koneshlou et al. [66]
Hardening (Q)	1020°C – vacuum-quenched	1040°C for 30mins – air-quenched
Tempering (T)	570°C for 3hrs	560°C for 2hrs
Cryotreatment (C)	-196°C for 35hrs	-196°C for 8hrs
Treatment order	QTTC	QTCT

The effects of various sub-zero treatments on fracture toughness have also been investigated by Das et al. [67], who focus their work on AISI D2 tool steel. Conducting three-point bend tests on specimens having undergone cold treatment (198K), SCT (148K) and DCT (77K), they observed that sub-zero treatments reduced the fracture toughness of the material in all cases, with the smallest reduction being seen following DCT (36.5MPa $m^{1/2}$ to 24.0MPa $m^{1/2}$). The SEM micrographs shown in Figure 15 identify the causes of fracture regions seen by Das et al. as being cracking of large, elongated primary carbides and the formation of microvoids caused by the decohesion of secondary carbides.

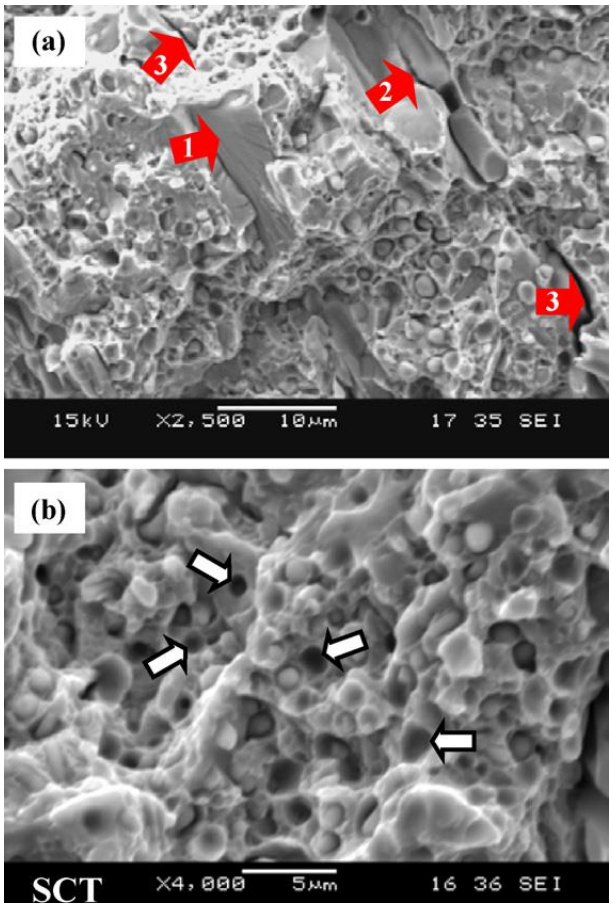

1. Cleavage facets in primary carbides.
2. Cracking of primary carbides.
3. Cracking at the interface between primary carbides and matrix.

White arrows indicate microvoids formed by decohesion of secondary carbides.

Figure 15 - SEM micrographs of fracture surfaces of AISI D2 steel as observed by Das et al. [67].

Baldissera investigated the effects of varied cryogenic treatments (soaking temperatures of 143K and 88K, soaking times of 9hrs and 24hrs) on the hardness and tensile properties [68], and the fatigue and corrosion resistance [69] of AISI 302 stainless steel. Although reported changes in tensile properties or hardness showed no conclusive trends, Baldissera highlights the need for an atomic scale approach to investigate the effects that cryogenic treatment may have on properties such as elastic modulus. Although DCT displayed no significant effects on the fatigue life or corrosion resistance of AISI 302 received as standard, it was shown to cause a significant improvement in the fatigue life of specimens having undergone solubilisation treatment at 1325K prior to DCT. Further, the results suggested that this improvement

was not dependent on an extensive soaking time, with no significant differences seen between specimens treated for 9hrs and 24hrs.

Zhirafar et al. [70] performed a range of treatments and mechanical tests on AISI 4340 steel, differing from many authors by choosing a relatively basic and commonly used material. After austenitising the steel at 845°C and performing an oil quench, a single tempering cycle of 200°C, 300°C or 455°C was applied, in half of the samples preceded by DCT using gaseous nitrogen for slow cooling and with a 24 hour soaking period. These treatment cycles are illustrated in Figure 16.

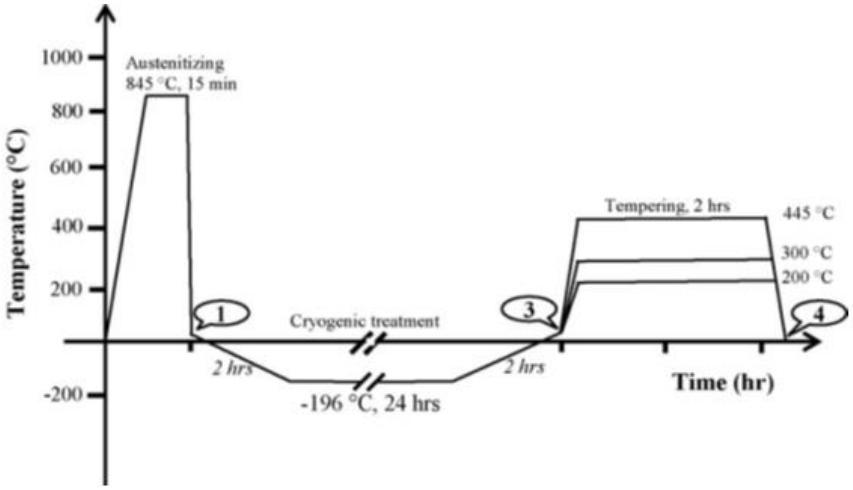

Figure 16 - Treatment cycles applied to AISI 4340 steel by Zhirafar et al. [70].

They reported that the greatest hardness was obtained by applying DCT immediately after quenching, with no tempering cycle. However, this gave a hardness value of 55.3 HRC compared to the just-quenched material at 54.5 HRC, which is within the margin of error given for their other data. The material hardness decreased with tempering, down to a minimum of 41 HRC and 42 HRC for the conventionally treated and cryotreated material respectively after the 455°C tempering cycle.

Contrary to other authors having applied a gaseous nitrogen cooling cycle, Zhirafar et al. reported that the impact energy of the steel decreased from 10.8J in the just-quenched condition to 7.7J after DCT (-28.7%), with the addition of tempering cycles significantly increasing the impact energy in all cases. These results are corroborated by the fracture features they observed, with reduced shear (S) fracture areas on the cryotreated specimen shown in Figure 17. Additionally, they showed that DCT increased the fatigue life of AISI 4340 steel and its fatigue stress limit by 25 – 30MPa at lifetimes of 10^7 cycles, which they attributed to increases in hardness and strength.

Research into the effects of cryogenic treatment on sintered carbides is largely confined to the last decade, with the majority of studies looking directly at the tool-life of cobalt-bonded tungsten carbide (WC-Co) tools under a variety of cutting conditions and when used to machine various common ferrous alloys. It appears that no work

has been published in the public domain on what effects cryogenic treatment has on the mechanical properties of these materials.

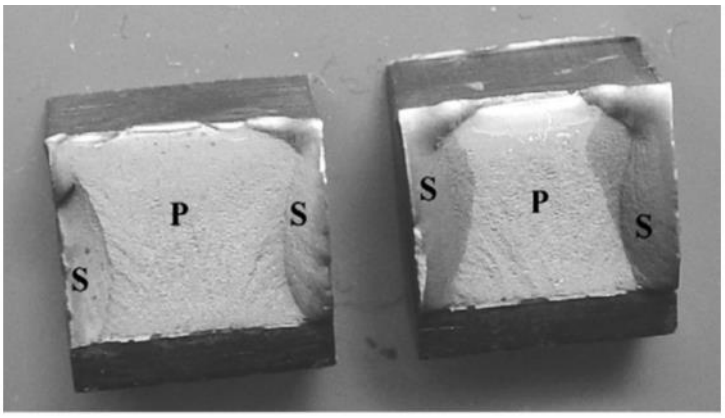

Figure 17 - Fracture features of AISI 4340 steel as observed by Zhirafar et al. [70].

A number of investigators have, however, determined the hardness of cryogenically treated WC-Co materials. Table 10 shows a summary of the reported data, from which it can be derived that the hardness of simpler WC-Co materials (those with minimal additional alloying components) is not typically affected by cryogenic treatment [71, 72], while more complex alloys show moderate improvements. Notable from the reported data are the studies of SreeramaReddy et al. [73], which indicate that cryogenic treatment may significantly improve the hot hardness of complex WC-Co alloys, as well as that of Gill et al. [45] which suggests that only shallow cryogenic treatments (163 – 193K) are required to increase the hardness of WC-Co.

Table 10 - Summary of hardness data reported for cryotreated WC-Co by previous investigators (where ?? indicates the presence of unknown additional alloying elements).

Investigators	Material description	Temp /°C	Treatment	Hardness (*change*)
Seah et al. [71]	WC-7Co-1??	Ambient	As-received	89.3 HRA
			Cryoquenched	89,4 (*+0.1%*)
			Cryotreated	89.4 (*+0.1%*)
			Cryo+Temper	89.4 (*+0.1%*)
			Cold treated	89.5 (*+0.2%*)
			Cold+Temper	89.7 (*+0.4%*)
Thakur et al. [72]	93WC-Co-??	Ambient	Untreated	17760 $HV_{19.6}$
			Cryotreated	17850 (*+0.6%*)
SreeramaReddy et al. [73]	Kennametal P-30	Ambient	Untreated / cryotreated	88.5 / 86.5 HRA (*-2.2%*)
	WC-17Co-1.4TiC-1.4TaC	100		85.0 / 86.0 (*+1.2%*)
		200		82.0 / 84.0 (*+2.4%*)
	Multilayer CVD coating: TiN: 1.5µm, TiCN: 12.5µm, Al_2O_3: 6µm, TiN: 5µm	300		81.0 / 83.0 (*+2.5%*)
		400		76.5 / 79.8 (*+4.3%*)
		500		73.0 / 78.0 (*+6.8%*)
		600		63.0 / 71.8 (*+14.0%*)
Gill et al. [45]	ISO-P25	Ambient	Untreated	88.2 HRA
	WC-6Co-1.4TiC		SCT	92.6 (*+5.0%*)
			DCT	92.8 (*+5.2%*)

Changes in binder and carbon concentrations at the surface, and the effects of compressive stresses induced in the WC phase as a result of cobalt hardening are known to influence the hardness of WC-Co materials. These factors are discussed in more detail in Section 2.2.3.

2.2.2. Tribological performance

The most significant portion of research into the effects of cryotreatment has focused on the abrasive wear resistance of ferrous-alloys in dry sliding conditions, due to the connection with industrial cutting processes. Of note as one of the earliest and wide-ranging studies is that already mentioned by Barron [3]. Abrasive wear tests were conducted using a block-on-ring type set up on twelve tool steels, three stainless steels and four others, having been subjected to DCT (77K) and SCT (189K). It was found that the wear resistance of some alloys increased by up to 718% (in the case of AISI D2 steel) due to DCT, whereas in others (including AISI A2, A6 and T2 steels) no significant changes were observed. This pattern of extreme performance improvements in some cases and no change in others is typical of the literature ever since. Reviewers have consistently drawn attention to this knowledge deficiency, with Gill et al. [5] noting that "the reported magnitudes of the enhancement in wear resistance and the proposed governing mechanisms for such enhancement do not provide any unified picture."

An exemplar of one of the few comprehensive studies so far has been that of Das et al. [74, 75] on the effects of sub-zero treatments on AISI D2 tool steel. Using pin-on-disc testing their investigation attempts to link wear resistance with the sub-zero treatment applied between conventional heat treatment (CHT) hardening and tempering cycles: cold treatment (CT: 198K), shallow cryogenic treatment (SCT: 148K) and deep cryogenic treatment (DCT: 77K). Discussing measured wear rates, mechanisms and features they conclude that all sub-zero treatments result in improved wear resistance, with the greatest improvement found following cryotreatment at the lowest temperature, i.e., after DCT. They also conclude that the magnitude of improvement over CHT decreases with the severity of wear test condition. Under a nominal contact pressure of 6.25MPa the improvements over CHT for CT, SCT and DCT were found to be 39%, 50% and 257% respectively, while at a pressure of 10.93MPa the improvements were 12%, 21% and 83% respectively. Hardness tests were also performed, indicating improvements in macro-hardness (HV_{60}) of 2.6%, 3.8% and 8.1% as well as improvements in micro-hardness ($HV_{0.05}$) of 2.9%, 4.3% and 11.4% due to CT, SCT and DCT respectively. It is therefore clear from these data that the improvement in wear resistance cannot solely be attributed to any increase in hardness following cryotreatment.

Similar, but less comprehensive laboratory-based tribological studies have been carried out on a range of materials; a summary of which is shown by Table 11. All report broad improvements in wear resistance due to cryotreatment, though significant differences can be seen in the magnitude of such improvements (even between similar materials) and the changes, or lack thereof in hardness and material microstructure as discussed in Section 2.2.3.

Table 11 - Summary of reported changes in hardness and wear resistance of ferrous alloys due to cryogenic treatment.

		Hardness		Wear resistance	
Investigators	Material	Low	High	Low	High
Dhokey et al. [76]	AISI D3 tool steel	-8%	0%	+118%	+1257%
Akhbarizadeh et al. [77]	AISI D6 tool steel	0%	+5%	+5%	+68%
Koneshlou et al. [66]	AISI H13 tool steel	0%	+20%	+25%	+67%
Yan et al. [64]	W9Mo3Cr4V high speed steel	0%	+2%	+20%	+240%
Bensely et al. [78]	En353 (case carburised) steel	+3%	+3%	+85%	+372%
Jaswin et al. [79, 80]	En52	+5%	+86%	+15%	+42%
	21-4N valve steels	+4%	+12%	+9%	+24%
Liu et al. [81-83]	High chromium cast irons	< +57%		< +25%	
Wang et al. [84]	High chromium cast iron	+7%	+15%	0%	+19%

Alongside laboratory-based studies is a wide range of application-based testing on tooling commonly used in turning, drilling and milling operations. The performance of AISI M2 steel was investigated by da Silva et al. [85] using 10mm lathe tools, 7.5mm diameter twist drills and a milling cutter with a 3µm TiN coating. Following conventional quenching and a triple tempering cycle, the tools underwent DCT (-196°C) with a soaking time of 20hrs, after which they underwent a triple heating cycle to 196°C before being stabilised at room temperature. This cycle is illustrated in Figure 18.

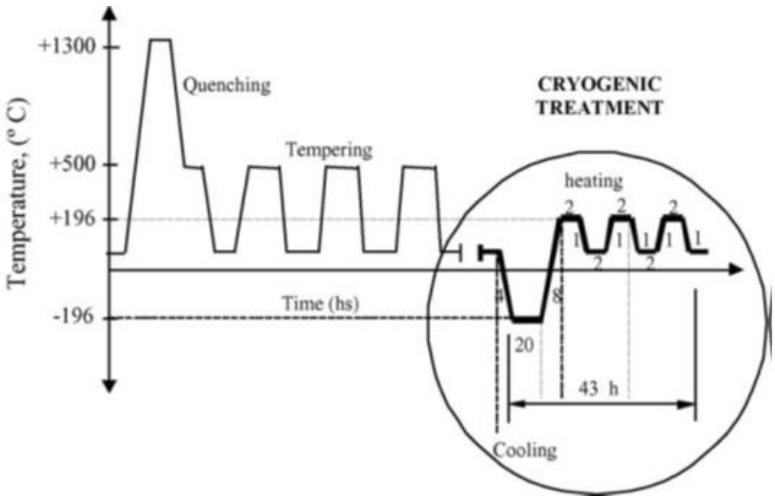

Figure 18 - Heat treatment cycle applied to AISI M2 HSS tools by da Silva et al. [85].

The lathe tools underwent Brandsma rapid facing tests in which an AISI 1020 disc undergoes face turning from the centre towards the periphery, with the spindle speed and feed rate kept constant such that the cutting speed increases throughout the test,

which ends with the destruction of the cutting edge. The cryotreated tools showed tool life increases of 12.5%, 44.0% and 21.0% at spindle speeds of 140, 180 and 224rpm respectively, indicating a greater wear resistance due to cryotreatment, but one that is strongly dependent on cutting conditions.

The twist drills were used to machine holes in AISI 8640 steel bars before tool wear was measured with an optical microscope and the rake and flank faces analysed by scanning electron microscopy (SEM). A cutting fluid was used to keep the tools cool during machining. In these tests the cryotreated tools showed greater tool lives by 147%, 65% and 343% at cutting speeds of 30, 35 and 40m/min respectively. These results correlate well with the data gathered by Firouzdor et al. [86] who found that the life of AISI M2 HSS drills were improved by 77-126% due to DCT, when drilling blind holes in carbon steel blocks.

The milling cutters were used by da Silva et al. [85] in industrial cutting conditions to shape an automotive gear component. It was found that the cryotreated cutters exhibited greater flank wear that the untreated tools, although the surface finish of the component was unaffected. Overall the cryotreated tools were able to produce 22.8% fewer parts than the untreated tools. The authors suggest that this was due to the difference in thermal expansion coefficients between the tool substrate and TiN coating, leading to fragmentation of the coating during cryotreatment.

Due to its widespread use in high-demand machining applications, there are also a range of studies focusing on the effects of cryotreatment on tungsten carbide cutting tool materials. The majority of these studies investigate the performance of tungsten carbide cutting inserts or tools, when tested under accelerated tool-life conditions. One of the more fundamental studies involving laboratory-based testing is that of Gill et al. [45], who conducted pin-on-disc testing using round ISO-P25 uncoated tungsten carbide cutting inserts (WC-6Co-1.4TiC) loaded against a rotating En32 steel disc (creating a line contact). At loads of up to 88N, with a sliding speed of 1.5m/s and a sliding distance of 1800m, they determined that shallow cryogenic treatment and deep cryogenic treatment resulted in reductions in wear rate, when compared with untreated specimens, of up to 24.5% and 41.7% respectively, with the greatest improvements found to be under the application of the greatest load.

Numerous published studies involve testing based on ISO 3685, 'Tool-life testing with single-point turning tools' [37], which recommends standard cutting parameters, machining conditions and workpiece materials for the testing of tool steel, hardmetal and ceramic cutting tools. Table 12 summarises some of these recent studies. The studies of Gill et al. [87, 88] highlight that which was reported by Silva et al. [85] regarding the effects of cryogenic treatment on tool coatings. Gill et al. determined

that deep cryogenic treatment offered the greatest benefit to uncoated ISO P-25 cutting inserts, while shallow cryogenic treatment gave the greatest improvement to the tool-life of TiAlN coated ISO P-25 inserts. Gill et al. concluded that deep cryogenic treatments diminish the adhesion strength of TiAlN coatings applied to tungsten carbide inserts; likely due to the difference in thermal expansion between the coating and the substrate, as was reported by Silva et al. for TiN coated AISI M2 drill bits.

Table 12 - Summary of cryotreated WC-Co tool wear data reported by other investigators based on ISO 3685.

Investigators	Tool material	Feed rate /(mm/rev)	Depth of cut /mm	Cutting speed /(m/min)	Tool-life changes reported
Gill et al. [87]	Sandvik ISO P-25 SPUN 120308 WC-6Co-1.4TiC	0.1	1.0	110 130 150 180	+27 – 36% +21 – 27% +19 – 25% +13 – 20%
Gill et al. [88]	Sandvik ISO P-25 SPUN 120308 WC-6Co-1.4TiC TiAlN coated	0.1	1.0	110 130 150 180	-3.9 – +34% +9.8 – 32% +15 – 24% +18 – 21%
SreeramaReddy et al. [73]	Kennametal ISO P-30 WC-17Co-1.4TiC-1.4TaC Multilayer CVD coating: TiN: 1.5µm TiCN: 12.5µm Al_2O_3: 6µm TiN: 5µm	0.22	1.0	200 250 300 350	+7.7% +22% +22% +15%

In contrast to the findings of other investigators, SreeramaReddy et al. [73] saw significant improvements (up to 22%) in the tool-life of ISO P-30 WC-Co-TiC-TaC inserts, with a multilayer CVD coating, after deep cryogenic treatment. Additionally, it was reported that the surface finish of the C45 steel workpieces used was improved when using cryogenically treated inserts. An increase in the electrical conductivity of the inserts suggested that an increase in thermal conductivity was partly responsible for the improved wear resistance of the tools.

The effect of temperature on the performance of cryotreated WC-Co tools has been investigated by other researchers by the use of coolants and interrupted machining modes. For instance, Yong et al. [89] (Figure 19, a) determined that by using coolant, the improvement in tool-life caused by deep cryogenic treatment could be increased by almost 10% in some cases, when face milling a medium carbon steel with a Sumitomo SPCH 42R G10E tungsten carbide insert. In a turning operation, Gill et al. [90] (Figure 19, b) observed that using an interrupted machining mode had a greater beneficial effect on the life of cryotreated tungsten carbide inserts than the use of a coolant to flood the cutting zone.

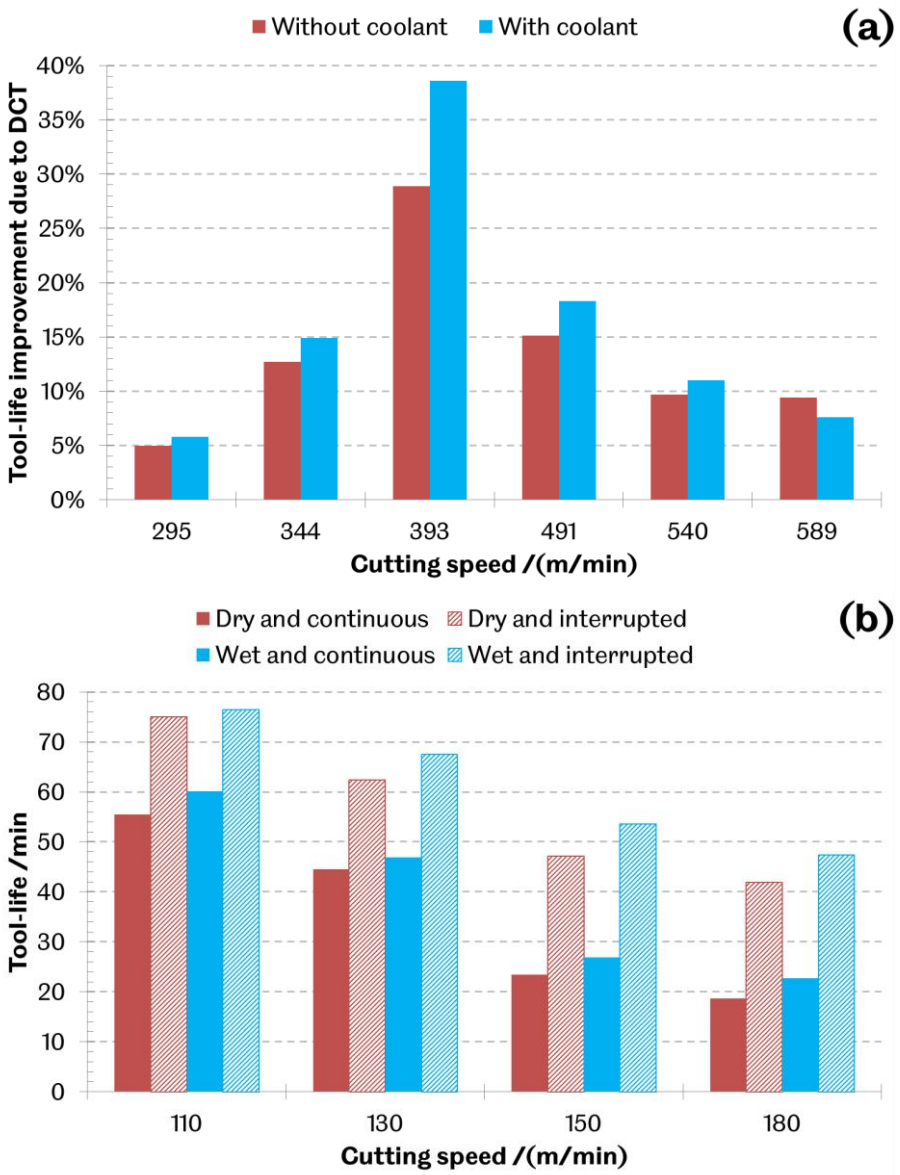

Figure 19 - Summary of results reported by (a) Yong et al. [89] and (b) Gill et al. [90] illustrating the effects of coolant on cryotreated WC-Co tools in face milling and turning respectively.

Studies such as these indicate that both shallow and deep cryogenic treatments offer significant performance improvements to WC-Co tools, but that these improvements are strongly dependent on other factors, such as coatings (where deep cryogenic treatment tends to have adverse effects), machining parameters (where the benefits of cryogenic treatment are minimised at both low and high cutting speeds) and tool temperature (where both the use of coolant and interrupted machining modes can enhance the performance of cryotreated tools).

2.2.3. Microstructural changes

Alongside their investigations into the wear behaviour of cryotreated AISI D2 steel (as discussed in Section 2.2.2), Das et al. [74, 75] conducted thorough microstructural analyses involving optical microscopy, X-ray diffraction (XRD) and SEM coupled with energy-dispersive X-ray (EDX) measurements. It has been suggested that in tool

steels, the improvement seen in wear resistance is as a result of three main phenomena: (i) the reduction or elimination of retained austenite (γ_R) from the microstructure [91, 92]; (ii) increased precipitation, dispersion and refinement of secondary carbides [93]; and (iii) the increase in matrix hardness due to DCT, although increases in bulk hardness are also reported for some tool steels [65, 74].

In their investigations Das et al. identify all three phenomena and quantify the proportions of retained austenite, martensite and carbides within the matrix after CHT, CT, SCT and DCT. Figure 20 shows the measured proportions of each feature along with a breakdown of the volume fraction of secondary carbides into small (0.1-1.0μm) and large (1-5μm) particles. They confirm the findings of many researchers that CT substantially reduces the proportion of retained austenite, while SCT and DCT may eliminate it from the matrix completely as cryotreatment takes steels below their martensite finish temperature; in the case of AISI D2 steel 148K. It can be seen that cryotreatment has little effect on primary carbides (≥5μm), which is expected as their characteristics are determined by the time and temperature of the pre-cryotreatment, high temperature austenitisation [93]. The volume fraction of secondary carbides by contrast, increases by 7%, 14% and 53% due to CT, SCT and DCT respectively. Also noted is the greater increase in the volume fraction of smaller secondary carbides (SSCs), than their larger counterparts (LSCs) due to DCT over any of the other treatments.

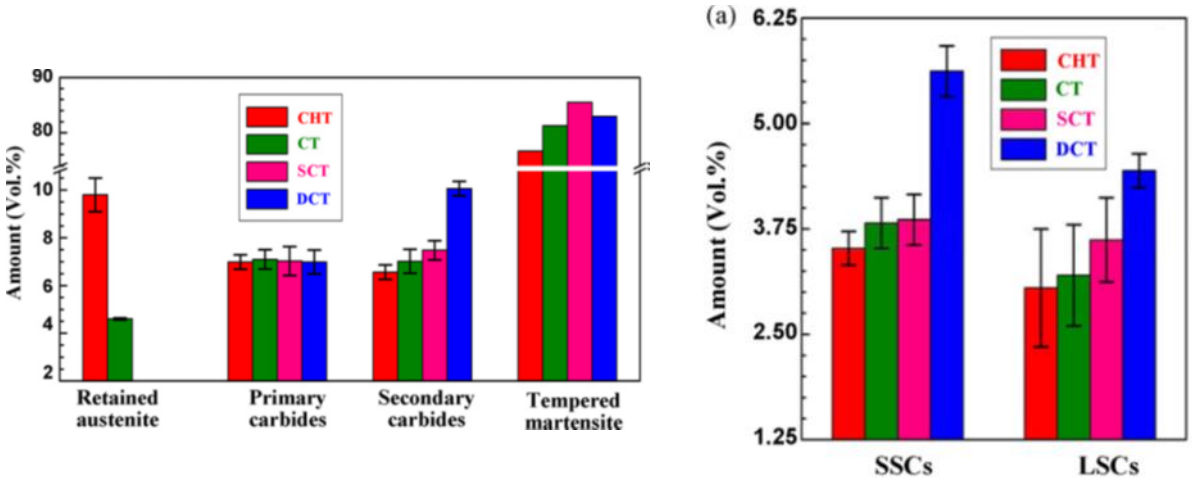

Figure 20 - From Das et al. [74]: (left) volume fractions of microstructural features and (right) breakdown of secondary carbide fraction into small secondary carbides (SSCs) and large secondary carbides (LSCs).

The progression of the development of carbides can be seen in Figure 21 from the conventionally heat treated specimen (a) to the deep cryotreated specimen (d). Figure 21 (e) and (f) illustrate the different categories of carbides discussed. Through XRD analysis the carbides are characterised as a mixture of M_7C_3, $M_{23}C_6$ (M = Fe, Cr, Mo, V) with a small amount of Cr_7C_3 in the D2 steel specimens after all treatments, confirming that cryotreatment has no effect on the nature of primary and secondary carbides. It is clear from the unchanged primary carbide proportions that cryogenic

treatment results in new dispersions of carbides, as opposed to modifying existing ones. This can be explained, as low temperatures during cryogenic treatment may be expected to cause a distortion of the lattice structure leading to dislocation concentrations to which carbon atoms may diffuse during subsequent tempering [7]. During tempering these carbide nuclei undergo limited growth based on the diffusion of local carbide forming elements, but have neither sufficient time nor energy to grow beyond around 100nm in size, or merge with other nearby carbide nuclei.

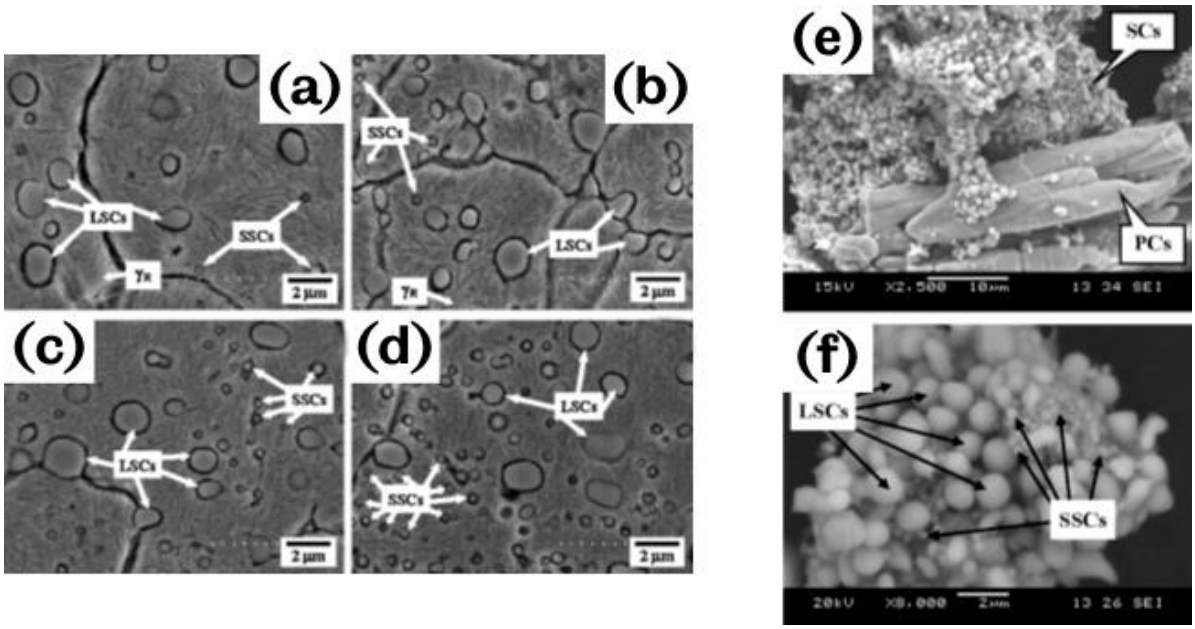

Figure 21 - From Das et al. [74], SEM micrographs showing (a) CHT, (b) CT, (c) SCT and (d) DCT specimens, (e) primary carbides (PCs), secondary carbides (SCs) and (f) large and small SCs.

However, this proposed mechanism is not unchallenged. Tyshchenko et al. [94] argue that, although the suggested diffusion distances for carbon atoms at low temperatures are small, at cryogenic temperatures they would be expected to be, to all intents and purposes, immobile. Furthermore, Gavriljuk et al. [95] point out that the energy required for carbon atoms to bond to dislocation sites is greater than that required for the dissolution of transient carbides and even cementite; hence carbon atoms around such dislocation concentrations would enter solution with the matrix material before forming new carbide nuclei. In this sense if carbon concentrations were to be present around dislocation sites during cryogenic treatment they would not promote new carbide precipitations, but rather inhibit them. Instead they suggest that such carbon concentrations could only be formed by the plastic deformation of martensite at cryogenic temperatures and the transport of carbon atoms by the corresponding movement of dislocations. It is this time-dependent movement of dislocations that causes the relationship between the duration of the cryogenic treatment and the number of fine carbides subsequently precipitated.

While the underlying mechanism remains a topic of debate, the precipitation of new fine carbide dispersions due to cryogenic treatment is beyond dispute. A recent study

which reinforces this effect, is that of Yan et al. [64]. Applying cryogenic treatments to high speed steel (W9Mo3Cr4V) before and after tempering, they demonstrated that the greatest improvements in hardness, impact toughness, sliding wear resistance and tool-life were achieved using deep cryogenic treatment followed by tempering. They observed that tempering after cryogenic treatments resulted in consistently greater numbers of sub-micron carbides than compared with tempering cycles applied prior to cryogenic treatments.

Other authors have suggested that even finer carbide precipitates may be the source of enhanced wear resistance in cryotreated materials. In their studies of Fe-12Cr-Mo-V-1.4C tool steel, Meng et al. [96] observed η-carbides; rod-like structures 5-10nm in cross-section and 20-40nm in length, as opposed to the larger carbides described by Das et al. [74]. Stratton [61] attributed the formation of nano-carbides to the time-dependent decomposition of martensite which occurs at deep cryogenic temperatures (77K), suggesting that longer soak times lead to greater nano-carbide formation and therefore, greater wear resistance than can be obtained through short cryotreatment cycles.

If the formation of these nano-carbides were to be decisively demonstrated, it is reasonable to suggest that such precipitates were present in many cryogenically treated samples reported in the literature and were in part responsible for the wide range of property and performance changes measured. However, the relatively infrequent use of high resolution techniques such as transmission electron microscopy has meant that these changes have gone unobserved. While greater numbers of nano-carbide nuclei may serve to limit their growth as a result of a wider dispersion of carbide forming material, it is likely that tempering parameters play a much more significant role. It is intuitive that these carbides will grow more extensively with tempering time and more rapidly with increasing temperatures due to their dependence on diffusion processes, assuming of course that temperatures do not rise sufficiently to cause their dissolution into the matrix material.

A recent review into the metallurgical effects of cryotreatment by Gill et al. [6] discusses in more detail how carbon content effects the transformation of retained austenite to martensite, highlighting that increasing carbon content in steels lowers both the martensite start and finish temperatures. Therefore, cryotreatment is likely to show greater beneficial effects in high-carbon steels which retain a significant proportion of austenite after conventional heat treatments. However, newly formed martensite is brittle and hence must be tempered. As has already been discussed, this tempering process is disputed, with some investigators [66, 70] choosing to pursue conventional elevated temperature treatments, whereas others [65, 74, 75] believe

DCT should follow any conventional heat treatment cycle, and may serve to temper martensite without further treatments.

The elimination of retained austenite from the structure has obvious benefits for subsequent tempering processes (as discussed in Section 1.2.2.3). As both the 'primary' martensite (that formed by the quench-hardening process) and 'secondary' martensite (that formed by cryogenic treatment) would be expected to remain brittle, the material would benefit from tempering to cause an increase in toughness and maximise the level of secondary hardening through carbide growth and dispersion.

Meng et al. [96] also suggest that the martensite formed due to cryotreatment has different lattice parameters than that formed during conventional treatments, leading to greater strength and toughness of the matrix. These have not been commonly reported in the literature, however as these martensite grains form subsequent to and under substantially different conditions from primary martensite grains, they may be expected to possess different lattice parameters and morphologies. The presence of the surrounding martensite, which has already expanded by 4% during its own transformation from austenite, may limit changes in the shape of new martensite grains, while growth is inhibited by low temperatures. Using transmission electron microscopy, Tyshchenko et al. [94] identified that martensite formed by cryogenic treatment at -150°C occupies smaller domains and has finer twinning than that formed by quenching to room temperature.

In their recent study, Gavriljuk et al. [95] provide evidence for both a lower temperature limit for the martensitic transformation to occur and for a time-dependent isothermal martensitic transformation that continues at cryogenic temperatures, in X153CrMoV12 high-carbon powder metallurgy alloy steel. Using Mössbauer spectroscopy they demonstrated that even after 96h held at -196°C, no conversion of retained austenite to martensite had taken place, while holding the material at -150°C caused an increase in martensite content (and corresponding decrease in retained austenite content) that was dependent on the duration of the treatment. They reason that this lower temperature transformation limit is as a result of such a reduction in atomic vibrations that there is insufficient thermal activation energy for the conversion of austenite to martensite to take place. Their findings also support differences in the lattice parameters of cryogenically formed martensite reported elsewhere. They rationalise that the reduced tetragonality of the crystal structure formed by this process as a result of the capture of carbon atoms by the movement of dislocations, reducing the distorting effect that these otherwise trapped interstitial carbon atoms would have on the structure.

Tungsten carbides, such as those used in the manufacture of cutting tools, typically contain four phases: (i) α-phase – tungsten carbide (WC); (ii) β-phase – cobalt binder (Co); (iii) γ-phase – cubic carbides (e.g. TiC, TaC, NbC, VC etc.) and (iv) η-phase – carbides of tungsten and miscellaneous metals. α, β and η-phases are shown in Figure 22. Even though γ-phase cubic carbides are present in the microstructure shown, they are difficult to resolve except at high magnifications.

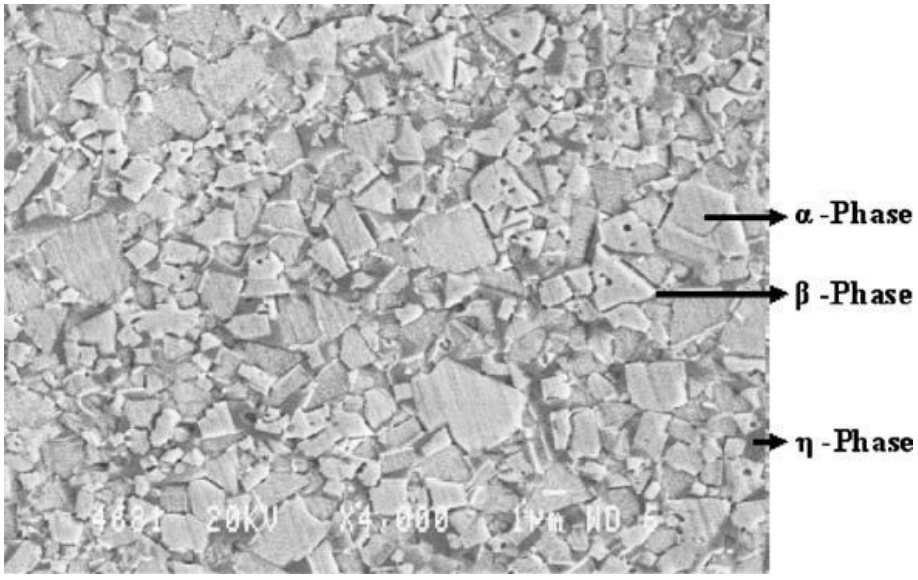

Figure 22 - Microstructure of ISO P-30 WC-17Co-1.4TiC-1.4TaC material showing typical phases [73].

While all tungsten carbides contain α and β phases, the presence of γ-phase is dependent on the addition of carbide formers such as Ti, Ta, Nb, V, Hf etc. It is often attempted to minimise the hard η-phase, which can result in reduced toughness of the material. η-phase is typically comprised of M_6C or $M_{12}C$ (where M = $Co_{3.2}W_{2.8}$ – Co_2W_4 or Co_6W_6 respectively) [45].

Conducting a low-magnification microstructural study on a WC-MC-7Co material, Seah et al. [71] observed no change in grain size (α-phase) or general microstructure due to cryogenic treatment. However, they did observe variations in the frequency and distribution of fine η-phase that were dependent on treatment parameters. While these had no significant effect on hardness, they were judged to improve the resistance of the tool to abrasive wear and plastic deformation during cutting. Thakur et al. [72] investigated the effects of different post-treatments (cryogenic treatment, heating and forced air cooling, heating and oil-quenching) on the microstructural characteristics of a 93WC-MC-Co material. Cryogenic treatment was determined to have a relatively subtle effect on the microstructure of the material, but was suggested to have resulted in the shrinkage or densification of the cobalt binder, contrary to the findings of Seah et al. This was thought to have the effect of exerting a compressive stress on carbide particles and therefore making them more resistant to wear by pullout. XRD analysis revealed no significant change in the material due to cryogenic

treatment. Changes in the cobalt binder were also reported by SreeramaReddy et al. [73] who observed that cryogenic treatment has the effect of reducing the volume of the β-phase, which is replaced by η-phase and enlarged carbides (α-phase). Cryogenic treatment was determined to improve the high temperature corrosion resistance of the cobalt binder, while improving the thermal conductivity of the tool due to increased grain contiguity.

The effects of cryogenic treatment on the η-phase have been more clearly defined by Vadivel et al. [35] who suggested that randomly distributed coarse particles are refined and stabilised by cryogenic treatment, resulting in a dense, tough and coherent matrix. They also suggest that cryogenic treatment can be used to reduce the stresses induced by coating processes, and therefore minimise the possibility of carbide fracture.

Following machining of medium-density fibreboard using double-flouted router bits, in their untreated and cryogenically treated conditions under various forced air cooling regimes, Gisip et al. [97] performed EDS analyses that were progressively removed from the cutting edges of the tools. They determined that after cryogenic treatment, removal of both the cobalt binder and tungsten carbide grains from the surface of the tools during use was significantly reduced, along with the tendency for high-temperature oxidation and corrosion to occur. The use of refrigerated air cooling was also found to reduce wear, oxidation and corrosion rates in cryogenically treated tools.

Cryogenic treatment is therefore reported to cause a number of changes in the microstructure of cobalt-bonded tungsten carbides. These include the densification or shrinkage of the cobalt binder, a swelling of the WC grains, and the refinement and stabilisation of fine η-phase particles. Combined, these effects may result in increases in wear resistance, toughness and thermal conductivity, although the limited studies conducted to date leave considerable uncertainty as to the extents of these changes and the range of operating conditions under which they are stable.

2.3. Summary

Modern uses of cryogenic treatment started in the first half of the 20th Century, following the liquefaction of nitrogen and helium in the late 19th Century. While a number of approaches to cryogenic treatment have been tried and tested, the majority of modern treatments involve the slow cooling of materials and components in insulated chambers by nitrogen gas, to avoid problems such as thermal shock and the surface damage resulting from vapour ice. Although a few published studies have reported improvements in the mechanical properties and wear behaviours of light alloys due to cryogenic treatments, the majority have focused on its effects on tool steels. Increases in hardness (up to 86%) and wear resistance (up to 1257%) are

commonly reported, along with a small number of studies reporting decreased toughness. Observed changes in tool steels due to cryogenic treatment include the reduction or elimination of retained austenite from predominantly martensitic microstructures, and the precipitation, dispersion and refinement of small (sub-micron and nanometre scale) carbides. Related to this latter change, cryogenic treatment has been observed to have the greatest effect on alloy steels; those which may have relatively large proportions of retained austenite and those with significant levels of carbide forming elements such as Cr, Mo and W. However, no investigations have been reported and no clear trends have emerged to suggest which (if any) of these chemical constituents has the greatest influence on the 'susceptibility' of a material to cryogenic treatments.

Soaking temperature, time, rate of cooling and post-cryotreatment tempering are all variables in cryogenic treatment processes, however it is the first of these that has been argued to be most significant. The reality is more complex, as the contribution of the parameters of soaking temperature, soaking time and post-cryotreatment tempering have been shown to change depending on the composition of the material and their relative magnitudes. For example, short soaking times may cause the almost complete transformation of retained austenite to martensite in low and medium carbon steels, but may largely preclude the formation of new fine carbides which appear strongly dependent on both the cryogenic soaking time and tempering parameters. In high carbon steels recent research has shown that extended soaking times allow for a greater transformation of retained austenite to martensite through a time-dependent isothermal process, which may be halted at deep cryogenic temperatures due to a lack of atomic vibrational energy. Extended soaking times have also been shown to be beneficial for increasing subsequent fine carbide precipitations that depend on the movement of dislocations due to plastic deformation of the material.

When applied to cobalt-bonded tungsten carbide tool materials, cryogenic treatments have been reported to increase their hot hardness and abrasive wear resistance (up to 36%), as well as their oxidation and corrosion resistance, and thermal conductivity. Reported microstructural changes include the densification of the cobalt binder, a swelling of tungsten carbide grains to form a more contiguous microstructure, and the refinement of fine η-phase (un-dissolved carbide) particles.

In both sets of materials, the limits of the effects of cryogenic treatments in terms of application conditions (cutting speeds, temperatures etc.) have yet to be fully established. While the metallurgical mechanisms responsible for the changes reported in martensitic carbon steels have been relatively well characterised, they remain to be described for other ferrous alloys and phases (such as grey cast irons

and pearlite) which are nonetheless commonly cryogenically treated. The application of cryogenic treatments to tungsten carbides represents a nascent field, in which changes in tool-life have been observed, with limited quantification of mechanical properties, no rigorous characterisation of changes in wear behaviour and with only basic microstructural analyses having been conducted.

3. Experimental methodologies

Investigations into the effects of heat treatments and the performance of materials typically involve a combination of solid mechanics and metallurgical techniques, with the complexity of each of these branches necessarily increasing as testing and analyses approach a realistic approximation of in-service applications. An outline testing and analysis map covering a range of tribological tests and microstructural analyses for assessing the effects of cryogenic processing is given as Figure 23. Note that other aspects of solid mechanics such as fatigue life, high temperature and pressure testing are excluded, being outside the remit of this study.

	Basic understanding	→	Applications testing
Tribology	T1: Comparative laboratory-based wear testing (on specimens before and after cryotreatment).	T2: Accelerated product wear testing under standard conditions.	T3: Extended trials with varied working parameters, contact materials and environmental conditions.
Metallurgy	M1: Comparative microstructural imaging (of materials before and after cryotreatment).	M2: Quantitative analysis of phase composition and precipitates.	M3: Analysis of effects of varied cryotreatments to enable optimisation of treatments by application.

Figure 23 - Tribological testing and metallurgical analysis map for investigating the effects of cryogenic treatments.

In this chapter, the methodologies and techniques applied are summarised and justified. These include common tribological testing methods, wear characterisation and analyses, initial comparative metallurgical observations and detailed microstructural analyses reserved for cases showing the greatest and most significant changes in wear performance and mechanical properties due to deep cryogenic treatment. Specific errors, uncertainties and limitations in the applied methodologies are subsequently discussed.

3.1. Summary of applied processes and techniques

Based on the objectives set out in Section 1.4 a number of experimental and observational techniques were employed to test materials and analyse results, essentially contributing data to areas T1, M1, T2 and beginning to contribute to the analyses described by M2 as set out in Figure 23. These techniques are summarised with their relevant test specimens in Table 13.

Tribological bench testing was separated into two sections: pin-on-disc testing for brake disc specimens and reciprocating sliding testing for tool steels. These methods were selected for their relationship with the application being investigated. As brake discs are subjected to predominantly unidirectional sliding (with the majority of braking cycles conducted to decelerate a vehicle from forward motion, as opposed to in reverse), pin-on-disc testing was deemed the most appropriate method, although, as is subsequently discussed, the combination of test parameters and materials did not and could not seek to replicate the real application. When used as cutting tools, tool steels are subjected to a combination of wear mechanisms (as discussed in Section 1.2.2.1) including abrasion and adhesion. The changing sliding velocity during reciprocating tests enables both of these mechanisms to be observed, although, as with the brake disc specimens, test parameters and materials prevented a replication of the wear conditions experienced in the application concerned.

Further testing to determine the effect of cryogenic treatment on tool wear development was accomplished by tool wear development testing, using a methodology based on ISO 3685 [37]. As mentioned in Section 2.2, the majority of studies involving tungsten carbide are conducted on cutting inserts and bits used in repeated machining operations. As well as providing a more realistic assessment of the performance of cryogenically treated tools under in-service conditions, it is often a more practical alternative to procuring suitable tungsten carbide blanks and machining them into specimens for other forms of testing.

Specimens underwent macro- and micro-hardness testing to determine bulk material and matrix hardness respectively. Volume and mass loss methods were used to evaluate levels of wear, while contact and non-contact profilometry, as well as optical microscopy were employed to characterise wear mechanisms.

Following testing, optical microscopy was used to observe the general structure of each material, before scanning electron microscopy (SEM) was employed for further comparative characterisation, of phases and precipitates, between materials in their as-received conditions and after cryogenic treatment. For the material which showed the greatest and most consistent improvement due to deep cryogenic treatment, the phase composition and crystallographic structures were subsequently characterised using X-ray diffraction (XRD), electron back-scatter diffraction (EBSD), transmission electron microscopy (TEM) and electron diffraction.

It is recognised (and subsequently discussed) that all of the techniques employed have limitations, and that the combination of techniques employed does not provide a comprehensive understanding of the effects of cryogenic processing on the materials tested in this study. However, the combination of techniques selected allows materials

to be first screened to determine whether cryogenic treatment has had any effect on their relative performance, before being analysed further to indicate what microstructural changes have taken place.

Table 13 - Summary of processes and techniques applied to specimens in this study.

Chapters	Specimens	Cryotreatment	Hardness testing	Pin-on-disc	Reciprocating sliding	Tool wear testing	Mass measurements	Profilometry	Interferometry	Microscopy	SEM	XRD / EBSD	TEM / electron diffraction
4, 7	SAE J431 G10 grey cast iron brake discs	×	×	×				×		×	×		
4, 7	C50R steel brake discs	×	×	×				×		×	×	×	×
4, 7	AISI A2 tool steel	×	×		×		×			×	×		
4, 7	AISI D6 tool steel	×	×		×		×			×	×		
4, 7	AISI M2 tool steel	×	×		×		×			×	×		
5, 7	H13A (WC) turning inserts	×	×			×	×		×	×	×		

The advantages and limitations of each technique are discussed in more detail in the following sections, while the limitations of this research are discussed and evaluated in Chapter 7.

3.2. Cryogenic processing

For all the investigations recorded here, half of the specimens were tested in their as-received state, while the other half underwent a consistent deep cryogenic treatment cycle provided by Cryogenic Treatment Services Ltd. (Nottinghamshire, UK). This involved specimens undergoing controlled cooling at a rate of 1-2K/min to the soak temperature of 93K, being held for 24h and then being returned to ambient temperature at 1-2K/min. Following cryotreatment specimens were aged or tempered: in the case of the ferrous alloys tested, at 333K for 1h before being returned to room temperature and in the case of the tungsten carbide inserts tested, at 443K for 2h before being returned to room temperature. These treatment cycles are shown in Figure 24. It should be noted that treatment parameters were controlled solely by Cryogenic Treatment Services Ltd., based on their experience and dependent upon the other parts being treated at the same time as the specimens used in the investigations recorded here.

In discussing microstructural changes to the materials, it is assumed that they were received in a metallurgically stable condition, when long-term changes in their microstructures had effectively ceased.

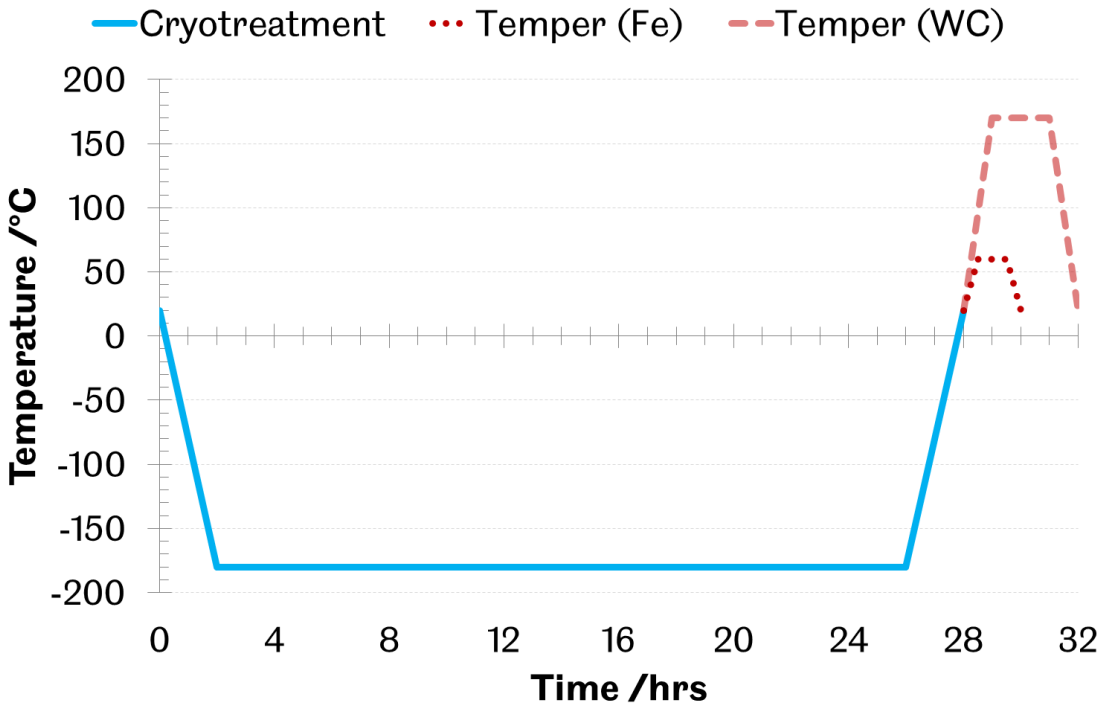

Figure 24 - Deep cryogenic treatment cycles applied to specimens used in this study.

3.3. Experimental techniques

3.3.1. Hardness testing

The hardness of a material can have a significant impact on its wear performance, and can be used to identify the scale of material features that are responsible for changes in its wear behaviour. While numerous types of techniques are available for measuring the hardness of materials (such as by abrasion, scratching or machining), indentation hardness techniques are commonly used for a wide range of metals. Table 14 provides a brief comparison of the three most commonly used bulk indentation techniques; Brinell, Vickers and Rockwell.

As the range of materials being tested included large components, stock materials and finished cutting tool inserts, the Vickers technique was selected as being suitable for all specimens. Both standard Vickers and Micro-Vickers testers were employed, to assist in characterising the scale of changes that occurred in materials during cryogenic treatment. With typical indentation sizes on the order of 100µm, standard Vickers measurements indicate the 'bulk' hardness of the material which is controlled by a whole range of microstructural features including phase composition, precipitate characteristics and dispersions, and grain interface properties. Indentation sizes for

Micro-Vickers tests are an order of magnitude lower, and therefore provide a direct measurement of the 'matrix' hardness – the effective hardness of clusters of grains and sometimes (depending on the average grain size in the material) individual phases. Micro-Vickers measurements can also be conducted on large, solid precipitates within the matrix.

Table 14 - Comparison of commonly used indentation hardness techniques for metals [98, 99].

Characteristic	Brinell	Vickers	Rockwell
Indentation geometry	Relatively large, spherical indenter.	Small, 136° pyramid shaped indenter.	Either conical with rounded point, or small spherical indenter.
Indenter material	Hardened steel or tungsten carbide.	Diamond.	Diamond and hardened steel respectively.
Typical test piece	Stock materials and part-finished products.	Finished products.	Finished products.
Surface preparation required	Minimal necessary.	Finely machined or roughly ground, to finely ground and polished depending on scale.	Minimal necessary, grinding/polishing preferable.
Test materials	Soft to medium hardness metals.	Hard metals.	Hard metals and metals of medium hardness.

Traditionally neither macro- or micro-hardness tests are conducted with instrumented equipment; that is to say they merely provide a singular value of hardness based on the calculated or projected area, or depth, of the residual indent that is left following any elastic relaxation of the material. Such is the case with the macro- and micro-hardness tests employed in the present studies.

By contrast nano-indentation techniques can only be effectively employed using instrumented indenters. Forming indents an order of magnitude lower again than micro-indentation techniques (~1μm), nano-indentation offers the ability to measure the hardness of even smaller samples of materials (typically individual grains) and may also be used to determine other mechanical properties such as the elastic modulus and fracture toughness by analysis of the elastic-plastic loading and elastic unloading curves captured by an instrumented indenter. Due to the size of the residual indents after unloading, electron microscopy or atomic-force microscopy (AFM) is required for their observation.

Nano-indentation is particularly effective in the analysis of thin films, small particles, and in the determination of the mechanical properties of separate phases of material. However, considering the greater resource required for reliable and repeatable results using this technique, it was not possible to employ it in the present studies.

3.3.1.1. Specimen preparation and measurement parameters

Macro- and micro-hardness testing was performed using standard Vickers pyramid-shaped indenters, with face angles of 136°, in accordance with BS EN ISO 6507 [100].

Specimens were cleaned with acetone and dried prior to macro-hardness tests. For micro-hardness tests, specimen surfaces were additionally ground and polished to 1μm before being cleaned with isopropanol and dried prior to testing, to ensure results were not significantly affected by surface roughness (compared to the size of the indenter) or the formation of oxide layers.

For macro-hardness tests a load of 20kgf (196.2N) was applied for 15s, with ten measurements being taken from each test piece. Micro-hardness tests were performed using a Mitutoyo HVM-101 micro-indenter at a load of 0.05kgf (0.4905N) which was applied for 15s, with ten measurements again being taken from each test piece. The mean values from these data are reported here, along with the coefficient of variation for each measurement set. In all cases (macro- and micro-) measurements were separated by several diagonal lengths with indents placed so as to avoid obvious particles or flaws where possible.

3.3.2. Wear testing

Tribological bench testing offers relatively quick and simple measures of the performance of materials in a variety of friction and wear situations. In the studies discussed here, pin-on-disc and reciprocating sliding tests were employed to provide comparative indications as to the performance of materials before and after deep cryogenic treatment. These tests did not seek to truly replicate the conditions experienced by the materials in their industrial applications. Rather they were designed to rapidly induce macroscopic wear at comparable contact pressures to those the components would experience and induce some of the dominant mechanisms the materials are typically subjected to: severe, primarily two-body abrasive wear, ploughing and localised plastic deformation.

While a number of factors contribute to the development of wear in a sliding contact (including the contact load and geometry, friction forces, localised heat generation and the chemical affinity of the material pair), Hertzian contact theory was used to estimate surface and subsurface stresses within the materials being tested, under the selected loads and contact conditions. Figure 25 illustrates the surface and subsurface stresses predicted in a Hertzian point contact (calculated using established relations for ball-on-flat contacts as in e.g. Williams [101], which accompany the experimental parameters presented in Appendix 10.4), and identifies the magnitudes and locations of the maximum tensile stress and maximum principal shear stress, which are critical parameters in the development of surface and subsurface deformation respectively.

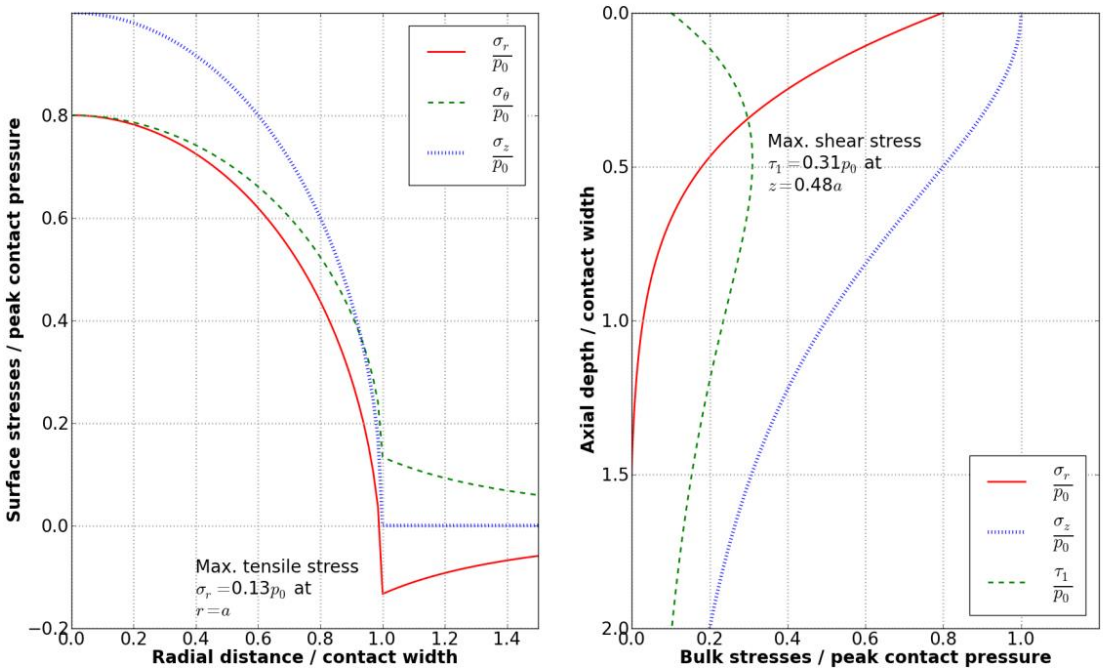

Figure 25 - Theoretical (left) surface and (right) subsurface stresses predicted for a Hertzian point contact.

In ductile metals two criteria are typically cited as indicating the point at which yielding occurs; namely the Tresca maximum shear stress criterion and von Mises strain energy criterion. In pure shear, yielding occurs when the shear yield stress is surpassed. The Tresca and von Mises criteria predict the shear yield stress (τ_y) is related to the tensile yield stress (σ_y) by Equations 3.1 and 3.2 respectively.

$$\tau_y = \frac{\sigma_y}{2} \tag{3.1}$$

$$\tau_y = \frac{\sigma_y}{\sqrt{3}} \tag{3.2}$$

Testing conditions and parameters are subsequently described in more detail. The discussion in Section 3.5 highlights some of the limitations of the techniques selected.

3.3.2.1. Pin-on-disc testing

Brake disc specimens were subjected to abrasive wear testing using a pin-on-disc method. Using a Plint TE99 (BICERI/Eyre) Universal Wear Testing Machine, brake discs were used as rotating counterfaces against which a 15mm diameter chrome steel (AISI 52100) ball was dead-weight loaded to act as a wear-inducing pin. This experimental setup is shown in Figure 26.

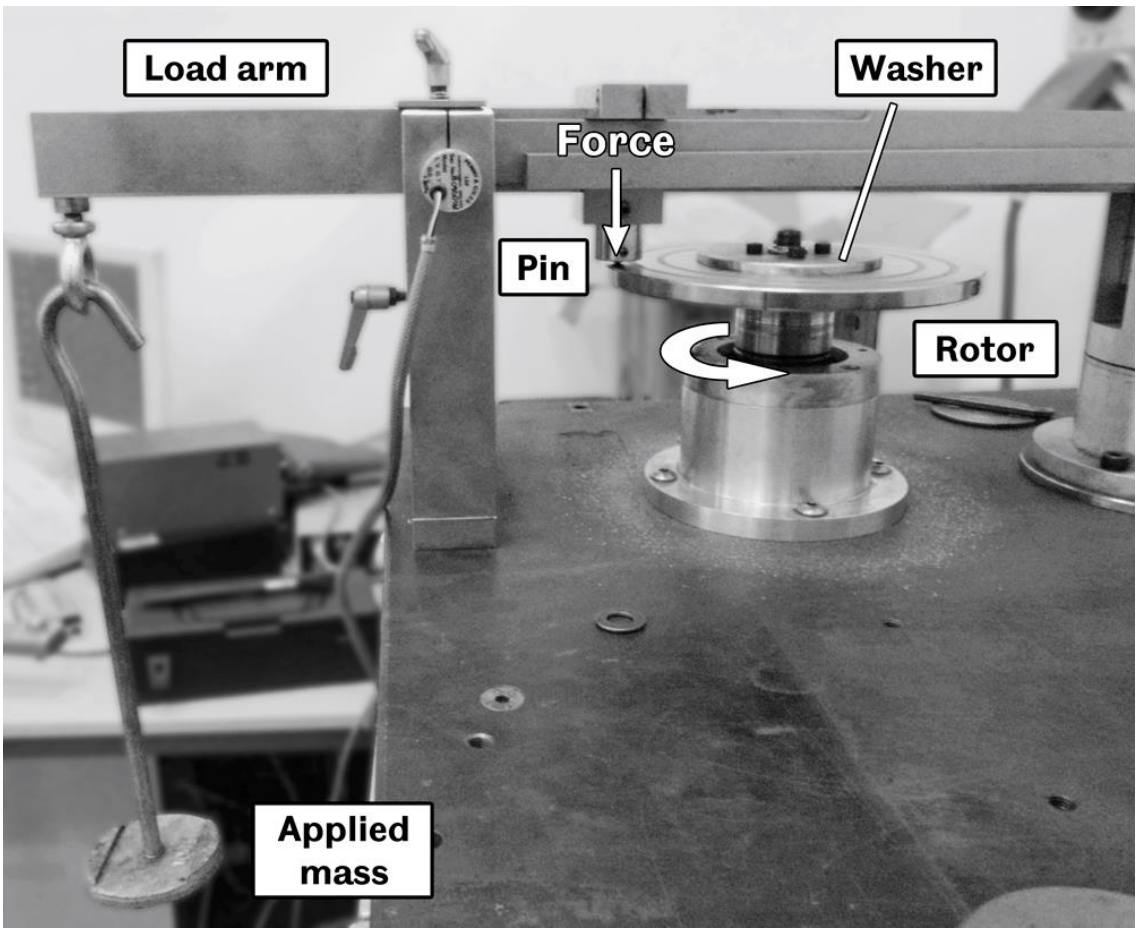

Figure 26 - TE99 in pin-on-disc mode with SAE J431 G10 brake rotor mounted on the spindle.

These wear-inducing pins were replaced between tests, to ensure an unworn surface was used. The properties of AISI 52100 steel are given in Table 15.

Table 15 - Properties of chrome steel, wear-inducing pins.

Material	$HV_{98.1}$ /MPa	$R_{a,max}$ /μm	Diameter /mm
AISI 52100	6878 – 8829	0.125	15

Pin-on-disc wear testing was conducted on the brake disc materials investigated in this study. Specific details on these materials can be found in Section 4.1, with test parameters and results presented in Sections 4.2.1 and 4.3.2.1 respectively.

3.3.2.2. Reciprocating sliding testing

Tool steel specimens were tested by a reciprocating sliding method. Using a TE77 High Frequency Friction Machine, tool steel specimens were used as stationary counterfaces against which a 5mm diameter ceramic (zirconia) ball was loaded to act as a wear-inducing pin. Figure 27 shows the TE77 in the experimental set up used in this study.

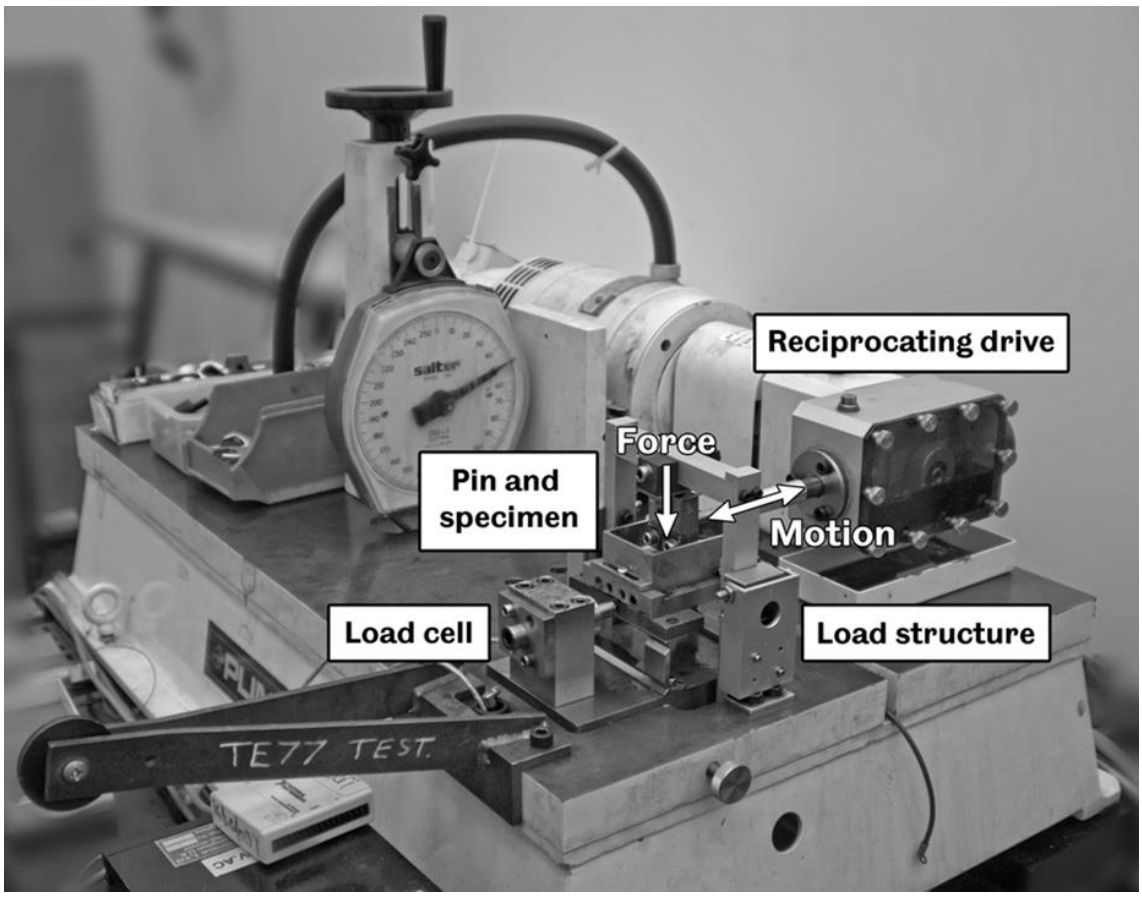

Figure 27 - TE77 in the experimental setup used in this study.

The zirconia wear-inducing pins were replaced between tests, to ensure an unworn surface was used. The properties of the zirconia balls are given in Table 16.

Table 16 - Properties of zirconia wear pins.

Material	HV /MPa	$R_{a,max}$ /µm	Diameter /mm
Zirconia (94.8% ZrO_2, 5.2% Y_2O_2)	11380	0.038	5

Reciprocating sliding wear testing was conducted on the tool steels investigated in this study. Specific details on these materials can be found in Section 4.1, with test parameters and results presented in Sections 4.2.2 and 4.3.2.2 respectively.

3.3.3. Tool wear development testing

Accelerated tool wear testing can be used to assess the relative performance of tools under realistic cutting conditions, and provide an indication as to what performance and lifespan may be expected for tools under normal use.

Various methods exist to assess tools used in orthogonal cutting, including rapid facing tests, taper turning tests and variable rate turning tests. The precept behind each of these methods is that a cutting tool will be used in cutting a 'typical, but not easy-to-machine' material that it may encounter in commercial or industrial use. Tools are often tested to a point at which a fixed amount of wear is achieved (such as maximum allowable flank wear) that is associated with a significant drop in performance of the

tool (increase in cutting forces or machine power requirements) or a significant deterioration in workpiece surface finish (by visual inspection or by increases in measured roughness) that indicates a worn or blunt tool. Tools may also be tested until catastrophic failure (such as fracture or breakage) occurs or, more simply, for a fixed period of time that may be determined by the tool completing a fixed number of machining operations.

Tool wear development testing was conducted to provide a more realistic comparison of the performance of cryogenically treated tool materials under complex tribological conditions, with mixed wear mechanisms and elevated temperatures. In the study presented here, commercially available tungsten carbide turning inserts were used to machine a typical workpiece material, with regular mass measurements, micrographs and topographs being taken to document the development of wear on the cutting faces, with comparisons drawn between standard inserts and those that had been cryogenically treated. Microstructural analyses were conducted on tools as-received and after cryogenic treatment, along with subsurface wear analyses after testing, to determine what effect normal operating conditions had on the cryogenically treated material structure.

Tool wear development testing was conducted using a methodology informed by ISO 3685, 'Tool-life testing with single-point turning tools' [37], with modifications made reflecting the limitations of the standard bench lathe used (in particular its discrete rather than continuously variable spindle speeds) and quantity of workpiece material available. Detailed material and testing parameters are given in Chapter 5.

3.3.4. Wear measurement and characterisation

A volume-loss method was used to estimate the wear rate of brake discs specimens, as their substantial size precluded precision mass measurements being taken. For this purpose a Mitutoyo Surftest SV-600 2D linear profilometer was used to take six measurements perpendicular to each wear scar, at 60° radial intervals. From these sections an average cross-sectional area was determined by numerical integration of the profiles, with a measurement pitch of 2µm producing >1000 measurement points across, and therefore a total of >6000 measurement points from, each wear track. A typical set of wear measurements taken from each disc is shown in Figure 28. While there appears to be substantial variation between each trace, the resulting uncertainty in the volume estimation of the wear track is acceptably small. A more detailed discussion of these uncertainties is given in Section 3.5.1.

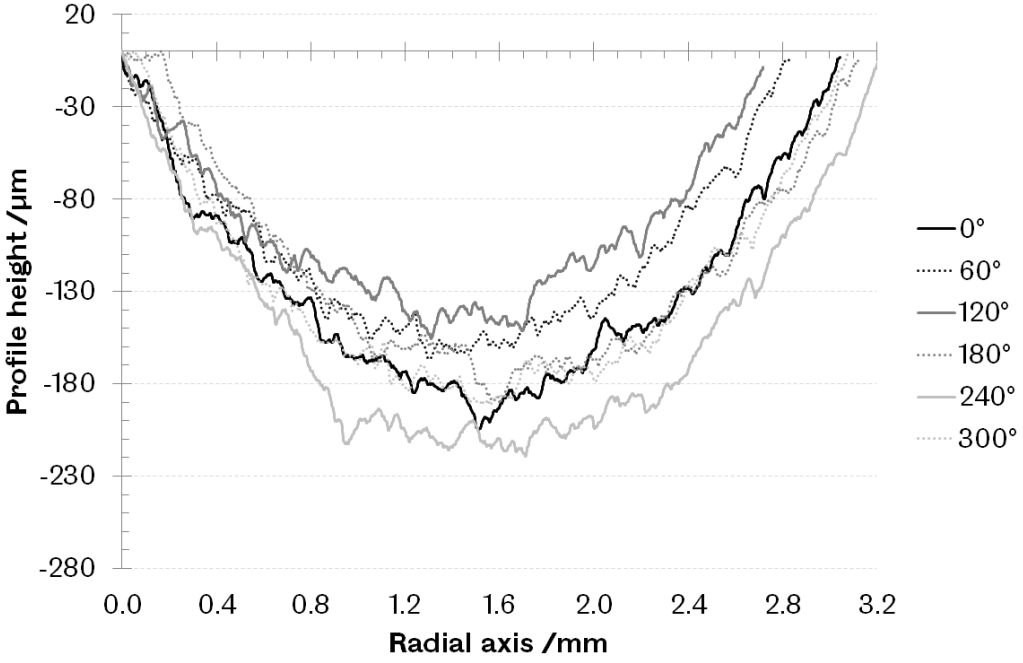

Figure 28 - Wear scar measurements used to estimate volume removed from each brake disc.

A mass-loss method was used to determine the wear rates from tool steel specimens. Using precision calibrated digital scales, with a resolution of 10µg, measurements were taken before and after testing of each specimen. Mean mass losses (based on 3 repeat tests at each sliding condition) are reported for specimens in their as-received and cryogenically treated conditions.

The wear on tungsten carbide tool inserts after machining was assessed both quantitatively and qualitatively. Flank wear and crater wear were quantitatively measured using a Carl Zeiss AxioImager optical microscope and Bruker ContourGT scanning light interferometer respectively, while surface and subsurface wear features were imaged by optical and scanning electron microscopy respectively.

Due to the comparative nature of the studies presented here, roughness measurements were made to ensure that sample surfaces were adequately similar prior to testing. While roughness measurements within wear scars may reveal more information concerning the wear mechanisms operating, the size of the wear scars generated (in the case of pin-on-disc tests) made this practically impossible to achieve to a meaningful extent using a stylus profilometer, such as was available when this study was conducted. It is acknowledged that a light interferometer, such as the Bruker ContourGT employed to measure tool wear, could have been used for this purpose had it been available. In the case of tool steel samples and tungsten carbide inserts, micrographs taken of the worn surfaces were thought adequate to characterise the dominant wear mechanisms.

3.4. Analysis techniques

3.4.1. Metallographic preparation

To enable initial microstructural observations to be conducted, material specimens were first prepared using standard metallographic preparation techniques. These involved taking small samples of material, mounting them in a holding medium, before progressively grinding and polishing the surface to achieve a nanoscale finish. Depending on the material, surfaces were either etched to reveal the microstructure, or imaged in their polished condition.

Ferrous alloys are often chemically etched; a process in which a polished surface is exposed to chemicals (often acidic) that attack or react to form precipitates with different microstructural constituents. These microstructural constituents are only reactive to certain etchants, and so etchants must be selected to reveal the key microstructural features of interest; whether they are particular phases, precipitates or grain boundaries.

Common acidic etchants for cast irons and steels include Nital (nitric acid and ethanol) and Picral (picric acid and ethanol), which will reveal the majority of microstructural phases, features and boundaries found in ferrous alloys. The chemical solutions and ferrous alloy features etched by Nital and Picral are given in Table 17.

Table 17 - Formulations and affects of selected ethants on ferrous alloys.

	Nital	Picral
Chemical constituents	Nitric Acid (2-5%) Ethanol/Methanol	Picric Acid (4%) Ethanol/Methanol
Etching performance	Reveals ferrite grain boundaries. Reveals martensite structure. Variable dissolution rate of ferrite (dependent on crystal orientation).	Reveals cementite in ferritic alloys. Uniform dissolution rate of ferrite.
Other notes	In high carbon steels (>0.5%C), white-etching phases may be present. These are typically ferrite, undissolved cementite or retained austenite.	

In brake disc specimens, radial slices were roughly cut from each brake rotor, before smaller specimens were sectioned. The sections were ground using silicon carbide (SiC) paper and polished using 6µm, 1µm and 0.25µm diamond suspensions. The microstructures of these samples were revealed by etching with Nital and an exposure of a few seconds, until the samples became slightly discoloured. A similar procedure was performed on tool steel samples, with cross-sections of each specimen being ground, polished and etched as described in Table 18. In the case of specimens which underwent high resolution scanning electron microscopy (Chapter 5), the final polishing stage utilised 0.04µm colloidal silica suspension rather than diamond, with

the final polish and etch repeated three times to achieve a finer finish with less deformation.

Tungsten carbide insert specimens were prepared differently, with samples mounted before being ground with diamond grinding papers to reveal a cross-section through the tool, which were then polished using diamond suspensions and colloidal silica as described above. Due to the clearly defined structure in sintered materials, comparative microstructural imaging can be conducted without the need for a chemical etchant. However, when these are used, they commonly dissolve the cobalt binder, rather than attack the tungsten carbide phase. Such an etchant that was suggested by Jung et al. [102] is included in Table 18 for reference.

Table 18 - Summary of etching procedures for each of the materials studied.

Specimen material	Etchant	Etching procedure
Ferrous alloys	Nital (3%)	Etched using a cotton wool swab and an exposure of a few seconds, until sample became slightly discoloured.
Sintered tungsten carbide	$90H_2O_2 + 10HNO_3$ (vol%)	Samples immersed in etchant at 60°C for approximately 12 minutes, until cobalt binder is preferentially dissolved out.

The microstructures of ferrous alloys (brake rotor materials and tool steels) presented were etched with Nital as described in Table 18. Tungsten carbide specimens were imaged without etching.

Following etching, ferrous samples were flushed with water, washed with neutral soap and cleaned with isopropanol before being allowed to dry. Their microstructures were subsequently observed using the techniques described in the following section.

Samples of EN10083 C50R were also prepared for transmission electron microscopy (TEM) and electron diffraction. For this, thin sections (1-2mm) were first cut using a precision abrasive saw, before being successively ground to create thick (0.5mm) foils. Circular samples (3mm diameter) were subsequently punched from these foils, further ground (to around 100µm thickness) before being electrolytically polished using a Metalthin twin jet electro-polisher. Samples were immersed in 220ml of electrolyte composed of 5% perchloric acid ($HClO_4$), 35% butoxyethanol and 60% methanol, the temperature of which was held at -50°C through the circulation of liquid nitrogen around the chamber. Electro-polishing was conducted using a current of 30mA until a small hole had formed in the centre of samples, creating thin (50nm) foils allowing for the transmission and scattering of electrons. Between steps and following electrolytic polishing, samples were flushed with water, cleaned with isopropanol and allowed to dry. Specimens were stored in isopropanol to prevent oxidation.

3.4.2. Microstructural observations

Optical micrographs and electron micrographs were generated from both ferrous alloy and tungsten carbide specimens. A Nikon LV150 light microscope with 50x and 100x objectives was used to take optical images with magnifications up to 1250x, while an FEI Inspect F high resolution field emission gun scanning electron microscope (FEG-SEM) was employed to further characterise the microstructures of each specimen. Microstructural features were initially imaged using accelerating voltages of 5-10kV and magnifications of up to 40000x, with high-resolution SEM at magnifications of 80000x subsequently used to observe precipitates in EN10083 C50R steel. The Inspect F was also used to conduct standardless energy-dispersive spectroscopy (EDS) to comparatively analyse the chemical composition of precipitates in AISI M2 tool steel specimens. EDS was conducted using an accelerating voltage of 20kV and a spot-size of 2.0 - 2.5nm, enabling analysis of features down to 0.5µm.

Transmission electron microscopy was used for high magnification (>80000x) imaging of EN10083 C50R samples. An FEI Tecnai 20 was used to identify fine precipitates and attempt to investigate grain boundary and interface regions using an accelerating voltage of 200kV.

Microstructural observations were correlated with wear resistance, wear mechanisms and hardness. Optical and electron microscopy features in Chapters 4, 5 (high resolution SEM and TEM of EN10083 C50R) and 6, while the results of EDS analyses are presented in Chapter 4.

3.4.3. Phase composition and crystallographic structure

A phase analysis of EN10083 C50R samples was attempted using a Siemens D5000 Diffraktometer with Bragg-Brentano geometry. Samples of as-received and cryogenically treated material were sectioned, before their surfaces were ground and polished using the techniques described in Section 3.4.1 to minimise X-ray scattering and therefore improving the overall signal-to-noise ratio.

X-rays were generated from a copper source with $K_{\alpha 1}$ and $K_{\alpha 2}$ radiation (mean wavelength 1.5418Å), using a tube voltage and current of 40kV and 40mA respectively. A secondary monochromator was fitted to strip out K_{β} radiation from the response and reduce the fluorescence effect that is common between Cu $K\alpha$ radiation and iron [103]. Following preliminary measurements to determine appropriate scan parameters, samples were analysed from 30 – 110° (2θ) using a step size of 0.02° and a step time of 5s. Further scans were then taken from 37 – 50° (2θ), using a step size of 0.02° but an increased step time of 10s, to better characterise the orthorhombic cementite peaks, which were numerous but found to be low in intensity in this region.

As is subsequently discussed in presenting these results, it was found that X-ray diffraction (using available equipment) was unable to provide the data required for a quantitative phase analysis of C50R steel, due to the radiation source / material pairing and issues with particle statistics as the X-ray beam was illuminating small numbers of grains and hence not a statistically representative sample of the material. As a result, one sample each of untreated and deep cryogenically treated C50R steel was sent off for neutron diffraction at the ISIS pulsed neutron and muon source at the Rutherford Appleton Laboratory in Oxfordshire, operated by the UK's Science and Technology Facilities Council using the Gem Xpress service. In contrast to X-rays, neutrons scatter based on their interaction with the atomic nucleus rather than the electron cloud, meaning that neighbouring elements in the periodic table can be clearly distinguished. More relevant to the current study, neutrons are highly penetrating as they have no net charge and interact only weakly with nuclei, making them ideal for the analysis of bulk samples with coarse grain structures [104]. Because of the long (and somewhat unpredictable) lead time of this service, it was not possible to obtain these data and conduct a quantitative phase analysis as part of the present study.

However, at a late stage, an opportunity presented itself to obtain some supporting data to the X-ray diffraction analysis using electron back-scatter diffraction. Only one sample was able to be analysed using this method, but was sufficient to clarify the phase composition and qualitatively assess the crystallographic texture of the material. Using an accelerating voltage of 15kV, a step size of 0.75µm and a grid of 911 × 683 pixels, an area of 683 × 512µm (0.35mm^2) was analysed. Although these parameters meant there was insufficient resolution to resolve cementite lamellae (of thickness 50 – 100nm when viewed in perpendicular section), the primary purpose of the analysis was to identify small grains or regions of austenite, and qualitatively assess the crystallographic texture of the sample. The sample analysed by this method was polished and lightly etched in line with those for high-magnification SEM. The results of the EBSD analysis are briefly discussed in Section 5.2.2.

Finally, electron diffraction was also used to characterise the crystal structure of phases in C50R steel specimens. The FEI Tecnai 20 employed for TEM was used for this purpose. By firing a focused electron beam through different locations on the thin foil samples, diffraction patterns are generated by the scattering effect of atoms within the crystal lattice, generating characteristic spot patterns that are dependent on the crystal structure, lattice type and orientation.

From these patterns lattice parameters can also be determined by relating the spot separation (R), camera length (L) and diffraction angle (2θ) as shown in Figure 29. Considering the small angle that the electron beam (wavelength, λ) diffracts by, the geometry of these patterns can be related to Bragg's Law and used to calculate the

lattice parameter (a) for the diffracting planes (spacing, d_{hkl}) as described by Equations 3.3 – 3.7.

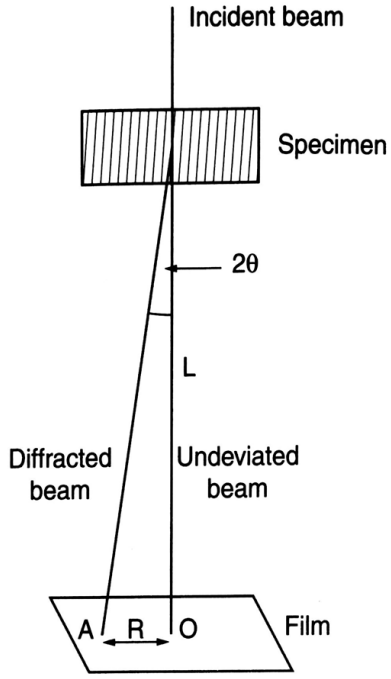

Figure 29 - Diagram illustrating the formation of spot patterns by diffraction of an electron beam [105].

Bragg's Law: $$\lambda = 2d_{hkl} \sin\theta \quad (3.3)$$

Diffraction pattern geometry: $$\frac{R}{L} = \tan 2\theta \quad (3.4)$$

Small angle approximation: $$\sin\theta \approx \theta;\ \tan 2\theta \approx 2\theta$$

Therefore, $$d_{hkl} = \frac{L\lambda}{R} \quad (3.5)$$

For a cubic crystal, $$d_{hkl} = \frac{a}{\sqrt{h^2 + k^2 + l^2}} \quad (3.6)$$

Therefore, $$a = \frac{L\lambda}{R}\sqrt{h^2 + k^2 + l^2} \quad (3.7)$$

3.5. Limitations of experimental methodologies

The methodologies selected represent a combination of basic tribological tests, more realistic in-service simulation tests, standard metrology techniques and microstructural analyses. While suitable to the purpose of comparatively assessing whether cryogenic treatment has had an appreciable effect on the wear performance and properties of the selected materials, the limitations of these methods must be recognised.

Tribological bench testing (such as the pin-on-disc and reciprocating sliding tests selected) is commonly used to provide initial estimates as to the performance of

materials. However, the use of idealised contacts (in this case circular point contacts), constraints on sliding speeds, temperatures and other environmental conditions, as well as different material pairs to those experienced by materials in-service, limit the extent to which the results of these types of tests can be related to real-life applications.

In reality the brake rotor materials tested would be subjected to greater sliding speeds, lower contact pressures and a wide range of temperatures and other environmental conditions compared with those reported in Chapter 4. They would also be in contact with complex composite materials, from which brake pads are made, as discussed in Section 1.2.1. A more realistic condition could arguably be achieved by using small specimens taken from brake pads, rather than chrome steel balls, as the wear-inducing pins. However, not only would this introduce size effects (due to the difference in the relative distribution of components of the brake pad materials in small sections when compared with the complete article), but also substantially increase the required duration of tests (from hours to days or weeks) to achieve measurable levels of wear.

When formed as cutting tools, the tool steels tested would come into contact with a variety of materials under a wide range of contact conditions (dependent on cutting parameters and cutting fluids). Rather than attempt to replicate this vast range of material pairs, contact pressures, temperatures and sliding speeds, it is more practical (for the purposes of an initial comparison) to test these materials against a hard material with which they have a low chemical affinity (zirconia), therefore allowing for changes in their wear resistance to be assessed independently of these complex variables.

For similar reasons, the results of machining tests conducted using tungsten carbide inserts (Chapter 5) must be seen in the context of the efforts of numerous other investigators (as discussed in Section 2.2). Only by testing a variety of common tool types under a range of cutting conditions and against numerous different workpiece materials can a complete picture be developed.

While the microstructural analysis techniques applied provided for comparisons of the structures of untreated and cryotreated materials to be made, they were not able to fully characterise each material. Limited access to resources meant that X-ray diffraction and transmission electron microscopy could only be utilised on one material showing the most significant wear performance and hardness changes following cryogenic treatment.

The results presented in subsequent chapters include measures of experimental variation, such as the coefficient of variation (standard deviation / mean), for each dataset where possible. Calculable uncertainties and errors, and limitations of the carbide analysis conducted in AISI M2 tool steel are also discussed in detail in Sections 3.5.1, 3.5.2 and 3.5.3.

3.5.1. Uncertainties in pin-on-disc wear measurements

It is common practice in tribology to use wear volume estimates, as comprehensive wear measurements can be extremely time consuming. Wear estimates are often necessitated by large wear scars, where small mass losses are indistinguishable from large nominal specimen masses, or where significant amounts of material adhesion may have occurred. Of the volume loss estimation methods available, those based on profilometry and interferometry are the most common.

The first method is that employed in the pin-on-disc studies reported in Section 4.3.2.1, in which a number of cross-sections are measured using a 2D stylus profilometer. The areas of these cross-sections are calculated, the mean determined, and a volume estimate produced by multiplying this mean cross-section by the nominal circumference of the wear track.

While the second method offers the possibility of a full volume measurement being made, in reality this is rarely practical due to the limitations in stage motion of modern interferometers and the difficulty of producing software or algorithms capable of accurately separating a wear track from an unworn surface. The commonly used alternative is an advancement of the profilometry technique already mentioned, in which small volume sub-sections are scanned to allow an estimate of the wear volume that is based on a significant percentage of the total wear track. One drawback to this method is the time requirement as, while a profile can be measured in a matter of seconds, even a small volume scan may take minutes.

Methods such as these can produce significant numerical uncertainties. In the case of pin-on-disc measurements, expressions developed by Colbert et al. [106] can be used to determine the uncertainty in pin-on-disc volume estimations based on the number of measurements of cross-sections that have been made. Given as Equation 3.8, Colbert et al. demonstrated that the uncertainty in wear volume (u_V) is dependent on the wear track radius (R), the number of cross-sections measured (N), the variation in the cross-sections (σ_A), the uncertainty in the wear track radius (u_R) and the mean area of the measured cross-sections (μ_A). It was also shown that if the uncertainty in radius was significantly less than the wear track radius ($u_R << R$) then a further simplification could be made, the result of which is given as Equation 3.9.

$$u_V \cong \frac{2\pi R}{\sqrt{N}} \sqrt{\sigma_A^2 + \frac{u_R^2}{R^2}(\sigma_A^2 + \mu_A^2)} \tag{3.8}$$

$$u_V \cong \frac{2\pi R}{\sqrt{N}} \sigma_A \tag{3.9}$$

Using Equation 3.9, it can be shown that the uncertainties in the pin-on-disc wear volume measurements subsequently reported lie between 3 – 23%. Coupled with other techniques such as the use of optical micrographs to characterise wear mechanisms, these potentially significant uncertainties can be effectively mitigated. Calculated numerical uncertainties are discussed along with the volume wear results for grey cast iron and carbon steel brake disc materials in Section 4.3.2.1.

3.5.2. Errors in tool wear crater depths

Due to the complexity in the topography of the rake faces of the cutting tool inserts that were scanned using light interferometry, no simple tilt correction function could be used to correct for the angle of the stage (which could be rotated about the x and y axes). This tilt could be manually corrected to leave an approximate 1% gradient in either direction. However, over the length of the sample measured (around 2mm), this resulted in a 20µm change in the vertical z-axis, which became significant when attempting to measure crater depths of the same order of magnitude. Figure 30 shows a typical topographic scan and profile traces taken from H13A tool inserts.

To correct for this gradient, additional points were identified on the nominally flat surface between the cutting edge and the chip breaker. These are identified in Figure 30, where the dotted lines correspond to the profile traces shown, points 1 – 4 indicate the lengths over which the x and y gradients were calculated, and the points c1 and c2 indicate the maximum crater depths recorded in the x and y directions respectively.

In summary, the gradients between the pairs of points (1, 2) and (3, 4) were used to calculate an adjustment to the crater wear depths measured at points c1 and c2. The mean of these two corrected depths was then compared to the level surface at point 1 (which was chosen as a reference) to provide the reported crater wear depth. A full explanation of this process is provided in Appendix 10.3.

However, errors remained in these measurements due to noise in the interferometric data, which meant that the apparent 'roughness' of the tool insert surface was of the order of ±3µm (compared to an accurate surface roughness measurement around a fifth of this value). This noise translated into errors in the gradients calculated in the x and y directions and therefore the adjustments made to the measured crater depths at points c1 and c2.

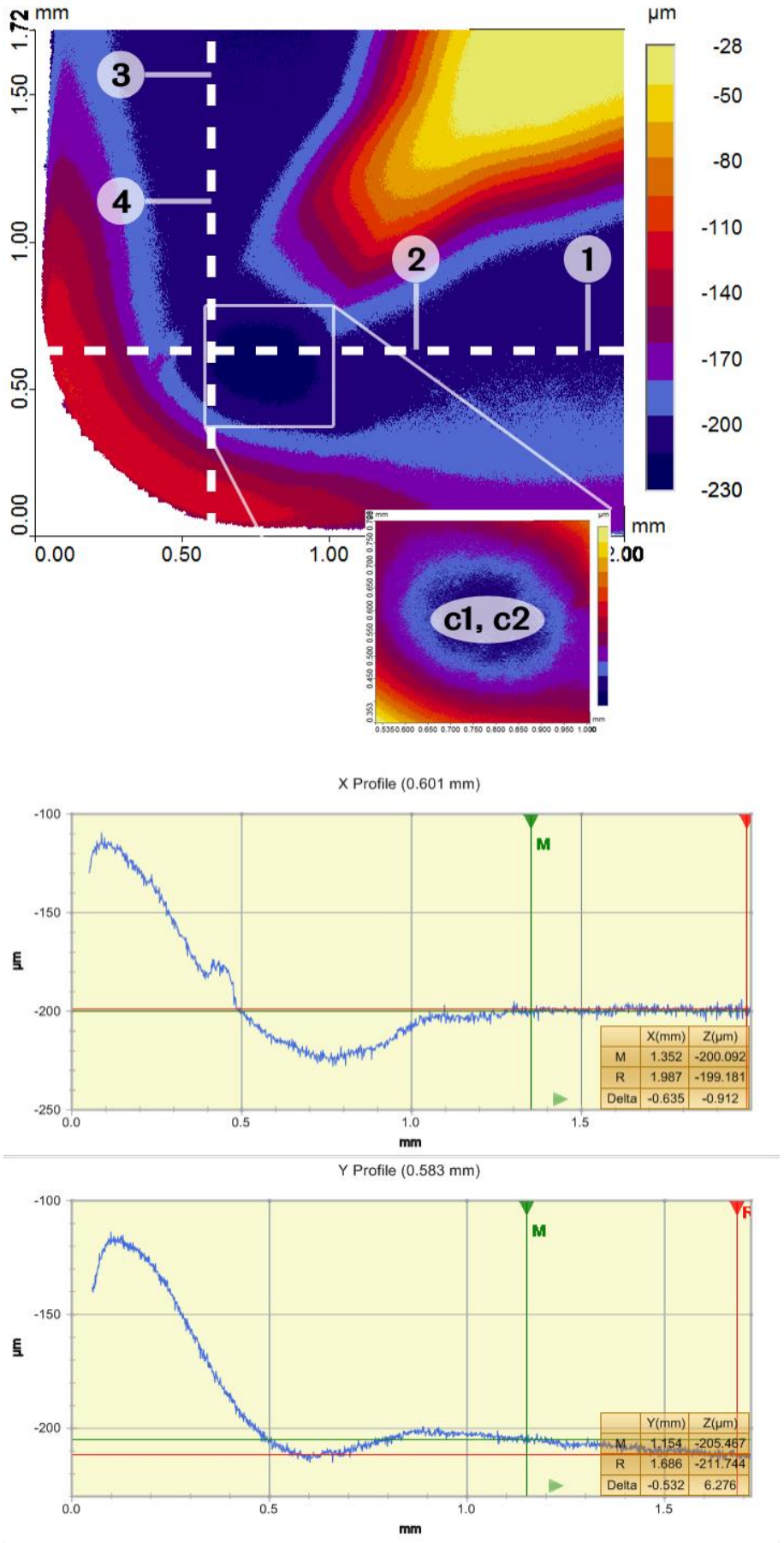

Figure 30 - Example of interferometric topograph and profiles measured from H13A tool inserts.

As point 1 was used as the reference point for crater depth corrections, intuitively any error in the gradient in the x direction will be dominant due to the comparatively large distance given by ($x_1 - x_c$) when compared with ($y_1 - y_c$). To mitigate these errors, it was ensured that the distance between points (1, 2) and (3, 4) was at least 500µm. From this minimum value (giving the maximum error condition), it can be shown that:

Where the gradient, $$k_x = \frac{z_1 - z_2}{x_1 - x_2} \quad (3.10)$$

The error in the gradient, $$\varepsilon(k_x) = \frac{\varepsilon_z}{x_1 - x_2} \quad (3.11)$$

If $\varepsilon_z = \pm 3\ \mu m$ and $x_1 - x_2 > 500\ \mu m$, $$\Rightarrow |\varepsilon(k_x)| < 6\ nm/\mu m$$

Where the crater depth correction, $$\Delta z_{c,x} = \big(k_x + \varepsilon(k_x)\big)(x_1 - x_c) \quad (3.12)$$

The error in the correction, $$\varepsilon\big(\Delta z_{c,x}\big) = \varepsilon(k_x)(x_1 - x_c) \quad (3.13)$$

If $x_1 - x_c > 1000\ \mu m$, $$\Rightarrow \big|\varepsilon\big(\Delta z_{c,x}\big)\big| < 6\ \mu m$$

3.5.3. Energy-dispersive vs wavelength-dispersive spectroscopy

Numerous methods can be used to analyse the structure and composition of materials. To name but a few common methods (and their typical uses): scanning electron microscopy (high magnification imaging), transmission electron microscopy and X-ray diffraction (phase composition and crystallographic structure determination), and energy-dispersive spectroscopy and wavelength-dispersive spectroscopy techniques such as X-ray fluorescence (chemical composition analysis).

While each technique provides unique capabilities and information about the materials being analysed, it was decided that information about chemical composition would be most relevant to the studies presented here (while also considering time and resource constraints). In particular, the need to analyse changes in the composition of tool steel carbides necessitated a technique that had good spatial resolution. Based on the comparison presented in Table 19, energy-dispersive spectroscopy was therefore selected, as it allowed at least a qualitative analysis of carbides down to 0.5µm in size. However, EDS offers relatively low accuracy in determining chemical composition when compared to WDS.

It is acknowledged that the carbide analysis using EDS in AISI M2 tool steel that is presented in Section 4.3.3.3 has severe limitations due to the small samples sizes of carbides analysed and the relative inaccuracy in the measurement technique already identified. More detailed analysis of these carbides would require their extraction from the material, after which techniques such as X-ray fluorescence and X-ray diffraction could be used to accurately determine their chemical and phase

compositions, while electron diffraction could be used to characterise their crystallographic structure.

Table 19 - Comparison of attributes of energy-dispersive and wavelength-dispersive spectroscopy techniques [107].

Attribute	Energy-dispersive spectroscopy	Wavelength-dispersive spectroscopy
Element detection	All elements where Z>4 Multiple elements simultaneously	All elements where Z>3 Multiple elements successively
Detection limit	0.1%wt (1-2%wt with severe overlap)	0.01%wt
Typical accuracy	<50% (for concentrations <5%wt) 5% (for concentrations >>5%wt)	1%
Scan size	0.5 µm	mm
Scan depth	<1.0 µm	10 µm
Advantages	Rapid measurements Ease-of-use Spot measurements	Excellent resolution of energy peaks Composition depth measurements
Disadvantages	Poor resolution of energy peaks (~100x natural peak width) Low peak-to-background ratio	Slower measurements Only area measurements

3.5.4. Particle statistics in X-ray diffraction

X-ray diffraction has a number of uses in analysing preferred orientation, strain, crystal structure determination and phase composition. The requirements for a successful analysis of phase composition are to have high resolution diffraction patterns, with narrow peaks to aid in distinguishing between reflections of phases with similar diffraction angles, as well as good counting or particle statistics such that diffraction patterns are reproducible to within ±2% [108].

This last requirement is directly related to the number of diffracting crystallites (in powder diffraction) or number of grains (for diffraction experiments involving solid samples). These factors are clearly affected by particle or grain size, as well as the area of the sample 'illuminated' by the incident X-ray beam, and its penetration into the material (which is further dependent on the mass absorption coefficient of the material for the incident radiation). More simply, being able to obtain a statistically representative diffraction pattern is dependent on having a sufficient number of diffracting grains within the volume of material that is scattering the incident radiation [109].

While there is no fixed value for such a 'sufficient number' that is required, a diffracted sample must contain a number of randomly oriented grains or crystallites that is representative of the bulk material. Although this is heavily influenced by factors including grain size, the number of different phases and their relative proportions, as well as texture (the preferred orientation and clustering of phases in polycrystalline materials), it has been argued that an ideal powder sample should contain 10^9

randomly oriented crystallites per cubic millimetre [103] for this criterion to be met. In other words, the average crystallite size should ideally be 1μm^3.

A number of relationships have been developed which can start to provide an estimate of the errors that can result from insufficient counting statistics. Given as Equations 3.14 – 3.16, these describe:

- An estimate of the fractional error dependent on the number of diffracting crystallites – note this is not the same as the number of 'illuminated' crystallites, but only those that meet the Bragg condition at any given diffraction angle.
- The predicted penetration depth that varies with diffraction angle (θ) and the linear absorption coefficient (μ) of the material. For the first diffraction peak in pure iron ferrite (2θ = 44°), using Cu Kα radiation (μ = 2550cm^{-1}), the resulting penetration depth is 5.1μm.
- The fraction of the diffracted intensity coming from the material between the surface and the given depth into the material. Again using the values for the first diffraction peak in pure iron and Cu Kα radiation, it can be shown that approximately 74% of the diffracted intensity results from the first 1μm of material from the surface.

Estimate of fractional error based on number of diffracting crystallites [110],

$$\sigma_{PS} = \frac{\sqrt{N_{diff}}}{N_{diff}} \tag{3.14}$$

Variation of penetration depth with linear absorption coefficient and diffraction angle [108],

$$t = \frac{3.45}{\mu}\sin\theta \tag{3.15}$$

Fraction of diffracted intensity with penetration depth, linear absorption coefficient and diffraction angle [109],

$$G_x = 1 - e^{-2\mu x/\sin\theta} \tag{3.16}$$

Smith [110] attempted to determine more realistic values for the number of diffracting crystallites than those given by volume estimates alone. Based on their data, the relationship between crystallite diameter and the number of diffracting crystallites shown on the left of Figure 31 was extrapolated. On the right, this can be compared with the fractional error calculated from Equation 3.14. An estimate for grain size, typical of a carbon steel, of around 20μm is suggested to result in around 80 diffracting crystallites (or grains) and a fractional error of approximately 11% – significantly greater than that required for quantitative phase analysis.

Indeed, in the analysis of Smith a sample of SiO_2 was analysed using a Cu Kα source for which the absorption coefficient (μ = 97.6cm^{-1}) is considerably smaller than that of Fe. Arguably, therefore, the number of diffracting crystallites for an Fe-based alloy would be significantly smaller still.

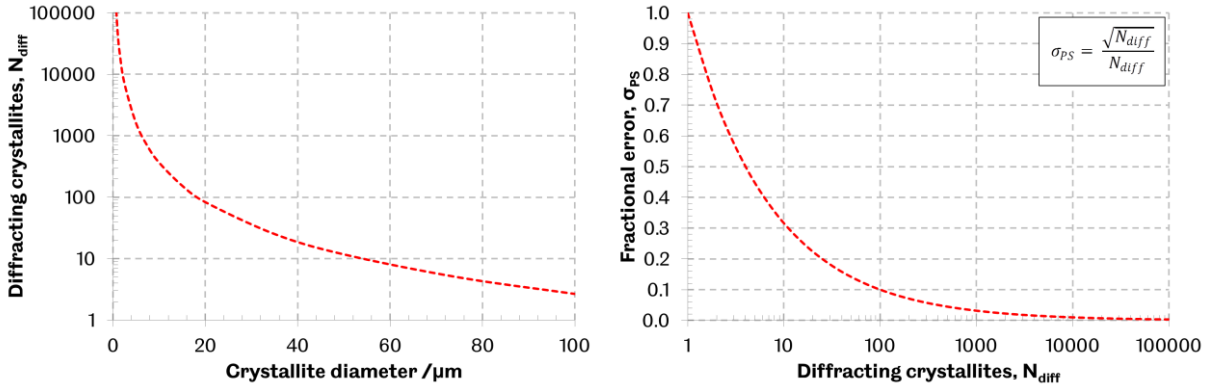

Figure 31 - The effect of crystallite size in powder diffraction: (left) estimate of number of diffracting crystallites based on their diameter (extrapolated from Smith [110]); (right) estimate of fractional error based on number of diffracting crystallites generated from Equation 3.14.

Considering Cu Kα radiation (such as what was available for the present study) incident on pure iron, the relationships described by Equations 3.15 and 3.16 have been plotted as Figure 32, from which the shallow penetration depths and significance of the contribution to the diffracted intensity from a thin surface layer can be seen.

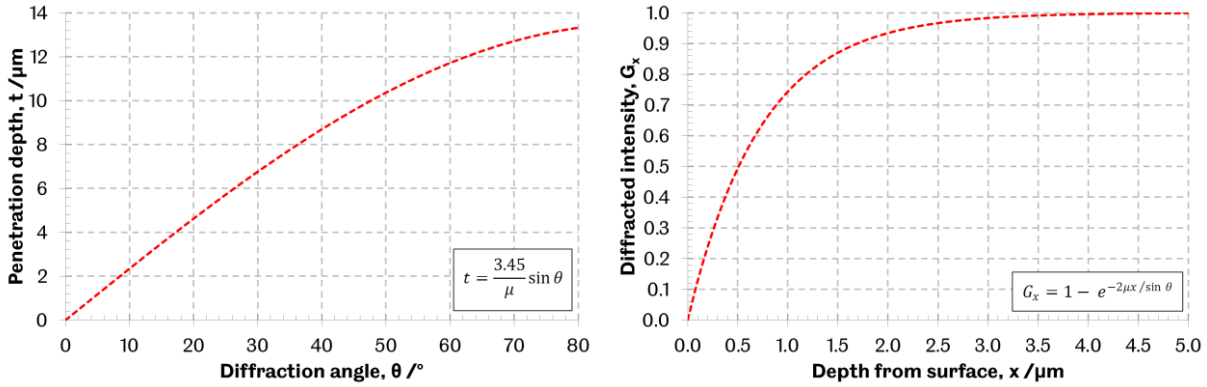

Figure 32 - Penetration depth as a function of diffraction angle (left) and fraction of diffracted intensity with penetation depth (right) based on Equations 3.15 and 3.16 respectively (μ = 2550 cm^{-1}, θ = 22°).

The problem of counting statistics is illustrated well by Figure 33, which shows Debye-Scherrer rings created using a back-reflection pinhole diffraction setup. It can be seen that, for large grain sizes in the recrystallised aluminium samples tested, only a few scattered spots are visible. As the grain size is progressively reduced from (a) to (d), the characteristic diffraction rings form. As diffraction patterns from Bragg-Brantano goniometers represent only sections of these rings (as indicated by the dotted lines), large grain sizes can result in a significant loss of information.

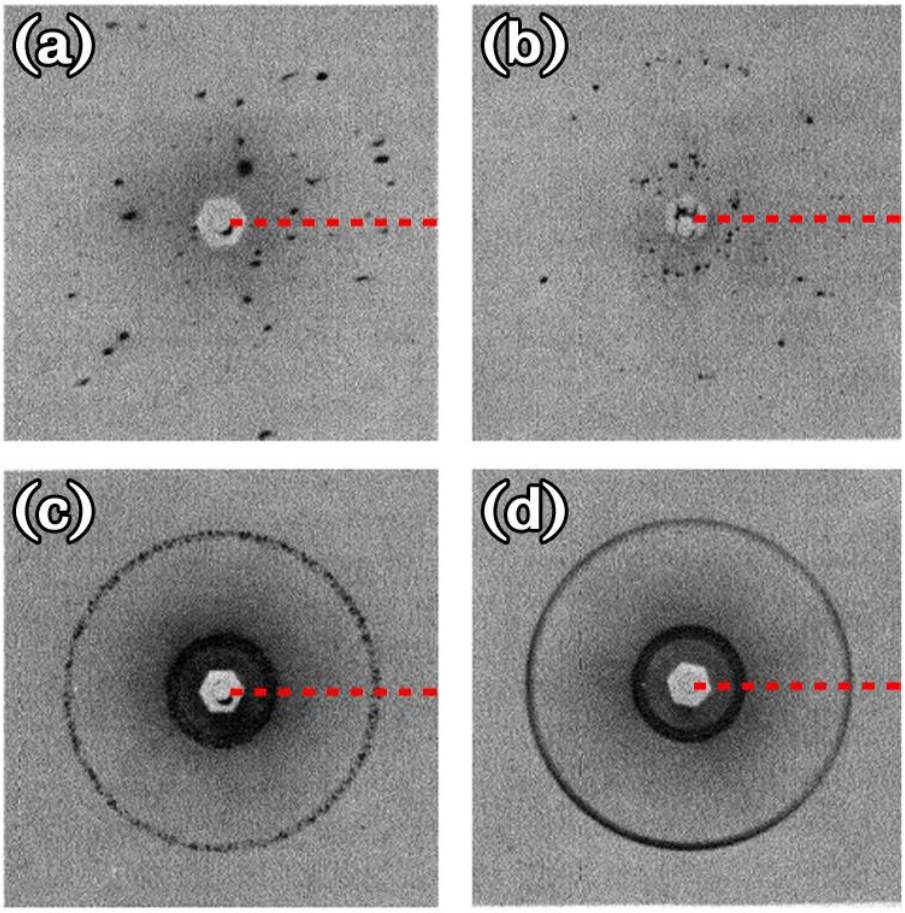

Figure 33 - Debye-Scherrer rings formed from recrystallised aluminium specimens with increasing grain size from (a) to (d) (adapted from Cullity [109]). Dotted lines illustrate sections that diffraction patterns would represent.

Although no alternatives were available for the present study (therefore limiting it to a qualitative phase analysis), the use of a different radiation source with a much lower absorption coefficient in iron (e.g. Cr Kα, $\mu = 905cm^{-1}$ or Mo Kα, $\mu = 300cm^{-1}$ [109]) would significantly improve the reproducibility of obtained diffraction patterns. Ideally, as described in Section 3.4.3, a neutron source would allow penetration through the entire bulk of the sample to provide robust data for quantitative analysis.

3.6. Summary

Investigations to assess the effects of new heat treatment techniques or materials require an extensive range of mechanical testing, wear testing and microstructural analyses to be conducted. Techniques were selected to complete the early stages of such an assessment of the effects of cryogenic treatment on a range of materials, using comparative laboratory-based wear testing, microstructural imaging and accelerated in-service wear testing.

Following controlled deep cryogenic treatment of all specimens, pin-on-disc testing was selected to test grey cast iron (SAE J431 G10) and pearlitic carbon steel (EN10083 C50R) brake rotor materials, while reciprocating sliding tests were chosen for three

as-cast tool steels (AISI A2, D6 and M2). The wear development of tungsten carbide turning inserts (SHM H13A) was tested by machining AISI 1045 / EN8 carbon steel.

Complimenting these test methodologies were a variety of measurement and observation techniques, including Vickers hardness testing (for all specimens), profilometry (for determining the volume loss from brake rotor specimens), mass measurements (to determine the mass loss and mass change in tool steel and tungsten carbide insert specimens respectively), optical microscopy (for analysing the dominant wear mechanisms in all specimens, and the extent of flank wear in tungsten carbide insert specimens), interferometry (for measuring the depth of crater wear in tungsten carbide insert specimens) and scanning electron microscopy (for microstructural imaging in all specimens, and subsurface wear analyses of tungsten carbide insert specimens). Additionally a brief study using energy-dispersive spectroscopy was used to analyse carbide compositions in AISI M2 tool steel specimens. The material showing the most significant wear performance and hardness changes (EN10083 C50R) was subjected to microstructural characterisation involving high-resolution scanning electron microscopy, transmission electron microscopy, X-ray and electron back-scatter diffraction, and electron diffraction. For microstructural analyses, samples were sectioned from brake rotor, tool steel and tungsten carbide insert specimens, before being prepared using standard metallographic techniques involving grinding, polishing and chemical etching.

The limitations of the selected techniques were discussed, highlighting their place as only the beginning of a more extensive testing and analysis process required to fully characterise the effects of deep cryogenic treatments on the materials tested, and in understanding their in-service performance under a variety of conditions. Particular uncertainties and errors in the determination of wear scar volumes from brake rotor specimens, the depth of crater wear in tungsten carbide insert specimens, and the composition of carbides in AISI M2 tool steel specimens were analysed. It was demonstrated that uncertainties of 3 – 23% existed in the volume loss determinations made from brake rotor specimens, that errors in the measured crater wear depths on tungsten carbide inserts were less than 6µm, and that while large uncertainties existed in the accuracy of carbide compositions reported, the use of energy-dispersive spectroscopy would still provide a useful preliminary qualitative comparison between untreated and cryogenically treated tool steel specimens. Finally, issues relating to counting statistics in the analysis of coarse grained steels were discussed, concluding that a quantitative phase analysis would require different X-ray radiation sources (unavailable at the time of this study) or neutron diffraction at a central facility.

4. Effects of deep cryogenic treatment on the sliding wear performance of ferrous alloys

In this chapter the testing parameters and results of pin-on-disc testing on SAE J431 G10 grey cast iron and EN10083 C50R non-alloy steel brake rotor materials, and reciprocating sliding testing on as-cast AISI A2, D6 and M2 tool steels are presented. Results are discussed, referring to published literature where relevant, before the conclusions of the study are presented.

4.1. Materials

Five ferrous-alloys, including a lamellar graphite cast iron (SAE J431 G10), pearlitic carbon steel (C50R) and three complex alloy tool steels (AISI A2, D6 and M2) were selected for basic tribological testing and microstructural analyses in a comparative study of the effects of cryogenic treatment on a range of commonly used engineering materials.

No single material standard contains specifications for all of these materials, and so Table 20 cross-references the relevant material designations across a number of standards. AISI/SAE designations were adopted to refer to all materials used in this study, except for the pearlitic carbon steel, where the EN10083 designation was used.

Table 20 - Cross-referenced specifications across material standards.

AISI/SAE	EN10027	Alternative (Standard)
J431 G10	-	Class 30 (ASTM 48)
-	1.1241	C50R (EN10083)
A2	1.2363	X100CrMoV5 (ISO 4957)
D6	1.2436	X210CrW12 (ISO 4957)
M2	1.3343	HS6-5-2C (ISO 4957)

4.1.1. Chemical composition

Table 21 and Table 22 show the material compositions of the brake materials and tool steels tested respectively, with the balance iron (Fe) content excluded. In the case of C50R, spark optical emission spectroscopy was used to determine the composition, as no nominal specification could be obtained from the manufacturer. It was reported to match the 080M50 grade as defined by the superseded BS970:1996 standard, and so the European designation C50R was adopted instead.

Table 21 - Compositions for grey cast iron and carbon steel brake materials studied (balance Fe).

%wt.	C	Si	Mn	P	S	Cr	Mo	Ni
SAE J431 G10	3.35-3.60	1.90-2.30	0.60-0.90	0.10	0.15	-	-	-
C50R	0.47	0.18	0.75	0.010	0.007	0.03	<0.01	0.03

Table 22 - Compositions for tool steels studied.

%wt.	C	Si	Mn	Cr	Mo	V	W	P	S
AISI A2	0.95-1.05	0.10-0.40	0.40-0.80	4.80-5.50	0.90-1.20	0.15-0.35	-	0.03 max.	0.03 max.
AISI D6	2.10	0.85	0.30	12.00	-	-	0.75	0.03 max.	0.03 max.
AISI M2	0.86-0.94	0.45 max.	0.40 max.	3.80-4.50	4.70-5.20	1.70-2.10	5.90-6.70	0.03 max.	0.03 max.

Although, particularly in the case of the tool steels, a simple binary phase diagram cannot accurately describe the isothermal systems of these materials, one has been provided for reference (Figure 34) with the approximate carbon contents of the five alloys tested overlaid. While the compositions of the two brake disc materials vary significantly, they both share a primarily pearlitic-ferritic microstructure and so were chosen to investigate whether carbon content or that of other alloying elements could be shown to significantly alter (support or prevent) any effects of cryogenic treatment. SAE J431 G10 grey cast iron additionally contains graphite flakes, as a result of the addition of silicon to stabilise this phase.

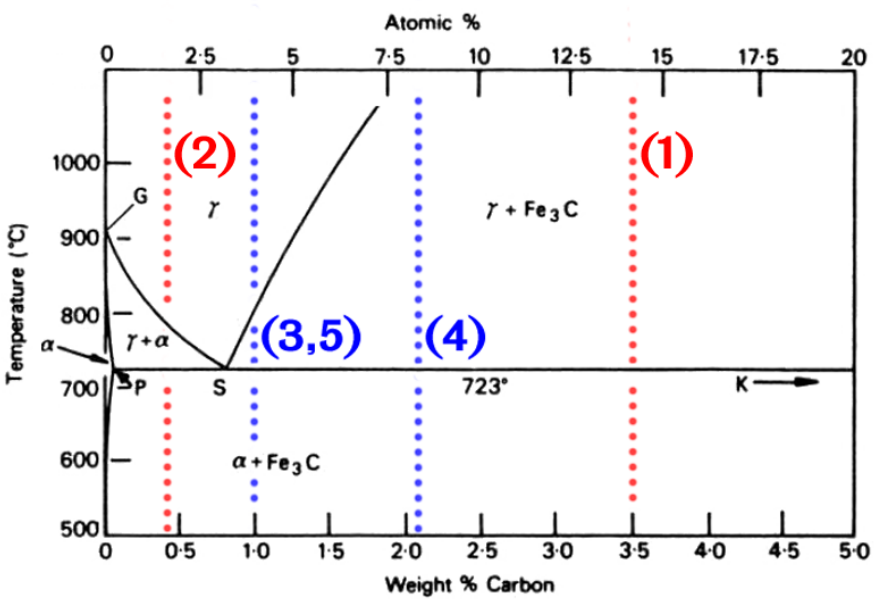

Figure 34 - Fe-Fe_3C binary phase diagram (adapted from Bhadeshia et al. [9]) with approximate carbon contents overlaid: (1) SAE J431 G10; (2) EN10083 C50R; (3) AISI A2; (4) AISI D6; (5) AISI M2.

The three tool steels also exhibit key compositional differences. While the fine grained A2 and M2 materials have comparable carbon (C) contents, the high carbon and chromium (Cr) content of D6 gives rise to a pro-eutectoid coarse carbide phase that remains un-dissolved at austenitising temperatures. A2 and M2 share molybdenum (Mo) and vanadium (V) as alloying elements, although both feature in significantly higher quantities in the latter. Both are strong carbide formers, typically added to enhance wear resistance. Similarly M2 contains substantially more tungsten (W) than

D6; tungsten being added to steel to enhance its wear resistance at elevated temperatures.

In the studies presented here, the brake rotor materials were tested as finished components, while the tool steels were tested in their annealed condition, as-received from the manufacturer. As discussed previously, investigations on martensitic tool steels are prevalent in the literature. This study instead investigates the effects of cryogenic treatment on ferritic-austenitic materials which, while unsuitable for the manufacture of cutting tools, may show other benefits that allow cryogenic treatment to be considered for alternative material processing routes. For instance, in their study on valve steels, Jaswin et al. [80] reported substantial increases in the hardness of austenitic En52 steel due to deep cryogenic treatment; suggesting that a large scale austenite to martensite transformation had occurred. In considering alternative processing routes for tool production, Akbari et al. [111] determined that nitriding depth in AISI M2 tool steel could be doubled by using the surface treatment on a fully annealed material when compared with a quench-hardened, martensitic material. Studies such as these suggest that, as well as the already understood applications of cryogenic treatment in enhancing martensitic tool steels, it may be useful as part of more unorthodox heat and surface treatment regimes, that may be used to create materials that have substantial wear resistance and toughness.

Tool steels received in their annealed condition were soaked above or near their eutectoid temperatures, before being slowly furnace and air cooled. Because of this, a ferrite-austenite matrix would have been present, along with any un-dissolved carbides, globular cementite and various alloy carbide precipitates. Table 23 and Figure 35 summarise the recent heat treatment history for the three tool steels. As the manufacturer would have been aiming to achieve maximum machinability by the annealing process, it has been assumed that the heat treatment cycles applied were designed to retain and stabilise as much of the austenite phase as possible to room temperature.

Table 23 - Recent heat treatment histories of tool steels tested.

AISI A2	AISI D6	AISI M2
Heated slowly to 850-870C	Heated to 800-840C	Heated to 850C
Held for 2hrs, lower to 730-750C	Furnace cooled	Held for 2hrs
Furnace cooled to 600C		Furnace cooled
Removed and air cooled		

After being received, all materials were kept in ambient conditions for periods of several months, before undergoing deep cryogenic treatment as described in Section 3.2. This period is indicated by the 'Transition' line in Figure 35.

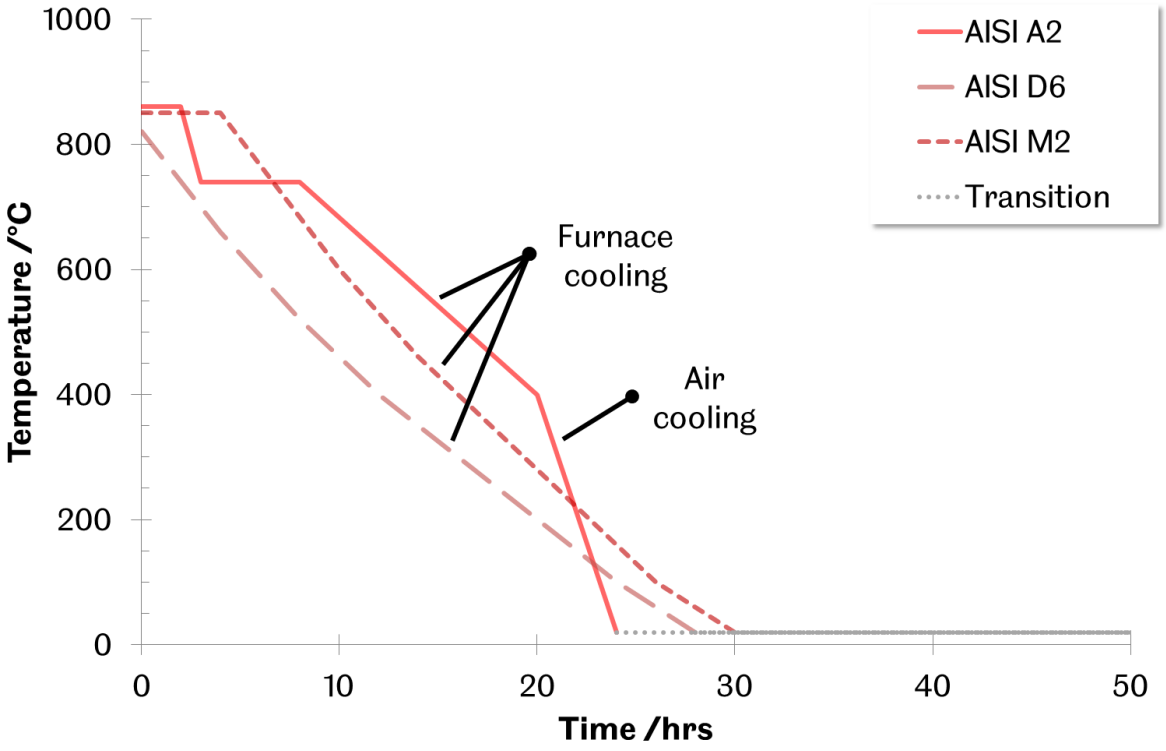

Figure 35 - Recent heat treatment histories of tool steels tested (cooling rates are indicative only) where the 'Transition' line indicates extended time in transit and storage prior to testing.

4.1.2. Mechanical properties

The known mechanical properties of the five materials tested were used to calculate testing parameters (detailed in Section 4.2). As discussed in Section 3.3.2, the Tresca and von Mises yield criterion are commonly used to predict the point of yield in pure shear, and are related to the tensile yield stress by Equations 3.1 and 3.2 respectively.

As both brake rotor materials conformed to known standards, nominal values for their mechanical properties along with measured hardness values (reported in Section 4.3.1.1) were available. These properties are summarised in Table 24 along with the manufacturer's data for AISI 52100 chrome steel that was used for the wear-inducing pins. By assuming that Archard wear behaviour exists between these materials (that is to say that the rate of wear of each material is proportional to its hardness), it was suggested that the wear on the AISI 52100 balls would be insignificant in comparison to either brake rotor material.

As the tool steels were tested in their as-cast or normalised conditions, finding reliable values of their tensile yield strengths proved impractical, with the only way to determine these parameters being to conduct separate tensile tests that were beyond the resource and time constraints of this project. Those properties that were available are summarised in Table 25 along with the hardness values reported in Section 4.3.1.1 and manufacturer's data for the zirconia balls used as wear-inducing

pins. From these data it could again be theorised that the wear loss from tool steel specimens would dominate.

Table 24 - Mechanical properties of brake materials and chrome steel material of wear-inducing pin.

Material	E /GPa	v	HV /MPa	σ_y /MPa	σ_{uts} /MPa
SAE J431 G10	87[s]	0.26[s]	2070[r] ($HV_{196.2}$)	-	207[s]
C50R	210	0.30	1622[r] ($HV_{196.2}$)	400	700
AISI 52100	210[m]	0.30[m]	7000-9000[m] ($HV_{98.1}$)	-	-

Unless otherwise cited:
m = manufacturer's data / r = experimental results (Section 4.3.1) / s = international standard.
All other data represents range or mean values from various industrial sources.

Table 25 - Mechanical properties of tool steels and zirconia material of wear-inducing pin.

Material	E /GPa	v	HV /MPa
AISI A2	203	0.30	2085[r] ($HV_{196.2}$)
AISI D6	207	0.30	2440[r] ($HV_{196.2}$)
AISI M2	207	0.30	2572[r] ($HV_{196.2}$)
Zirconia	225[m]	0.28[m]	11400[m] ($HV_{98.1}$)

Unless otherwise cited:
m = manufacturer's data / r = experimental results (Section 4.3.1) / s = international standard.
All other data represents range or mean values from various industrial sources.

4.2. Testing parameters

4.2.1. Grey cast iron and carbon steel brake rotor materials

Eight SAE J431 G10 grey cast iron brake rotors and six C50R were used in this study; half of each having undergone deep cryogenic treatment. Pin-on-disc testing was used to compare the performance of cryogenically treated materials against 'off-the-shelf' components, rather than to compare the two materials against one another.

Brake disc materials were assessed over a range of conditions. In the case of the grey cast iron brake rotors, three initial Hertzian contact pressures and sliding speeds were used; with test durations determined by the emergence of a dominant wear mechanism and a visible (and therefore measurable) amount of wear. The pressures and sliding speeds applied were 375.0, 562.5, 750.0MPa and 1.34, 1.78, 2.24m/s respectively.

C50R brake rotors were also subjected to three initial contact pressures, but only one sliding speed of 1.18m/s and fixed test durations of 20 minutes, which preliminary trials had shown to be sufficient for generating significant amounts of wear and establishing a dominant wear mechanism. Contact pressures of 1000, 1300, 1600 MPa were applied. Table 26 summarises the Hertzian contact conditions for each test and compares them with the Tresca and von Mises yield criteria (using the mechanical properties summarised in Table 24).

Table 26 - Contact pressures, material stresses and yield criteria predicted for brake material pin-on-disc testing.

Material	Peak contact pressure (p_0) /MPa	Max. tensile stress ($\sigma_{t,max}$) /MPa	Max. shear stress ($\tau_{1,max}$) /MPa	Tresca shear yield stress (τ_y) /MPa	von Mises shear yield stress (τ_y) /MPa
SAE J431 G10	375.0	60.2	116.6	103.5	119.5
	562.5	90.0	174.3		
	750.0	120.0	232.6		
C50R	1000	133.3	309.8	200.0	230.9
	1300	173.4	403.1		
	1600	213.3	495.9		

It can be seen from Table 26 that differing wear mechanisms may be expected from wear tests on grey cast iron, with the first contact condition creating a predicted shear stress of 116.6MPa; in between the yield stresses predicted by the Tresca and von Mises criterion. In particular it was suggested that subsurface wear mechanisms would become more significant in tests conducted at higher initial contact pressures, while the tensile yield stress of neither material should be exceeded.

The methodology used for testing G10 brake rotors meant that no exact repeat tests were conducted. Instead the wear data was normalised against different test parameters to discern what trends were present. Three repeat tests were conducted on C50R brake materials for each contact condition. Wear quantities on both materials were determined using the volume-loss method described in Section 3.3.2.1.

4.2.2. AISI A2, D6 and M2 tool steels

Electro-discharge machining was used to cut tool steel bars into 2mm thick discs for testing using the TE77 as described in Section 3.3.2.2. A fixed 80N load was applied, causing an initial Hertzian peak contact pressure of 3.23 – 3.25GPa. Using a stroke length of 10.7mm and a reciprocating frequency of 5Hz resulted in an arithmetic mean sliding speed of 107mm/min for all tests. Three repeat tests were conducted at each sliding distance of 100, 150 and 200m, with wear quantities determined by the mass-loss method described in Section 3.3.2.2. Table 27 summarises the Hertzian contact conditions for each test, based on the mechanical properties summarised in Table 25. While insufficient data was available to compare these data against the Tresca and von Mises yield criteria, their magnitude (in all cases at least twice that of contact pressures applied to brake rotor specimens) suggested that both criterion would be exceeded and that severe wear mechanisms would develop during testing.

Table 27 - Contact pressures, material stresses and yield criteria predicted for tool steel reciprocating sliding testing.

Material	Peak contact pressure (p_0) /MPa	Max. tensile stress ($\sigma_{t,\,max}$) /MPa	Max. shear stress ($\tau_{1,\,max}$) /MPa
AISI A2	3230	430.5	1000.9
AISI D6	3250	433.4	1007.7
AISI M2	3250	433.4	1007.7

4.3. Results

4.3.1. Hardness

4.3.1.1. Grey cast iron and carbon steel brake rotor materials

Bulk hardness measurements, taken from the surface of brake specimens, are shown in Table 28. It can be seen that deep cryogenic treatment had no significant effect on the hardness of G10 brake rotors (with the 1.9% increase in the mean value lying well within one standard deviation), while the hardness of C50R brake materials was observed to increase by 27.7%.

Table 28 - Macro-hardness test results from brake rotor surfaces.

Specimen type	Treatment	$HV_{196.2}$ /MPa	Coefficient of variation
SAE J431 G10	Standard	2070	3.5%
	Cryotreated	2109 (+1.9%)	4.9%
C50R	Standard	1622	4.3%
	Cryotreated	2071 (+27.7%)	1.8%

Similar trends were observed from micro-hardness measurements (Table 29), with G10 brake material showing no significant change due to deep cryogenic treatment, while the matrix hardness of C50R was found to have increased by 16.5%. Although less than the increase in bulk hardness recorded, this increase was still significantly greater than the standard deviation in the data.

Table 29 - Micro-hardness test results from brake rotor samples.

Specimen type	Treatment	$HV_{0.4905}$ /MPa	Coefficient of variation
SAE J431 G10	Standard	3600	17.2%
	Cryotreated	3679 (+2.2%)	11.8%
C50R	Standard	1927	2.6%
	Cryotreated	2244 (+16.5%)	2.0%

It should be noted that macro- and micro-hardness test results are not readily comparable due to size effects caused by different material constituents. The large variation in the macro- and micro-hardness reported for G10 brake material between Table 28 and Table 29 is likely a result of this. The large coefficient of variation found from micro-hardness measurements is indicative that indents were strongly affected by the different microstructural features of the material; namely graphite flakes, pearlite clusters and ferrite grains.

4.3.1.2. AISI A2, D6 and M2 tool steels

The results of bulk hardness measurements from AISI A2, D6 and M2 tool steels are given in Table 30. In no cases were the changes recorded thought to be significant, with the largest change (-3.1% in the case of AISI A2) lying on the threshold of one standard deviation.

Table 30 - Macro-hardness test results from tool steel surfaces.

Specimen type	Treatment	$HV_{196.2}$ /MPa	Coefficient of variation
AISI A2	N	2085	4.1%
	C	2021 (-3.1%)	3.0%
AISI D6	N	2440	2.2%
	C	2449 (+0.4%)	4.1%
AISI M2	N	2572	3.3%
	C	2621 (+1.9%)	3.1%

Similarly insignificant changes were observed following micro-hardness testing. Among large standard deviations AISI D6 steel displayed the largest change of 3.6%, although this represents less than one quarter of one standard deviation from the mean. It was suspected that the large standard deviations reported were as a result of large carbides near the surface; a supposition that is sustained by the optical and scanning electron microscopy presented in Section 4.3.3.2.

Table 31 - Micro-hardness test results from tool steel samples.

Specimen type	Treatment	$HV_{0.4905}$ /MPa	Coefficient of variation
AISI A2	Standard	2460	2.2%
	Cryotreated	2454 (-0.2%)	2.9%
AISI D6	Standard	3043	21.9%
	Cryotreated	3152 (+3.6%)	14.9%
AISI M2	Standard	2950	5.3%
	Cryotreated	2943 (-0.2%)	12.2%

4.3.2. Wear performance

4.3.2.1. Grey cast iron and carbon steel brake rotor materials

Wear tests conducted on the G10 brake materials gave mixed results. In some cases there appeared to be substantial improvements in wear resistance, while in others there were no obvious changes or deteriorations in performance apparent from the discs having undergone DCT. Consequently, the results are viewed from two perspectives: firstly by comparing overall wear rates against sliding speed and initial contact pressure, and secondly by comparing wear rates against sliding distance and contact pressure. For the latter perspective it is assumed that the variation in wear rate due to sliding distance is more significant than the variation due to sliding speed,

as a result of the non-linearity of the wear development that occurs in dry sliding between metallic materials.

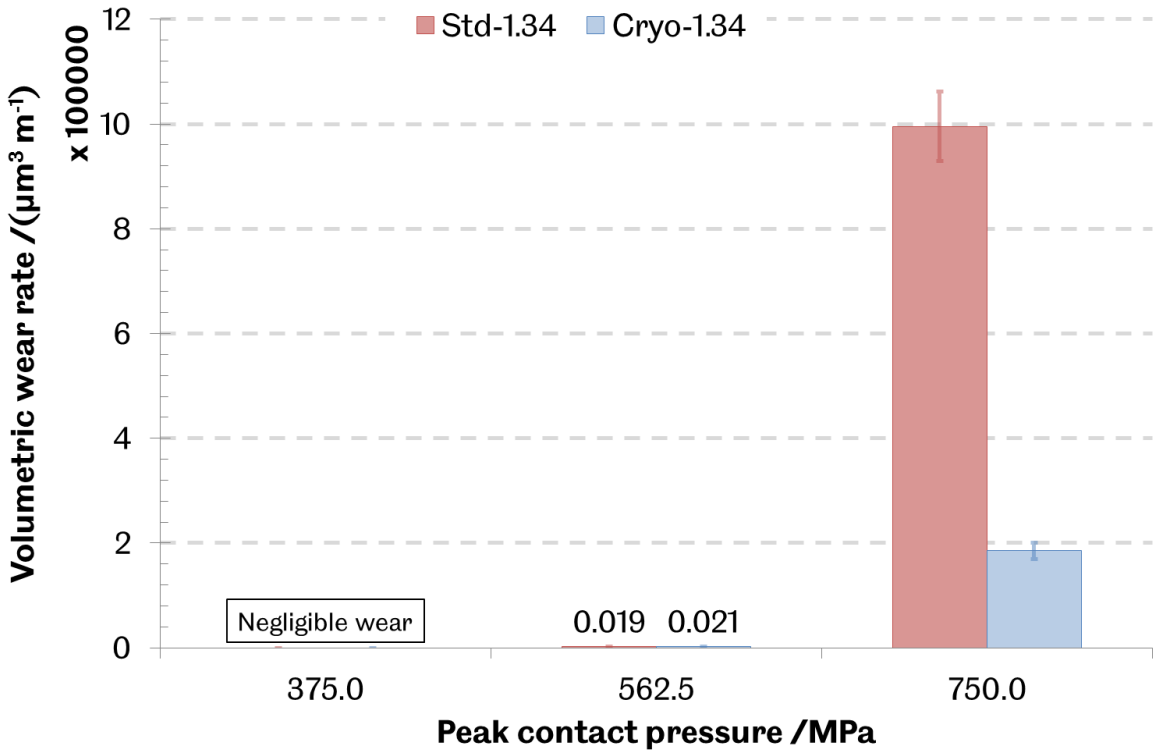

Figure 36 - Volumetric wear rates (including measurement uncertainties) determined from GCI pin-on-disc tests at 1.34m/s.

Figure 36 displays the wear data obtained at each of the three contact pressures with a sliding speed of 1.34m/s. While insignificant amounts of wear were recorded at an initial contact pressure of 375.0MPa, the mean wear rate of the cryogenically treated material at 750.0MPa showed an 81% improvement to that determined from the standard material. At 562.5MPa a small deterioration in the performance of the cryogenically treated material was apparent, with a 15% increase in wear rate.

From Figure 37 the wear results from tests conducted at 1.78m/s can be seen. As with the lower sliding speed of 1.34m/s, no significant wear was recorded at a contact pressure of 375.0MPa. Improvements in the performance of the material after cryogenic treatment were determined at contact pressures of 562.5MPa and 750.0MPa, with 51% and 9% lower wear rates respectively.

Only at the highest sliding speed of 2.24m/s were significant levels of wear measured at all three contact pressures. As shown in Figure 38, deterioration in the performance of the GCI material after cryogenic treatment was measured under an initial contact pressure of 375.0MPa, of around 24%. At both 562.5MPa and 750.0MPa however, increases of 25% and 29% were measured respectively.

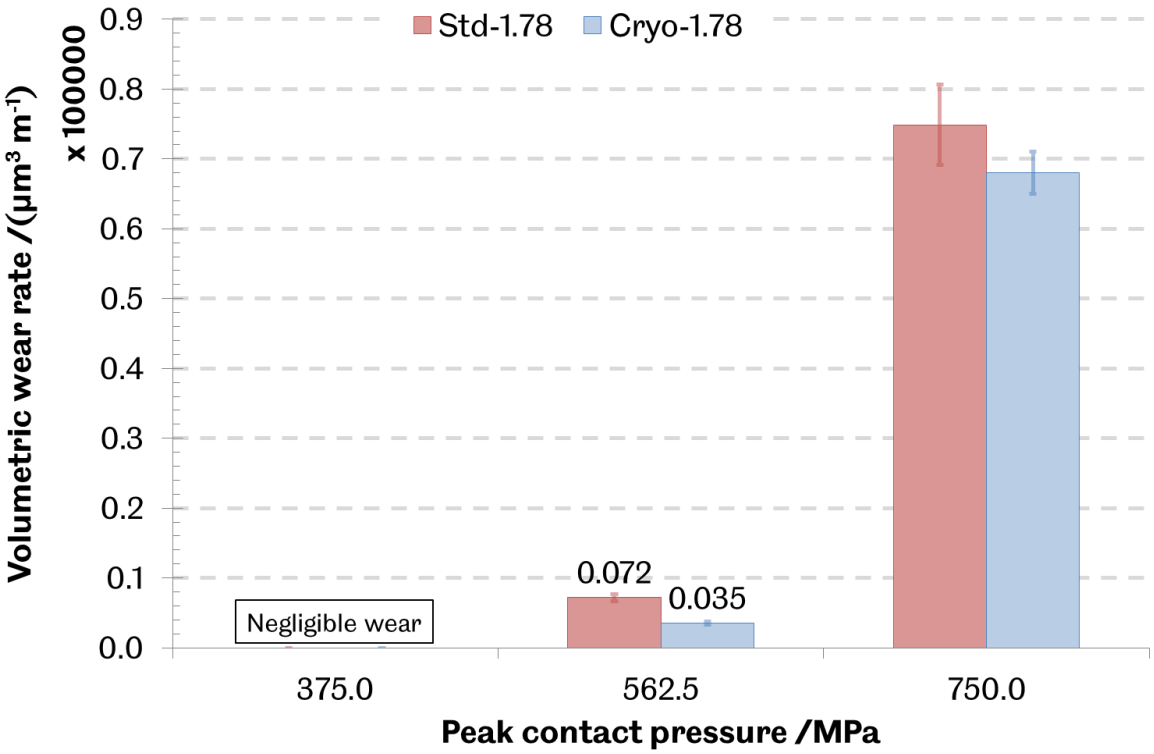

Figure 37 - Volumetric wear rates (including measurement uncertainties) determined from GCI pin-on-disc tests at 1.78m/s.

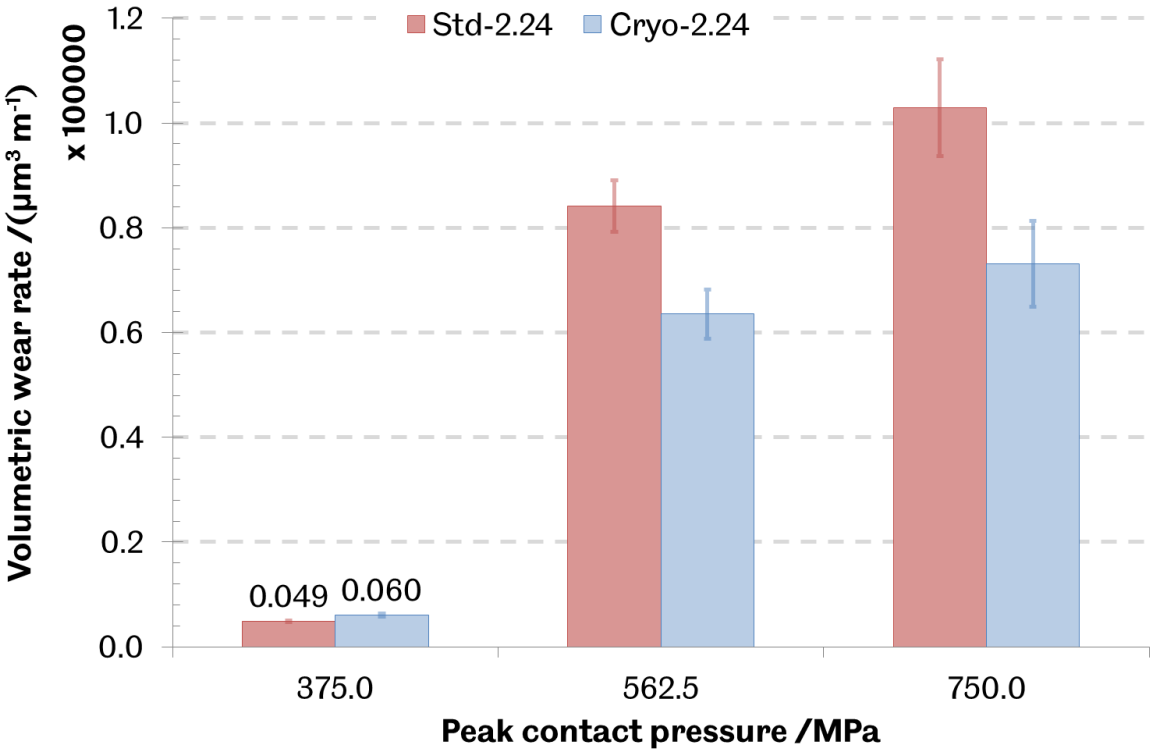

Figure 38 - Volumetric wear rates (including measurement uncertainties) determined from GCI pin-on-disc tests at 2.24m/s.

Wear performance changes from all tests are summarised in Figure 39. While the results are mixed, it is suggested that cryogenic treatment may offer wear performance benefits in the GCI brake material only at higher contact pressures.

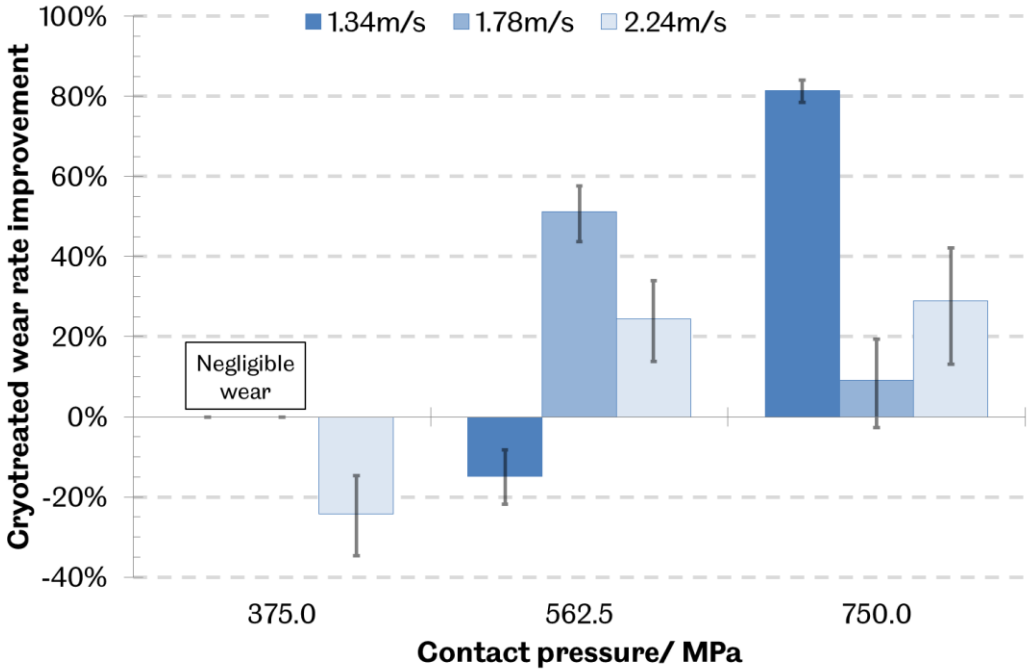

Figure 39 – Wear performance changes (including effects of measurement uncertainties) determined from GCI pin-on-disc tests.

Figure 40 is an alternative view of the results, where the measured data points are normalised against sliding speed; effectively assuming that the variation in wear rate due to sliding speed is insignificant in the range tested. It is striking, although not conclusive, that substantial increases in wear resistance in specimens that have undergone cryogenic treatment are seen only at lower sliding distances and therefore higher contact pressures, while a fully conformal contact between the pin and the disc is still developing.

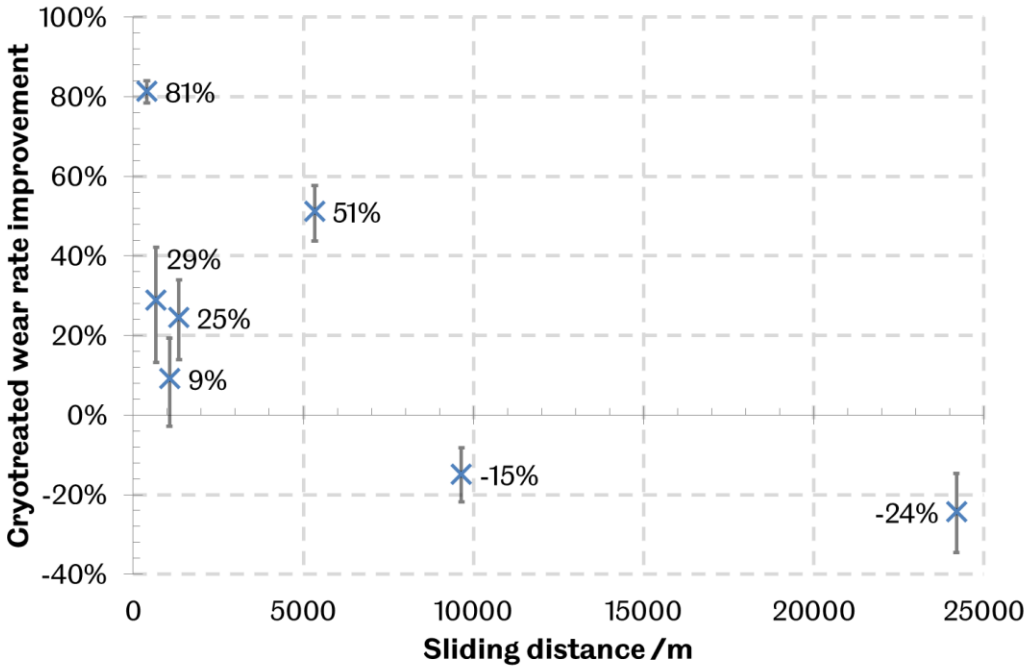

Figure 40 – Wear performance changes (including effects of measurement uncertainties) determined from GCI pin-on-disc tests, plotted against sliding distance.

One final perspective on the results is presented as Figure 41, in which the changes in wear rate due to cryotreatment are considered against the 'tribological stresses' applied (or the rate of energy transfer between two surfaces, commonly considered for dry bearings [101]), which is the product of the initial contact pressure and sliding speed. This again supports the superior performance of cryotreated specimens tested under more severe conditions, although it is indeterminable as to whether sliding distance is a significant factor, or whether the performance of cryotreated specimens would have been sustained over longer test durations.

Figure 42 shows typical micrographs taken of the wear scars developed in the G10 brake rotors – the case shown was a test run at 562.5MPa and 2.24m/s. In all cases where significant levels of wear were recorded, characteristic features of severe, primarily two-body abrasive wear were seen. These included deep grooves running parallel to the sliding direction, as well as surface cracking and pitting. While graphite from grey cast iron is known to form a third-body layer when worn [112], there was no evidence that this layer itself contributed to the abrasion of the material. The significance of this graphite layer is discussed in more detail in Section 4.4.

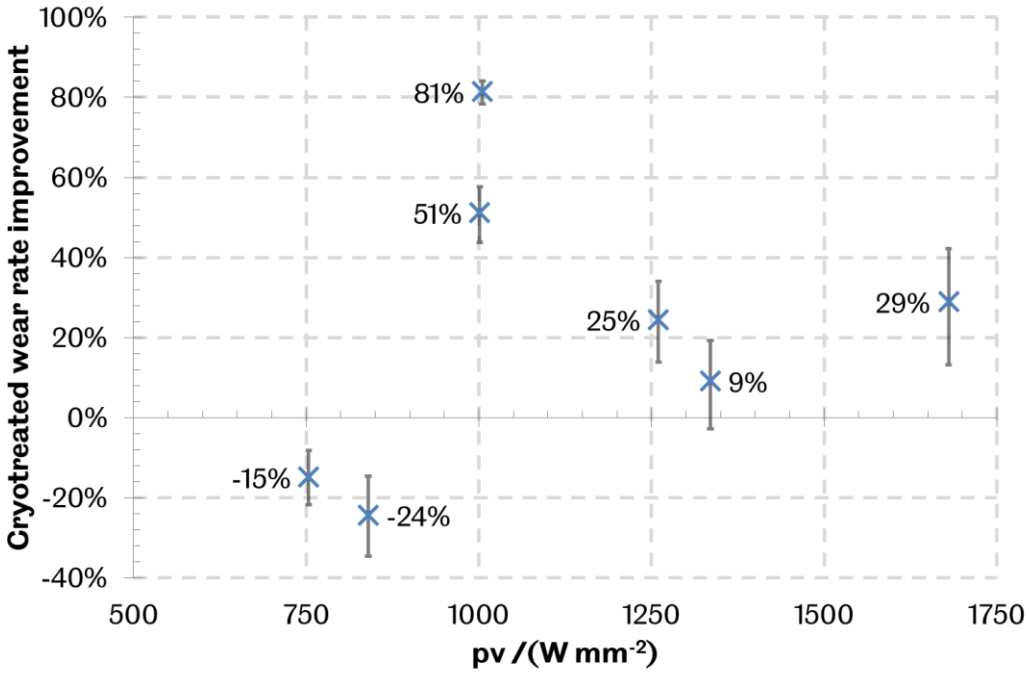

Figure 41 - Wear performance changes (including effects of measurement uncertainties) determined from GCI pin-on-disc tests, plotted against tribological stress (pressure*velocity).

For those tests where significant levels of wear were not observed, 'worn' surfaces were instead smoother than the surrounding material, with a scuffed appearance. Nominal roughness measurements made within the wear scars using a 2D stylus profilometer supported these observations.

Following each test the surface of the AISI 52100 pins were visually observed to identify any material transfer. In all cases no such transfer was observed, with the contact

surfaces of each ball slightly flattened and showing similar signs of abrasive wear to those seen on the discs.

By contrast, pin-on-disc testing of C50R brake rotors revealed that deep cryogenic treatment significantly improves its wear resistance. As shown by Figure 43 (with 'Std' and 'DCT' referring to discs tested in their as-received and cryotreated conditions respectively), mean wear rates for cryogenically treated rotors had reduced by 14.4% and 12.1% at contact pressures of 1000MPa and 1300MPa respectively, although these changes were statistically marginal, being within one standard deviation from the mean. At a contact pressure of 1600MPa, the reduction in wear rate (22.7%) had more significance, being approximately one standard deviation from the mean.

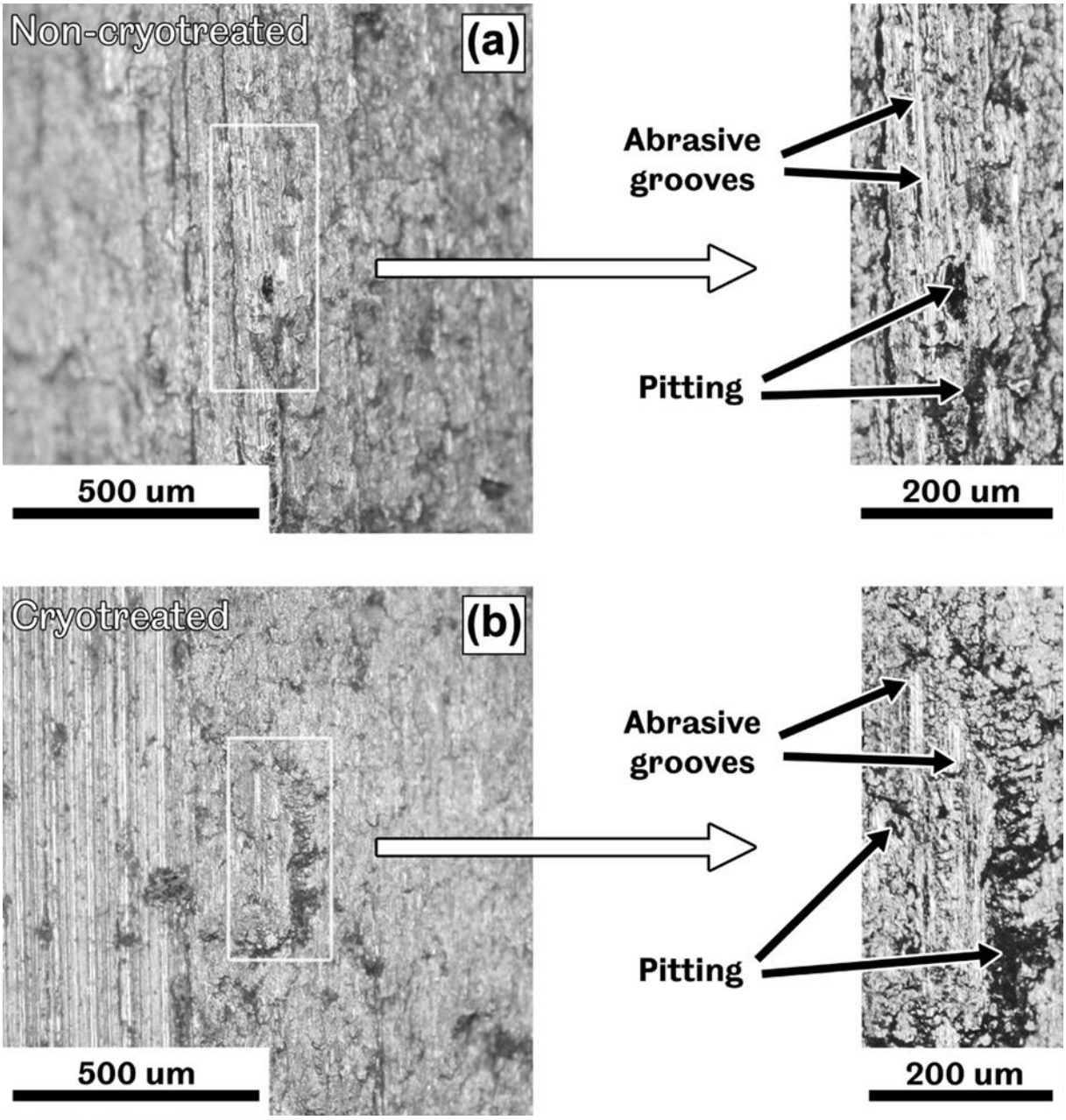

Figure 42 – Typical wear scars developed from wear tests on (a) non-cryotreated and (b) cryotreated G10 material.

Typical micrographs of wear scars found in C50R specimens are shown in Figure 44. In both standard and cryogenically treated specimens, parallel grooves and pitting were observed. Visual observations made of the AISI 52100 pins after testing revealed no evidence of material transfer, with only some flattening and abrasive wear features visible.

As the dominant wear mechanism observed in all cases was primarily two-body abrasive wear, the results from C50R wear testing were normalised against contact pressure, with a mean wear rate reduction in cryogenically treated brake materials of 17.5% determined. Coefficients of variation for standard and cryotreated specimens were found to be 20.1% and 21.7% respectively.

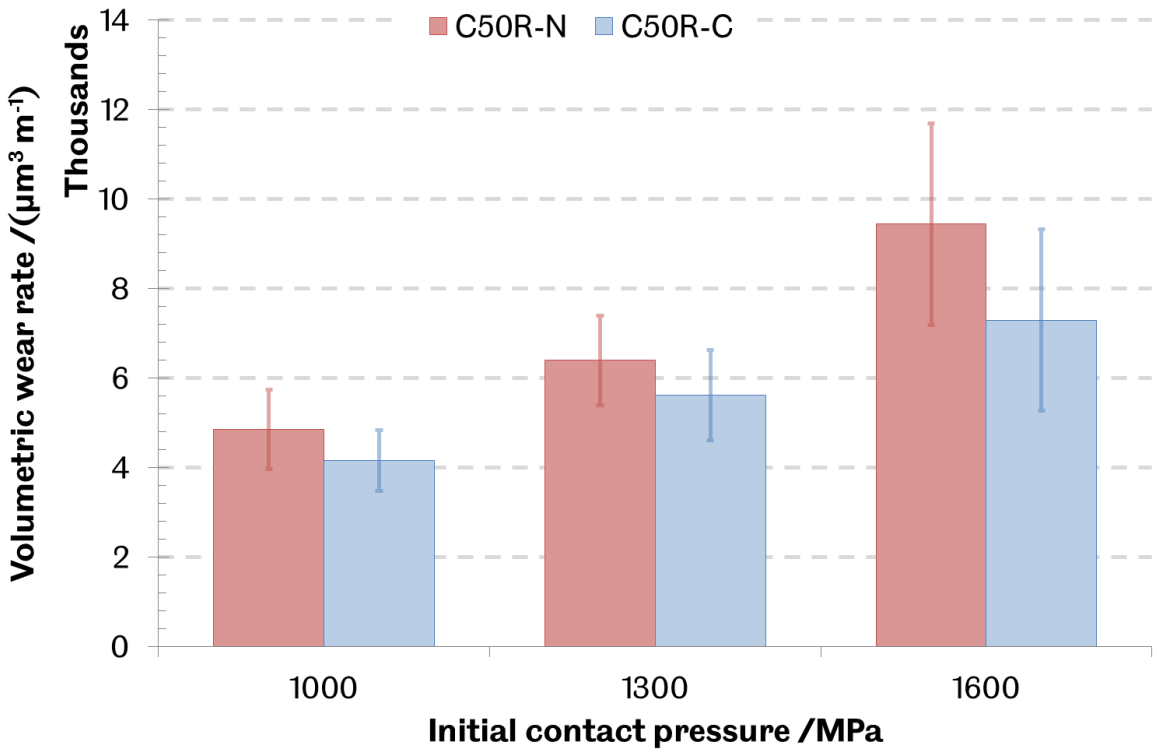

Figure 43 - Volumetric wear rates (±1σ) determined from carbon steel brake pin-on-disc tests.

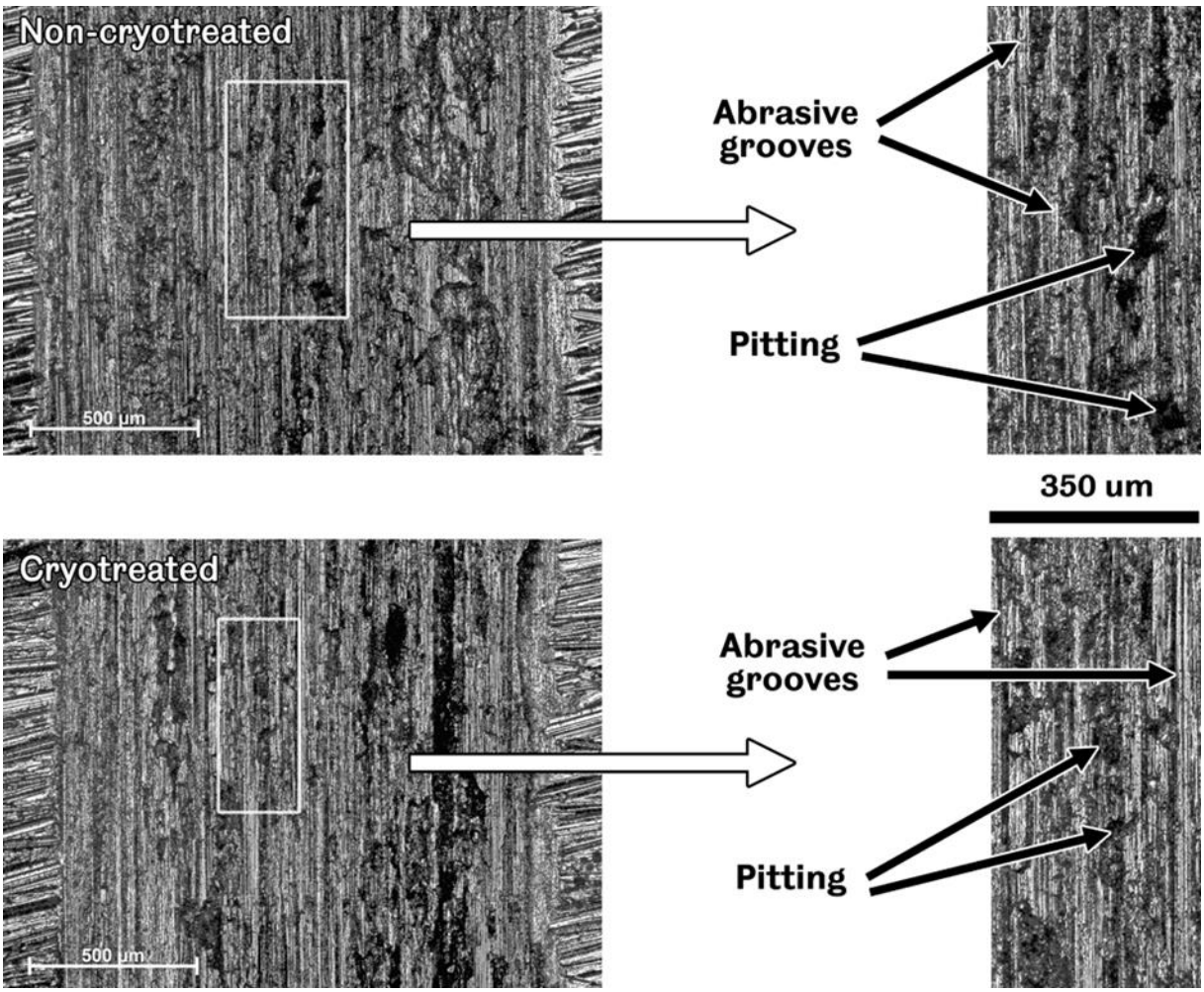

Figure 44 - Typical wear scars developed in (top) standard treated and (bottom) cryotreated C50R steel rotors.

4.3.2.2. AISI A2, D6 and M2 tool steels

The results of wear testing conducted on tool steel specimens in shown in Figure 45, from which it can be seen that the mean wear rates were lower for all specimens that had been cryogenically treated (denoted '-C', shown in blue) when compared with their related specimens tested in their as-received condition (denoted '-N', shown in red). In all cases it was found that cryogenically treated specimens exhibited greater wear resistance, although the difference between mean mass losses for different specimen sets had varying degrees of statistical significance.

Wear rate reductions measured due to cryogenic treatment in AISI A2 tool steel were seen to increase with increasing sliding distances, with improvements of 13%, 15% and 26% determined for sliding distances of 100m, 150m and 200m respectively. It was also observed that the level of significance of these improvements increased with sliding distance, with less than one standard deviation separating the results at 100m increasing to greater than one standard deviation at 200m.

The opposite trends were seen with AISI D6 tool steel specimens. Over sliding distances of 100m, 150m and 200m, the reductions in wear rate due to cryogenic

treatment were determined to be 30%, 15% and 5% respectively. Simultaneously the significance of these changes reduced, from approximately one standard deviation at 100m to a statistically insignificant change at 200m.

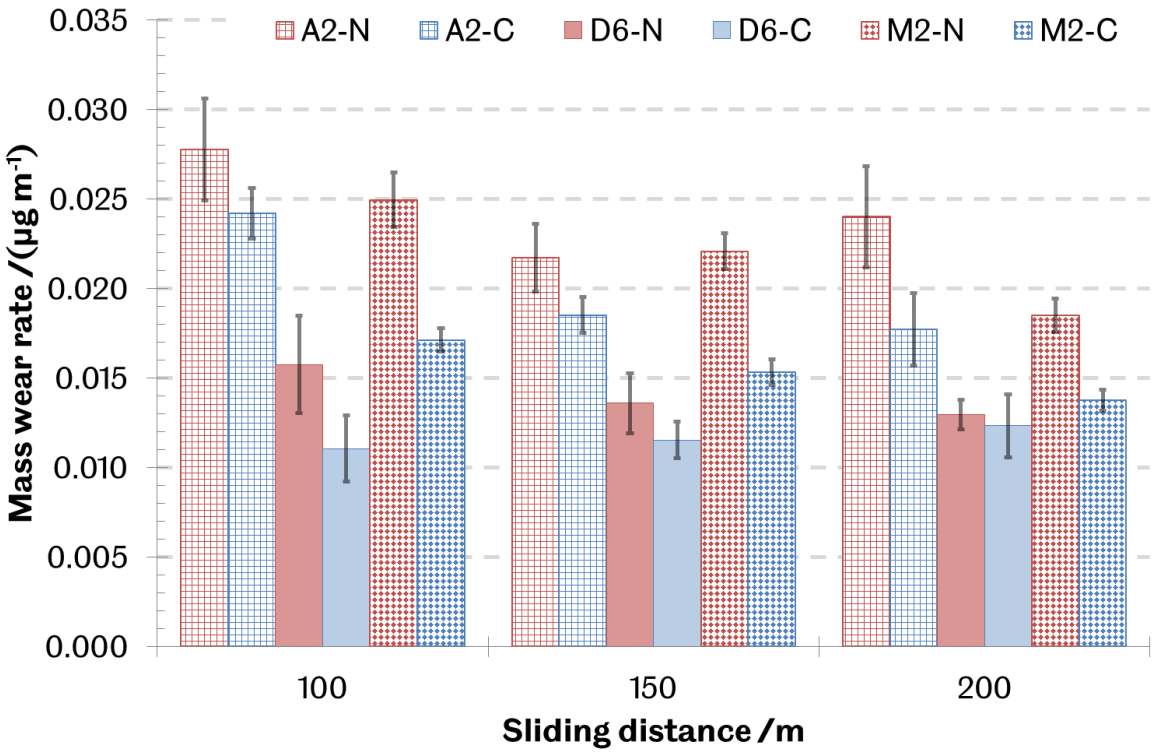

Figure 45 - Mass wear rates (±1σ) determined from tool steel reciprocating sliding tests.

AISI M2 tool steels were observed to respond most significantly and consistently to cryogenic treatment, with reductions in wear rate of 31%, 31% and 26% over sliding distances of 100m, 150m and 200m respectively. In all cases mean wear rates between standard and cryogenically treated specimens were separated by greater than two standard deviations.

Optical micrographs were subsequently used to investigate the wear morphologies of worn surfaces. Figure 46 shows a typical wear scar mid-section and end pair, taken from a non-cryotreated AISI A2 specimen. It can be seen that the reciprocating sliding causes mixed wear modes, with evidence of both abrasive and fatigue-related wear mechanisms. These are indicated by deep parallel grooves and pitting resulting from the growth and merger of cracks, leading to pieces of material separating from the surface. Greater pitting and plastic deformation is visible at the ends of wear scars, due to the low magnitude but rapidly changing sliding velocity. In some specimens, what appeared to be brittle fracture was observed in the plastically deformed region, after localised work hardening of the material. Typical wear features from AISI A2, D6 and M2 specimens were contrast-enhanced and are shown as Figures 47, 48 and 49 respectively.

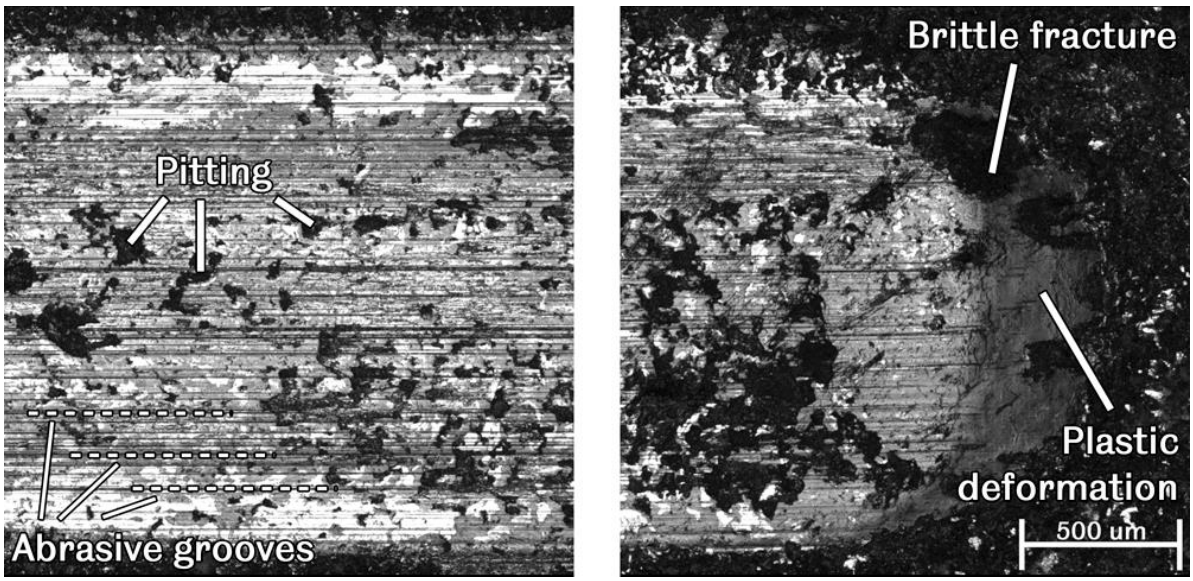

Figure 46 – Typical optical micrographs of wear scars observed on tool steel specimens.

Observing the mid-sections of the wear scars in tool steel specimens, it can be seen that, in all cases, severe abrasive wear has taken place. All specimens display deep parallel grooves running along their wear scars, with ploughed ridges around the edges. However, the wear behaviour in non-cryotreated and cryotreated specimens was observed to differ in a number of ways.

In Figure 47 more extensive pitting was observed in non-cryotreated AISI A2 specimens, while cryotreated specimens displayed a more cracked surface. Comparing the extent of pitting and ploughing seen in non-cryotreated specimens with the surface cracking visible in cryotreated specimens, it can be argued that while the wear mechanisms operating in both examples are similar, their development is more advanced in non-cryotreated specimens. This correlates with the greater amount of wear measured and therefore supports the significance of the difference in wear rates determined by testing.

The wear scars in AISI D6 specimens (those with the least significant change in wear rate) displayed largely similar morphologies (Figure 48), although arguably the extent of pitting observed in cryotreated specimens was greater than in non-cryotreated specimens. While minimal ploughing is evident in both specimens, cryotreated specimens displayed more extensively broken up surfaces, as a result of work hardening and subsequent cracking processes, rather than plastic deformation, which is indicative of a harder material. Comparing these features with the abrasive grooves and less extensive pitting seen in non-cryotreated specimens leads to the suggestion that the toughness of AISI D6 tool steel has reduced as a result of cryogenic treatment.

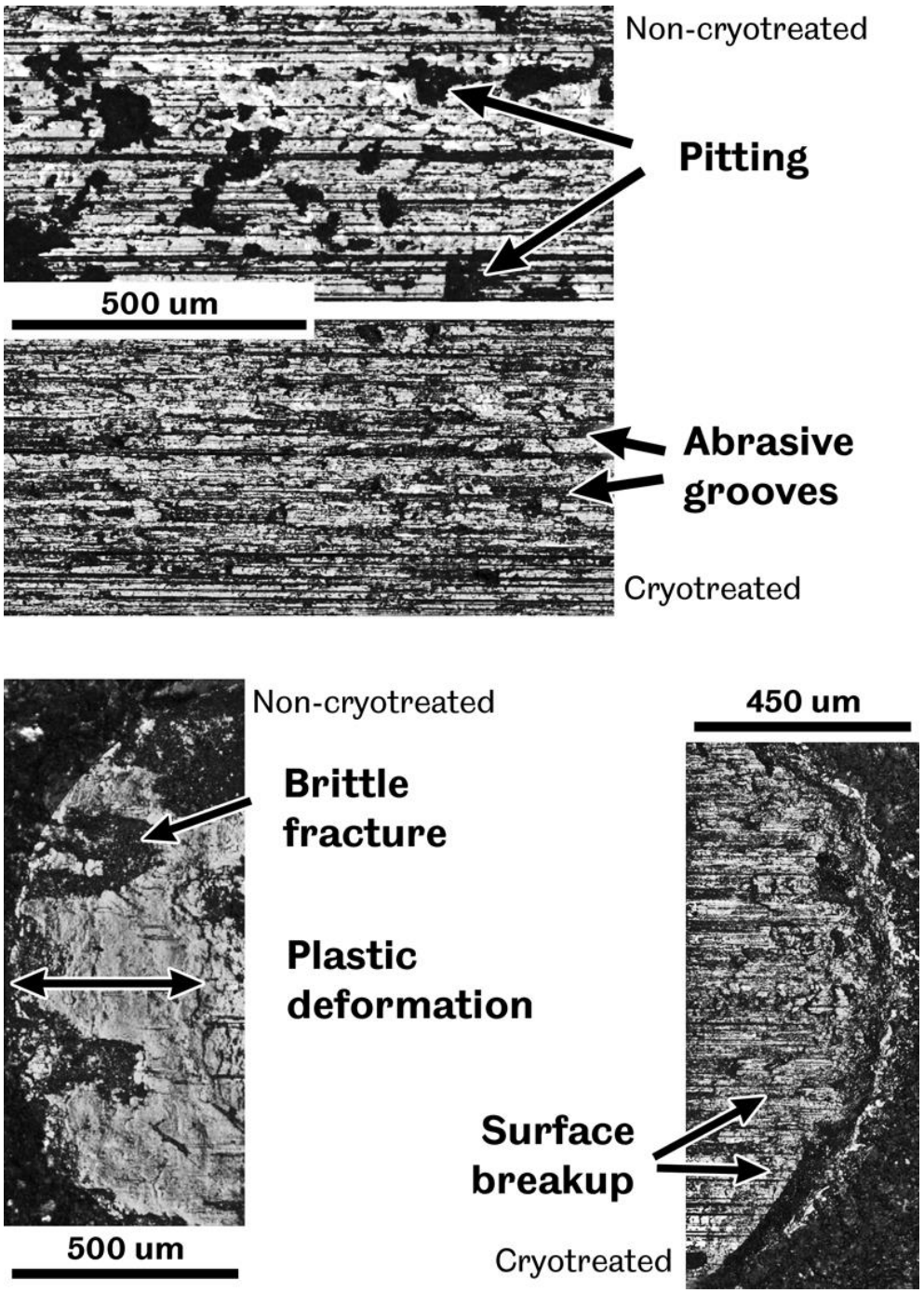

Figure 47 - Enlarged and contrast-enhanced wear features from A2 specimens.

Of the tool steels tested, the most consistent wear morphologies were observed in AISI M2 specimens. Acknowledging the greater depth of wear scars in non-cryotreated specimens (corresponding to the higher wear rates measured), it can be seen from Figure 49 that both specimens display similar grooves and ploughed regions, with substantial, but comparable, amounts of pitting. Both display evidence of brittle fracture in the plastically deformed (and subsequently work-hardened) regions, and a broken up worn appearance due to the combination of surface deformation and cracking.

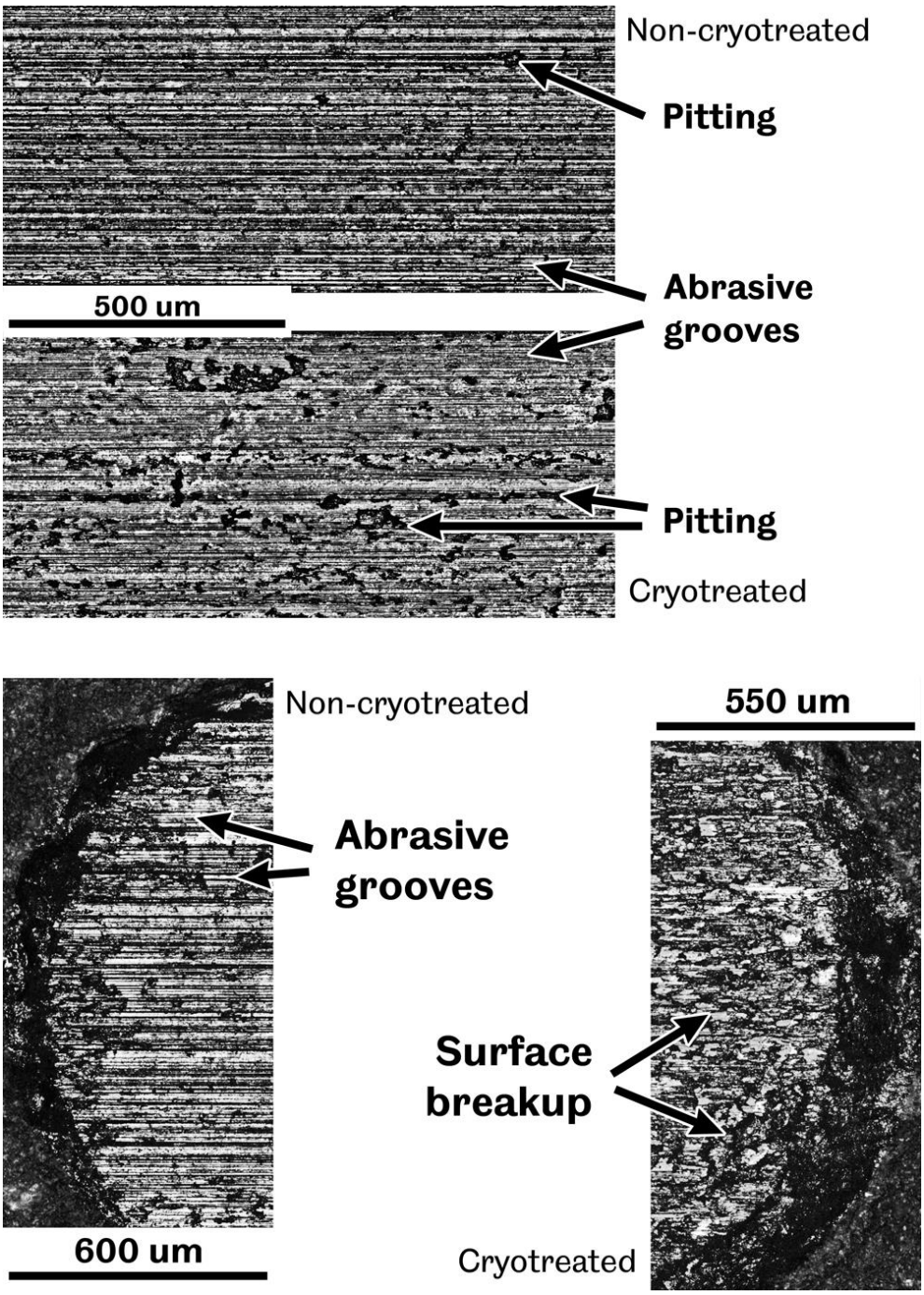

Figure 48 - Enlarged and contrast-enhanced wear features from D6 specimens.

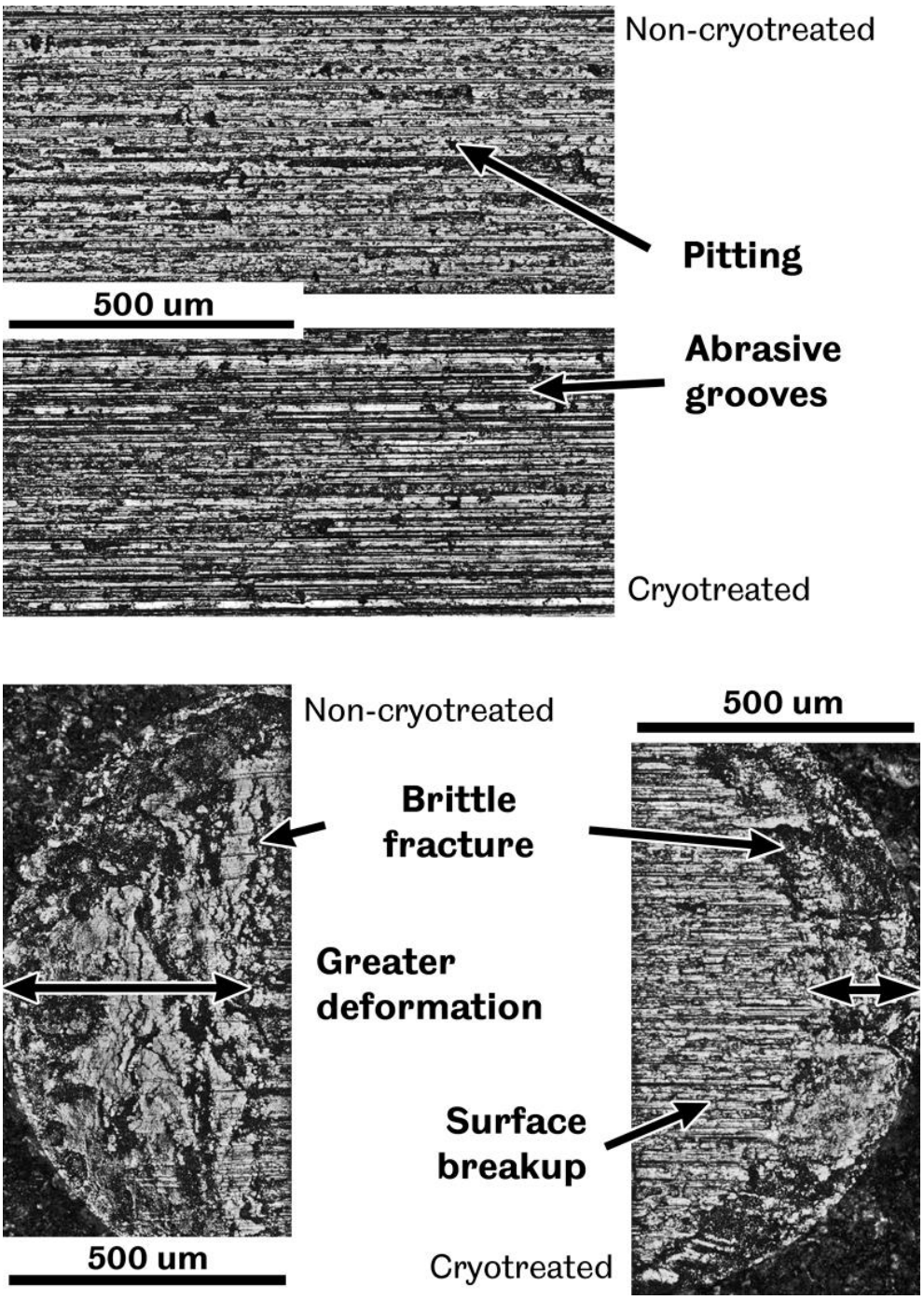

Figure 49 - Enlarged and contrast-enhanced wear features from M2 specimens.

4.3.3. Microstructural observations

4.3.3.1. Grey cast iron and carbon steel brake disc materials

Darkfield optical micrographs taken from G10 specimens are shown in Figure 50. Microscopy revealed that pearlite (A: bands of cementite (Fe_3C, white) in a ferrite (black) matrix) was the predominant phase structure in G10 specimens, along with randomly distributed lamellar graphite (C: dark flakes). Also seen were inclusions of manganese sulphide (MnS; small bright spots).

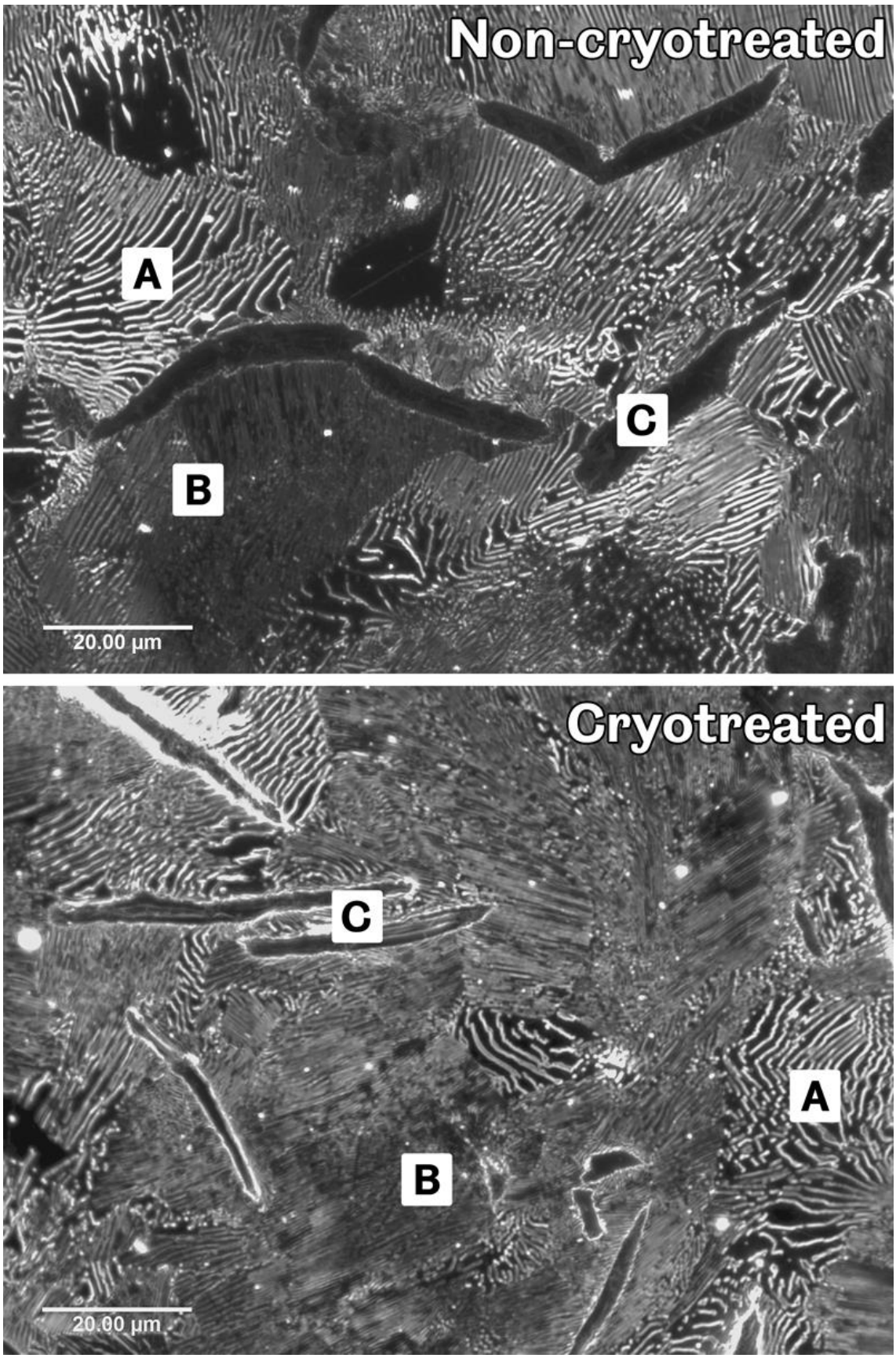

Figure 50 - Optical micrographs of non-cryotreated (top) and cryotreated (bottom) SAE J431 G10 material.

In cryotreated specimens, a fine pearlite phase (B) could be seen to cover a much greater area, in which distinct cementite bands were difficult to resolve optically, while

the graphite flakes, surrounded by a bright boundary (in the darkfield images shown) that may be indicative of a cementite-rich region, appeared narrower.

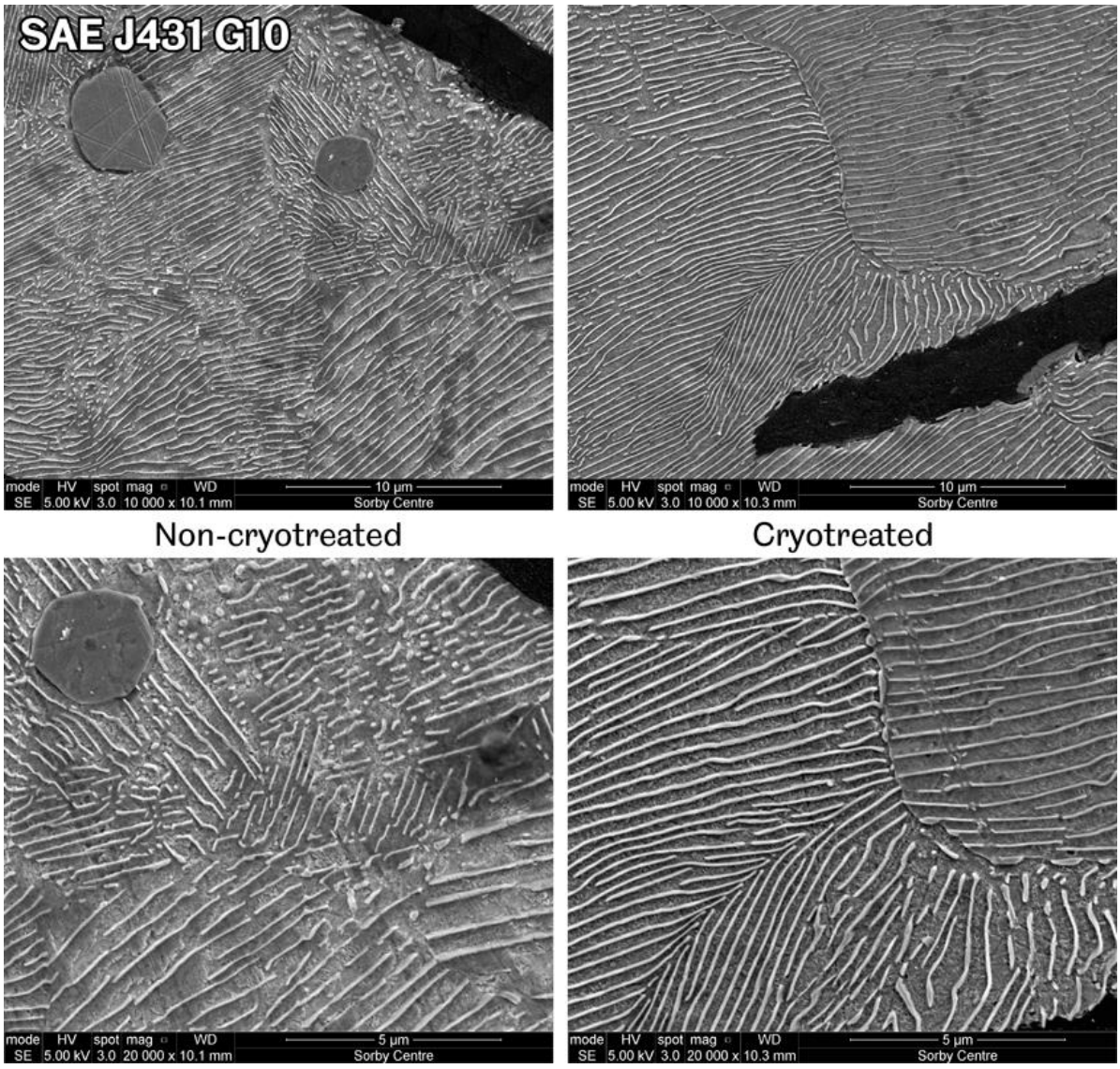

Figure 51 - Electron micrographs from SAE J431 G10 non-cryotreated and cryotreated material.

SEM (Figure 51) was used to resolve the microstructures further. Using this technique, the fine pearlite (B, Figure 50) could be resolved. Based upon a number of micrographs taken at different locations and after different grinding and polishing cycles, a qualitative observation was made that the interlamellar spacing appeared less in non-cryotreated G10 specimens, compared with cryotreated specimens. While it should be noted that the orientation of pearlite lamellae will alter their apparent spacing (with lamellae perpendicular to the plane of observation appearing more widely spaced than those near parallel with the same plane) this would also have the effect of making individual lamellae appear broader. This second observation was not seen in this case.

A reduced interlamellar spacing would have a positive impact on wear resistance and hardness, but would require a thermally driven microstructural change to occur, with

the cementite lamellae undergoing complete dissolution before re-solidifying as a finer structure in a diffusion controlled process. Material variation (which may be localised or indicative of the bulk material), rather than cryogenic treatment, was therefore considered to be the underlying cause of this observation.

The deterioration in the structure of graphite flakes may, however, have been caused by cryogenic treatment if there was sufficient difference between the thermal distortion of the surrounding ferrite and the graphite flakes. Furthermore, this would likely have been detrimental to the wear performance of the cryotreated grey cast iron. Both these features are discussed more thoroughly in Section 4.4.

Optical microscopy of C50R specimens (Figure 52) revealed a largely pearlitic (A) and ferritic (C, large black areas) microstructure. Similarly to the G10 material, after cryogenic treatment, there was a greater proportion of a finer pearlite phase (B) in C50R specimens.

Use of FEG-SEM allowed this finer pearlite phase (B, Figure 52) to be resolved further. Illustrated in Figure 53, a review of a number of electron micrographs once again suggested a finer interlamellar cementite spacing in cryotreated C50R specimens when compared with non-cryotreated specimens. As with the G10 pearlite, this apparent difference is not thought to be as a result of cryogenic treatment, but would explain some of the wear resistance and hardness differences if it were to be taken as representative of all the brake rotors that underwent cryogenic treatment.

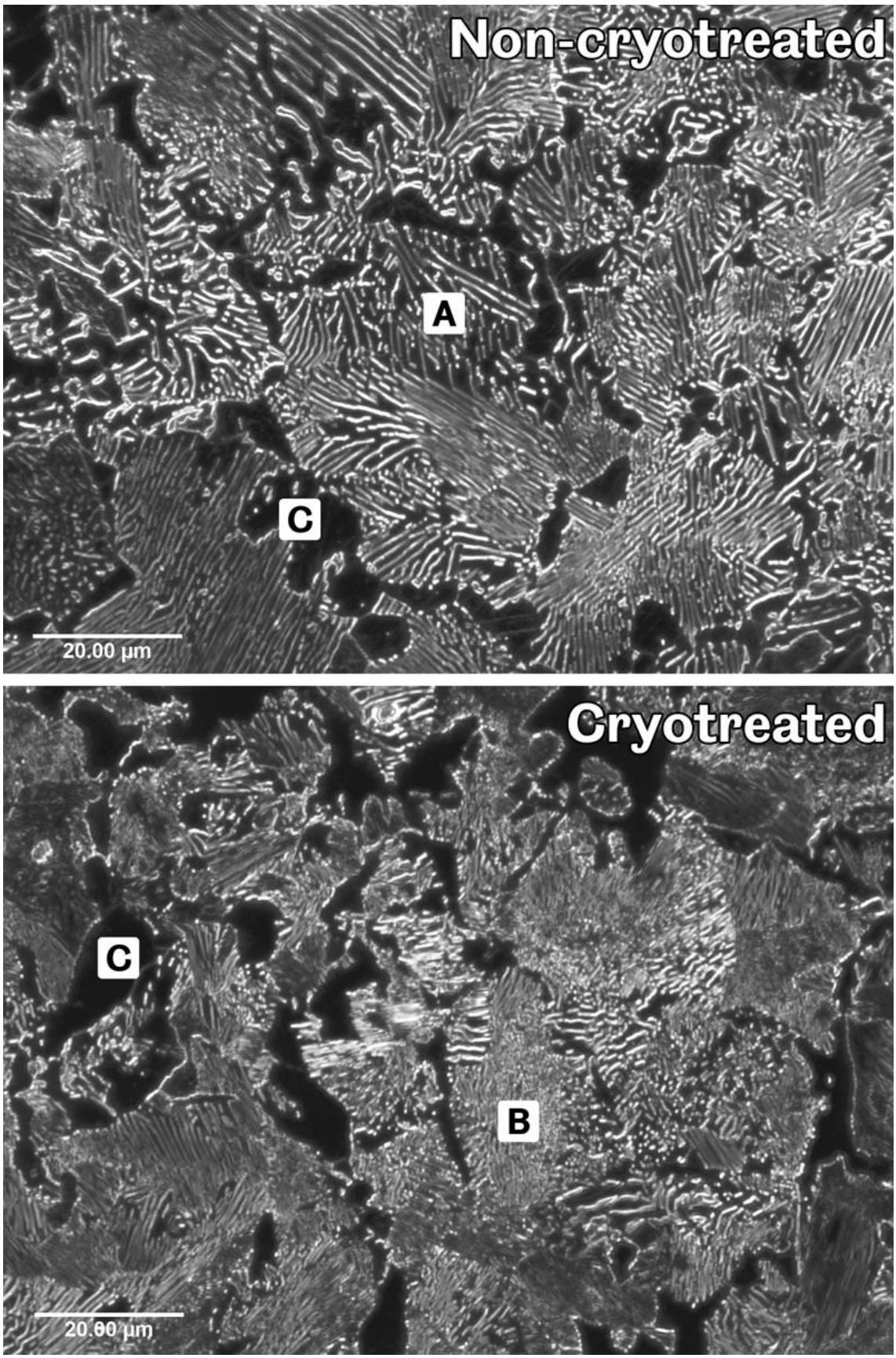

Figure 52 - Optical micrographs of non-cryotreated (top) and cryotreated (bottom) C50R material.

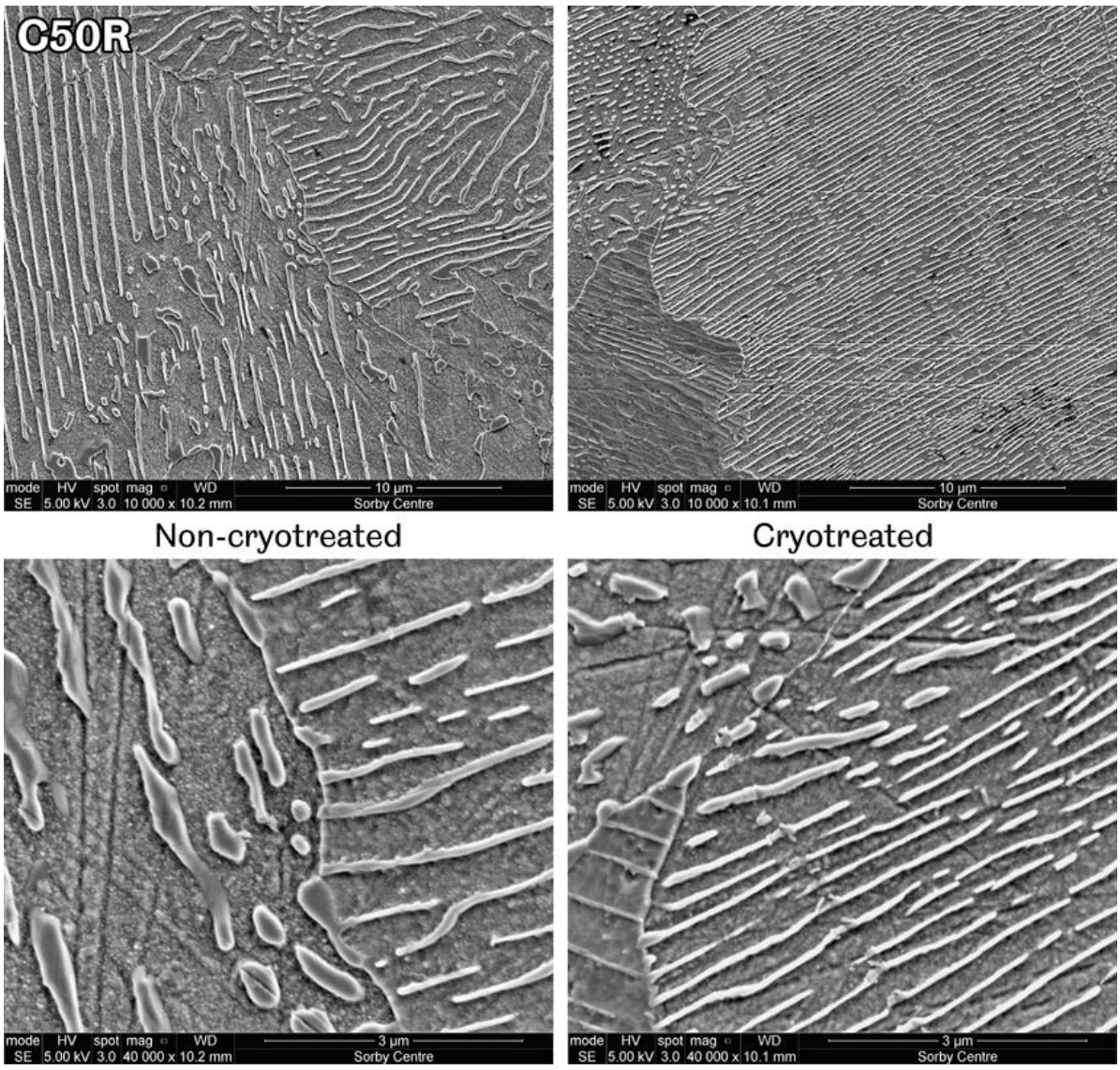

Figure 53 - Electron micrographs from C50R non-cryotreated and cryotreated material.

4.3.3.2. AISI A2, D6 and M2 tool steels

Tool steels have much finer microstructures than compared with typical cast irons and non-alloy steels. As such optical microscopy is unable to resolve a number of typical microstructural features, such as fine carbides. However, it is still a useful tool to observe large scale changes. In the optical micrographs shown in Figure 54, these carbides can be seen pervading the entire microstructure of AISI A2 tool steel.

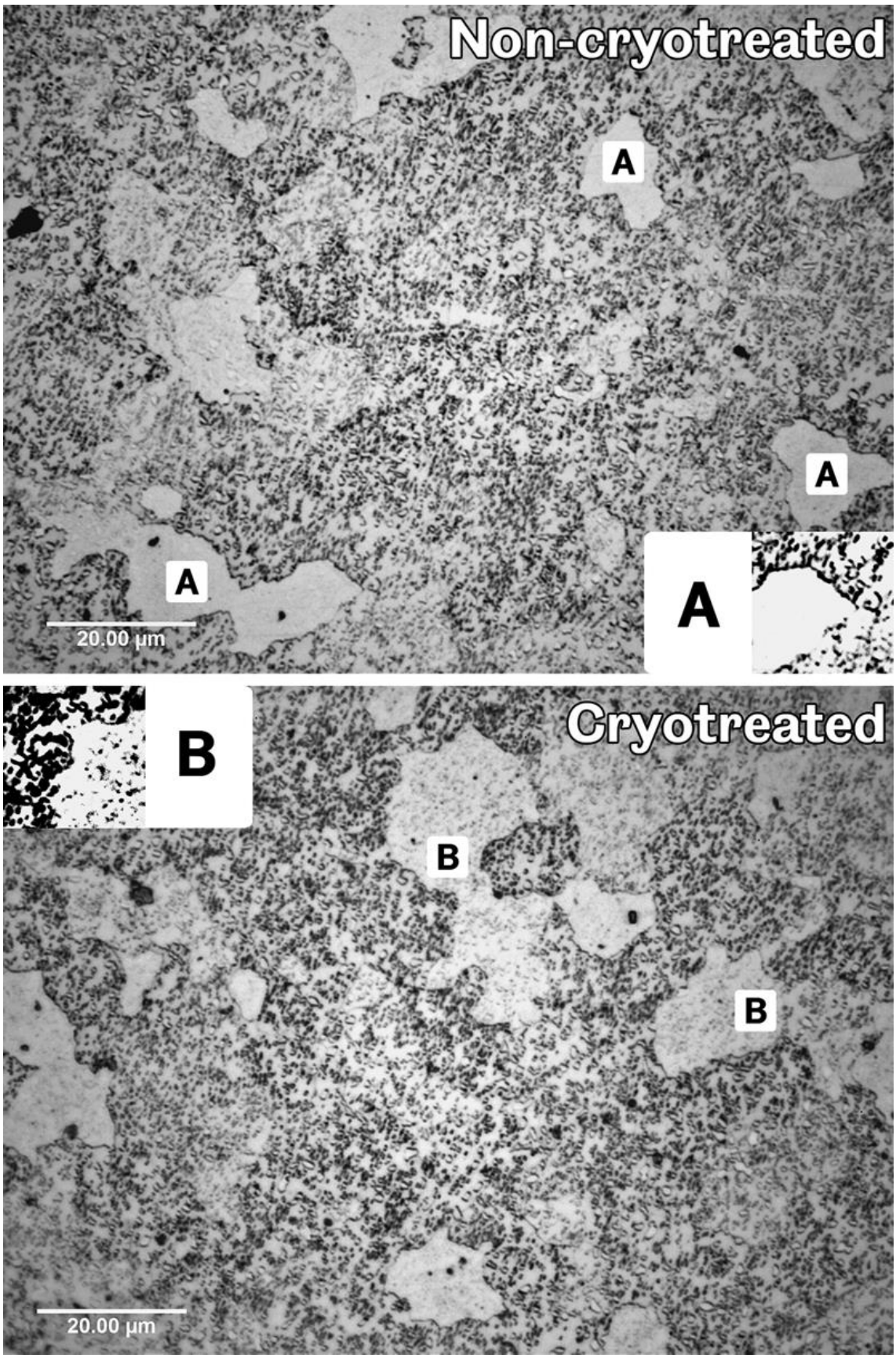

Figure 54 - Optical micrographs of non-cryotreated (top) and cryotreated (bottom) AISI A2 material.

Larger, more distinguishable grains were also observed. In particular a light phase (A), that did not noticeably etch, appeared to be significantly reduced by cryogenic

treatment, instead being replaced by an etched phase (B) in which carbide precipitates were visible.

The electron micrographs shown in Figure 55 allow these carbides in AISI A2 tool steel to be resolved. In both non-cryotreated and cryotreated specimens a range of sizes that are <1.5µm can be seen. In cryotreated specimens there appeared to be greater numbers of 0.1 – 0.2µm carbides, when compared with the 0.5µm carbides that are prevalent in the non-cryotreated material. An increase in such a fine carbide precipitation would support the increased wear resistance observed during testing. However it was noted that these were not uniformly distributed throughout the microstructure.

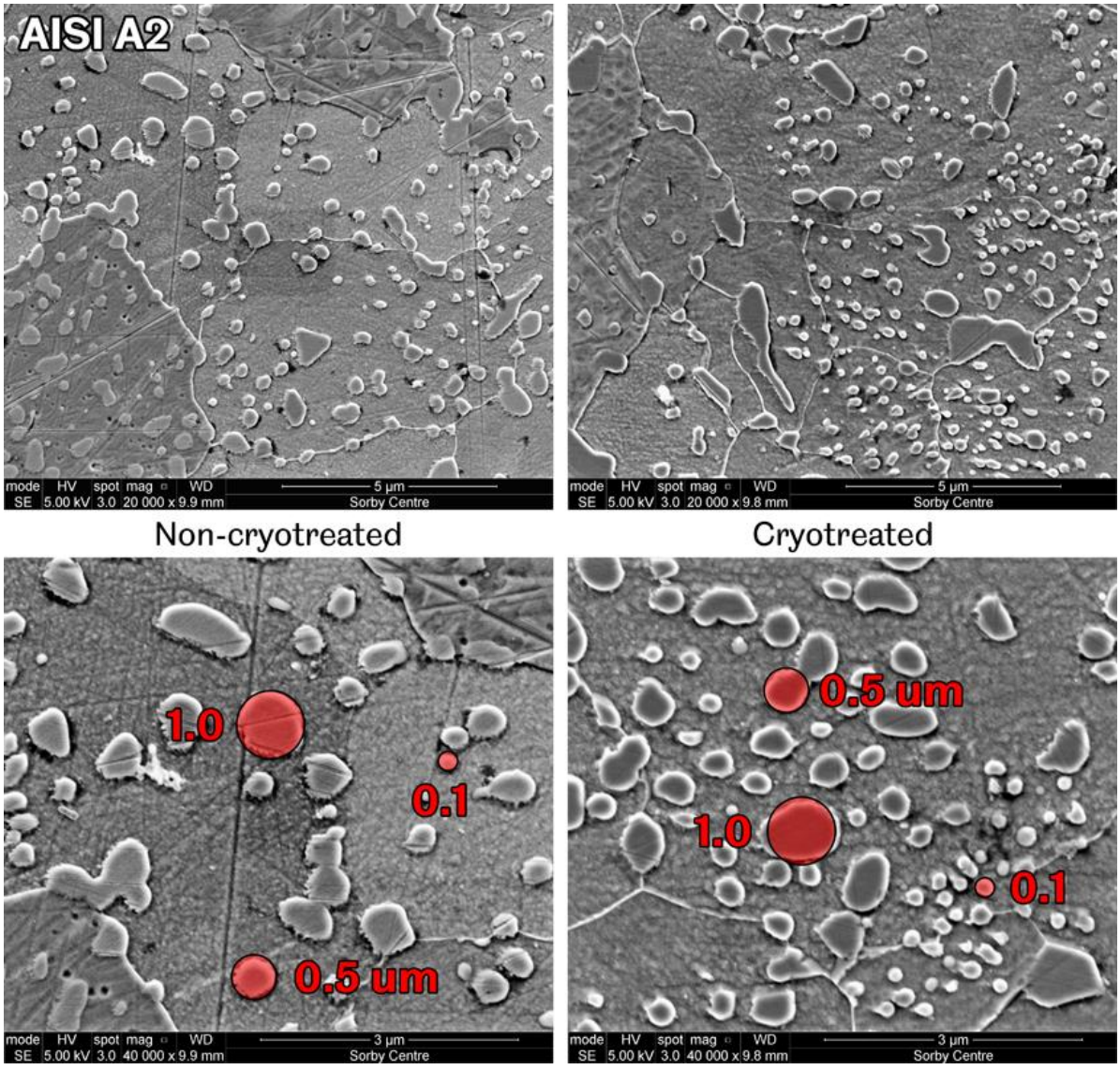

Figure 55 - Electron micrographs from AISI A2 non-cryotreated and cryotreated material.

In optical micrographs of AISI D6 tool steel (Figure 56), irregular chromium carbides (A), which do not dissolve during the normalising treatment of the material, can be observed in both non-cryotreated and cryotreated specimens. Other large carbides (B) of 1 – 5µm can also be seen, along with a lighter etched phase with fine carbide

precipitates (C). As observed in AISI A2 specimens, cryogenic treatment appears to have slightly increased the proportion of this lighter phase.

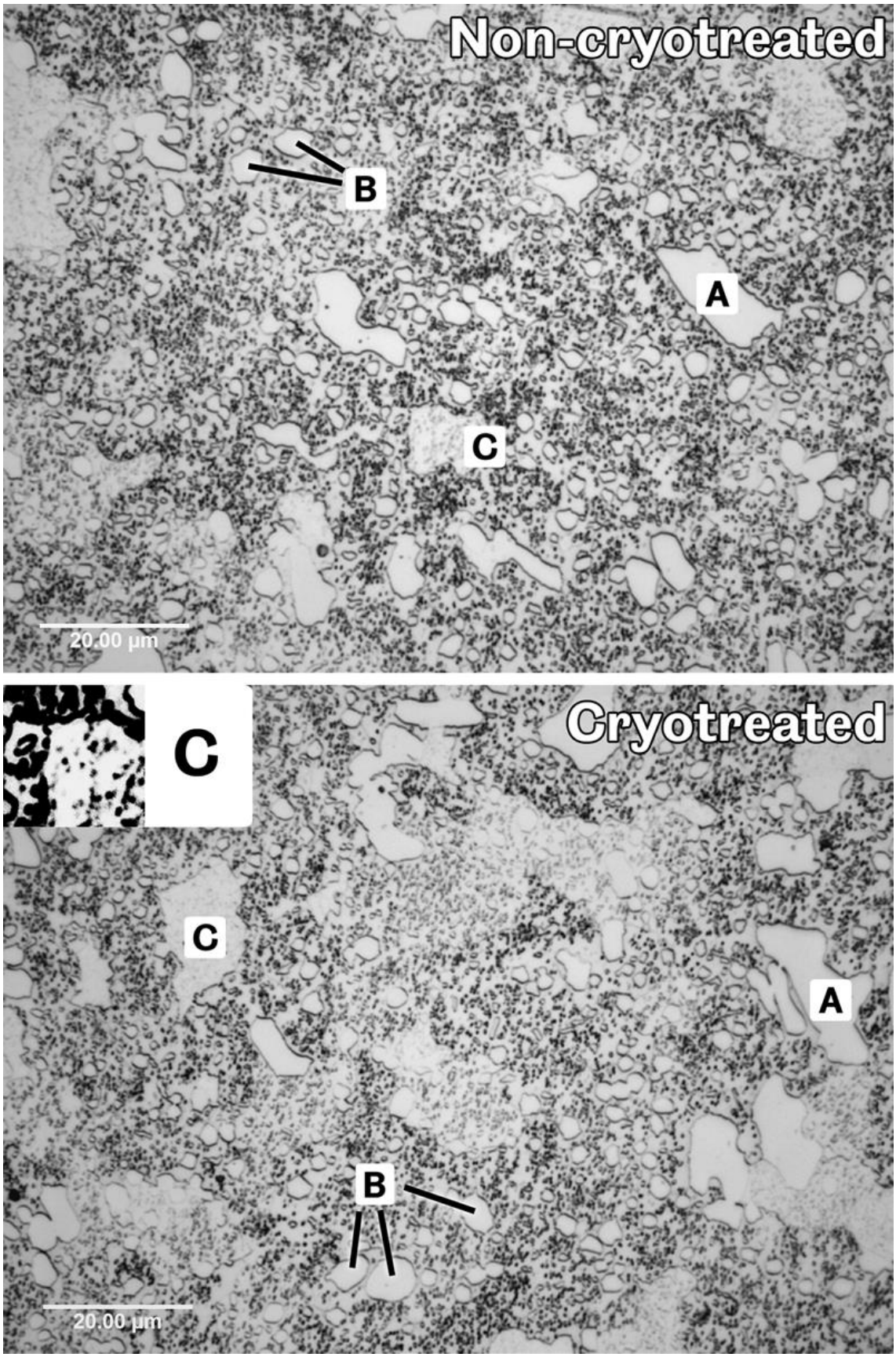

Figure 56 - Optical micrographs of non-cryotreated (top) and cryotreated (bottom) AISI D6 material.

Electron micrographs allow this complex microstructure to be resolved. In Figure 57 both the un-dissolved chromium carbides and other large carbides (A and B, Figure 56) can be seen as the darker areas, while at least two distinct phases appear to be present. While it was difficult to determine conclusively whether the proportion of these phases had changed significantly due to cryogenic treatment, a review of a number of micrographs suggested a slight increase in the proportion of smaller (0.1 – 0.2µm) carbides, although this should be recognised as a qualitative rather than a quantitative assessment. These subtle changes may explain the similarity in wear rates determined from non-cryotreated and cryotreated AISI D6 tool steel specimens.

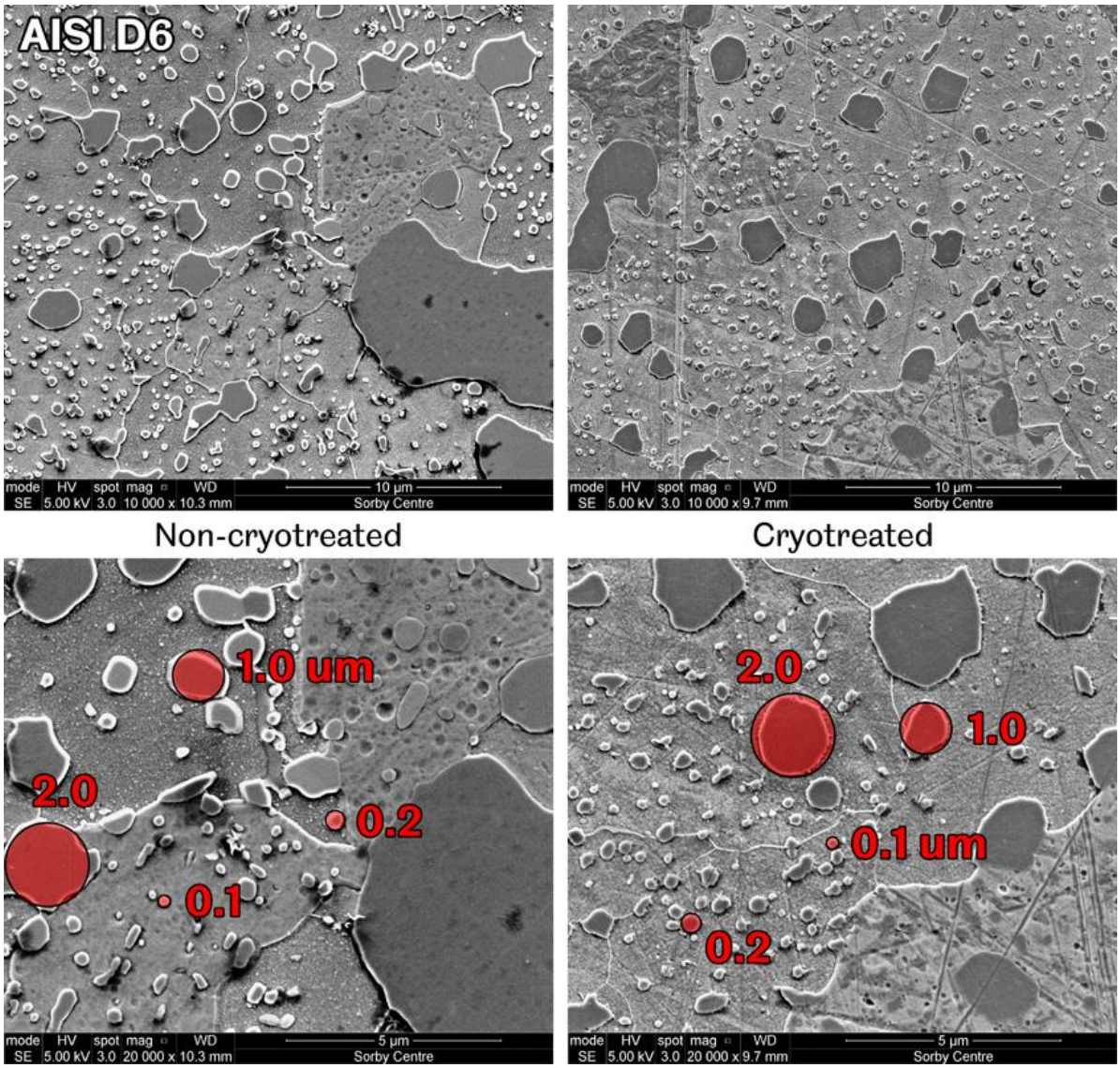

Figure 57 - Electron micrographs from AISI D6 non-cryotreated and cryotreated material.

Optical micrographs of AISI M2 tool steel specimens (Figure 58) revealed a dense microstructure with numerous varied carbides (light and dark spots) present. Similarly to AISI A2 steel, an apparently un-etched phase (A) was seen to substantially reduce due to deep cryogenic treatment, while the proportion of a lighter phase in which carbide precipitates were observed (B) was seen to increase.

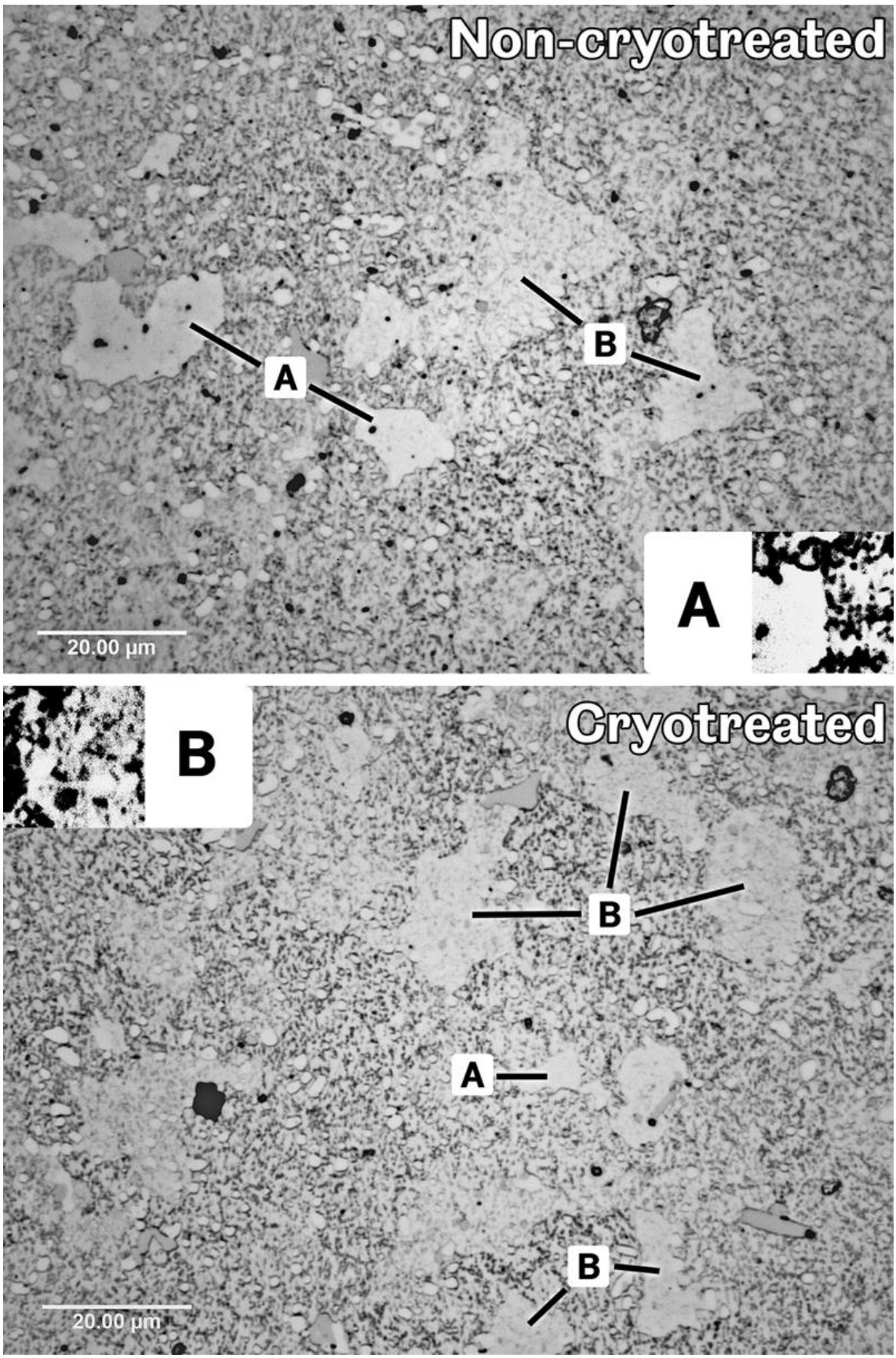

Figure 58 - Optical micrographs of non-cryotreated (top) and cryotreated (bottom) AISI M2 material.

The scales of various carbides found in AISI M2 specimens are shown in the electron micrographs of Figure 59. Although three different size groups (>1µm, 0.5 – 1.0µm and <0.5µm) of carbides are apparent in both samples, it was observed that the frequency

of 0.1 – 0.2µm carbides increased substantially following cryogenic treatment. Additionally, these small carbides appeared distorted or elongated in cryogenically treated specimens, suggesting a phase change in the surrounding material matrix. While this hypothesis could be not be substantiated with the available observation techniques, it is suggested that any such phase change could not have occurred extensively, as neither the bulk nor matrix hardness of AISI M2 specimens was seen to change significantly due to deep cryogenic treatment.

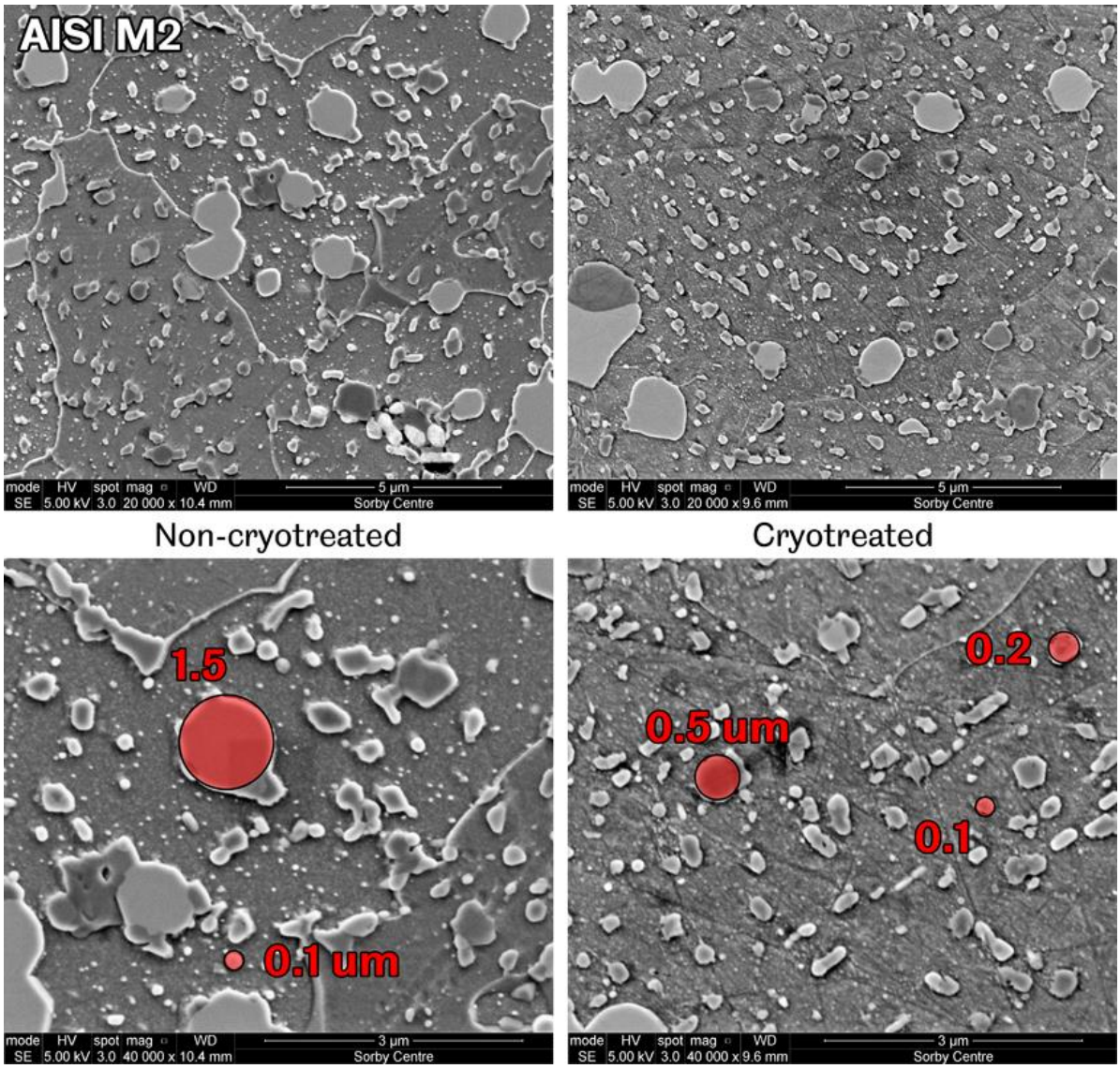

Figure 59 - Electron micrographs from AISI M2 non-cryotreated and cryotreated material.

4.3.3.3. EDS of AISI M2 tool steel

As the tool steel that had shown the greatest and most consistent wear performance change due to cryogenic treatment, AISI M2 specimens were subjected to energy-dispersive spectroscopy to provide an initial assessment as to whether carbide compositions may have been significantly altered. Figure 60 illustrates the areas analysed using EDS in untreated and cryotreated specimens. Under backscattered

electron (BSE) mode (insets in Figure 60), two main types of carbide were observed that appeared as bright white and darker grey areas; the former accounting for the majority of the carbides observed. Both were observed in the size ranges described in Section 4.3.3.2 (>1µm, 0.5 – 1.0µm and <0.5µm), with a greater number of 0.1 – 0.2µm carbides observed in the cryotreated sample.

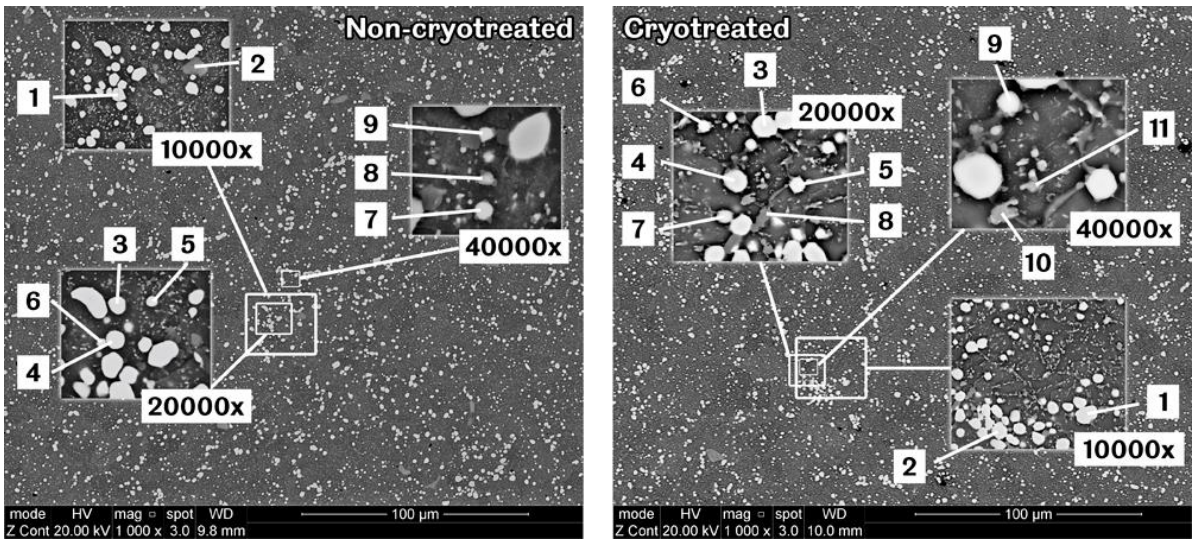

Figure 60 - Electron micrographs indicating locations and carbides analysed by EDS in untreated (left) and cryotreated (right) specimens.

From the results of the EDS analysis, it was evident that the brighter carbides were rich in tungsten and molybdenum, while the darker grey carbides found to be rich in vanadium. The atomic weight percentages of the carbides labelled in Figure 60, as determined by EDS measurements, are listed in Table 32 and Table 33 for non-cryotreated and cryotreated specimens respectively. (Note that only six major elements were analysed; traces of silicon, manganese, phosphorous and sulphur would also be expected, although these were omitted as they do not form carbides in alloy steels [113]).

Table 32 - Atomic weight percentages of carbides analysed by EDS in non-cryotreated AISI M2 tool steel.

		at%					
Label	Size /µm	C	W	Mo	V	Cr	Fe
N1	>1.0	29.30	15.43	15.60	3.96	4.47	31.23
N2	>1.0	45.81	7.32	7.64	31.61	3.00	4.62
N3	>1.0	39.86	13.01	12.78	3.57	3.94	26.84
N4	>1.0	41.68	12.52	12.98	2.66	3.80	26.35
N5	0.5 – 1.0	50.54	8.15	8.27	1.83	3.12	28.09
N6	0.5 – 1.0	49.91	7.24	7.34	2.25	2.81	30.45
N7	<0.5	53.46	6.67	7.61	3.31	2.96	25.99
N8	<0.5	41.59	3.72	3.61	1.12	4.56	45.40
N9	<0.5	44.94	8.85	9.15	2.48	4.09	30.49

Table 33 - Atomic weight percentages of carbides analysed by EDS in cryotreated AISI M2 tool steel.

		at%					
Label	Size /µm	C	W	Mo	V	Cr	Fe
C1	>1.0	48.59	10.88	10.93	3.00	3.17	23.42
C2	>1.0	45.25	11.55	11.84	3.55	3.38	24.43
C3	>1.0	57.72	9.88	8.10	2.58	2.39	19.33
C4	>1.0	54.95	8.68	9.00	2.21	3.16	22.01
C5	0.5 – 1.0	59.89	8.01	7.87	1.70	2.67	19.87
C6	0.5 – 1.0	55.20	9.38	8.65	1.82	3.25	21.69
C7	0.5 – 1.0	52.94	6.64	6.06	1.67	3.12	29.57
C8	0.5 – 1.0	61.01	2.52	3.33	11.27	2.96	18.91
C9	<0.5	52.34	7.10	6.06	1.53	3.03	29.93
C10	<0.5	54.12	3.27	4.19	12.86	3.51	22.07
C11	<0.5	52.24	3.57	3.87	10.79	3.63	25.90

Because of the infrequency of the vanadium-type carbides, it was difficult to find readily comparable examples (on the basis of size) between the two samples. However, comparing the large carbide of this type in the non-cryotreated sample (N2, >1µm) with two smaller carbides in the cryotreated sample (C8, 0.5 – 1.0µm; C10, <0.5µm; C11, <0.5µm) it was observed that those in the cryotreated sample had significantly higher carbon contents (54 – 61% compared with 46%), with a corresponding reduction in vanadium (11 – 13% compared with 32%). This increased carbon content was seen in the brighter cryotreated carbides (C1 – 7, 9) as well, with a mean carbon content of 53% compared to 44% for non-cryotreated carbides (N1, 3 – 9).

From the data collected, it could be suggested that cryogenic treatment had the effect of reducing the dissolution limit of alloying elements in iron, forcing them out of solution and resulting in existing carbides becoming 'enriched'. It was noted however, that the sample size examined here was statistically very small, and that the smallest carbides (<0.3µm), the bulk of which were observed following cryogenic treatment, could not be analysed by a typical SEM-EDS system.

4.4. Discussion

4.4.1. Grey cast iron and carbon steel brake rotor materials

Pin-on-disc testing to assess what effect deep cryogenic treatment had on the wear resistance of SAE J431 G10 grey cast iron produced mixed results. It was seen that, over the range of contact pressures and sliding speeds under which specimens were tested (375.0 – 750.0MPa and 1.18 – 2.24m/s respectively), changes in wear resistance were largely dependent on sliding distance (Figure 40). Specimens that had been cryogenically treated were seen to have improved wear resistance (by up to 81.4%) over shorter distances (<5000m), which subsequently deteriorated (down to -24.3%)

with continued testing. It was also determined that deep cryogenic treatment had no significant effect on the bulk or matrix hardness of G10 grey cast iron.

EN10083 C50R pearlitic steel was shown to respond significantly to deep cryogenic treatment, with bulk and matrix hardness increases of 27.7% and 16.5% respectively, and improvements in wear resistance (14.4, 12.1, 22.7%) across the range of contact pressures tested (1000, 1300, 1600MPa) at a sliding speed of 1.18m/s.

In both materials a common microstructural observation was made: the interlamellar spacing in the pearlite structures of cryotreated samples appeared to be less (Figure 51 and Figure 53). However, the dependence on diffusion for the formation of these large structures effectively rules out cryogenic treatment as a cause of this. Instead it is likely that these were existing features of the samples themselves. Instead, it was thought that finer microstructural changes (beyond those resolvable using standard SEM magnifications, such as nano-precipitates or changes in dislocation distributions) must be responsible for the significant increases in hardness and wear resistance measured. It is also difficult to discount the anecdotal evidence provided by the widespread use of cryogenic treatment to enhance the performance of brake discs for low-cost sports cars, which was identified as a major market for cryogenic processing companies in Section 1.2.

The mixed results from G10 grey cast iron were thought to be as a result of competing factors. Firstly, an increased wear resistance resulting from small scale microstructural changes (similarly to C50R) and secondly, a reduction in wear resistance resulting from degradation of graphite flakes due to deep cryogenic treatment (Figure 50). Graphite flakes in grey cast iron are known to play important roles in both its thermal conductivity and wear resistance. Due to the relatively short durations of the tests and only slight warming of specimens noted as a result, the role of graphite in wear resistance is thought to be more significant. Previous investigations have determined that the presence of graphite allows grey cast irons to produce a solid lubricant layer when being abraded [112], although they can also be considered as cracks in the material, due to their inferior mechanical properties to ferrite or pearlite [114]. It is suggested that deep cryogenic treatment may have deteriorated this capability and therefore reduced the effective wear resistance of the material over longer sliding distances; the mechanism for which could be as simple as a distortion of the graphite structure caused by competing thermal distortion with the surrounding ferrite at deep cryogenic temperatures. Following treatment the shearing of these graphite flakes (along basal planes which are known to have considerably higher strength [115]) may no longer have occurred consistently. While thermal properties are not thought to have been significant in the studies presented here, a change in graphite flake morphology as a result of cryogenic treatment would

have implications for the use of grey cast iron as brake discs. It has previously been shown that larger graphite flakes imbue grey cast irons with greater thermal diffusivity, as a result of their interlocking structure increasing the thermal conductivity of the material [10].

4.4.2. AISI A2, D6 and M2 tool steels

Reciprocating sliding testing conducted on AISI A2, D6 and M2 tool steels to determine what effects deep cryogenic treatment had on the wear performance of annealed materials indicated improvements in all cases, although with varying degrees of significance, as summarised by Table 34. Macro- and micro-hardness testing, however, showed no significant changes as a result.

Table 34 - Summary of significance of wear rate improvements in annealed tool steels due to deep cryogenic treatment.

Material	Sliding distance /m	WR improvement due to DCT	Significance measure /standard deviations
AISI A2	100	13%	1.3
	150	15%	1.7
	200	26%	2.2
AISI D6	100	30%	1.7
	150	15%	1.2
	200	5%	0.8
AISI M2	100	31%	5.2
	150	31%	6.8
	200	26%	5.1

As discussed previously, two changes are typically held responsible for improvements in the hardness and wear resistance of tool steels due to deep cryogenic treatment: 1) The complete transformation of retained austenite to martensite, and 2) an increased precipitation of fine carbides throughout the material matrix. It is clear from the results of hardness testing that no large-scale phase changes have taken place in the three tool steels studied, such as the transformation of austenitic EN52 steel reported by Jaswin et al. [80], as such a change would cause a measurable change in hardness. It is believed that, in most steels, the transformation of retained austenite to martensite requires only shallow cryogenic temperatures (163 – 193K) to occur [7] and as such might have been expected in the tool steels studied. It should be noted that the case reported by Jaswin et al. of a large scale austenite to martensite transformation stands in isolation, with other investigators reporting on the transformation of small pockets of retained austenite in otherwise martensitic steels.

The precipitation of fine carbides was observed to have occurred in all three tool steels tested (Figure 55, Figure 57 and Figure 59), although the mechanism for this remains unclear. Other investigators have reported that the precipitation of fine carbides due to deep cryogenic treatment is as a result of the increased amounts of

tempered martensite available, from which fine carbides can precipitate during post-cryotreatment tempering [74]. However, due to the negligible amounts of martensite present in the annealed tool steels tested, and the low-temperature (60°C) temper applied following cryogenic treatment, this mechanism could not have been responsible for the precipitations observed. While it is evident that low temperatures will reduce the solid solubility of alloying elements within the material matrix and, as a result of the movement of these rejected atoms by shifting dislocations due to thermal distortions in the material, create new sites for nucleation within the material, it is unclear how these precipitate nuclei are then able to grow. Conventional metallurgical theory dictates that the necessary diffusion of atoms would not occur due to insufficient energy being available at cryogenic temperatures [14], while the low temperature and short duration tempering occurring afterwards would not have allowed carbides of around 100nm to grow, rather precipitates that were an order of magnitude smaller in size would seem more likely. The 'enrichment' of carbides studied by the limited EDS analyses conducted on AISI M2 tool steel specimens support the idea that existing fine carbides may grow as a result of the rejection of alloying elements from the surrounding matrix during cryogenic treatment. This mechanism would also remove the requirement for energy for precipitates to form in the first place. However, it was also noted that very few carbides could be studied by this method, and more detailed examinations involving the extraction of carbides and subsequent analysis using X-ray diffraction and other techniques (with greater resolution for different characteristic wavelengths of elements) would yield far superior results. These issues are discussed further in Section 7.3.

4.5. Conclusions from sliding wear testing

Five ferrous alloys, including a grey cast iron (SAE J431 G10), a non-alloy steel (EN10083 C50R) and three tool steels (AISI A2, D6 and M2) were subjected to sliding wear testing, hardness measurements and comparative microstructural imaging. From pin-on-disc wear testing of G10 and C50R brake discs it was determined that:

- Deep cryogenic treatment resulted in mixed changes in the performance of SAE J431 G10 grey cast iron (from -24.3 – 81.4%), with improvements in performance observed over shorter sliding distances (<5000m), while causing no significant change in either the matrix or bulk hardness.
- Deep cryogenic treatment resulted in reductions in wear rate (from 12.1% - 22.7%) of EN10083 C50R non-alloy steel along with significant increases in both the bulk and matrix hardness (27.7% and 16.5% respectively), however no microstructural changes were observed to explain this improvement.

- Deep cryogenic treatment appeared to degrade the structure of graphite flakes in SAE J431 G10 grey cast iron, thought to be as a result of their differing rates of thermal contraction with the surrounding material during cryogenic treatment, resulting in a thinner and rougher appearance.

From reciprocating sliding testing of annealed AISI A2, D6 and M2 tool steels it was determined that:

- Deep cryogenic treatment resulted in reductions in the wear rates of all three tool steels of between 5 – 31%. These changes were greatest and most significant in AISI M2 tool steel (26 – 31%, >5σ change) followed by AISI A2 (13 – 26%, 1.3 – 2.2σ) and AISI D6 (5 – 30%, 0.8 – 1.7σ).
- Deep cryogenic treatment had no significant effect on the bulk or matrix hardness of AISI A2, D6 and M2 tool steels; indicating that no large scale phase changes (e.g. austenite – martensite) had taken place.
- Deep cryogenic treatment appeared to increase the number of fine carbide precipitates (~100nm) from AISI A2, D6 and M2 tool steels, along with slight changes in the etched appearances of phases within the microstructure.
- Deep cryogenic treatment may cause the rejection of alloying elements from solid solution, resulting in existing fine carbides becoming 'enriched' with these liberated atoms and subsequently growing during post-cryotreatment tempering. However, detailed characterisation of these carbides (e.g. by XRD, TEM etc.) would be required to substantiate this hypothesis.

Limited work has been published concerning the effects of cryogenic treatments on grey cast iron, pearlitic carbon steels or austenitic tool steels. The findings presented here, which indicate changes in the wear behaviour of SAE J431 G10 grey cast iron and EN10083 C50R pearlitic carbon steel, suggest potential new areas of investigation. Similarly, the growth of fine carbides during tempering in austenitic tool steels following deep cryogenic treatment is previously unreported in the literature, and, if substantiated through further investigation, may offer alternative methods for producing tough but wear resistant materials.

Due to the limitations of resources available, further analysis could only be conducted on one material. As the alloy demonstrating the greatest and most consistent improvements in hardness and wear resistance, EN10083 C50R pearlitic steel was selected for more detailed microstructural and crystallographic characterisation, the results of which are presented in Chapter 5.

5. Effects of deep cryogenic treatment on the microstructure of pearlitic carbon steel

In this chapter further studies are presented that attempt to identify the microstructural changes occurring in EN10083 C50R pearlitic carbon steel as a result of deep cryogenic treatment, with it having shown the greatest improvements in hardness and abrasive wear resistance (>15% in both cases, as described in Section 4.3). Scanning and transmission electron microscopy were used to observe any morphological changes while X-ray, electron back-scatter and electron diffraction were used to identify changes in phase composition and crystallographic structure respectively.

5.1. Further microstructural observations (SEM and TEM)

With no phase changes available to either the body-centred cubic ferrite or primitive orthorhombic cementite present in C50R (unlike the transformation of retained austenite to martensite in hardened steels), the focus of the SEM and TEM study was to try to identify and begin to characterise changes in fine carbide precipitates. Three locations were considered for investigation:

- Within primary ferrite grains or within the secondary ferrite comprising the pearlite structure with cementite lamellae;
- At ferrite-ferrite or ferrite-pearlite grain boundaries;
- At cementite-ferrite interfaces in pearlite.

Figure 61 summarises the results of the SEM study, which focused on the primary and secondary ferrite as locations for carbide precipitations. Although the negatives of the micrographs taken of both non-cryotreated and cryotreated C50R (Figure 61 (a) and (b) respectively) arguably show an increase in precipitates (of <100nm size) in the primary ferrite following cryogenic treatment, a significant crystallographic etching effect (whereby ferrite grains of different orientations react with the Nital acid at different rates) was apparent amongst the prepared specimens. Those shown represent areas selected because they appeared to have etched similarly.

Considering the micrographs showing equivalent areas of secondary ferrite in the pearlite grains of both non-cryotreated and cryotreated C50R (Figure 61 (c) and (d) respectively), it is clear that this etching effect obscures any difference in precipitates that would otherwise be visible. No evidence of precipitates or any other microstructural changes were visible at the cementite-ferrite interfaces.

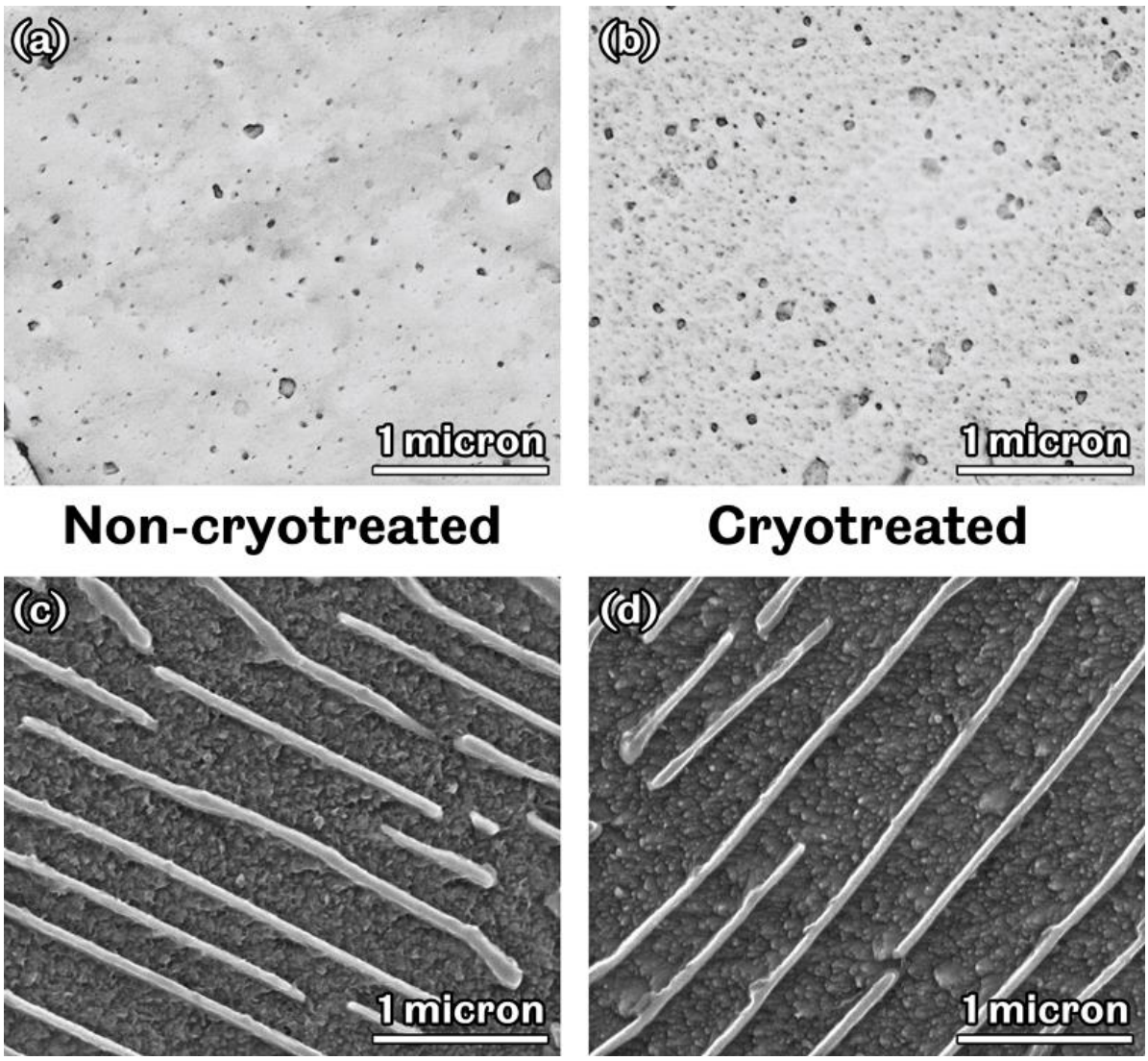

Figure 61 - SE micrographs showing: (a) non-cryotreated and (b) cryotreated nano-precipitates in primary ferrite (inverted, contrast enhanced); (c) non-cryotreated and (d) cryotreated secondary ferrite and cementite lamellae.

To overcome the effects of crystallographic etching, to better observe the nano-precipitates present in C50R and to attempt probe the grain boundaries and cementite-ferrite interfaces, transmission electron micrographs were generated. Figure 62 summarises the observations made.

Nano-precipitates were observed in both non-cryotreated and cryotreated samples, with no apparent difference in quantity, distribution or morphology. In both cases precipitates were observed only in select grains of both ferrite and pearlite, while being largely absent from the rest of the matrix. Three distinct morphologies were observed (highlighted by red arrows in Figure 62 (a) and (b)): the largest (50 – 150nm) having a hexagonal shape, with smaller (10 – 50nm) spherical and tiny (<10nm) rod-like precipitates. Even smaller (<5nm) seemingly spherical precipitates could also be seen, but proved difficult to adequately resolve. When present in either ferrite or pearlite grains, these precipitates did not appear to favour grain boundaries or cementite-ferrite interfaces. Based on the chemical composition of the steel (Table 21, Section 4.1.1), it was thought likely that the observed precipitates were predominantly iron

carbides (Fe_xC_y) and therefore hexagonal or orthorhombic in nature (discounting the monoclinic Hägg carbide (Fe_5C_2) due to the low alloy content of C50R) [113, 116].

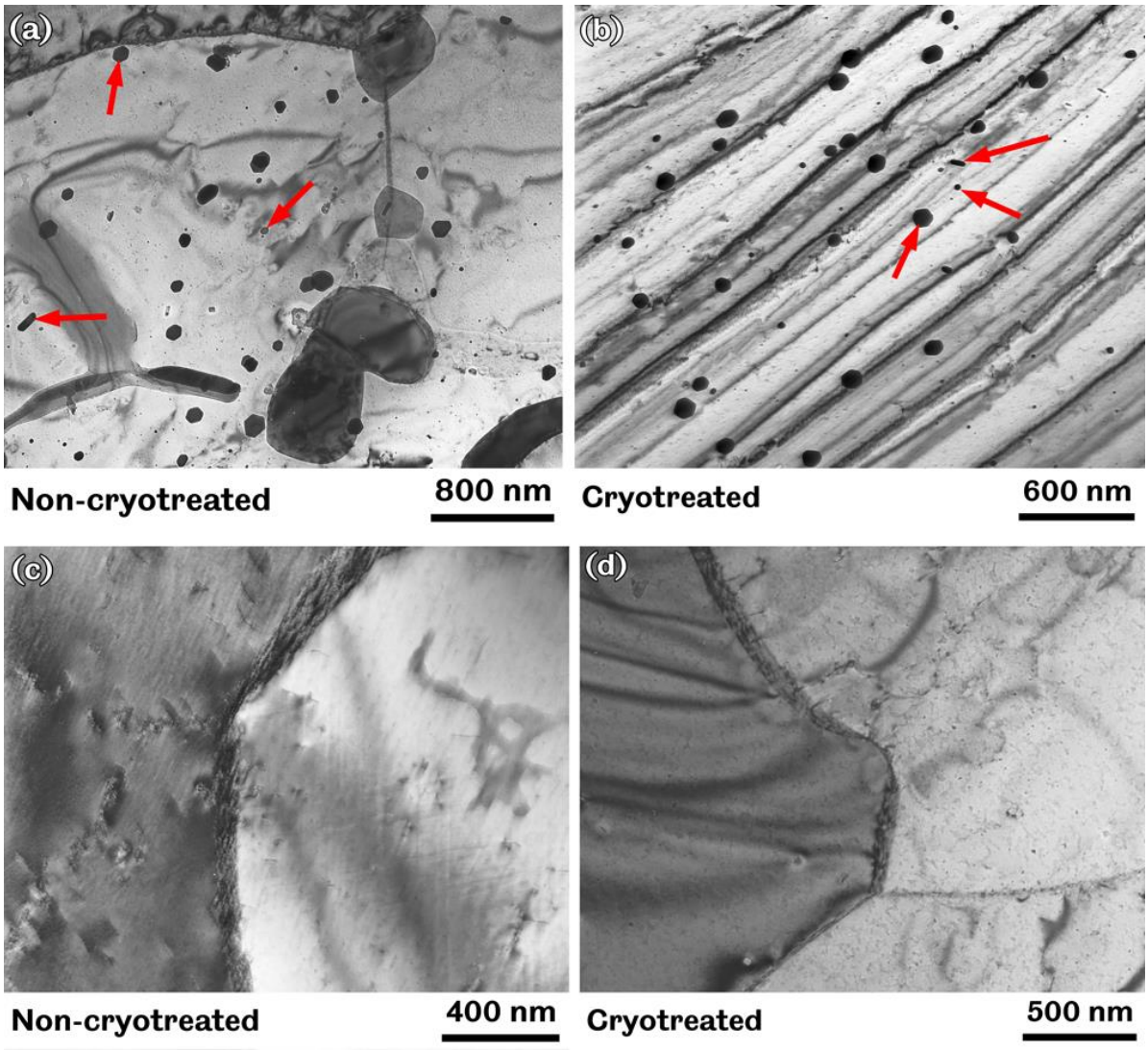

Figure 62 - TE micrographs showing: (a) non-cryotreated and (b) cryotreated nano-precipitates in ferrite; (c) non-cryotreated and (d) cryotreated ferrite-ferrite grain boundaries.

Transmission electron micrographs were also generated of grain boundaries in non-cryotreated and cryotreated samples (Figure 62 (c) and (d) respectively). Although any precipitates present could not be directly imaged because of a lack of contrast with the grain boundaries themselves, it was thought that a significant change in the relative prevalence of these carbides may become manifest as visible distortion or deformation of the near grain boundary material. This was not, however, evident from the micrographs generated. It was attempted to extract precipitates from these regions, so that they may be imaged directly, using carbide replicas. However, either insignificant numbers of precipitates were present or they failed to be captured by the replicas, as none were found using this technique.

5.2. Analysis of phase composition

5.2.1. X-ray diffraction

Although initial investigations using optical and scanning electron microscopy gave no indication of phases present other than ferrite and cementite, X-ray diffraction was used to investigate whether small quantities of austenite were present in the material, that may have undergone transformation as a result of deep cryogenic treatment and therefore explain some of the hardness and wear resistance improvements previously determined. In Figure 63 the diffraction patterns obtained are presented. Due to the limitations of the equipment available (as discussed in Section 3.5.4) scans were made over both a wide range of diffraction angles ($35° < 2\theta < 100°$; Figure 63 main plot) and over a small range ($37° < 2\theta < 50°$; Figure 63 inset plot) to identify the cementite phase which, due to its lower symmetry and morphology, developed comparatively smaller peaks when compared with the ferrite phase.

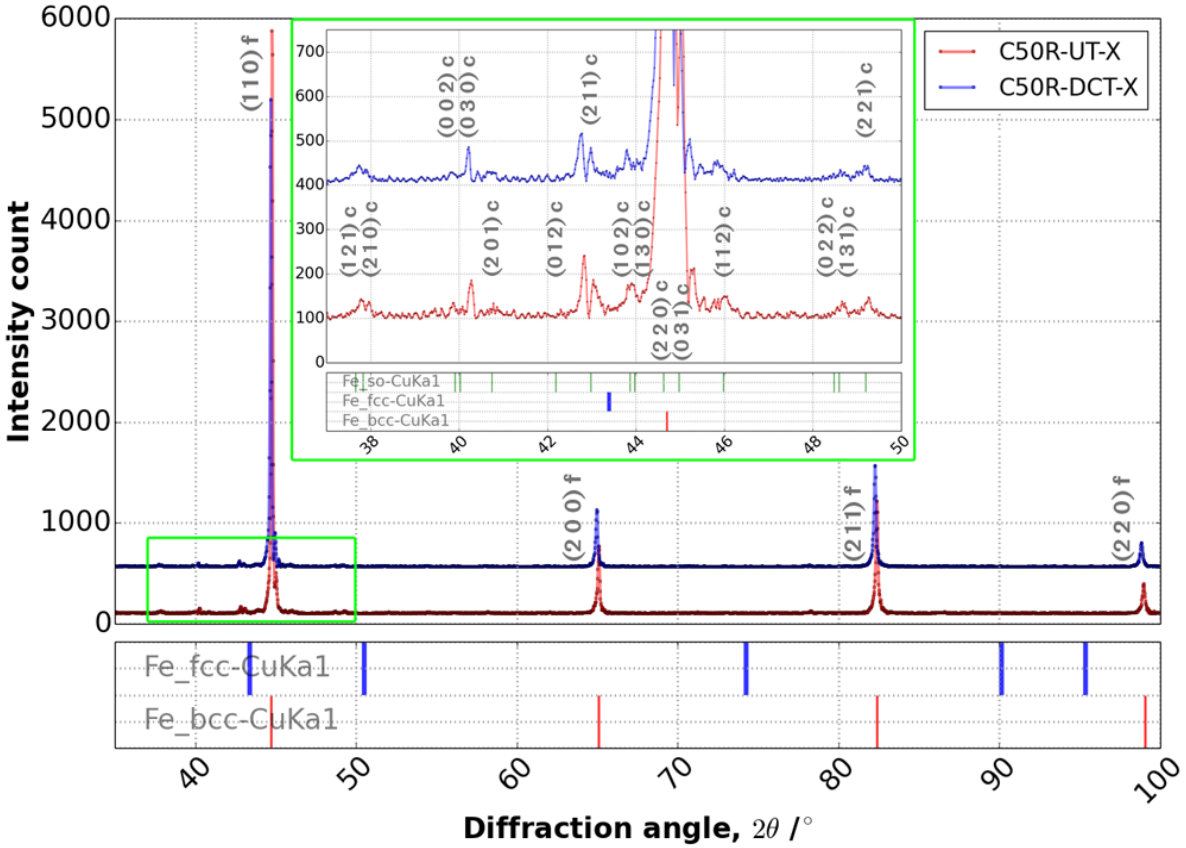

Figure 63 - XRD patterns for C50R steel: (main) wide-angle traces revealing body-centred cubic ferrite peak positions and (inset) narrow-angle trace revealing primitive orthorhombic peak positions in (red) non-cryotreated and (blue) cryotreated samples. (Subplots show theoretical peak positions for pure Fe bcc and fcc, and primitive orthorhombic (so) crystals).

Also shown (as subplots in Figure 63) are the theoretical peak positions of body-centred and face-centred cubic as well as primitive orthorhombic iron (ferrite, austenite and cementite respectively). By comparing these with the obtained

diffraction patterns it was determined that no measurable quantity of austenite was present in any of the samples.

The observed peak positions for ferrite were used to calculate plane spacings and lattice parameters by comparison with Bragg's Law (and the relationships developed as Equations 3.3 – 3.7, Section 3.4.3). Given in Table 35, a slight expansion of the ferrite unit cell dimensions (+0.14%) was determined. However, given the sensitivity of these values to the diffraction angles of the indexed peaks and, in turn, their dependence on the precise positioning of the specimen surface relative to the incident X-ray beam (as discussed in Section 5.4), this was not thought significant.

Table 35 - Lattice constants determined for body-centred cubic ferrite phase using plane indices (hkl) and diffraction angle (2θ) to calculate plane spacing (d_{hkl}) and lattice parameter (a).

Plane indices			Non-cryotreated			Cryotreated		
h	k	l	2θ /°	d_{hkl} /Å	a /Å	2θ /°	d_{hkl} /Å	a /Å
1	1	0	44.78	2.022	2.860	44.70	2.026	2.865
2	0	0	65.10	1.432	2.863	64.98	1.434	2.868
2	1	1	82.38	1.170	2.865	82.28	1.171	2.868
2	2	0	98.98	1.013	2.866	98.86	1.014	2.868
				Mean	2.863		Mean	2.867

A similar procedure was used to determine the plane spacings and lattice parameters for the orthorhombic cementite phase. Using the parameter ratios given by Powder Diffraction File (PDF) 04-014-3159 (stored by the International Centre for Diffraction Data (ICDD) from the time-of-flight neutron diffraction data for cementite of Wood et al. [117] collected at 300K) plane spacings were calculated from the identifiable peak positions and used to calculate lattice parameters by the necessary rearrangement of Equation 5.1 and appropriate substitution of parameter ratios (b/a, c/a, c/b).

For an orthorhombic crystal,

$$\frac{1}{d_{hkl}^2} = \frac{h^2}{a^2} + \frac{k^2}{b^2} + \frac{l^2}{c^2} \qquad (5.1)$$

From the values given in Table 36, it can be seen that between the non-cryotreated and cryotreated cementite phases there was no significant change, with only a 0.02% reduction in the mean lattice parameters calculated compared with standard deviations an order of magnitude greater than this. Although the standard error and coefficient of variation from the cryotreated data were greater than those determined from the non-cryotreated data, they remained small and were judged to be insignificant.

Table 36 – Lattice constants determined for primitive orthorhombic cementite phase using plane indices (hkl) and diffraction angle (2θ) to calculate plane spacing (dhkl) and lattice parameters (a, b, c). Ratios: (b/a, c/a, c/b) = (1.330, 0.889, 0.669) from Wood et al. [117].

Plane indices			Non-cryotreated					Cryotreated				
h	k	l	2θ /°	d_{hkl} /Å	a /Å	b /Å	c /Å	2θ /°	d_{hkl} /Å	a /Å	b /Å	c /Å
2	1	0	37.78	2.379	5.084	6.761	4.520	37.74	2.382	5.089	6.768	4.524
0	0	2	39.88	2.259	5.081	6.752	4.517	39.84	2.261	5.086	6.759	4.522
0	3	0	40.28	2.237	5.046	6.711	4.490	40.22	2.240	5.053	6.721	4.496
2	0	1	40.78	2.211	5.073	6.746	4.510	40.64	2.218	5.090	6.768	4.525
0	1	2	42.30	2.135	5.064	6.730	4.502	42.48	2.126	5.043	6.703	4.484
2	1	1	42.84	2.109	5.093	6.772	4.528	42.78	2.112	5.100	6.781	4.534
1	0	2	43.82	2.064	5.082	6.754	4.518	43.80	2.065	5.084	6.757	4.520
1	3	0	43.90	2.061	5.084	6.762	4.523	44.02	2.055	5.071	6.745	4.512
1	1	2	46.00	1.971	5.075	6.745	4.512	46.22	1.963	5.052	6.715	4.491
1	3	1	48.66	1.870	5.070	6.742	4.510	48.62	1.871	5.074	6.747	4.513
2	2	1	49.26	1.848	5.071	6.743	4.509	49.24	1.849	5.073	6.746	4.511
				Mean	5.075	6.747	4.513		Mean	5.074	6.746	4.512
				Std err	0.38%	0.50%	0.32%		Std err	0.54%	0.74%	0.47%
				CoV	0.25%	0.25%	0.23%		CoV	0.35%	0.36%	0.34%

Although there were known limitations with the X-ray diffraction study conducted (as discussed in Section 3.5.4), sufficient data was obtained to perform a qualitative phase analysis and suggest that no significant quantity of austenite was present in the non-cryotreated C50R material that may have transformed to martensite during cryogenic treatment. This mechanism cannot therefore be used to explain some of the wear resistance and hardness improvements previously observed. Additionally, calculations of lattice parameters of both the ferrite and cementite phases present in C50R indicated no significant change in crystal geometry.

5.2.2. Electron back-scatter diffraction

To provide greater certainty in the results of the X-ray diffraction analysis (Section 5.2.1), an unexpected opportunity was utilised to analyse one specimen by electron back-scatter diffraction. Accordingly, a phase map and an Euler map were generated for a sample of C50R steel that had not undergone cryogenic treatment. These are presented as Figure 64 and Figure 65 respectively.

Although the relatively large area (0.35mm^2) analysed precluded the resolution of individual cementite lamellae, it ensured that a robust sample was investigated for the presence of austenite. As can be seen from the singular red colour of Figure 64, no austenite was present in the sample, which corresponded to the results of the X-ray diffraction study.

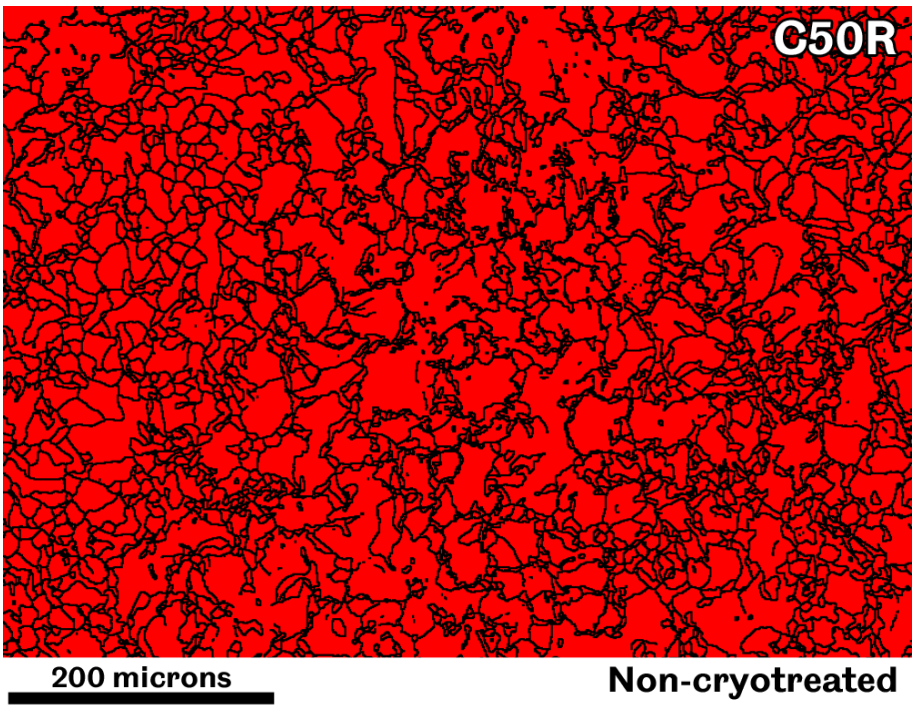

Figure 64 – EBSD phase map showing (red) ferrite throughout the sample. Cementite lamellae were too fine to resolve within the large area selected, while austenite (if present) would be coloured blue.

The second objective of the brief EBSD study was to qualitatively assess crystallographic texture, thought to be quite strong in the material based on the variation observed in gathered X-ray diffraction patterns from remote locations in the same samples. The Euler map generated and presented as Figure 65 confirms this supposition, with large regions of similarly coloured grains representing large regions with common crystallographic orientations.

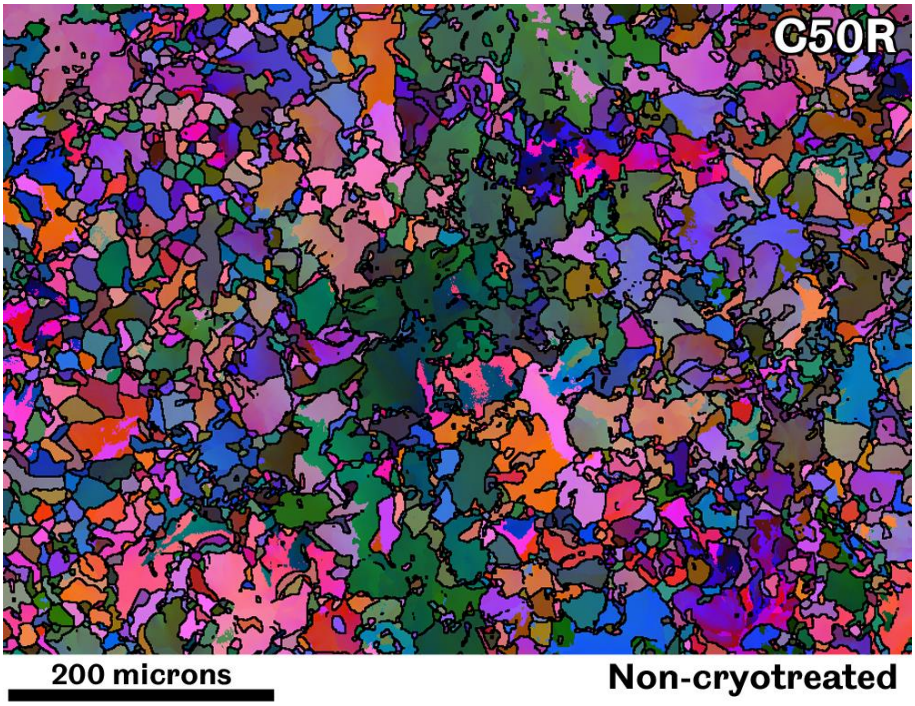

Figure 65 - Euler map generated by EBSD. Areas of similar colours indicate grains of similar orientation. From this image the strong texture of the material (with large areas of similarly oriented grains) can be seen.

In simple terms, the different colours in the image represent a combination of three angular rotations through which each point on the sample would have to undergo such that its orientation matched the crystallographic reference angle of the incident beam. Presuming the relatively large area imaged is representative of the sample, it is clear that strong texture was a contributing factor to the variable peak intensities observed by X-ray diffraction that prevented a quantitative analysis from being undertaken.

5.3. Analysis of crystallographic structure

Gathered electron diffraction patterns were indexed by comparison with standard patterns for common lattices (variously presented in e.g. [105, 118]) with lattice parameters determined by the method described in Section 3.4.3. Electron diffraction patterns gathered from C50R steel were used to confirm the absence of even very small grains or regions of austenite that were perhaps not detectable over the background noise present in XRD patterns and unresolvable by EBSD. Typical diffraction patterns gathered for this purpose are illustrated in Figure 66.

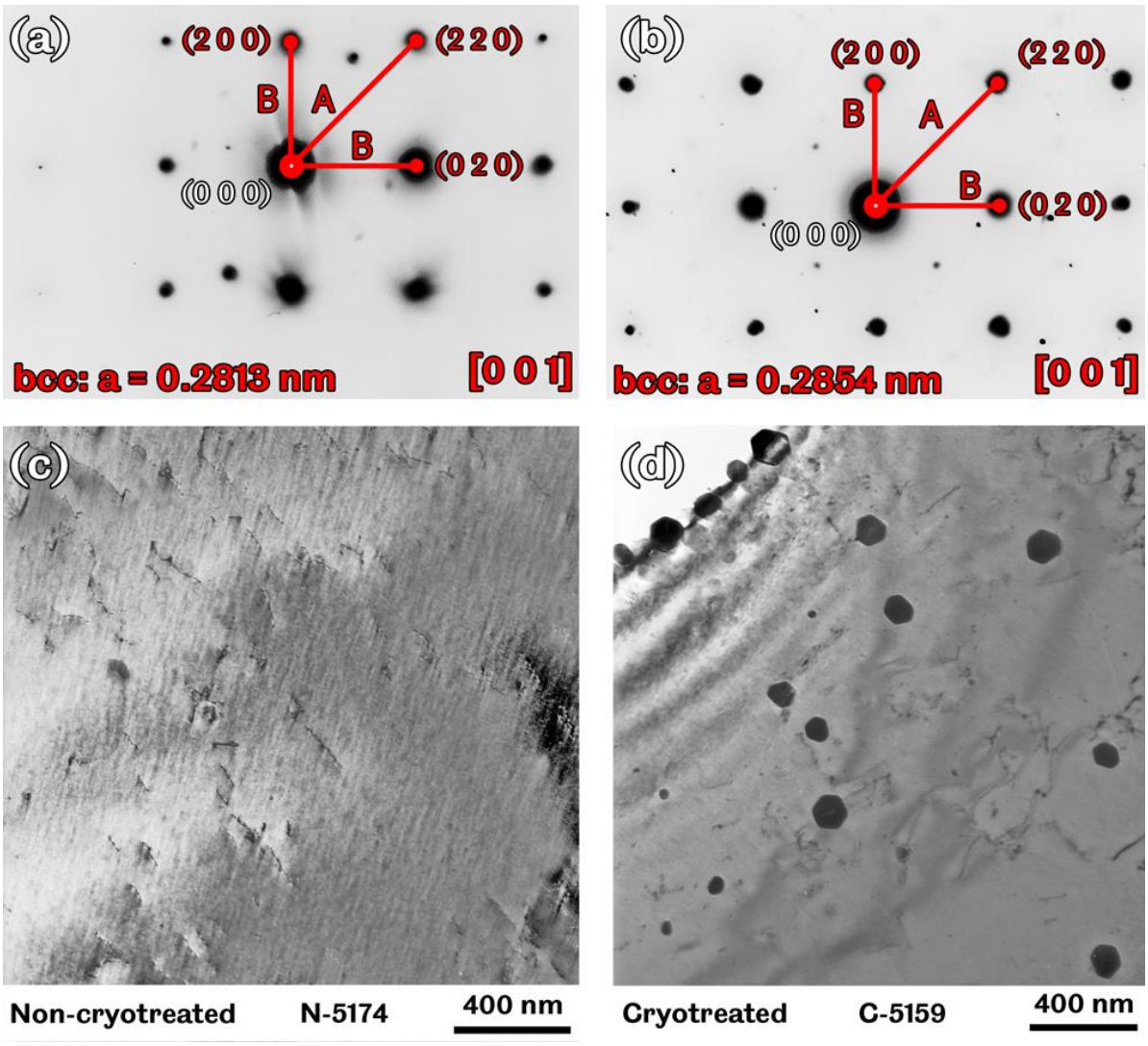

Figure 66 - Electron diffraction patterns from primary ferrite in (a, c) non-cryotreated and (b, d) cryotreated C50R showing the indexed planes (hkl), calculated lattice parameter (a) and zone axis [UVW].

Although lattice parameters determined by this method (for non-cryotreated and cryotreated C50R, Figure 66 (a) and (b) respectively) are acknowledged to be significantly less accurate determinations than those provided by X-ray diffraction, they were used to confirm observed diffraction patterns belonged to body-centred cubic ferrite (as opposed to face-centred cubic austenite).

As plane reflections were often missing, this determination of lattice parameters was necessary to distinguish between cubic phases (with $a_{Fe,\ bcc}$ = ~0.286nm and $a_{Fe,\ fcc}$ = ~0.359nm) and ensure that small regions of austenite were not present. Indeed, the absence of austenite was confirmed using this method.

5.4. Discussion

Further microstructural analyses to attempt to explain the causes of increased hardness and wear resistance in pearlitic EN10083 C50R steel investigated two possibilities (based on the range of observations reported by previous investigators reviewed in Section 2.2.3) thought likely to be responsible:

- The presence of small regions or austenite in the predominantly pearlitic-ferritic matrix that may be susceptible to transform to martensite as a result of deep cryogenic treatment.
- An increase in fine carbide precipitates following deep cryogenic treatment and subsequent tempering.

Although there were limitations with the X-ray diffraction experiments conducted, as a result of the radiation source available and the microstructural characteristics of the material (as discussed in Section 3.5.4), the diffraction patterns gathered (Figure 63) provided strong evidence against the presence of austenite in the material, beyond quantities that may be hidden within the noise of the data.

Determinations of lattice parameters for both the body-centred cubic ferrite phase (a = 0.286nm) and the orthorhombic cementite phase (a = 0.508nm, b = 0.675nm, c = 0.451nm) based on identifiable peak positions and calculated plane spacings showed no significant change due to deep cryogenic treatment. Although there were slight variations between mean values (a 0.14% increase and 0.02% decrease in the lattice parameters for ferrite and cementite respectively), these were not thought to be anything other than errors resulting from the accurate determination of the middle of peaks from X-ray intensities separated by discrete angle spacings, or the precise positioning of the specimen surface relative to the incident X-ray beam.

From the experimental setup used, the error in determining each peak position accurately from the diffraction data can be assumed to be similar to the step size (in

this case 0.020° 2θ). Using Equation 5.2 (BS EN 13925 [119]) it can be shown that, over the 2θ range tested (36 - 100°), a further error of 0.046 – -0.010° would result from a specimen height displacement (Δh) error of 100μm (thought to be a reasonable estimate when aligning the specimen within the holder using a flat surface, and considering the elastic properties of the temporary adhesive used to hold the specimens in place) on a goniometer with a radius (R) of 200mm, such as the Siemens D5000 used.

Diffraction angle error:
$$\Delta 2\theta = -\left(\frac{2\Delta h}{R}\right)\cos 2\theta \qquad (5.2)$$

While a more rigorous approach to finding the lattice parameters for the cementite phase would involve solving the system of equations presented by the plane indices (hkl) and the lattice parameters (a, b, c), the use of published ratios for lattice parameters was deemed acceptable given the comparative nature of the study, and the much more significant errors already discussed in the identification of peak positions and calculated plane spacings. If a significant change in one or more lattice parameters had occurred due to cryotreatment, this would have been discernible from significant increases in the distribution of calculated values. While the coefficient of variation found from the cryotreated sample (0.35%) was greater than that of the non-cryotreated sample (0.25%), it was still of extremely low magnitude and therefore not thought significant.

The absence of austenite in the material was further confirmed by the brief electron back-scatter diffraction experiment conducted on non-cryotreated C50R steel (Figure 64) and the electron diffraction patterns generated (Figure 66). Additionally, the Euler map generated by EBSD (Figure 65) indicated strong crystallographic texture in the material that would have contributed to significant variations in peak intensities recorded by X-ray diffraction, not representative of the bulk component, thereby preventing a quantitative phase analysis from being conducted. In any case, such an analysis would only have succeeded in confirming the phase fractions of ferrite and cementite in the material, which are of little relevance to the present study.

It was originally intended to extract and characterise fine precipitates from the material by means of carbide replicas and electron diffraction. However, as previously discussed (Section 5.1), creating these replicas proved problematic, either as a result of the absence of sufficient numbers of fine precipitates so that they could be readily observed, or due to some other physical characteristic of the material that prevented their extraction using metallographic etchants that are common for this purpose and material type.

However, considering observations indicating no phase transformations or changes in carbide precipitations within ferrite or pearlite grains as a result of deep cryogenic treatment, it is the author's opinion that grain boundary and phase interface precipitates remain the most likely explanation for the significant changes in hardness and wear resistance previously determined (Sections 4.3.1.1 and 4.3.2.1 respectively). If these were to develop following tempering after deep cryogenic treatment (presumably from carbon rejected from the grain structure and carried to boundaries by the physical movement of dislocations by thermal distortion of the matrix at cryogenic temperatures, as discussed in Section 2.2.3), they may be expected to effectively 'pin' these boundaries and prevent sliding between grains.

Such a change would therefore inhibit bulk deformation of the material and cause an increase in hardness (as measured by micro- or macro-measurement methods) and abrasive wear resistance. In the absence of being able to directly observe grain boundary regions or extracting fine precipitates from the material, nano-indentation testing is suggested as a technique that may be used to support this hypothesis. If the mechanical properties of the both the primary ferrite and secondary (pearlite phase) ferrite could be accurately determined and found to be unchanged by deep cryogenic treatment (while bulk mechanical properties are), this would support the grain boundary and phase interface precipitates hypothesis.

5.5. Conclusions from microstructural analyses of C50R steel

EN10083 C50R pearlitic carbon steel was prepared for a range of microstructural observation and characterisation techniques including scanning electron and transmission electron microscopy, X-ray, electron back-scatter and electron diffraction to attempt to determine the physical changes responsible (and ultimately the mechanisms of microstructural change during deep cryogenic treatment) for the increased hardness and abrasive wear resistance previously determined (Sections 4.3.1.1 and 4.3.2.1 respectively). From these studies it was determined that:

- EN10083 C50R material, such as was tested, contained no measurable quantities of austenite prior to, and no martensite after, deep cryogenic treatment. This was therefore ruled out as a possible explanation for changes in mechanical properties and wear performance. By means of a qualitative phase analysis it was shown to be overwhelmingly formed of phases having previously been observed by optical and scanning electron microscopy; these being pearlite containing lamellar cementite and ferrite.
- By means of scanning and transmission electron microscopy, fine carbide precipitates (ranging from <10 – 150nm) were observed in both ferrite and pearlite grains. However, these were not seen to alter in terms of either physical

characteristics (e.g. size or shape) or frequency distribution due to deep cryogenic treatment.

- EN10083 C50R samples had strong crystallographic texture (regions of similarly oriented grains) that prevented X-ray diffraction data being collected that was sufficient for a quantitative analysis.
- Deep cryogenic treatment did not alter the lattice parameters of the main ferrite and cementite phases (either directly or indirectly by e.g. changes in residual strain).

Although a full characterisation of fine precipitates or a detailed investigation of grain boundaries and phase interfaces within EN10083 C50R steel could not be conducted in the present study, the findings presented have ruled out a number of possibilities for microstructural change due to deep cryogenic treatment in this example of an important class of engineering steels. In the author's opinion, it remains the most likely possibility that changes in the nature of these precipitates, boundaries and/or interfaces could still explain the significant improvements in bulk hardness and abrasive wear resistance previously determined.

Two approaches are therefore suggested to investigate these possibilities. Firstly, the use of nano-indentation to accurately determine the mechanical properties of the ferrite phase and further narrow down the regions of interest for materials characterisation. Secondly, 'metallurgically precise' samples should be prepared to ensure accurate control of both the chemical composition and microstructure of the material. Reducing the grain size, grain size distribution and crystallographic texture present in the material analysed will increase the chances of making representative observations of the microstructure. Furthermore, the increase in total grain boundary area would be expected to facilitate fine precipitate observation, extraction and characterisation.

6. Effects of deep cryogenic treatment on the wear development of tungsten carbide cutting tools

In this chapter the machining parameters and results of tool wear development testing using SHM H13A cobalt-bonded tungsten carbide turning inserts in cutting AISI 1045 (EN8) carbon steel under the fully lubricated condition are presented. Wear behaviours are related to microstructural observations, before the results are discussed in the context of published literature and the conclusions of the study are presented.

6.1. Cutting inserts

The specimens tested were single-point H13A tungsten carbide turning inserts (SCMT 120408 –KM H13A), typically used for medium to roughing cuts. 20 inserts were utilised for the testing plan outlined in Section 6.2, which was conducted on a standard Colchester 600 series bench lathe. Figure 67 and Table 37 summarise the insert and machining geometries.

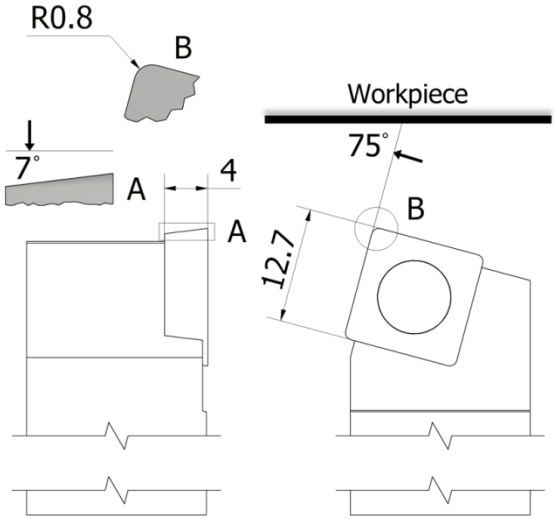

Figure 67 - Illustrated insert and toolholder geometric parameters.

Table 37 - Geometric parameters for H13A inserts and CoroTurn 107 toolholder.

Parameter	Value
Insert size /mm	12.7
Insert thickness /mm	4
Nose radius, r_ε /mm	0.8
Clearance angle, α_n	7°
Lead angle, κ_r	75°
Cutting inclination, λ_s	0°

AISI 1045 / EN8 plain carbon steel bars as recommended by ISO 3685 [37] were used as the workpiece material to be machined. Bars with a 400mm machinable length and 80mm initial diameter were used for testing. Workpieces were cleaned using a sharp cutting tool to remove the outer oxide layer prior to insert specimens being tested, before a parting tool was used to cut slots in the bar and divide the initial 400mm cutting length into four 95mm lengths, to allow for shorter measurement intervals.

6.2. Testing parameters

ISO 3685 provides standard cutting conditions with which tool-life tests are typically conducted. However, as highlighted in Section 2.2, while there have been a number of recent tool-life studies involving cryogenically treated tungsten carbide cutting tools, few have looked in detail at whether the critical wear (and therefore failure) mechanisms of these tools has changed.

Therefore, for the purposes of this study, it was decided to focus on initial wear development of tool inserts instead of conducting complete tool-life tests. The ranges of recommended cutting parameters and the parameters adopted for tool wear development testing on the Colchester 600 series bench lathe are given in Table 38.

Table 38 - Ranges of standard cutting parameters and those adopted for tool wear development testing.

Parameter	Range defined by ISO 3685 [37]	Parameters used
Feed (mm/rev)	0.10 – 0.63	0.2
Depth of cut (mm)	1.0 – 2.5	0.5
Corner radius (mm)	0.4 – 1.2	0.8
Spindle speeds (rpm)	-	260, 470, 840

ISO 3685 suggests that cutting speeds be separated by a ratio of at least 1.12 for tungsten carbide tools [37]; a ratio which was easily exceeded by selecting cutting speeds of 50, 95 and 140m/min. Given the discrete spindle speeds available, each of these cutting speeds was achieved to within ±10%. Each insert was subjected to five separate passes of the workpiece, with wear measurements and observations taken after machining each 95mm length along the workpiece. Depending on the spindle speed, this represented intervals of 34 – 110s. Given the improved performance reported by Yong and Gill et al. [89, 90] when using coolant with cryotreated WC-Co tools, it was decided to apply cutting fluid to flood the contact during the tool wear development testing presented here. Table 39 summarises the testing plan that was implemented.

Table 39 - Matrix summarising tool wear development testing conducted.

V_c /(m/min)	$46 < V_c < 53$		$93 < V_c < 97$		$134 < V_c < 154$	
Repeat	Standard	Cryotreated	Standard	Cryotreated	Standard	Cryotreated
1	×	×	×	×	×	×
2	×	×	×	×	×	×
3	×	×	×	×	×	×

6.3. Wear measurement and analysis

One standard and one cryogenically treated insert were separated prior to testing. Their flank and rake faces were imaged using a Carl Zeiss AxioImager optical microscope (brightfield 10x and 5x objectives respectively) and scanned using a Bruker ContourGT light interferometer (using narrowband green light and a 10x objective) to

characterise the initial state and determine the initial roughness of the flank and rake faces of the tool inserts. Three standard (N2 – N4) and three cryogenically treated (C2 – C4) inserts underwent micro-hardness testing as described in Section 3.3.1, with indents made on surfaces away from the cutting edge. All cutting inserts had their mass measured prior to testing using precision digital scales (Sartorius Analytical Balance BP210D).

Following each pass of the workpiece, the residue of the cutting fluid and loose debris were removed from the inserts by ultrasonic cleaning in acetone. Inserts were then weighed and their rake faces scanned by light interferometry so that crater wear measurements could be made. Optical microscopy of the rake and flank faces allowed for wear features and mechanisms to be characterised, and the extent of flank wear to be measured.

After tool wear development testing was concluded, one standard and one cryogenically treated insert that had been subjected to each cutting regime were sectioned and prepared for microstructural analyses along with the unused inserts (as described in Section 3.4), so that the effects of machining on the development of subsurface wear and microstructure could be observed.

6.4. Results

6.4.1. Hardness

The results of low-force hardness measurements taken from H13A inserts indicated a modest increase of 9.2% due to deep cryogenic treatment. Although this increase lay within a standard deviation of both the untreated and cryotreated sample means, the statistical significance of the sample sizes (30) should be noted.

Table 40 - Low-force hardness test results from H13A inserts.

Specimens	$HV_{4.905}$ /MPa	Coefficient of variation
Untreated (N2 – N4)	20740	15.6%
Cryotreated (C2 – C4)	22640 (+9.2%)	15.5%

6.4.2. Tool wear development

The cutting speeds selected for testing caused a variety of wear features on the tools being tested. While no flank wear or built-up edge (BUE) was apparent at the lowest cutting speed (50m/min) tested, both of these mechanisms became significant at the higher cutting speeds (95 and 140m/min). By contrast, while crater wear depth was the only parameter that could be reliably measured on inserts after machining at 50m/min, it could not be accurately measured on the remaining inserts as a result of the pervasion of adhered material in the primary crater wear zone. As a result only

selected wear mechanisms and behaviours are discussed with relation to wear development at each cutting speed. These are summarised in Table 41.

Table 41 - Wear mechanisms measured and discussed for each cutting condition.

	Cutting speed /(m/min)		
Mechanism	50	95	140
Crater wear	✓		
Flank wear		✓	✓
Notch wear			✓
Built-up edge		✓	✓
Mass change	✓	✓	✓

While inserts were subjected to different durations of machining and used in removing differing quantities of workpiece material, for convenience results are expressed with relation to the number of passes they made of 95mm cutting lengths. Table 42 provides a reference correlating the number of passes made with the machining duration and material removed for each cutting speed.

Table 42 - Relationships between machining passes, duration and material removed dependent on cutting speed.

	Cumulative cutting time /min			Cumulative material removed /mm^3		
Passes completed	V_c = 50	V_c = 95	V_c = 140	V_c = 50	V_c = 95	V_c = 140
1	1.83	1.01	0.57	8850	9700	7900
2	3.67	2.03	1.14	17800	19600	16000
3	5.52	3.05	1.71	26700	29400	24000
4	7.38	4.09	2.29	35800	39400	32100
5	9.21	5.10	2.85	45000	49500	40500

6.4.2.1. Crater wear

The results from tool wear development tests at 50m/min (Figure 68) indicated no performance benefit due to deep cryogenic treatment, with crater wear measurements from both sets of inserts indicating crater depths of around 26µm after 5 passes (9 minutes of machining). It is suggested that the reduction in the growth rate of these craters was related to the inserts increase in mass in the latter stages of testing (Figure 69), as the rake face micrographs taken (Figure 70) showed the inserts to have begun collecting adhered workpiece material along with isolated incidences of the development of BUE.

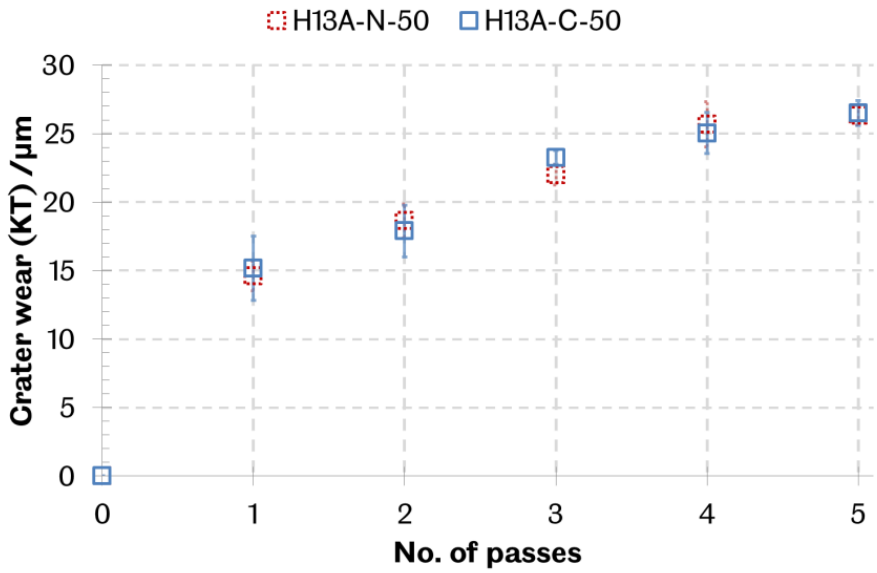

Figure 68 - Development of crater wear on inserts during machining at 50m/min, where '-N' and '-C' denote the results from untreated and cryotreated tools respectively.

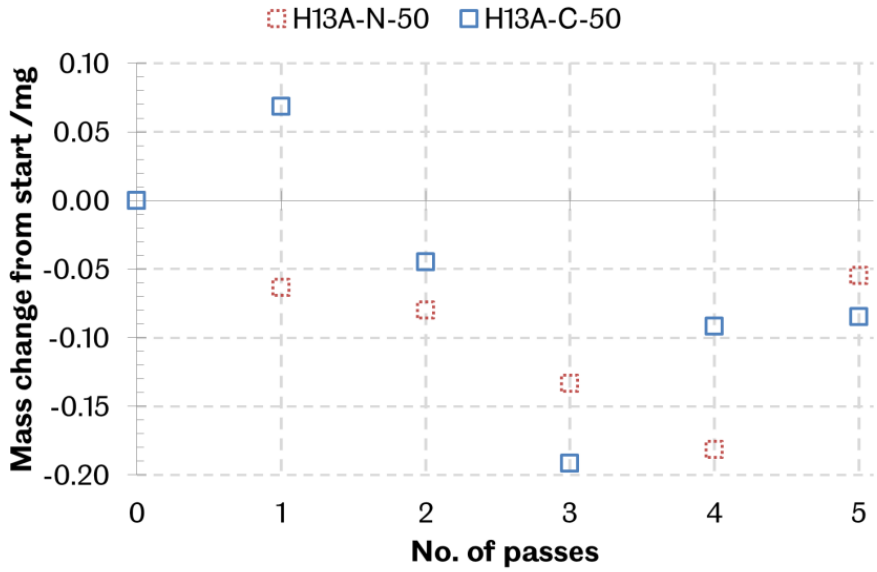

Figure 69 - Change in insert mass during machining at 50m/min, where '-N' and '-C' denote the results from untreated and cryotreated tools respectively.

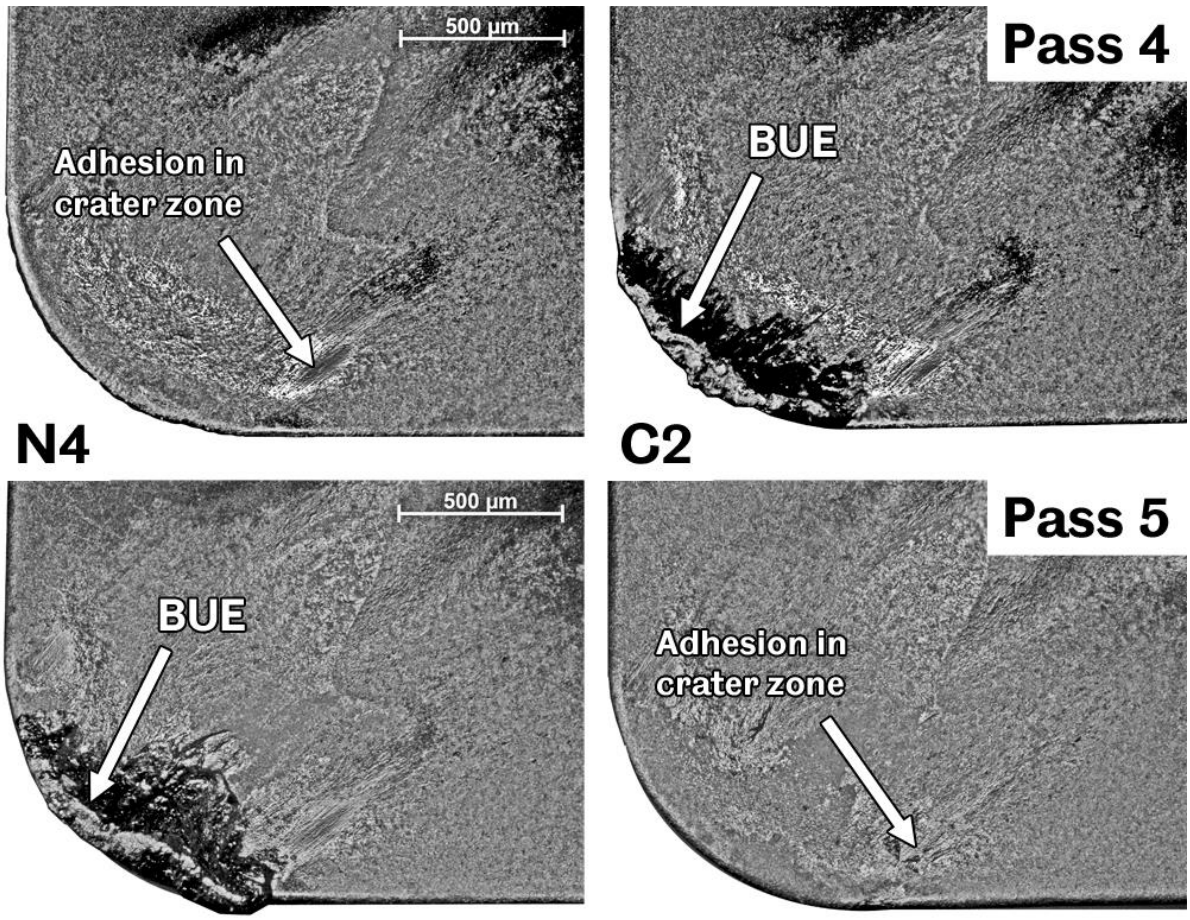

Figure 70 - Rake face micrographs showing workpiece material adhesion and BUE in latter stages of testing at 50m/min.

While crater wear was observed on inserts after testing at 95 and 140m/min, its accurate measurement was prevented by the development of large BUE and the adhesion of workpiece material in the crater wear zone.

6.4.2.2. Flank wear

Flank wear was not observed on inserts during machining at 50m/min, which indicated that under these conditions the cutting fluid had effectively lubricated the tool-workpiece flank interface. At 95m/min flank wear development was determined to be steady state throughout the test (after the initial pass), with cryogenically treated inserts developing a mean of 6% less flank wear than untreated inserts (Figure 71).

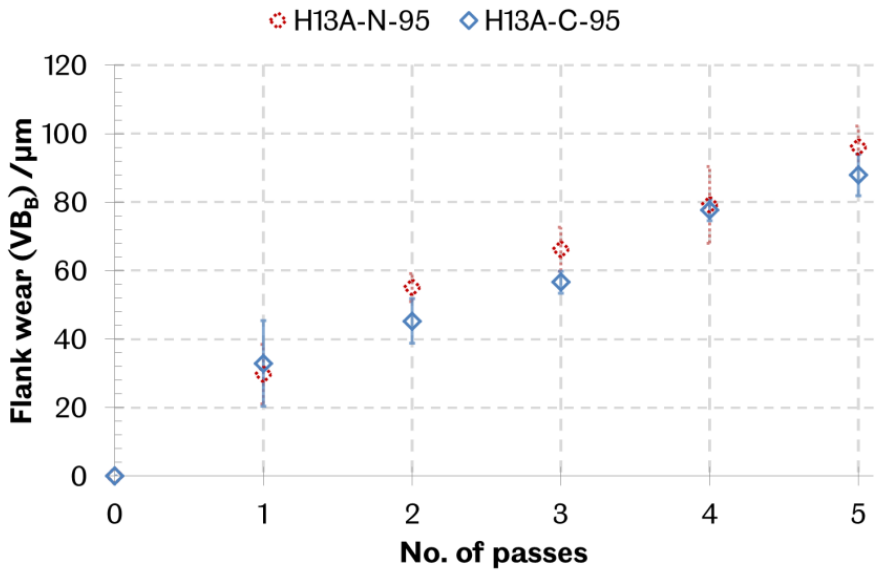

Figure 71 - Development of flank wear on inserts during machining at 95m/min, where '-N' and '-C' denote the results from untreated and cryotreated tools respectively.

While this could be taken to indicate a greater abrasive wear resistance as a result of deep cryogenic treatment, it was also determined that mean BUE heights on cryotreated tools were 19% greater than untreated tools (Figure 72). As these built-up edges often protruded from the cutting edge (Figure 74), they are likely to have protected the flank face of cryotreated tools to a greater extent, by increasing the separation and effective relief angle with the workpiece.

The increased BUE behaviour on cryotreated tools was also indicated by mass measurements (Figure 73), which showed an increased mass throughout testing. Both sets of inserts ultimately displayed no overall mass change after 5 passes (5 minutes) machining the workpiece.

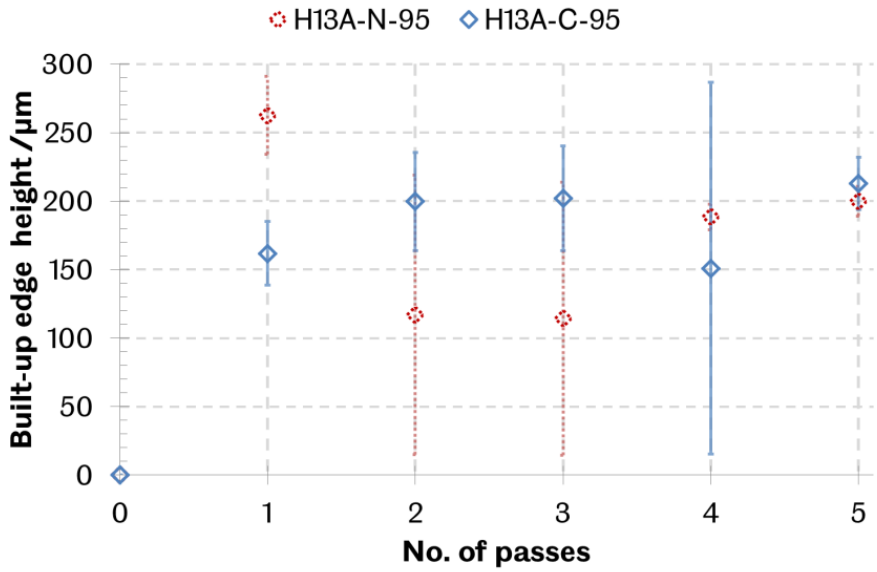

Figure 72 - Built-up edge heights recorded on inserts during machining at 95m/min, where '-N' and '-C' denote the results from untreated and cryotreated tools respectively.

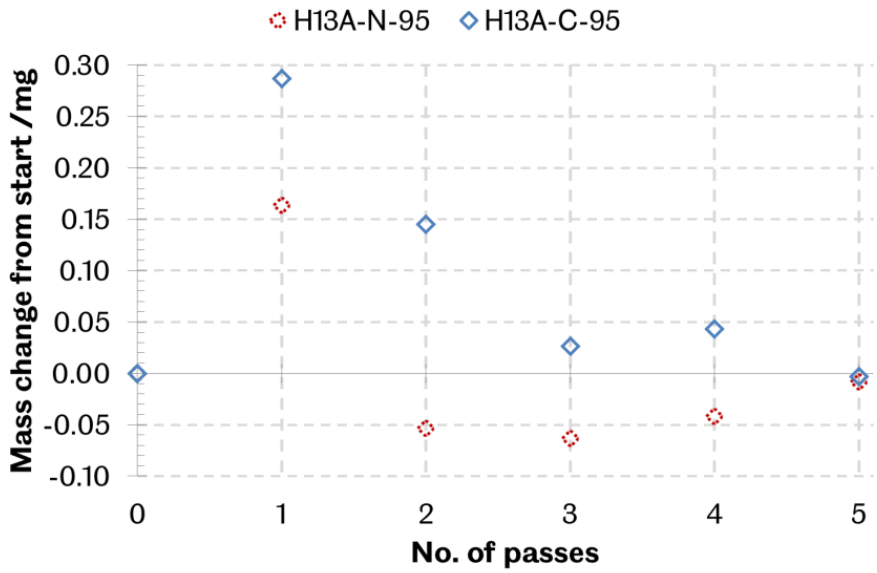

Figure 73 - Change in insert mass during machining at 95m/min, where '-N' and '-C' denote the results from untreated and cryotreated tools respectively.

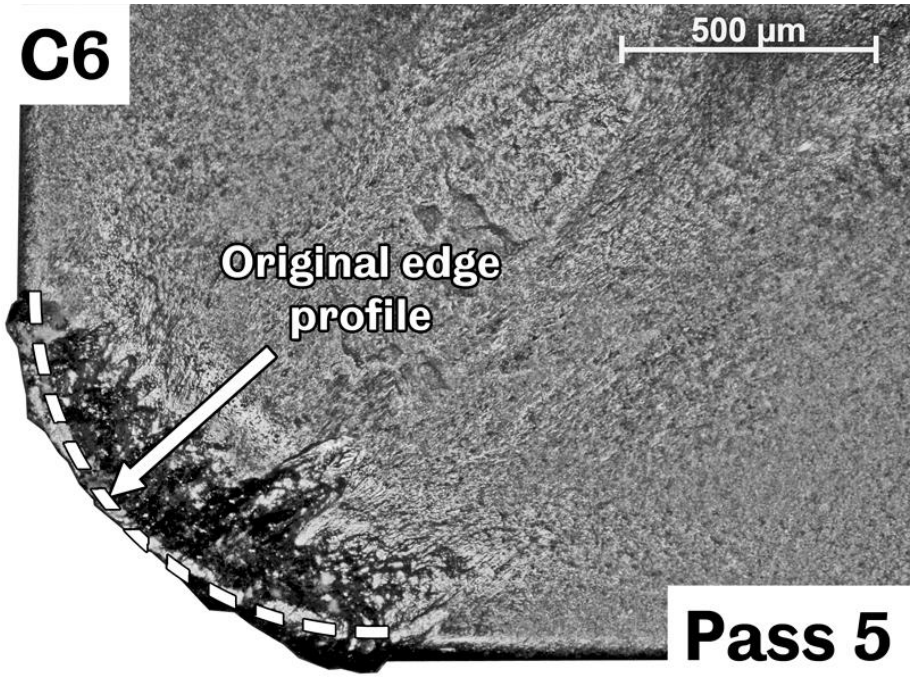

Figure 74 - Example of protrusion of BUE from cutting edge, resulting in reduced flank wear.

As well as developing flank wear, inserts tested at 140m/min also developed notch wear centred on the cutting line (Figure 75). While cryotreated inserts were shown to perform marginally better at 95m/min, at 140m/min both flank and notch wear were found to be greater on cryotreated tools (by means of 5% and 3% respectively, Figure 76). However, these differences were significantly within the standard deviations obtained from each set of repeat tests.

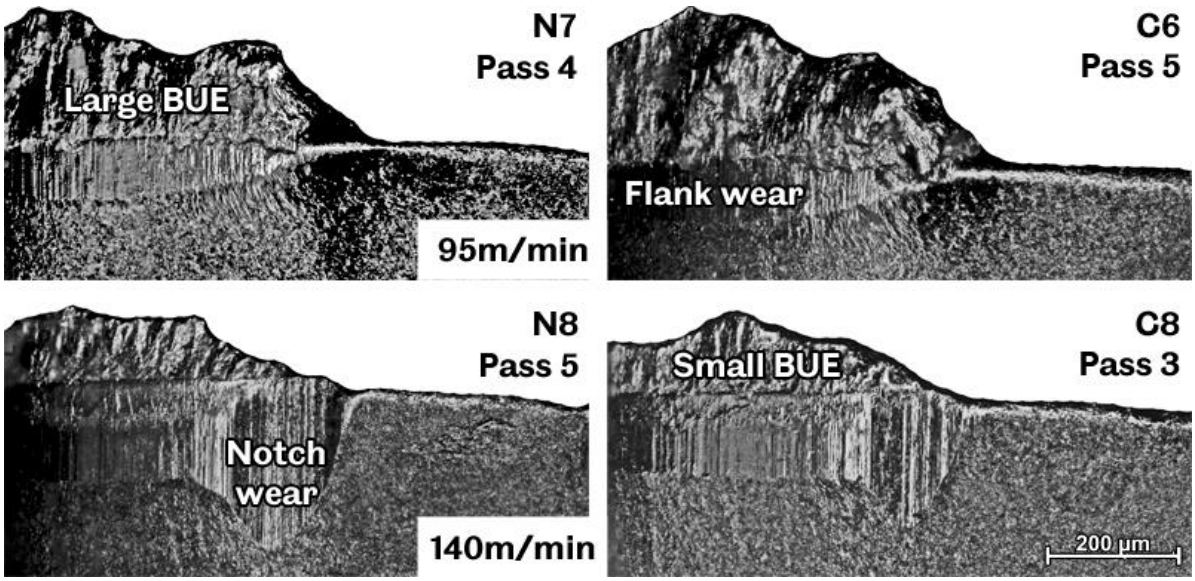

Figure 75 - Differences in flank wear and built-up edge behaviour on tools tested at 95 and 140m/min.

As with previous tests, the extent of flank wear was thought to be influenced by the development of BUE. In the case of inserts tested at 140m/min BUE heights were determined to be a mean of 12% less on cryotreated tools, although within the significant variation of BUE heights on untreated tools (Figure 77).

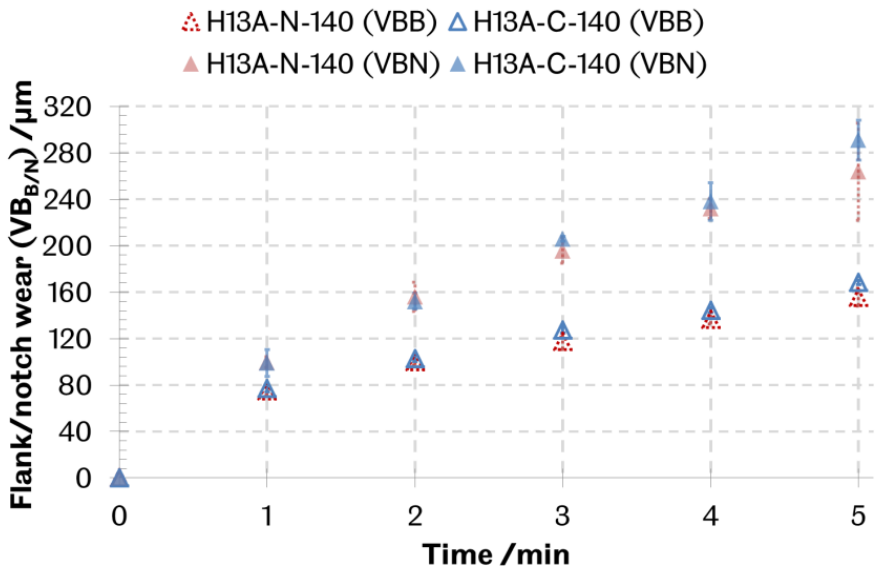

Figure 76 - Development of flank and notch wear on inserts during machining at 140m/min, where '-N' and '-C' denote the results from untreated and cryotreated tools respectively.

Of all the cutting conditions tested, only inserts used at 140m/min displayed a consistent reduction in their mass (Figure 78) that was indicative of the significance of abrasive and chemical wear mechanisms over the development of BUE and adhesion of workpiece material. This corresponds with the observations that mean BUE heights on inserts tested at 140m/min were 38% less than on inserts tested at 95m/min, and that the extent of flank wear was greater.

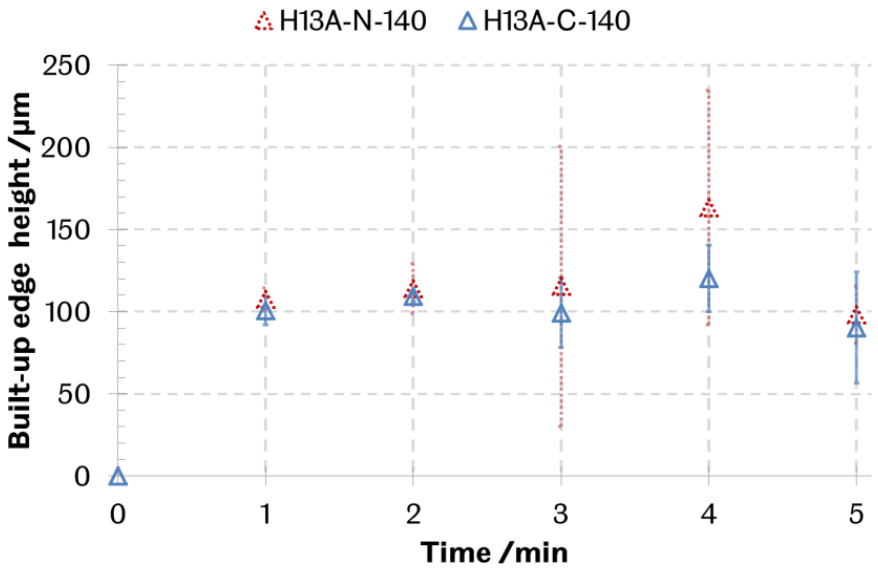

Figure 77 - Built-up edge heights recorded on inserts during machining at 140m/min, where '-N' and '-C' denote the results from untreated and cryotreated tools respectively.

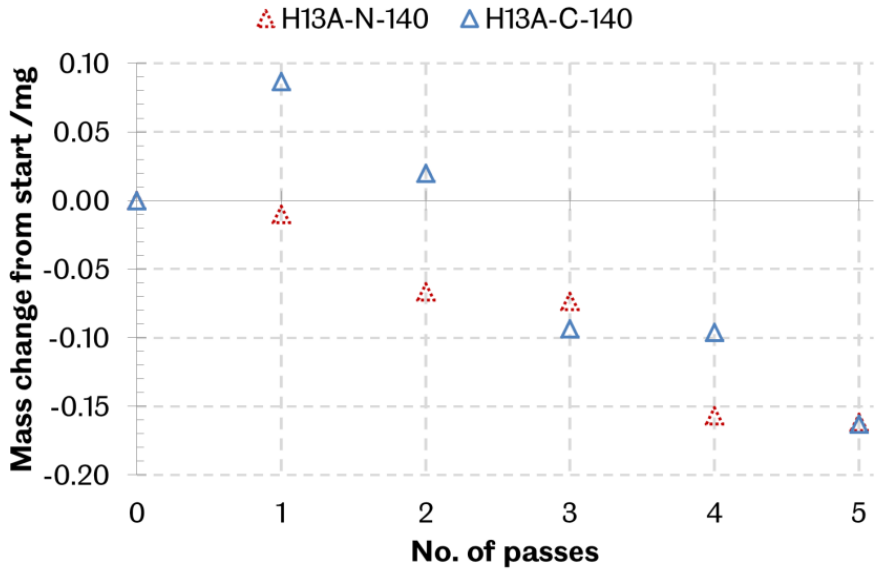

Figure 78 - Change in insert mass during machining at 140m/min, where '-N' and '-C' denote the results from untreated and cryotreated tools respectively.

6.4.2.3. Subsurface wear

Electron micrographs were generated of the key areas of subsurface damage in cutting inserts following tool wear testing, by taking cross-sections perpendicular to the flank faces of inserts, along a plane that passed through the main crater wear zone. Figure 79 shows such sections taken through an unused cutting edge, illustrating the tungsten carbide grain structure (bright) held within the cobalt binder matrix (dark) of the material, and the defects caused by carbides 'missing' from the surface.

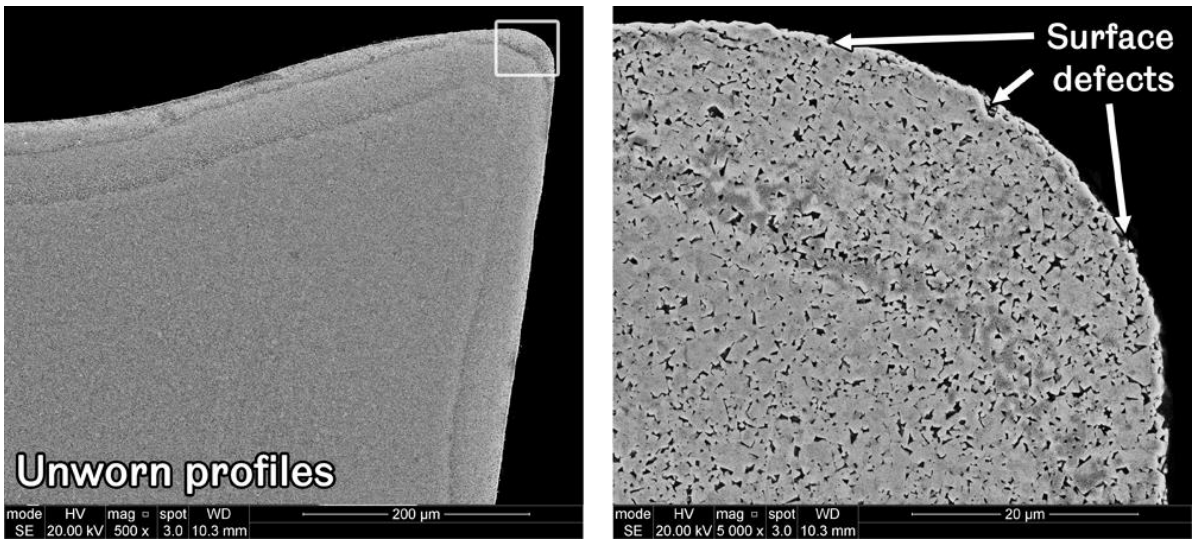

Figure 79 - Electron micrographs illustrating unworn cutting edge profile and nose surface.

In the case of inserts tested at 50m/min a number of micrographs were taken and combined, to provide images of the crater wear and nose wear subsurfaces (as illustrated in Figure 80). For inserts tested at 95 and 140m/min similar micrographs were generated for the nose and built-up edge, and flank wear regions (Figures 81 and 82 respectively).

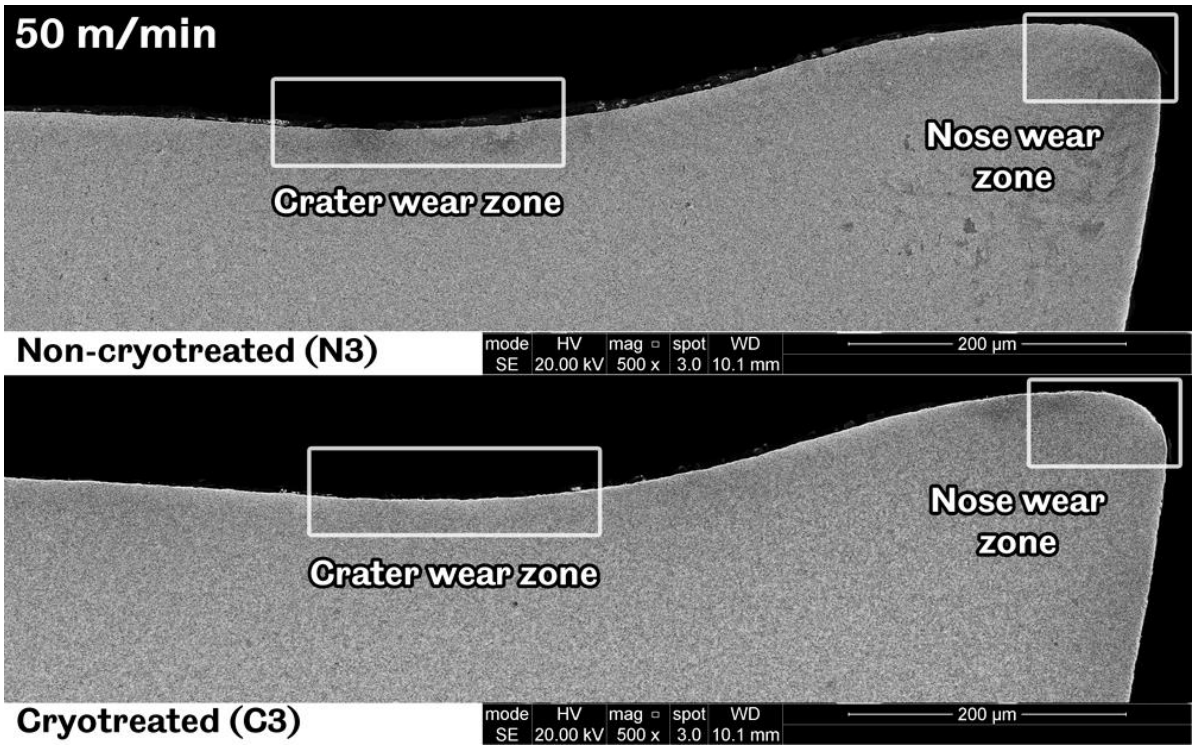

Figure 80 - Electron micrographs of insert sections after testing at 50m/min, indicating main wear zones.

Comparing the micrographs of insert sections after testing at 50m/min (Figure 80) and those after testing at 95 and 140m/min (Figures 81 and 82 respectively), it can be seen that while crater wear is visible in all insert sections, in those tested at 95 and 140m/min it is covered by an approximately 10µm thick tribofilm. Comprised of steel fragments (from the workpiece) and torn out tungsten carbide grains, this film would

be responsible for significant abrasion of the insert surface under the sliding action of newly formed chip.

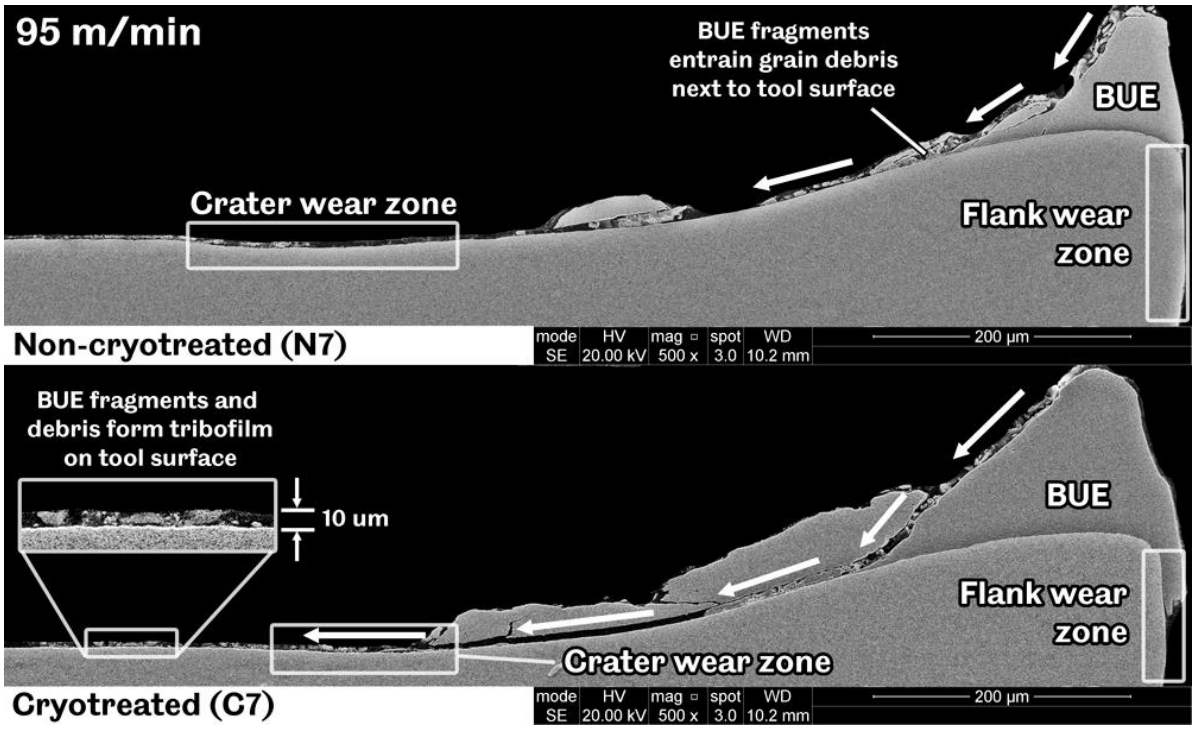

Figure 81 - Electron micrographs of insert sections after testing at 95m/min (arrows indicate motion of steel fragments and tungsten carbide grains that form tribofilm).

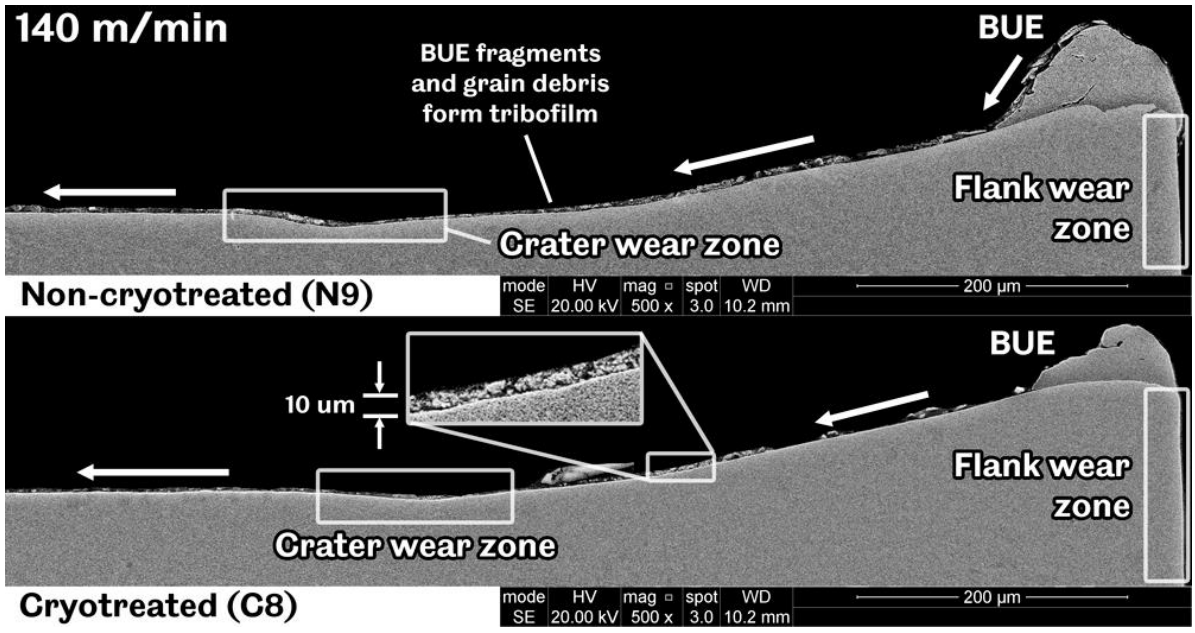

Figure 82 - Electron micrographs of insert sections after testing at 140m/min (arrows indicate motion of steel fragments and tungsten carbide grains that form tribofilm).

Sections taken from inserts after testing at 95m/min (Figure 81) confirm the BUE height measurements made (Figure 72) and illustrate the greater bulk of workpiece material adhered to the nose of the cryotreated cutting tool. While it appears as though the BUE quickly separated from the tool material (apart from some small fragments) in the case of untreated inserts, substantial amounts of steel are seen to intrude into the crater wear zone of the cryotreated tool section. Less difference is

apparent between the BUE on untreated and cryotreated inserts after testing at 140m/min (Figure 82), although it is subsequently shown in Figure 85 that the interaction between the tool and workpiece material appears markedly different.

Observations of the nose wear subsurface zone of inserts after testing at 50m/min (Figure 83) revealed a greater frequency of instances of grain removal in untreated inserts, resulting in a smoother cutting edge in cryotreated inserts after testing. Overall the structure of the materials appeared similar in these regions, except for evidence of the grain structure becoming more compacted (grains moving closer together and therefore the cobalt matrix deforming) in the near surface region of cryotreated inserts, that was not apparent from untreated inserts.

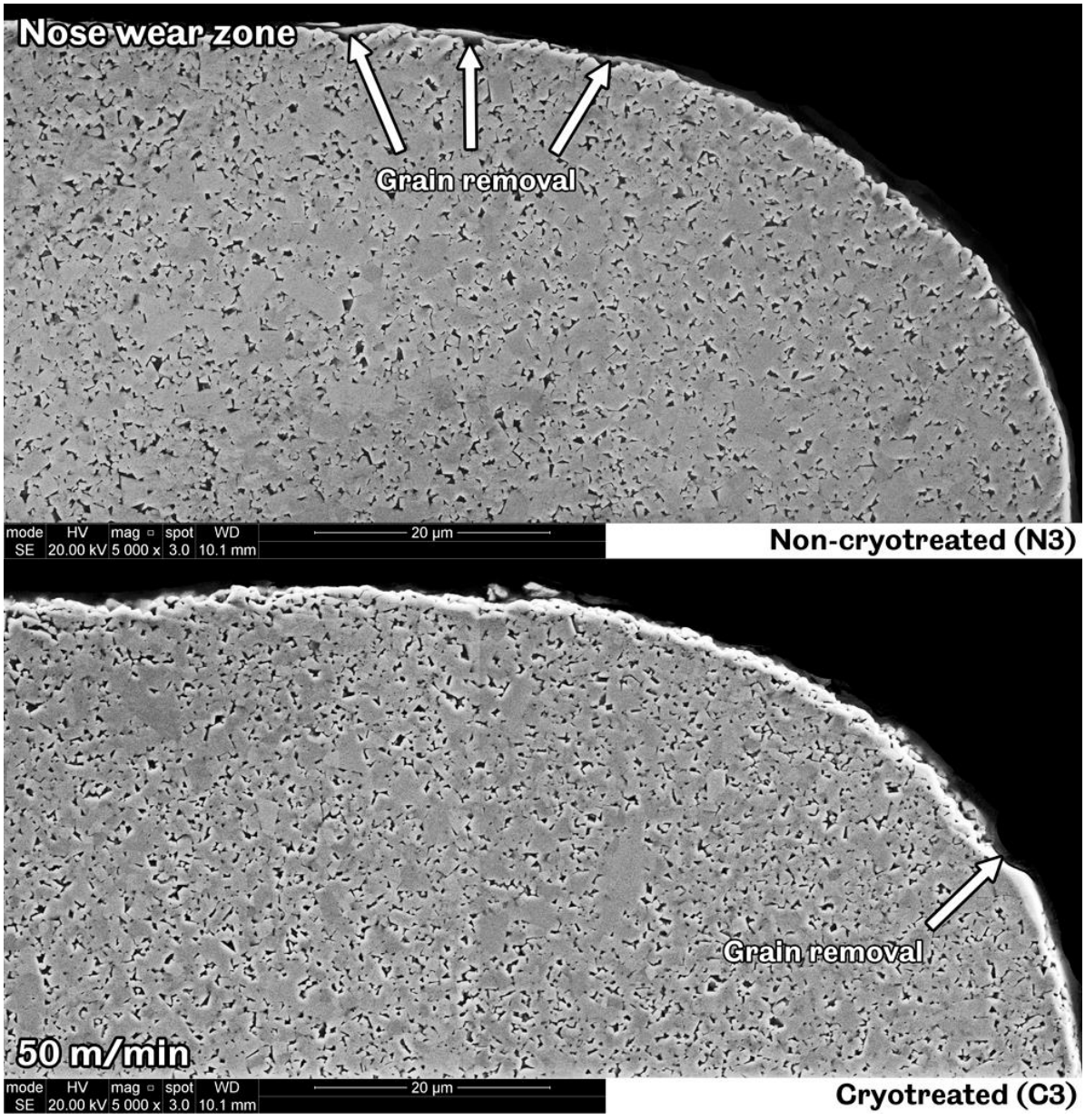

Figure 83 - Electron micrographs of insert nose sections after testing at 50m/min.

Similar observations were made from electron micrographs taken of the crater wear regions of inserts after testing at 50m/min (Figure 84), with the untreated material

having suffered more grain removal from the surface and with the near subsurface appearing to have started to break up as a result. By contrast the surface of cryotreated inserts in the crater wear zone appeared smoother, with the grain structure in a 3 – 5μm layer near the surface having been compacted.

It should be noted that the increased brightness of the surface layer and the 'glow' seen at the tungsten carbide – cobalt interfaces, in the micrographs presented of cryotreated specimens, is not as the result of inconsistent sample preparation or the effects of digital enhancement. Pairs of inserts from each cutting speed (one untreated and one cryotreated) were prepared identically to one another and imaged using the same microscope parameters. In all cryotreated specimens this increased brightness, suggesting a change in electrical conductivity, was observed. The significance of this is discussed in Section 6.5.

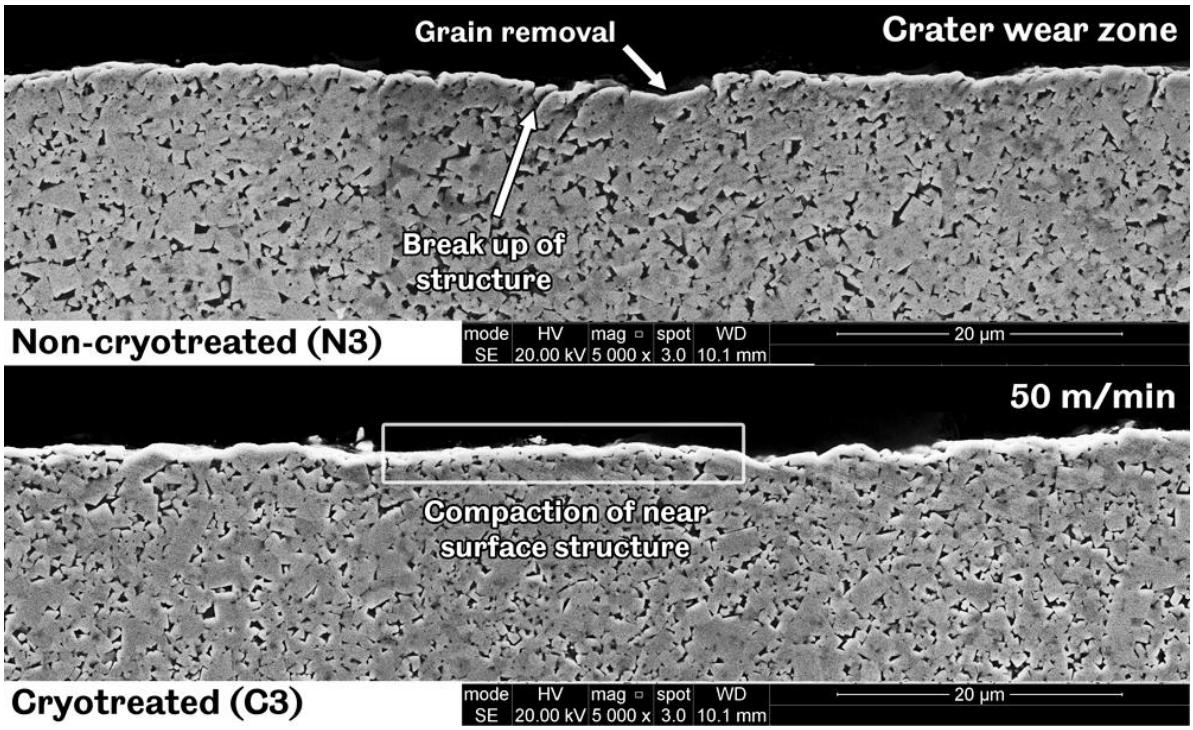

Figure 84 - Electron micrographs of insert crater wear zones after testing at 50m/min.

Examining the built-up edge and insert nose wear behaviours in more detail yielded further insights. Figure 85 shows a number of magnified sections of the nose areas of the cutting tool sections shown in Figures 81 and 82, illustrating the state of the cutting edge, the point of separation between the BUE and tool material, and the 'tail' of the BUE where grain debris become entrained with fragments of the workpiece material.

Similarly to the observations made of crater wear sections, untreated inserts were observed to show greater evidence of carbide grain removal than cryotreated inserts in the nose region after testing at 95m/min (Figure 85, (a) and (b) respectively). Evidence of greater adhesion between workpiece material and cryotreated insert was also seen. Whereas the built-up edge began to break up and separate from the

untreated inserts away from the nose, in the cryotreated insert examined this point marked the start of a substantial crack propagating through the material. It was noted that the size of the BUE increases the separation between the point of application of the cutting force and the bulk of the tool material resisting it. The possible consequences of this are discussed in Section 6.5.

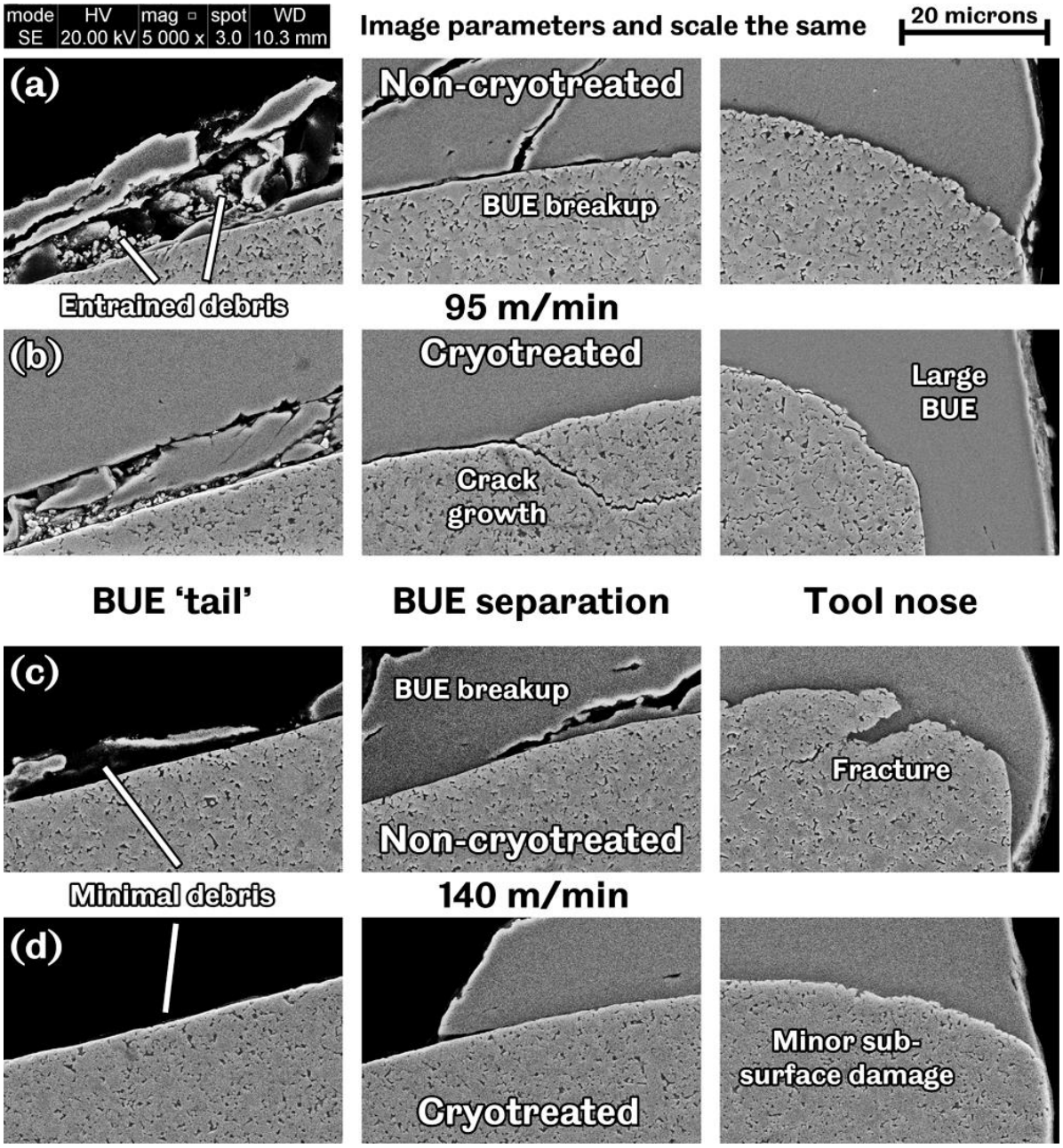

Figure 85 - Electron micrographs of nose and built-up edge sections in untreated and cryotreated inserts after testing at 95m/min (a and b respectively) and after testing at 140m/min (c and d respectively).

Tungsten carbide debris entrainment was observed in the 'tail' of the built-up edge in both untreated and cryotreated samples, although, as previously described, with a greater amount of BUE fragments in the case of the cryotreated sample.

After testing at 140m/min the observed built-up edges were smaller in both untreated and cryotreated inserts (Figure 85, (c) and (d) respectively). In the nose region the

untreated insert had begun to fracture, with a crack propagating further into the material, with closer investigation revealing that this crack was propagating through the cobalt binder. Possible causes of this are discussed in Section 6.5.

By contrast the subsurface of the cryotreated inserts showed only minimal signs of wear, with some grain removal and structure compaction, but no severe damage. The tendency for the workpiece material to adhere to the cryotreated insert material rather than break up (as when separating from the untreated insert) was seen again, although in neither case was a significant BUE 'tail' or entrainment of carbide debris observed.

The subsurface of tool flank faces appeared similar in all cases, with a smooth edge (when viewed in section) and some compaction of the grain structure near the surface. The only differences (as reported in Section 6.4.2.2) were in the extents of flank wear observed.

6.4.3. Microstructural observations

Electron micrographs taken of the as-polished microstructures of unused H13A insert materials (Figure 86) suggested that deep cryogenic treatment had modified the cobalt binder. In the cryotreated insert greater lengths of the tungsten carbide grain boundaries were visible, based on the visual assessment of a number of micrographs taken of insert microstructures away from (heat-affected) cutting edges. This is suggestive of the cobalt binder being more readily removed by the action of the polishing media. However, it was not possible to quantitatively assess this change based on the samples available. To do so, it is suggested that the mechanical properties and microstructures of higher cobalt-content carbides should be tested and analysed.

Without further characterisation, of both the phase composition and residual strain of the binder phase (i.e. by X-ray diffraction), it is difficult to suggest what changes may have taken place and therefore what effect this would be expected to have on the performance of the cutting insert. Hypothetically, an increase in abrasive wear resistance of the material could be caused either by some form of microstructural refinement or by applying a compressive stress on the tungsten carbide grains (which were not observed to expand or contract, and which were presumed to be in equal quantities and size distributions in each sample), in doing so preventing grain pull-out from occurring as readily. However, to cause this would require either an expansion of the cobalt phase, which is thermodynamically unlikely given the extreme low temperatures involved, or perhaps a precipitation of fine carbides from it. This second change seems more likely and it would also have resulted in a loss of toughness, as a result of less solid solution strengthening, while reducing the effective mean free path

length in the binder phase. These proposed changes could therefore explain the observations made of crater wear and nose wear after testing at 50m/min (with untreated inserts displaying greater evidence of grain removal) as well as those made of subsurface crack propagation in cryotreated inserts after testing at 95m/min.

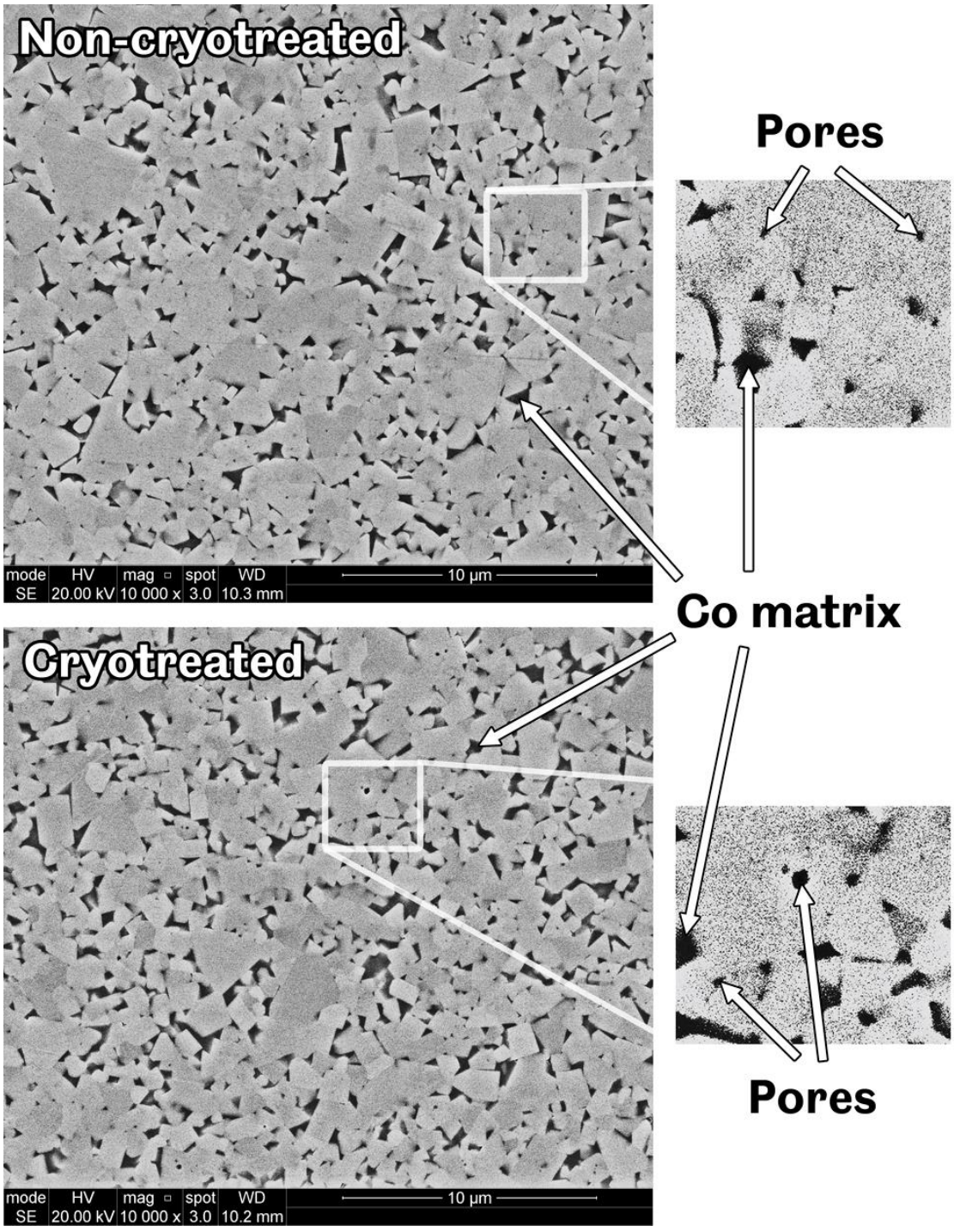

Figure 86 - Electron micrographs showing polished microstructures of H13A inserts tested with tungsten carbide grains (bright), cobalt binder phase (dark) and porosity.

6.5. Discussion

Turning testing to assess what effect deep cryogenic treatment had on the surface and subsurface wear development of H13A tungsten carbide cutting inserts, when used to

machine AISI 1045 / EN8 plain carbon steel in in the fully lubricated condition, indicated an improvement in abrasive wear resistance along with evidence of a decrease in toughness. With a fixed depth of cut of 0.5mm and a fixed feed rate of 0.2mm/rev, a variety of dominant behaviours were observed. These are summarised along with references to their related figures in Table 43.

Table 43 - Summary of wear behaviours seen on H13A inserts during machining tests.

Cutting speed /(m/min)	Surface behaviours *Subsurface behaviours*	Figure references
50	Crater wear; cutting edge wear; abrasion *Grain removal; compaction of grain structure*	68, 70 *80, 83, 84*
95	Flank wear (abrasion); built-up edge *Grain removal; compaction; crack propagation*	72, 73, 74, 75 *81, 85*
140	Flank and notch wear (abrasion); built-up edge *Grain removal; crack propagation; fracture*	75, 76, 77 *82, 85*

Overall cryotreated inserts displayed greater abrasive wear resistance. After testing at 50m/min, unlike on untreated inserts there was no visible cutting edge wear on cryotreated inserts and less instances of tungsten carbide grain removal in the crater wear zone. After testing at 95m/min the mean extent of flank wear on cryotreated inserts was 6%, less, with less evidence of grain removal than in untreated inserts. While grain removal was clearly visible from the nose of cryotreated inserts after testing at 140m/min, the extent of this was limited and the tool had not suffered catastrophic damage due to fracture like the untreated insert observed. Based upon the observation made that the crack was propagating through the cobalt binder phase, it is suggested that a concentrated loss of tungsten carbide grains from the surface (by abrasion or dissolution into the workpiece material) at the nose of the tool, which exposed the weaker cobalt binder, may have allowed the initiation of this crack that resulted in the subsequent fracture.

The combination of surface and subsurface observations of the BUE behaviour suggested a change in the interaction between the tool and workpiece material. After testing at 95m/min mean BUE heights were determined to be 19% greater on cryotreated tools than on untreated tools. Subsurface observations indicated that, rather than break up and separate from the tool surface, after testing at 95m/min a significant amount of workpiece material would remain close to the cryotreated tool surface.

Although mean BUE heights were greater on untreated tools during testing at 140m/min, they also displayed significantly greater variation. It was thought that the increased BUE on cryotreated inserts may have, to some extent, protected the flank face of the tools. However, subsurface cracking originating from the point of

separation between the BUE and insert material indicated that the tool had been subjected to greater stresses as a result.

It is suggested that the increased BUE would have increased the separation between the bulk of the tool material and the point of application of the cutting force, thereby increasing the shear stress it experiences. The direction of the bending moment on the tool due to the cutting force would encourage crack growth back towards the flank face of the tool, as was shown in Figure 85 (b). Based on the observations made it is thought likely that the insert in question would have suffered a partial or complete fracture of the cutting edge had testing continued.

Microstructural observations (Figure 86) suggested that deep cryogenic treatment had caused a change in the material. However, contrary to the densification of the cobalt binder reported by other investigators [72, 73] , the binder phase was observed to be more readily removed by polishing (based on numerous observations made of the polished microstructure of a number of insert samples, away from the heat-affected cutting edge). While further characterisation of the phase composition, residual strain or through high-resolution electron microscopy of the binder phase would be necessary to confirm any hypothesis, possible changes include a rejection of W, C from the binder phase, allowing new carbides to form during subsequent tempering. No significant change was observed in the tungsten carbide phase, in contrast with other investigators who have reported carbide grain swelling [73].

Suggested reasons for this lie in variations in the composition of the carbides tested, or in the heat treatment cycles applied. While the deep cryogenic treatment of H13A inserts used in the study presented here was largely similar to that applied in other studies that have reported tool-life improvements [73], there is much greater variation in the tempering cycles applied by other investigators (from no temper [72, 73], to a single tempering cycle [present study] to double tempering cycles [87, 88]). It is theorised that any growth of tungsten carbide grains following cryogenic treatments is dependent on the temperature and duration of these tempering cycles, although it is acknowledged that no clear correlation between these factors and reported changes in performance is apparent from the literature.

Although no clear microstructural changes were been observed, an increase in wear resistance could be caused by a compressive stress applied to the tungsten carbide phase resulting from either an expansion of the binder phase (which, in the author's opinion, is thermodynamically unlikely) or the precipitation of fine carbides which may induce a residual strain. However, such a change would also reduce the effect of solid solution strengthening, and reduce the mean free path length, in the binder phase.

This supports the evidence of the propagation of cracks through the cobalt binder in some cryotreated insert sections (Figure 85 (b)).

Although not directly observed during the present study, other investigators have reported an increase in the number of hard eta-phase precipitates due to cryogenic treatment [35, 71], which may improve abrasive wear resistance. However, without sufficient refinement these precipitates are also likely to reduce toughness and indeed, it is common industrial practice to try and minimise their formation.

Enlarged carbide grains reported by other investigators resulted in a more contiguous microstructure that has been suggested to improve thermal conductivity [73]. As this was not observed in the present study it may therefore be suggested that the ability of cryotreated H13A to remove heat from the cutting zones is reduced, leading to higher cutting temperatures, likely greater dissolution of the tool material into the workpiece and perhaps greater adhesion between the materials.

While numerous tool-life studies have been reported by other investigators [73, 87-90], none have examined the development of wear in cryogenically treated tungsten carbide tools to the same extent as in the present study. As the cutting conditions have a critical effect on the life of tools it is important that changes in wear behaviours and tool-workpiece interactions as a result of cryogenic treatments are understood.

As previously discussed in Section 3.5.2, the measurement of crater depths carried potential errors of ±6µm (Equations 3.10-3.13). Clearly errors of this magnitude could have a significant effect on the conclusions drawn from the results of testing at 50m/min, although the low coefficients of variation seen between repeats (3 – 15%) adds confidence that the results from the two sets of inserts are comparable.

It is also noted that complete characterisation of a material requires further analyses than the comparative microstructural observations presented. As highlighted in Section 3.5.3 information about material phase compositions and crystal structure are necessary for this purpose, along with higher magnification imaging to observe changes in fine carbide precipitates. Relating to the present study, energy-dispersive spectroscopy would allow for an evaluation as to whether the contribution of diffusion to the wear of cutting tools was effected by cryogenic treatment. By taking measurements from the bulk and near surfaces of the cutting tools (similar to measurements made by Gisip et al. [97]) and built-up edges, changes in chemical distribution could be determined. Although these types of analyses were beyond the constraints of the present study, they are discussed in the context of further investigations in Section 7.5.

6.6. Conclusions from tool wear development testing

20 SHM H13A (SCMT 120408 –KM) were used in a study to determine the effects of deep cryogenic treatment on the wear development of cobalt-bonded tungsten carbide inserts when machining AISI 1045 (EN8) steel. Cutting fluid was used to flood the contact, with a fixed feed rate and depth of cut of 0.2mm/rev and 0.5mm respectively. The cutting speeds over which testing was conducted were 50, 95 and 140m/min ±10%. It was determined that deep cryogenic treatment resulted in:

- An increase in hardness of 9.2% based on a sample of 30 measurements from three untreated and 30 measurements from three cryotreated inserts, with resulting coefficients of variation of 15.6% and 15.5% respectively.
- A reduction in the abrasive wear of the cutting edges of inserts when machining at 50m/min, as determined by optical microscopy.
- No significant change in the extent of crater wear when machining at 50m/min, although cryotreated inserts were observed to have less subsurface wear damage such as the grain pull-out and the separation of carbides that was observed in untreated inserts.
- A mean reduction in flank wear of 6% when machining at 95m/min. This was thought to be as a result of a combination of increased abrasive wear resistance (as indicated by the less worn cutting edges at 50m/min) and an increase in the height of stable built-up edge of 19% compared to untreated inserts, which acted to protect the flank face of cutting inserts.
- An increase in adhesion between the workpiece and insert materials, as evidenced by greater built-up edges with a reduced tendency to break up and separate from the cutting tool along its rake face, when compared with untreated inserts.
- Indirect evidence of changes in the binder phase, which was observed to propagate cracks more readily following deep cryogenic treatment. An increase in abrasive wear resistance could be the result of new fine carbide precipitates in the binder phase (although these were not observable with the techniques applied in the present study) at the cost of a reduction in toughness.

While numerous studies have been published reporting on the effects of cryogenic treatments on the life of cobalt-bonded tungsten carbide cutting tools, few, if any, have investigated its effects on their wear development in detail. The findings presented here, which indicate changes in the wear performance and material interactions between uncoated H13A turning inserts and AISI 1045 (EN8) steel, begin to cast light on this important area of concern. It is also suggested that the effects of tool material composition and the entire heat treatment cycle (including post-cryotreatment

tempering) needs to be investigated to determine how to maximise the benefits of cryogenic treatments in cobalt-bonded tungsten carbides.

7. Discussion of the effects of deep cryogenic treatment

In this chapter, the evidence gathered (through wear testing and analyses) is considered and cross-referenced with published literature and the experiences of stakeholders to assess the certainties of the findings made and propose the microstructural changes and mechanisms responsible. Methodologies are then suggested for assessing the benefits of cryogenic treatments from an applications-based and a metallurgical perspective.

7.1. Summaries of findings

The studies conducted have presented mixed results on the wear performance and wear development of cryogenically treated alloys. A summary of the observed changes in sliding wear performance due to cryogenic treatment is presented in Table 44, while a summary of changes in the development of tool wear is given in Table 45.

Table 44 - Summary of changes in wear performance due to deep cryogenic treatment.

Material	Improvements	Unchanged due to DCT	Deteriorations
SAE J431 G10 grey cast iron	Abrasive wear resistance (up to 81%)	Bulk and matrix hardness Surface wear mechanisms	Self-lubricating properties
EN10083 C50R carbon steel	Bulk (+28%) and matrix (+17%) hardness Abrasive wear resistance (up to 23%)	Surface wear mechanisms	None determined by techniques employed
AISI A2 tool steel	Wear resistance (up to 26%) Less surface pitting and plastic deformation	Bulk and matrix hardness	Greater brittle fracture
AISI D6 tool steel	Wear resistance (up to 30%)	Bulk and matrix hardness	Greater brittle fracture
AISI M2 tool steel	Wear resistance (up to 31%) Less surface pitting and plastic deformation	Bulk and matrix hardness	None determined by techniques employed

Alongside these wear studies, comparative microstructural observations have been made using optical and scanning electron microscopy. A brief study using energy-dispersive spectroscopy to qualitatively determine the composition of carbides in AISI M2 tool steel was also presented. In the case of EN10083 C50R steel, transmission electron microscopy, X-ray diffraction, electron back-scatter diffraction and electron diffraction were additionally employed to characterise its microstructure. A summary of the key findings from these analyses is presented in Table 46. Each material group

(brake rotor materials, tool steels and tungsten carbide inserts) is subsequently discussed separately.

Table 45 - Changes in SHM H13A tool wear development due to deep cryogenic treatment.

Cutting speed /(m/min)	Rake face	Flank face	Subsurface
50	Decrease in cutting edge wear No change in crater wear Increase in adhesion of workpiece material	No change in flank wear (negligible under both conditions)	Decrease in grain pull-out from nose and crater wear zones Grain structure compacted near (3 – 5μm) surface
95	19% increase in BUE height Increase in adhesion of workpiece material	6% decrease in flank wear extent	Increase in BUE adhesion; decrease in BUE breakup Visible crack propagation
140	12% decrease in BUE height Increase in adhesion of workpiece material	5% increase in flank wear extent 3% increase in notch wear extent	Increase in BUE adhesion; decrease in BUE breakup No evidence of fracture (seen in untreated sample)

Table 46 - Observed changes in material microstructures due to deep cryogenic treatment.

Material	Suggested improvements	Suggested deteriorations
SAE J431 G10 pearlitic-ferritic grey cast iron	None observed by techniques employed	Distortion/shrinkage of graphite flakes
EN10083 C50 pearlitic carbon steel	None observed by techniques employed Fine grain boundary / phase interface precipitates (hypothesised)	None observed by techniques employed
AISI A2 tool steel	Increase in fine (<100nm) precipitates	None observed by techniques employed
AISI D6 tool steel	Increase in fine (<100nm) precipitates	None observed by techniques employed
AISI M2 tool steel	Increase in fine (<100nm) precipitates Alloy enrichment of carbide precipitates	None observed by techniques employed
SHM H13A cobalt-bonded tungsten carbide	Compressive stress on tungsten carbide grains (hypothesised)	Less contiguous microstructure

7.2. SAE J431 G10 and EN10083 C50R brake rotor materials

Although the grey cast iron (SAE J431 G10) and carbon steel (EN10083 C50R) tested had significantly different chemical compositions, they bore some microstructural similarities in as much as they both contained ferrite and pearlite. In the case of G10 ferrite was observed to occupy only a small volume (perhaps 5%, estimated from Figure 50), with a range of pearlite structures (with observed interlamellar spacings ranging between 0.5 – 4μm) occupying the majority of the remainder. These were

interspersed with graphite flakes, typically of around 50µm length and 5µm thickness when viewed in section. In C50R the ferrite content was greater (10 – 15%, estimated from Figure 52) with the remaining volume occupied by coarse pearlite (observed interlamellar spacings ranging between 1 – 3µm).

Although, in both cryotreated G10 and C50R specimens, pearlite with lesser interlamellar spacings was observed, this could not have been as a result of deep cryogenic treatment (as this parameter depends on the rate of formation of cementite lamellae from solid solution in austenite as the material is cooled below the eutectoid temperature). Rather this was part of the random variation expected from a low-cost alloy likely manufactured with loosely toleranced process parameters.

Further microstructural investigations employing SEM, TEM, XRD, EBSD and electron diffraction (Chapter 5) confirmed the absence of austenite in C50R that was theorised to offer an explanation for the increase in hardness and wear resistance, by its transformation to martensite, during cryogenic treatment. Although there were weaknesses in the studies conducted due to equipment availability and material characteristics (as discussed in Section 3.5.4), these investigations also indicated no change in the lattice parameters of the material.

However, as previously discussed (Section 4.4), it is known that a strong correlation exists between interlamellar spacing in pearlite structures and the strength and wear resistance of a material [120], with a closely packed lamellae reducing the stress concentrations that exist at the interface between hard cementite and soft ferrite, therefore reducing the likelihood for crack formation and micro-fractures to occur that initiate macroscopic wear processes. Therefore, considering the lack of evidence of any microstructural changes provided by the detailed materials characterisation that was undertaken of C50R (Chapter 5), it seems likely that, at least in part, a finer pearlite structure was responsible for some of the improvements in hardness and wear resistance seen, rather than as a direct consequence of the application of cryogenic treatment. To overcome this uncertainty further evidence is considered.

Six C50R brake discs from three different packs (of 2) were used for wear testing. One brake disc from each pack was subjected to deep cryogenic treatment while the other was kept at ambient temperature before testing. On each brake disc, a single test at each of three contact pressures (1000, 1300, 1600MPa) was conducted, resulting in three data points for each contact condition and for each treatment condition, where each data point came from a different disc. While there was substantial variation (standard deviations of approximately 20% of the mean values) in the results obtained, there was a clear trend in all cases that the cryotreated rotors had suffered less wear volume loss (by 14, 12, and 23% at each contact pressure

respectively). Due to the selection method it is therefore considered highly unlikely that this was as a result of manufacturing variation. Similarly, hardness measurements were taken from three different specimens, which again suggested that cryogenic treatment rather than manufacturing variation was responsible for the changes measured (+28% and +17% increases in bulk and matrix hardness respectively).

It should be noted, however, that the further characterisation undertaken (Chapter 5) was not able to exhaust all possibilities for microstructural change in C50R. In particular, grain boundaries present locations where fine precipitates could cause significant changes in the performance of the bulk material, for instance by 'pinning' grains together and preventing easy sliding along these interfaces, and therefore restricting bulk deformation and improving mechanical properties such as hardness and abrasive wear resistance. Unfortunately, attempts to probe these regions were unsuccessful, so these locations remain a priority for further investigation.

The results from G10 brake rotor materials are more uncertain, due to differences in the testing methodology and because of the added complexity of its microstructure and wear behaviour. Unlike testing with C50R, there were no direct repeats of tests on G10 brake rotors. Instead brake rotors were tested at different contact pressures (375.0, 565.5, 750.0MPa) and sliding speeds (1.34, 1.78, 2.24m/s) until measurable volumes of wear had formed. In addition to this, the results obtained and observations made suggested that there were different factors contributing to the apparent wear resistance; in particular the self-lubricating properties given to grey cast iron by its graphite flakes. As they shear they form a soft, thin film in the contact that reduces the coefficient of friction and rate of wear [112].

As wear scar observations indicated no change in the dominant wear mechanisms of any of the tested specimens (where measurable wear volumes were present), the effect of the sliding speeds selected was considered to be negligible. When comparing measured changes in wear rates it was observed that the benefits of cryogenic treatment decreased with increasing sliding distance (Figure 40). As discussed in Section 4.4, this was explained as follows:

- Over small sliding distances, the abrasive wear resistance of grey cast iron is governed by the pearlite-ferrite structure. Although cryogenic treatment does not directly affect this structure, grain boundary changes (such as has been hypothesised for C50R) could be responsible for increasing its abrasive wear resistance;
- As sliding distance increases, the graphite film formed by the wearing of the graphite flakes starts to act to lubricate the contact. In the case of cryogenically treated grey cast iron these graphite flakes appeared to have deformed, which

may prevent their clean and consistent shearing along basal planes, and stop particles of sufficient size necessary for its self-lubricating properties being produced.

This process is supported by the studies of Sugishita and Fujiyoshi [112], which demonstrated that the coefficient of friction and wear rate in grey cast irons is dependent on both load and speed. At higher loads and speeds the graphite film covering the grey cast iron surface broke down or was displaced, exposing the material to greater contact with the wear inducing body. In a recent study by Ghasemi and Elmquist [121], a 'closing mechanism' was described whereby under abrasive wear conditions, plastic deformation of the surrounding ferrite and pearlite obscures graphite flakes from the surface, thereby contributing to an increase in friction and rate of wear. This supports the deterioration in the wear resistance of SAE J431 G10 over longer test durations, as a result of the deformation of its graphite flake structure, and a reduction in its self-lubricating properties. One other factor not previously considered, was that of humidity. Previous work has shown that the coefficient of friction with a self-lubricating cast iron increases substantially with atmospheric moisture content [122]. However, the unavailability of a humidity-controlled testing environment or humidity monitoring during testing prevents this factor from being anything but an additional uncertainty.

It is acknowledged that, even considering the effect of sliding speed to be negligible in this case, the methodology adopted (that of running tests until a significant amount of wear had occurred) resulted in a large number of data points over small sliding distances (<2000m) and only two data points over larger sliding distances (>9000m). Considering the measured improvements in wear performance against the 'tribological stress' or product of contact pressure and velocity (Figure 41) supports the argument that deep cryogenic treatment benefits the material under more severe contact conditions as described. However, this assessment suffers the same uncertainty as those previously discussed in that there were insufficient data points for this to be considered a conclusive trend.

7.3. AISI A2, D6 and M2 tool steels

With the vast majority of published work focusing on hardened, largely martensitic steels, it has been suggested that the improvements seen in wear resistance and hardness is as a result of two key microstructural changes:

- The reduction or elimination of retained austenite by conversion to martensite;
- The increased precipitation, dispersion and refinement of secondary carbides.

There is little published work investigating the effects of cryogenic treatment on alloys with large ferrite or austenite contents, such as those presented here. An exception to this is the work of Jaswin et al. [80] who reported on the cryogenically-induced martensite transformation in bulk austenite in 21-4N valve steel. Although it is difficult to compare this material (due to the significant differences in composition and heat treatments) with the tool steels tested, it is possible that such a transformation was prevented by the stabilisation of the austenite phase during the extended period between casting and cryogenic treatment. Recently highlighted by Gill et al. [6], Gulyaev reported such an effect in an early study of sub-zero treatments on high speed steels, suggesting that room temperature aging prevented the complete transformation of austenite to martensite even at cryogenic temperatures [123]. When also considering the work of Gavriljuk et al. [95], who suggested that there is a lower temperature limit for the martensitic transformation to occur during cryogenic treatment, it is possible that both room temperature aging and the treatment parameters employed may have prevented any significant transformation from taking place in the materials tested.

Similarly, the precipitation of carbides reported in the literature focuses on those carbides forming from cryogenically treated martensite, with investigators reporting that cryogenic treatment forms martensite with different lattice parameters and occupying smaller domains, with finer twinning [94, 96] which decomposes when held at cryogenic temperatures, resulting in the nucleation of numerous sub-micron carbides [61]. As argued by Tyshchenko et al. [94], post-cryogenic treatment tempering is necessary for the effective precipitation of these fine carbides, which are suggested to be enabled by the plastic deformation of martensite at cryogenic temperatures, causing the transport of carbon atoms by the movement of dislocations [95]. This dependence on the movement of dislocations (and therefore time-dependence) could be used to explain the findings of other investigators that the number of fine carbides precipitated is dependent on the duration of the cryogenic treatment soaking period [61, 62].

While important, these findings do not explain the increased precipitation of carbides seen from the cast and cryotreated specimens examined here. However, similar arguments could be made for the austenite found in cast tool steels. At cryogenic temperatures carbon atoms and carbide forming elements are rejected from the austenitic matrix and transported by the movement of dislocations caused by plastic deformation of the material. Upon subsequent tempering, these atoms nucleate new precipitates, whose number and rate of growth is dependent on the tempering parameters used. At these low temperatures, even using shifting dislocations, movements could only be expected on the order of atomic spacings. Due to the

relatively short time periods involved for tempering samples in the present study, the necessary diffusion processes allowing large numbers of these newly liberated carbon atoms to nucleate and grow or migrate and merge would be very slow. This may explain why dramatic increases in the numbers of fine carbide precipitates (such as those seen by Das et al. [74]) were not observed in the present study.

However, it should be noted that martensite, as a supersaturated phase, would be expected to more readily reject carbon than austenite during cryogenic treatments. Taking this into consideration and noting the small numbers of specimens that were able to be comparatively imaged using SEM for this study, it would be prudent for further investigations to be conducted before robust conclusions are drawn on the microstructural changes occurring and the mechanisms responsible.

7.4. SHM H13A cobalt-bonded tungsten carbide turning inserts

Research into the effects of cryogenic treatments on cobalt-bonded tungsten carbides has been growing over the past decade, due to their importance in high volume manufacturing operations. Similarly to tool steels, investigators have tended to coalesce around a small number of changes in tungsten carbides to explain performance changes due to cryogenic treatments:

- The densification or shrinkage of the cobalt binder (β-phase), which induces a compressive stress on the WC grains (α-phase), resulting in an increase in wear resistance (by resisting grain pull-out);
- The swelling of WC grains, which reduces porosity and results in a more contiguous microstructure which improves thermal conductivity;
- The precipitation, refinement and stabilisation of hard η-phase particles, resulting in an increase in abrasive wear resistance and toughness.

While the micrographs taken of the H13A inserts tested (Figure 86) indicated a change in the cobalt binder phase, this did not appear to be the densification or shrinkage suggested by other investigators. Instead the cobalt was observed to be more readily removed by polishing in the cryogenically treated material. In itself, this does not explain the seemingly greater resistance to tungsten carbide grain pull-out observed (Figure 84 and Figure 85). However, this may be indicative of a change in the composition or residual strain in the binder phase. While this cannot be as a result of a phase transformation (such as the austenite to martensite transformation in steels, as fcc Co is stable in WC-Co materials [46]), this could result from the precipitation of some of the dissolved W, C content in Co which would alter its lattice parameters and result in new strain fields being established within the binder phase. This may, in turn, also have the effect of reducing the toughness of the material, due to a less contiguous

grain structure allowing easier crack propagation through the (now weakened) cobalt phase. The swelling of WC grains, resulting in a more contiguous grain structure reported by some investigators, was not apparent and neither was a precipitation or refinement of η-phase particles (although this could simply be as a result of making observations at insufficient magnifications). Had the necessary facilities been available, magnetic saturation and coercivity tests could have been used to measure changes in the cobalt and WC phases respectively. Briefly, the first of these techniques can be used to measure the quantity of pure cobalt in the material, from which deductions about the η-phase structure and cubic carbides can be made. The second allows for the mean WC grain size to be determined, by measuring the size of the cobalt 'pockets' in the material.

Considering the range of tool-life changes reported by investigators from -3.9 – +36% (incidentally, both by Gill et al. [87, 88]) there are clearly a range of factors that must be reflected upon. Thus far no study has been conducted with enough breadth to address the effects of material composition and treatment parameters on the performance changes seen due to cryogenic treatments. In particular, it is thought that post-cryotreatment tempering may be of significance in allowing for the nucleation and growth of fine precipitates ($Co_xW_yC_z$) in the Co phase (assuming, of course, this theory for microstructural change is observed). In the two studies already mentioned, following cryogenic treatments samples were subjected to double tempering cycles of 150°C for 6hrs, whereas the study presented here used a single tempering cycle of 170°C for 2hrs. Other investigators have used triple tempering cycles (200°C, no hold time) [71] or no tempering cycle at all [72, 73].

The precipitation and refinement of η-phase particles as a means to improving tungsten carbides is a contentious one. Industry sources would suggest that η-phase particles, or un-dissolved carbides, remain as a result of poor process control or an incorrect powder mixture, and that they only serve to reduce the toughness of the material. However, investigators argue that sufficiently refined particles can act as 'fillers' to produce a more coherent and therefore tougher matrix [87]. It is also argued that cryogenic treatment relieves stresses introduced during the sintering process [72], which industry sources again suggest would only remain as a result of poor process control.

It is suggested that some of these differences of opinion arise due to the significant variation in product quality between different carbide manufacturers. Therefore cryogenic treatment may be an economic solution to correcting flaws introduced in earlier stages of manufacturing, or it may offer its own unique benefits. To resolve these questions, both broader and more detailed studies than those currently

published in this nascent area are required. These are discussed in more detail in Section 7.5.

7.5. Methodologies for understanding the effects of cryotreatment

Research into the effects of cryogenic treatments on the properties and performance of materials has been pursued continuously for almost 40 years (in the case of ferrous alloys and primarily tool steels). In spite of this there remains a considerable amount of uncertainty as to the fundamental mechanisms responsible for the improvements in properties such as hardness and wear resistance; a point which has been consistently highlighted by reviewers [5-7, 74, 124] of this field.

The fundamental reasons for this lack of consensus result from the vast range of factors to be considered when assessing the 'benefits' of cryogenic treatments, whether these be simple increases in hardness or basic wear resistance (as may be determined by tribological testing) or improvements in component service life (with complex tribological systems and environmental conditions at work). Furthermore, it is often the case that material processing routes prior to cryogenic treatments and material compositions (both chemical and phase) are insufficiently described to allow other investigators to gauge the state of the material prior to cryogenic treatment, where this has not been explicitly analysed and reported on.

Addressing cryogenic treatment parameters themselves, the lack of agreement among the scientific community is reflected in the range of treatment parameters offered by industry (as highlighted by Table 5, Section 1.3.1). This phenomenon has a somewhat self-perpetuating aspect, in that scientific investigators (including this one) are often constrained by the treatment cycles offered by commercial providers rather than having the facilities to modify treatment parameters ad infinitum.

Of considerable variation are the post-cryotreatment tempering cycles reported in the literature and offered by industry. Based on the literature studies (Sections 1.3, 2.2) and discussions (4.4, 6.5, 7.2-7.4) presented, it is suggested that this factor needs to be thoroughly addressed by investigators, and that it is likely crucial in optimising the precipitation of sub-micron carbides in tool steels, and controlling changes in cobalt-bonded tungsten carbides, whether these are ultimately determined to be fine η-phase precipitates or other precipitates from rejected atoms from the binder phase.

Finally, the conditions of the application of cryogenic materials and components must be considered. It is apparent (particularly from the tool-life studies reviewed [73, 85-90]) that the stability of changes caused by cryogenic treatment must be assessed, so that end-users can have confidence in treated products. The problem of optimising cryogenic treatments is therefore an iterative one, where the parameters of the

applications themselves may need to be adjusted to reap the maximum benefits. Considering these key factors, an overview of the process required to optimise the use of cryogenic treatments for a particular application is given in Table 47.

Of course, complete characterisation of the mechanical and physical properties of cryogenically treated materials is also important. To predict the performance of treated materials in a wide range of applications and so that appropriate metallurgical theory can be derived to allow for the accurate modelling of these materials, experimental values of their tensile, compressive, shear and impact properties (among others) and examinations to characterise their phase composition, microstructure, and to define their crystallography are necessary. This metallurgical route is summarised in Table 48.

Of particular importance, with regards to the metallurgical route of investigation, and as evidenced by the difficulties encountered with the materials characterisation conducted on EN10083 C50R steel in the present work (Chapter 5), is the need to base (at least initial) studies of this nature around specially prepared samples. Accurate control of the chemical composition and heat treatment of these (small) samples of material will ensure consistent and repeatable microstructures, such that features like large grain sizes and strong crystallographic texture would not frustrate materials analyses. While the mechanical properties of such specimens would undoubtedly be different from (especially low cost) commercial materials, the results from such studies could still be applied to real engineering components.

Table 47 - Overview of process to optimise use of cryogenic treatment for a particular application.

Step	Title	Description
1	Select candidate materials	Choose materials to evaluate, primarily from existing compositions and after standard treatment regimes.
2	Cryogenic treatment	Apply treatments using a discrete range of parameters such as: SCT and DCT → 24h soak → no temper / temper cycle
3	Screening tests	Quick, standard tribological tests. Select most suitable: Material pairing, contact pressures and sliding speeds, replicable environmental conditions (moisture, lubrication, heat etc.)
4	Comparative analyses	Surface and subsurface analyses to compare wear mechanisms. Microstructural imaging (optical / electron microscopy)
5	Applications testing	Choosing 'best' material and cryogenic treatment from screening tests, conduct accelerated or in-service testing.
6	Optimisation	Adjust material composition, treatments and operating parameters to maximise benefits.

Table 48 - Overview of process to characterise the effects of cryogenic treatments on materials.

Step	Title	Description
1	Select candidate materials	Choose material types to evaluate, representing a range of compositions and heat treatments. Obtain and prepare samples with precise chemical compositions and heat treatments to achieve consistent microstructures and phase composition.
2	Cryogenic treatment	Apply treatments using a wide range of parameters such as: 77-193K → 1-96h soak → 0-3x tempering at 373-773K
3	Mechanical tests	Battery of mechanical tests to quantify material properties: Strength, fatigue resistance, hardness, toughness etc.
4	Microstructural analyses	Analyses to quantify phase composition, crystal and lattice structures, carbide compositions, sizes and distributions etc.
5	Applications testing	Choosing theoretically most appropriate material and cryogenic treatment from mechanical tests and microstructural analyses, conduct accelerated or in-service testing using real engineering components.
6	Optimisation	Adjust material composition, treatments and operating parameters to maximise benefits.

While these two routes bear a number of similarities, it is likely that the 'applications-focused' route (Table 47) would result in the more immediate use of cryogenic treatment to finished products and therefore has more immediate commercial value. The 'materials-focused' route (Table 48) would result in deeper understanding and ultimately enable wider exploitation of cryogenic treatments to other applications. Therefore, both are clearly essential to advancing the uses of this process.

8. Conclusions

A combination of tribological wear and tool wear development testing, surface and subsurface wear and microstructural analyses have been conducted. Through these it has been shown that deep cryogenic treatment causes a range of changes in the properties and performance of grey cast iron (SAE J431 G10), non-alloy steel (EN10083 C50R), as-cast tool steels (AISI A2, D6, M2) and cobalt-bonded tungsten carbide inserts (SHM H13A). In this final chapter, these findings are related back to the project aim and objectives, their significance summarised and the methodologies applied evaluated.

8.1. Achievements against project aim and objectives

8.1.1. Objective 1

Reviewing the state of the art in cryogenic processing and techniques, its effects on industrial important materials and the focus of current research efforts, it was determined that while numerous studies have been conducted (primarily in the last 40 years and predominantly focused on martensitic tool steels), that there were a number of gaps in research efforts and understanding.

Of particular interest it was noted that the bulk of commercial cryogenic treatments are conducted on automotive brake rotors and cutting tools, where the former had received little consideration in the published literature. While numerous tribological and tool-life tests had highlighted increased wear resistance in cryogenically treated (martensitic) tool steels, cryogenic treatment had not been considered as an option to form part of an alternative processing route to conventional hardening techniques. The last ten years have seen an increase in research investigating the effects of cryogenic treatments on cobalt-bonded tungsten carbide cutting tools, and while a number of studies had reported increases in tool-life, none had so far investigated the wear behaviour of cryogenically treated tools in detail.

Based on these findings, it was decided to investigate the effects of deep cryogenic treatment on two brake rotor materials (SAE J431 G10 grey cast iron, EN10083 C50R non-alloy steel), three austenitic tool steels (as-cast AISI A2, D6, M2) and cobalt-bonded tungsten carbide (SHM H13A) turning inserts. Basic tribological testing was selected to provide initial assessments of the brake rotor materials (by pin-on-disc method) and tool steels (by reciprocating sliding method), while a tool wear development study using H13A turning inserts in machining AISI 1045 / EN8 steel was also planned.

8.1.2. Objective 2

Laboratory-based tribological tests used to assess the relative performance of ferrous alloys (brake rotor materials and tool steels), provided comparative data indicating a range of changes due to deep cryogenic treatment. In particular, EN10083 C50R non-alloy steel and AISI M2 tool steel were found to respond favourably to the treatment.

It was determined that, in the case of SAE J431 G10 grey cast iron, deep cryogenic treatment increased its abrasive wear resistance over short (<2000m) sliding distances, but over larger distances (>9000m) its wear resistance was seen to decrease below that of the untreated material. This was judged to be as a result of microstructural changes (see Objectives 4 and 5) which reduced the ability of the material to self-lubricate, although it was acknowledged that the methodology adopted for testing left a high level of uncertainty in these findings (see Section 7.2 for full discussion).

Deep cryogenic treatment was found to significantly increase the hardness and the abrasive wear resistance of EN10083 C50R non-alloy steel under the conditions and over the test durations applied. While statistical variation in the results obscured the exact improvement achieved, a clear trend was found in favour of cryogenic treatment. As the material demonstrating the greatest and most significant improvements due to deep cryogenic treatment, C50R was selected for further microstructural characterisation (see Objectives 4 and 5). While these analyses provided no direct evidence of microstructural changes to explain these performance changes, further possibilities were theorised that could be used to support these findings.

AISI A2, D6 and M2 as-cast tool steels demonstrated an increase in wear resistance following deep cryogenic treatment. In the case of A2 and D6 the level of this improvement was between 0.8 – 2.2 standard deviations while the wear resistance improvement in M2 tool steel was more significant, with a measured changes between 5.1 – 6.8 standard deviations. Wear scar observations indicated greater brittle behaviour in A2 and D6 tool steels following cryogenic treatment, while in M2 less surface pitting and plastic deformation was apparent. Qualitative observations suggesting microstructural changes (see Objectives 4 and 5) partially supported these findings, but did not give any indications as to why deep cryogenic treatment had a significant effect on AISI M2 tool steel, but only a minimal effect on AISI A2 and D6 tool steels.

8.1.3. Objective 3

The results of workshop-based tool wear development tests provided comparative data that indicated changed wear behaviours in SHM H13A cobalt-bonded tungsten

carbide uncoated turning inserts in machining AISI 1045 / EN8 steel in the fully lubricated condition. These behaviours were found to be strongly dependent on cutting speed and presumably therefore, temperature.

At low cutting speeds (50m/min), it was observed that cryogenically treated inserts suffered no visible abrasive cutting edge wear, and that the tendency for grain pull-out in the tool nose and crater wear zones had reduced. Mass measurements suggested that the amount of adhesion of the workpiece material onto the tool surface had increased.

At cutting speeds typical of those recommended for the inserts (95m/min), a reduction in flank wear (primarily abrasive in nature) was observed, with a substantial increase in the height of built-up edges forming on the nose of the tool inserts. Subsurface observations indicated that while the increased BUE helped to protect the insert material from abrasive wear, it also increased the stress on the cutting edge, resulting in potentially catastrophic crack propagation.

At higher cutting speeds (140m/min), no significant difference in flank wear or BUE behaviour was observed as a result of deep cryogenic treatment. However, subsurface observations indicated severe grain pull-out and fracture of the untreated insert examined, with only minimal grain pull-out from the nose of the treated insert, but a greater tendency towards brittle cracking of the cobalt-binder.

8.1.4. Objectives 4 and 5

Comparative and qualitative microstructural examinations (using optical and scanning electron microscopy) were conducted on the six materials studied. Through these examinations, it was attempted to observe large scale and morphological changes due to deep cryogenic treatment.

In the case of SAE J431 G10 grey cast iron (largely pearlitic structure interspersed with large graphite flakes) and EN10083 C50R non-alloy steel (largely pearlitic with ferrite), deep cryogenic treatment was not observed (with consideration of the significant microstructural variation present in low-cost materials and components) to cause any clear changes, except from the apparent deformation of the graphite flakes in G10. On the basis of these observations the increased hardness and wear resistance measured in C50R steel could not be explained, but the deformation of graphite flakes may perhaps explain the decreased wear resistance of G10 specimens over longer distances, where the self-lubricating properties of graphite become significant.

It was theorised that the distortion of graphite flakes may simply result from the thermal contraction of the surrounding material at cryogenic temperatures, as the

strength of the graphite flakes is negligible to that of the surrounding iron matrix. This distortion may then prevent the characteristic shearing of these graphite flakes along crystallographic planes and prevent the formation of the graphite films necessary for self-lubrication. Without this lubrication the cast iron will wear rapidly, as the effective voids left by graphite flakes present pre-formed notches from which cracks can grow and facilitate material removal.

In all three tool steels tested qualitative observations suggesting new distributions of sub-micron precipitates were made, which supported the increased wear resistance measured. These were suggested to arise from the rejection of carbide formers from the austenitic matrix due to the plastic deformation occurring at deep cryogenic temperatures which, following subsequent tempering, resulted in the nucleation of new carbides. Their small size and wide distribution was attributed to the lack of energy at low temperatures to allow for the long-distance diffusion and migration of carbides. However, it was acknowledged that as austenite has a high solubility limit for carbon (unlike martensite which is a supersaturated phase), further investigations would be required to confirm this theory.

Deep cryogenic treatment was indirectly observed to cause changes in the structure of the cobalt binder, which was removed more readily by polishing prior to subsurface examinations. It was theorised that the cobalt-binder (similarly to martensite in steels) may reject dissolved W, C resulting in a reduction in solid solution strengthening. If, with subsequent tempering of the material, these rejected atoms were to form fine precipitates, a change in residual strain in the material could be expected. The resulting compressive stress on WC grains that this could cause would then explain the reduced tendency for grain pull-out in cryogenically treated inserts. However, these changes would also make the material more vulnerable to cracks propagating through the weaker cobalt binder phase interspersed with hard precipitates. To confirm these theories further characterisation of the phase composition, residual strain and microstructure of the material prior to and following cryogenic treatment and tempering is required. Further chemical analyses of the near surface areas of inserts would be necessary to confirm whether the contribution of dissolution to the wear of H13A tungsten carbide inserts due to deep cryogenic treatment had been altered.

8.2. Significance of findings

The studies and findings presented represent parts of 'applications-focused' testing frameworks that were previously outlined (Table 47, Section 7.5). The significance of the findings presented must be considered within this context. A number of important engineering materials were selected, with some subjected to tribological screening

tests (brake materials and tool steels) and others to more realistic experimental applications simulations (tungsten carbide turning inserts).

Based on the evidence discussed, further investigations into the effects of cryogenic treatments on pearlitic steels are clearly needed. Firstly, so that additional wear testing can be performed reinforce the findings presented here (through additional repeats) but under different conditions and those that more realistically replicate the applications of these materials. Secondly, samples should be prepared to allow for a robust quantitative analysis of any changes that cryogenic treatments cause in the microstructures of these materials. As discussed in Section 7.5 and summarised in Table 48, such samples would possess precisely controlled chemical compositions and small cross-sections, such that the microstructures produced during controlled heat treatment processes will be consistent and lacking strong crystallographic texture that may otherwise frustrate microstructural characterisation efforts. Similar work is required to assess the effects of cryogenic treatments on lamellar graphite cast irons, as the findings presented here indicate potentially damaging changes as a result. As discussed (Sections 4.4, 7.2), changes in graphite flake structure may reduce the self-lubricating properties and thermal performance of these materials.

From testing conducted on tool steels, there is a clear impetus to investigate the effects of cryogenic treatments on as-cast AISI M2 tool steel further. While additional tests could clarify the extent of improvement expected following deep cryogenic treatment, it may offer an alternative processing route for producing a wear resistant and tough variant of this material. Coupling cryogenic treatment with surface treatments or coatings may yield some interesting results. For instance, as highlighted previously (Section 4.1.1), it has been shown that the effective depth of plasma nitriding is greater in austenitic as opposed to martensitic AISI M2 high-speed steel [111]. Microstructural analyses must also be advanced, so that changes in phase structure and carbide sizes, distributions and compositions can be quantified.

The results of the tool wear development study using tungsten carbide turning inserts suggests that caution is needed in applying cryogenic treatments to these materials. While abrasive wear resistance and resistance to grain removal does appear to have improved, undesirable 'side-effects' were also observed. As is required before the adoption of any new tool material or coating, the acceptable operating parameters for cryogenically treated tools must be determined, to maximise their benefits while avoiding premature failures. These parameters can of course be established by more extensive tool wear and tool-life testing (using different machining parameters, lubrication conditions and workpiece materials), but should also be informed by investigating the changes that occur in mechanical properties and microstructures as a result of cryogenic treatments.

8.2.1. Evaluation of applied methodologies and analyses

Previously, specific uncertainties and errors in pin-on-disc wear volume estimations, tool wear measurements, the limitations of using energy-dispersive spectroscopy to analyse carbides and the errors resulting from poor particle statistics in X-ray diffraction have been discussed in detail (Section 3.5). Remaining uncertainties in the findings presented have been discussed following on from the results of testing (Sections 4.4, 5.4, 6.5) and by cross-referencing with published literature and industrial opinions (Chapter 7). While the majority of these limitations have arisen from resource constraints (funding for additional specimens and analyses, access to equipment etc.) and time limitations, it is acknowledged that improvements could be made to the methodologies employed.

A more comprehensive list of suggested improvements is provided in Table 49, however the areas of greatest importance for further investigation (on the basis of uncertainties in the findings presented) are:

- The use of a molybdenum- or chromium-based radiation source for X-ray diffraction of C50R steel, so that robust data can be gathered that may be used to conduct an analysis of residual strain. This technique should then be extended to AISI M2 tool steel and H13A tungsten carbide, as the other materials showing significant changes due to deep cryogenic treatment.
- The production of replicas to allow the independent study of carbides in cryogenically treated materials. Through the use of TEM-EDX examination the chemical composition of these carbides can be determined and their crystallographic structures revealed by electron diffraction.
- The use of energy-dispersive spectroscopy to study changes in chemical contributions in the near surface of SHM H13A tool inserts and adhered workpiece material, to support or refute suggestions of increased adhesion and assess the contribution of chemical diffusion to cutting insert wear behaviour;
- Further pin-on-disc testing of SAE J431 G10 grey cast iron with specific, discrete test durations to provide repeats of previous results and complete the assessment of wear performance changes with sliding distance (Figure 40).

Table 49 - Summary of suggested improvements to methodologies employed.

Technique	Suggested improvements
Cryogenic treatment	Control over treatment parameters to allow for: - Investigation of shallow (133-193K) cryogenic treatments; - Shorter and longer soaking times; - Different post-cryotreatment tempering cycles.
Hardness testing	Use of nano-indentation techniques to measure: - Changes in mechanical properties of constituent phases of materials.
Pin-on-disc testing	Use of light interferometry to scan sections of wear tracks to: - Reduce uncertainties in wear volume measurements; - Quantify changes in worn roughness, to highlight subtle changes in wear behaviours. *In the case of SAE J431 G10 grey cast iron:* - Using a range of discrete test durations to investigate stages of wear development; - Conducting repeat tests to determine experimental scatter; - Modify set up to allow for collection of friction data, to quantitatively assess suggested changes in graphite behaviour. - During testing, monitoring the atmospheric temperature and humidity as these are known to significantly effect the self-lubricating performance of graphite. *In the case of EN10083 C50R non-alloy steel:* - Additional repeats to refine experimental results.
Reciprocating sliding testing	To clarify and expand study: - Using a wide range of discrete test durations and test parameters to investigate stages of wear development and changes in wear behaviours; - Additional repeats to refine experimental results.
Tool wear development testing	To clarify and expand study: - Use of coercivity and magnetic saturation testing to evaluate changes in the cobalt binder and mean WC grain size; - Use of energy-dispersive spectroscopy to assess degree of adhesion between tool and workpiece materials and whether the contribution of diffusion processes has changed; - Additional specimens to test in continuous cutting mode, so that original results can be related to other machining applications; - Further specimens to test at intermediate cutting speeds to determine transition points between wear behaviours.
Microstructural analyses	To confirm observed changes: - Preparation and analysis of samples specifically for microstructural characterisation, to investigate what microstructure changes may occur in materials such as those evaluated in the present study, from which the mechanisms of metallurgical change may be derived. To characterise microstrucures: - Transmission electron microscopy to image nano-carbides, precipitates and particles; energy-dispersive spectroscopy and electron diffraction to characterise the chemical and crystallographic properties of such carbides; - X-ray diffraction using appropriate radiation sources to allow for quantitative phase analyses and residual strain measurements.

8.3. Publications arising from this work

The studies presented here resulted in three refereed journal papers. These are listed in Table 50 along with their related experimental chapters.

Table 50 - Journal articles arising from this work.

Authors, title, journal, year	DOI	Primary reference chapter
R. Thornton, T. Slatter, A. H. Jones, R. Lewis, The effects of cryogenic processing on the wear resistance of gray cast iron brake discs, Wear, 2011. *Presented at the 18th International Wear of Materials Conference, Philadelphia PA, USA, 2011.*	10.1016/j.wear.2010.12.014	4
R. Thornton, T. Slatter, H. Ghadbeigi, Effects of deep cryogenic treatment on the dry sliding wear performance of ferrous alloys, Wear, 2013.	10.1016/j.wear.2013.06.005	4
R. Thornton, T. Slatter, R. Lewis, Effects of deep cryogenic treatment on the wear development of H13A tungsten carbide inserts when machining AISI 1045 steel, Production Engineering, 2014.	10.1007/s11740-013-0518-7	6

9. References

1. Bond, K., *Cryogenic Treatment of Gears*, in *Gear Solutions*. 2009. p. 6.
2. Barron, R.F., *Effect of cryogenic treatment on lathe tool wear.* Progress in Refrigeration Science and Technology, 1973. **1**: p. 529-533.
3. Barron, R.F., *Cryogenic treatment of metals to improve wear resistance.* Cryogenics, 1982: p. 409-413.
4. Barron, R.F. and C.R. Mulhern, *Cryogenic Treatment of AISI T-8 and C1045 Steels.* Advances in Cryogenic Engineering, 1981. **27**: p. 20.
5. Gill, S.S., et al., *Cryoprocessing of cutting tool materials - a review.* International Journal of Advanced Manufacturing Technology, 2010. **48**: p. 175-192.
6. Gill, S.S., et al., *Metallurgical principles of cryogenically treated tool steels - a review on the current state of science.* International Journal of Advanced Manufacturing Technology, 2011. **54**: p. 59-82.
7. Collins, D.N., *Deep cryogenic treatment of tool steels: A review.* Heat Treatment of Metals, 1996. **23**(2): p. 40-42.
8. Breuer, B. and K.H. Bill, *Brake Technology Handbook*. 1st ed. 2008, Pennsylvania: SAE International. 576.
9. Bhadeshia, H.K.D.H. and R.W.K. Honeycombe, *Steels Microstructure and Properties*. 3rd ed. 2006: Elsevier Ltd.
10. Hecht, R.L., R.B. Dinwiddie, and H. Wang, *The effect of graphite flake morphology on the thermal diffusivity of gray cast irons used for automotive brake discs.* Journal of Materials Science, 1999. **34**(19): p. 4775-4781.
11. Barraclough, K.C. and I.C.H. Hughes, *Constitutent Elements in Steel and Cast Iron*. 1961, Sheffield, England: London & Scandinavian Metallurgical Company Ltd. 79.
12. Rollason, E.C., *Metallurgy for Engineering*. 3rd ed. 1965, London: Edward Arnold.
13. Honeycombe, R.W.K. and H.K.D.H. Bhadeshia, *Steels Microstructure and Properties*. 2nd ed. Metallurgy and Materials Science Series, ed. P.S.R. Honeycombe and P.P. Hancock. 1995, London: Edward Arnold.
14. Ashby, M.F. and D.R.H. Jones, *An Introduction to Microstructures, Processing and Design*. 3rd ed. Engineering Materials. 2008, Oxford, England: Elsevier Ltd. 451.
15. Cueva, G., et al., *Wear resistance of cast irons used in brake disc rotors.* Wear, 2003. **255**: p. 1256-1260.
16. Nakanishi, H., et al., *Development of aluminum metal matrix composites (Al-MMC) brake rotor and pad.* Jsae Review, 2002. **23**(3): p. 365-370.
17. Hutton, T.J., B. McEnaney, and J.C. Crelling, *Structural studies of wear debris from carbon-carbon composite aircraft brakes.* Carbon, 1999. **37**(6): p. 907-916.
18. Jang, G.H., et al., *Tribological Properties of C/C-SiC Composites for Brake Discs.* Metals and Materials International, 2010. **16**(1): p. 61-66.
19. Blau, P.J., et al., *Tribological investigation of titanium-based materials for brakes.* Wear, 2007. **263**: p. 1202-1211.
20. Roubicek, V., et al., *Wear and environmental aspects of composite materials for automotive braking industry.* Wear, 2008. **265**(1-2): p. 167-175.
21. Blau, P.J., *Compositions, Functions, and Testing of Friction Brake Materials and Their Additives*. 2001, Oak Ridge National Laboratory: Oak Ridge, Tennessee. p. 29.
22. Eriksson, M., F. Bergman, and S. Jacobson, *On the nature of tribological contact in automotive brakes.* Wear, 2002. **252**(1-2): p. 26-36.
23. Oehl, K.H. and H.G. Paul, *Bremsbeläge in Straßenfahrzeugen*, in *Bibliothek der Technik*. 1990, Verlag Moderne Industrie AG & Co: Landsberg am Lech. p. 14-18.
24. Severin, D. and F. Musiol, *Der Reibprozeß in trockenlaufenden mechanischen Bremsen und Kuppulungen.* Konstruktion, 1995. **47**: p. 10.
25. Österle, W. and I. Urban, *Third body formation on brake pads and rotors.* Tribology International, 2006. **39**(5): p. 401-408.
26. Trent, E. and W. Wright, *Metal Cutting*. 4th ed. 2000: Butterworth-Heinemann. 464.
27. Buryta, D., R. Sowerby, and I. Yellowley, *Stress distributions on the rake face during orthogonal machining.* International Journal of Machine Tools & Manufacture, 1994. **34**(5): p. 721-739.

28. Iqbal, S.A., P.T. Mativenga, and M.A. Sheikh, *A comparative study of the tool-chip contact length in turning of two engineering alloys for a wide range of cutting speeds.* International Journal of Advanced Manufacturing Technology, 2009. **42**(1-2): p. 30-40.
29. Schulz, H. and T. Moriwaki, *High-Speed Machining.* Annals of the CIRP, 1992. **41**(2): p. 7.
30. Davoodi, B. and H. Hosseinzadeh, *A new method for heat measurement during high speed machining.* Measurement, 2012. **45**(8): p. 2135-2140.
31. Abukhshim, N.A., P.T. Mativenga, and M.A. Sheikh, *Heat generation and temperature prediction in metal cutting: A review and implications for high speed machining.* International Journal of Machine Tools & Manufacture, 2006. **46**(7-8): p. 19.
32. Zemzemi, F., et al., *New tribometer designed for the characterisation of the friction properties at the tool/chip/workpiece interfaces in machining.* Tribotest, 2008. **14**: p. 11-25.
33. Robinson, G.M., M.J. Jackson, and M.D. Whitfield, *A review of machining theory and tool wear with a view to developing micro and nano machining processes.* Journal of Materials Science, 2007. **42**(6): p. 2002-2015.
34. Rech, J., C. Claudin, and E. D'Eramo, *Identification of a friction model - Application to the context of cry cutting of an AISI 1045 annealed steel with a TiN-coated carbide tool.* Tribology International, 2009. **42**: p. 738-744.
35. Vadivel, K. and R. Rudramoorthy, *Performance analysis of cryogenically treated coated carbide inserts.* International Journal of Advanced Manufacturing Technology, 2009. **42**(3-4): p. 222-232.
36. Astakhov, V.P., *The assessment of cutting tool wear.* International Journal of Machine Tools & Manufacture, 2004. **44**: p. 11.
37. ISO, *Tool-life testing with single-point turning tools*. 1993, International Organization for Standardization. p. 56.
38. Subramanian, S.V., S.S. Ingle, and D.A.R. Kay, *Design of coatings to minimize tool crater wear.* Surface & Coatings Technology, 1993. **61**: p. 7.
39. Van Stappen, M., et al., *State of the art for the industrial use of ceramic PVD coatings.* Surface & Coatings Technology, 1995. **74-75**(1-3): p. 629-633.
40. Zhang, D., B. Shen, and F. Sun, *Study on tribological behavior and cutting performance of CVD diamond and DLC films on Co-cemented tungsten carbide substrates.* Applied Surface Science, 2010. **256**(8): p. 2479-2489.
41. Roberts, G.A., G. Krauss, and R. Kennedy, *Tool steels*. 5th ed. 1998: ASM International.
42. Gu, L., J. Huang, and C. Xie, *Effects of carbon content on microstructure and properties of WC–20Co cemented carbides.* International Journal of Refractory Metals and Hard Materials, 2014. **42**(0): p. 228-232.
43. Andrén, H.-O., *Microstructures of cemented carbides.* Materials & Design, 2001. **22**(6): p. 491-498.
44. Kalpakjian, S. and S.R. Schmid, *Manufacturing Engineering and Technology*. 5th ed. 2006, Upper Saddle River, NJ: Pearson Prentice Hall. 1295.
45. Gill, S.S., et al., *Metallurgical and mechanical characteristics of cryogenically treated tungsten carbide (WC-Co).* International Journal of Advanced Manufacturing Technology, 2012. **58**(1-4): p. 119-131.
46. Exner, H.E., *Physical and chemical nature of cemented carbides.* International Materials Reviews, 1979. **24**(1): p. 149-173.
47. Sun, L., C.-C. Jia, and M. Xian, *A research on the grain growth of WC–Co cemented carbide.* International Journal of Refractory Metals and Hard Materials, 2007. **25**(2): p. 121-124.
48. Fernandes, C.M. and A.M.R. Senos, *Cemented carbide phase diagrams: A review.* International Journal of Refractory Metals & Hard Materials, 2011. **29**(4): p. 405-418.
49. Haglund, S. and J. Ågren, *W content in Co binder during sintering of WC–Co.* Acta Materialia, 1998. **46**(8): p. 2801-2807.
50. Mingard, K.P., et al., *Some aspects of the structure of cobalt and nickel binder phases in hardmetals.* Acta Materialia, 2011. **59**(6): p. 2277-2290.
51. Dogra, M., et al., *Tool Wear, Chip Formation and Workpiece Surface Issues in CBN Hard Turning: A Review.* International Journal of Precision Engineering and Manufacturing, 2010. **11**(2): p. 341-358.
52. Samantaray, C.B. and R.N. Singh, *Review of synthesis and properties of cubic boron nitride (c-BN) thin films.* International Materials Reviews, 2005. **50**(6): p. 313-344.
53. Polini, R., et al., *Dry turning of alumina/aluminium composites with CVD diamond coated Co-cemented tungsten carbide tools.* Surface & Coatings Technology, 2003. **166**: p. 8.

54. Kumar, M.S., et al., *An experimental investigation on the mechanism of wear resistance improvement in cryotreated tool steels.* Indian Journal of Engineering and Materials Sciences, 2001. **8**(4): p. 198-204.
55. Lulay, K.E., K. Khan, and D. Chaaya, *The effect of cryogenic treatments on 7075 aluminum alloy.* Journal of Materials Engineering and Performance, 2002. **11**(5): p. 479-480.
56. Asl, K.M., A. Tari, and F. Khomamizadeh, *Effect of deep cryogenic treatment on microstructure, creep and wear behaviors of AZ91 magnesium alloy.* Materials Science and Engineering a-Structural Materials Properties Microstructure and Processing, 2009. **523**(1-2): p. 27-31.
57. Sun, Q.Y., et al., *Mechanical behavior and deformation mechanisms of Ti-2.5Cu alloy reinforced by nano-scale precipitates at 293 and 77 K.* Materials Science and Engineering a-Structural Materials Properties Microstructure and Processing, 2004. **364**(1-2): p. 159-165.
58. Xiong, C.X., et al., *Effects of cryogenic treatment on mechanical properties of extruded Mg-Gd-Y-Zr(Mn) alloys.* Journal of Central South University of Technology, 2007. **14**(3): p. 305-309.
59. Zhang, Z.Z., et al., *Enhanced wear resistance of hybrid PTFE/Kevlar fabric/phenolic composite by cryogenic treatment.* Journal of Materials Science, 2009. **44**(22): p. 6199-6205.
60. Preciado, M., P.M. Bravo, and J.M. Alegre, *Effect of low temperature tempering prior cryogenic treatment on carburized steels.* Journal of Materials Processing Technology, 2006. **176**(1-3): p. 41-44.
61. Stratton, P.F., *Optimising nano-carbide precipitation in tool steels.* Materials Science and Engineering a-Structural Materials Properties Microstructure and Processing, 2007. **449**: p. 809-812.
62. Darwin, J.D., D.M. Lal, and G. Nagarajan, *Optimization of cryogenic treatment to maximize the wear resistance of 18% Cr martensitic stainless steel by Taguchi method.* Journal of Materials Processing Technology, 2008. **195**(1-3): p. 241-247.
63. Das, D., K.K. Ray, and A.K. Dutta, *Influence of temperature of sub-zero treatments on the wear behaviour of die steel.* Wear, 2009. **267**(9-10): p. 1361-1370.
64. Yan, X.G. and D.Y. Li, *Effects of the sub-zero treatment condition on microstructure, mechanical behavior and wear resistance of W9Mo3Cr4V high speed steel.* Wear, 2013. **302**(1-2): p. 854-862.
65. Molinari, A., et al., *Effect of deep cryogenic treatment on the mechanical properties of tool steels.* Journal of Materials Processing Technology, 2001. **118**(1-3): p. 350-355.
66. Koneshlou, M., K.M. Asl, and F. Khomamizadeh, *Effect of cryogenic treatment on microstructure, mechanical and wear behaviors of AISI H13 hot work tool steel.* Cryogenics, 2011. **51**(1): p. 55-61.
67. Das, D., et al., *Influence of sub-zero treatments on fracture toughness of AISI D2 steel.* Materials Science and Engineering a-Structural Materials Properties Microstructure and Processing, 2010. **528**(2): p. 589-603.
68. Baldissera, P., *Deep cryogenic treatment of AISI 302 stainless steel: Part I - Hardness and tensile properties.* Materials & Design, 2010. **31**(10): p. 4725-4730.
69. Baldissera, P. and C. Delprete, *Deep cryogenic treatment of AISI 302 stainless steel: Part II - Fatigue and corrosion.* Materials & Design, 2010. **31**(10): p. 4731-4737.
70. Zhirafar, S., A. Rezaeian, and M. Pugh, *Effect of cryogenic treatment on the mechanical properties of 4340 steel.* Journal of Materials Processing Technology, 2007. **186**(1-3): p. 298-303.
71. Seah, K.H.W., M. Rahman, and K.H. Yong, *Performance evaluation of cryogenically treated tungsten carbide cutting tool inserts.* Proceedings of the Institution of Mechanical Engineers Part B-Journal of Engineering Manufacture, 2003. **217**(1): p. 29-43.
72. Thakur, D., B. Ramamoorthy, and L. Vijayaraghavan, *Influence of different post treatments on tungsten carbide-cobalt inserts.* Materials Letters, 2008. **62**(28): p. 4403-4406.
73. SreeramaReddy, T.V., et al., *Machinability of C45 steel with deep cryogenic treated tungsten carbide cutting tool inserts.* International Journal of Refractory Metals & Hard Materials, 2009. **27**(1): p. 181-185.
74. Das, D., A.K. Dutta, and K.K. Ray, *Sub-zero treatments of AISI D2 steel: Part I. Microstructure and hardness.* Materials Science and Engineering a-Structural Materials Properties Microstructure and Processing, 2010. **527**(9): p. 2182-2193.
75. Das, D., A.K. Dutta, and K.K. Ray, *Sub-zero treatments of AISI D2 steel: Part II. Wear behavior.* Materials Science and Engineering a-Structural Materials Properties Microstructure and Processing, 2010. **527**(9): p. 2194-2206.
76. Dhokey, N.B. and S. Nirbhavne, *Dry sliding wear of cryotreated multiple tempered D-3 tool steel.* Journal of Materials Processing Technology, 2009. **209**(3): p. 1484-1490.

77. Akhbarizadeh, A., A. Shafyei, and M.A. Golozar, *Effects of cryogenic treatment on wear behavior of D6 tool steel.* Materials & Design, 2009. **30**(8): p. 3259-3264.
78. Bensely, A., et al., *Enhancing the wear resistance of case carburized steel (En 353) by cryogenic treatment.* Cryogenics, 2005. **45**(12): p. 747-754.
79. Jaswin, M.A., D.M. Lal, and A. Rajadurai, *Effect of Cryogenic Treatment on the Microstructure and Wear Resistance of X45Cr9Si3 and X53Cr22Mn9Ni4N Valve Steels.* Tribology Transactions, 2011. **54**(3): p. 341-350.
80. Jaswin, M.A., G.S. Shankar, and D.M. Lal, *Wear Resistance Enhancement in Cryotreated En 52 and 21-4N Valve Steels.* International Journal of Precision Engineering and Manufacturing, 2010. **11**(1): p. 97-105.
81. Liu, H.H., et al., *Effects of deep cryogenic treatment on property of 3Cr13Mo1V1.5 high chromium cast iron.* Materials & Design, 2007. **28**(3): p. 1059-1064.
82. Liu, H.H., et al., *Effects of cryogenic treatment on microstructure and abrasion resistance of CrMnB high-chromium cast iron subjected to sub-critical treatment.* Materials Science and Engineering a-Structural Materials Properties Microstructure and Processing, 2008. **478**(1-2): p. 324-328.
83. Liu, H.H., et al., *Effect of cryogenic treatment on property of 14Cr2Mn2V high chromium cast iron subjected to subcritical treatment.* Journal of Iron and Steel Research International, 2006. **13**(6): p. 43-48.
84. Wang, J., et al., *Effects of high temperature and cryogenic treatment on the microstructure and abrasion resistance of a high chromium cast iron.* Journal of Materials Processing Technology, 2009. **209**(7): p. 3236-3240.
85. da Silva, F.J., et al., *Performance of cryogenically treated HSS tools.* Wear, 2006. **261**(5-6): p. 674-685.
86. Firouzdor, V., E. Nejati, and F. Khomamizadeh, *Effect of deep cryogenic treatment on wear resistance and tool life of M2 HSS drill.* Journal of Materials Processing Technology, 2008. **206**(1-3): p. 467-472.
87. Gill, S.S., et al., *Flank Wear and Machining Performance of Cryogenically Treated Tungsten Carbide Inserts.* Materials and Manufacturing Processes, 2011. **26**(11): p. 1430-1441.
88. Gill, S.S., et al., *Investigation on wear behaviour of cryogenically treated TiAlN coated tungsten carbide inserts in turning.* International Journal of Machine Tools & Manufacture, 2011. **51**(1): p. 25-33.
89. Yong, A.Y.L., K.H.W. Seah, and M. Rahman, *Performance of cryogenically treated tungsten carbide tools in milling operations.* International Journal of Advanced Manufacturing Technology, 2007. **32**(7-8): p. 638-643.
90. Gill, S.S., et al., *Wear behaviour of cryogenically treated tungsten carbide inserts under dry and wet turning conditions.* International Journal of Machine Tools & Manufacture, 2009. **49**(3-4): p. 256-260.
91. Huang, J.Y., et al., *Microstructure of cryogenic treated M2 tool steel.* Materials Science and Engineering a-Structural Materials Properties Microstructure and Processing, 2003. **339**(1-2): p. 241-244.
92. Surberg, C.H., P. Stratton, and K. Lingenhole, *The effect of some heat treatment parameters on the dimensional stability of AISI D2.* Cryogenics, 2008. **48**(1-2): p. 42-47.
93. Das, D., A.K. Dutta, and K.K. Ray, *On the refinement of carbide precipitates by cryotreatment in AISI D2 steel.* Philosophical Magazine, 2009. **89**(1): p. 55-76.
94. Tyshchenko, A.I., et al., *Low-temperature martensitic transformation and deep cryogenic treatment of a tool steel.* Materials Science and Engineering: A, 2010. **527**(26): p. 7027-7039.
95. Gavriljuk, V.G., et al., *Low-temperature martensitic transformation in tool steels in relation to their deep cryogenic treatment.* Acta Materialia, 2013. **61**(5): p. 1705-1715.
96. Meng, F., et al., *Role of Eta-Carbide Precipitations in the Wear Resistance Improvements of Fe-12Cr-Mo-V-1.4C Tool Steel by Cryogenic Treatment.* ISIJ International, 1994. **34**(2): p. 206-210.
97. Gisip, J., R. Gazo, and H.A. Stewart, *Effects of cryogenic treatment and refrigerated air on tool wear when machining medium density fiberboard.* Journal of Materials Processing Technology, 2009. **209**(11): p. 5117-5122.
98. Benham, P.P., R.J. Crawford, and C.G. Armstrong, *Mechanics of Engineering Materials*. Second Edition ed. 1996, Harlow, England: Pearson Prentice Hall. 627.
99. Suga, N., *Metrology Handbook - The science of measurement*, ed. P. Rollings. 2007, Andover, England: Mitutoyo (UK) Ltd. 259.

100. BSi, *Metallic materials - Vickers hardness test*, in *Part 1: Test method*. 2005, British Standards Institute. p. 30.
101. Williams, J.A., *Engineering Tribology*. 2005, New York: Cambridge University Press. 488.
102. Jung, S., J. Kim, and S.J.L. Kang, *Etching for Microstructural Observation of Cemented Submicrometer-Sized Carbides.* Journal of American Ceramic Society, 2001. **84**(4): p. 3.
103. Dinnebier, R.E., et al., *Powder Diffraction: Theory and Practice*. 2008, Cambridge, United Kingdom: RSC Publishing, The Royal Society of Chemistry.
104. Cranswick, L.M.D., et al., *Principles and Applications of Powder Diffraction*. 2009, Chichester, UK: John Wiley & Sons Ltd. 397.
105. Champness, P.E., *Electron Diffraction in the Transmission Electron Microscope*. Microscopy Handbooks, ed. R.M. Society. 2001, Oxford, United Kingdom: BIOS Scientific Publishers Ltd. 170.
106. Colbert, R.S., et al., *Uncertainty in Pin-on-Disk Wear Volume Measurements Using Surface Scanning Techniques.* Tribology Letters, 2011. **42**: p. 3.
107. Brundle, C.R., C.A. Evans, and S. Wilson, *Surfaces, Interfaces, Thin Films*, in *Encylopedia of Materials Characterization*, L.E. Fitzpatrick, Editor. 1992, Butterworth-Heinemann: Stoneham, MA. p. 770.
108. David, W.I.F., et al., *Structure Determination from Powder Diffraction Data*. IUCr Monographs on Crystallography, ed. I.U.o. Crystallography. Vol. 13. 2006, Great Clarendon Street, Oxford, United Kingdom: Oxford University Press.
109. Cullity, B.D., *Elements of X-ray diffraction*. 1st ed. 1956, Reading, Massachusetts, USA: Addison-Wesley Pub. Co.
110. Smith, D.K., *Particle statistics and whole-pattern methods in quantitative X-ray powder diffraction analysis.* Powder Diffraction, 2001. **16**(4): p. 6.
111. Akbari, A., et al., *Effect of the initial microstructure on the plasma nitriding behavior of AISI M2 high speed steel.* Surface & Coatings Technology, 2010. **204**(24): p. 4114-4120.
112. Sugishita, J. and S. Fujiyoshi, *The effect of cast iron graphites on friction and wear performance I: Graphite film formation on grey cast iron surfaces.* Wear, 1981. **66**: p. 13.
113. Hetzner, D.W. and W. Van Geertruyden, *Crystallography and metallography of carbides in high alloy steels.* Materials Characterization, 2008. **59**(7): p. 825-841.
114. Gabryszewski, Z. and W. Śródka, *Thermal effects during the deformation of grey cast iron.* International Journal of Solids and Structures, 1986. **22**(5): p. 497-509.
115. Hinrichs, R., et al., *A TEM snapshot of magnetite formation in brakes: The role of the disc's cast iron graphite lamellae in third body formation.* Wear, 2011. **270**(5–6): p. 365-370.
116. Jack, D.H. and K.H. Jack, *Invited review: Carbides and nitrides in steel.* Materials Science and Engineering, 1973. **11**(1): p. 1-27.
117. Wood, I.G., et al., *Thermal expansion and crystal structure of cementite, Fe3C, between 4 and 600 K determined by time-of-flight neutron powder diffraction.* Journal of Applied Crystallography, 2004. **37**(1): p. 82-90.
118. Edington, J.W., *2. Electron Diffraction in the Electron Microscope*. Monographs in Practical Electron Microscopy in Materials Science. 1975, London: The Macmillan Press Ltd. 122.
119. BSi, *Non-destructive testing. X-ray diffraction from polycrystalline and amorphous materials. Procedures*. 2003, British Standards Institute. p. 26.
120. Modi, O.P., et al., *Effect of interlamellar spacing on the mechanical properties of 0.65% C steel.* Materials Characterization, 2001. **46**: p. 6.
121. Ghasemi, R. and L. Elmquist, *The relationship between flake graphite orientation, smearing effect, and closing tendency under abrasive wear conditions.* Wear, 2014. **317**(1–2): p. 153-162.
122. Sugishita, J. and S. Fujiyoshi, *The effect of cast iron graphites on friction and wear performance II: Variables influencing graphite film formation.* Wear, 1981. **68**: p. 14.
123. Gulyaev, A.P., *Improved methods of treating high speed steels to improve the cutting properties.* Metallurgy, 1937. **12**.
124. Kalsi, N.S., R. Sehgal, and V.S. Sharma, *Cryogenic Treatment of Tool Materials: A Review.* Materials and Manufacturing Processes, 2010. **25**: p. 25.

10. Appendices

10.1. Introduction

Cryogenic processing companies and services

Table 51 - Extended summary of cryotreatment companies and services offered (from Table 5).

Company (location)	Products and services offered	Treatment description
300 Below Cryogenic Tempering Services, Inc. (Illinois, USA)	"...dry deep freezing process using flashed Liquid Nitrogen (LN_2)..." Model 921 computer-controlled cryogenic processor: electrical cooling to -100°F (-73C / 200K) before using LN_2; 1500lb (682kg) capacity; 220V single phase 11.2A (2.5kW).	-300°F (-184°C / 88K) soak temperature, cooling and heating controlled to within 1°F (0.6K), 72hr soak time. Treatment performed using compressed nitrogen vapour atmosphere.
Controlled Thermal Processing, Inc. (Illinois, USA)	Cryogenic treatment, REM polishing and liquid helium processing. Applied Cryogenics, Inc cryogenic processors: post-cryo tempering; 7-42ft^3 (0.2-1.2m^3) capacity; 220V single phase 20-50A (4.4-11kW).	-300°F (-184°C / 88K) soak temperature for cryogenic processing. Treatment performed using LN_2 to cool air via heat exchangers, which is then circulated around components. -450°F (-267°C / 5K) for liquid helium processing.
CryoPlus, Inc. (Ohio, USA)	"...cryogenic service to the woodworking, stamping, tool and die, shearing, slitting, welding, punching, musical, shooting and racing industries."	Pre-cryotreatment tempering at up to 350°F (177°C / 450K) for 1hr before -300°F (-184°C / 88K) soak temperature for 10hrs. Treatment performed using LN_2 sprayed into the cooling chamber and vaporised into an expanded gas, circulated by fans.
Cryogenic Institute of New England, Inc. (Massachusetts, USA)	Cryogenic treatment, thermal cycling, helium processing; uphill quenching; cryogenic shrink fitting; cryogenic deburring and deflashing; dry ice deburring, deflashing and blast cleaning. Batch and continuous cryogenic treatment equipment: -300-1120°F (-184-604°C / 88-878K) temperature range, analog or PLC controls.	-300°F (-184°C / 88K) soak temperature for 24hrs, thermal cycling also offered. Treatment performed using LN_2 immersion. -450°F (-267°C / 5K) for liquid helium processing. Uphill quenching involves immersing parts in LN_2 before transfer to boiling water, steam or convection heating.
Cryogenic Treatment Services Ltd. (Nottinghamshire, UK)	Cryogenic treatment through cooling and reheating curves between -195°C and 300°C (78K and 573K)	-195°C (78K) soak temperature for 24hrs, cooling and reheating controlled to within 1-2K/min, before tempering at up to 300°C (573K).
Cryogenics International (Arizona, USA)	Deep cryogenic processing using extended soaking times at temperatures around -320°F (-196°C / 78K). Cryogenic treatment systems up to	-320°F (-196°C / 78K) soak temperature for at least 24hrs, cooling and heating controlled to within 0.5°F/min (0.3K/min), 36-

	around 30ft^3 (0.8m^3) capacity.	74hrs total process time. Treatment performed using compressed nitrogen vapour atmosphere.
Frozen Solid (Cambridgeshire, UK)	Deep cryogenic processing as well as liquid helium processing and multi-stage tempering facilities.	-196°C (78K / -320°F) soak temperature for a set period (dependent on material), cooling and heating accurately controlled.

10.2. A review of cryogenic processing technology, treatments and effects

Alloying elements in cast iron and steel

Table 52 - Common alloying elements of the iron-carbon system [11].

	Name	wt%	
C	Carbon	0.05	Maximum solubility in α-ferrite at 715°C.
		0.77	Eutectoid (austenite ←→ ferrite + cementite) point of iron-carbon system.
		0.84	Typical content in high-strength steels. With appropriate heat treatment, beneficial carbide precipitation occurs.
		1.8	Maximum solubility in γ-austenite at 1130°C.
		<2.1	Steel.
		>2.1	Cast iron. Contains either carbide eutectic, graphite eutectic, or both. In grey iron, carbon rejected from austenite during cooling precipitates on graphite flakes. Carbon can be present as eutectic graphite or cementite together with pearlite or ferrite.
		4.3	Eutectic (liquid ←→ austenite + cementite) point of iron-carbon system.
		6.67	Maximum solubility of carbon in pure iron.
Si	Silicon	-	*Has a strong affinity for oxygen; used as a deoxidant in steels. Hardens ferrite by solid solution and increases the hardenability of austenite. During tempering, sustains hardness by solid solution. Strong graphitiser.*
		0.30-0.35	Range in which silicon starts to affect mechanical properties of steels; increasing hardenability and strength.
		1.5	Minimum quantity found in grey cast irons. Decreases the carbon content of the eutectic and alters graphite distribution. Carbon content of eutectoid decreased by ~0.1% per 1% increase in silicon.
		2.0	Solid solubility in γ-austenite.
		2.2	Solubility in γ-austenite at 1170°C.
		2.5-4.5	Tensile and yield strength of steel increases.
		4.5-6.0	Tensile and yield strength of steel decreases.
		9.0	Solid solubility in γ-austenite with 0.35%C.
		18.5	Solid solubility in α-ferrite.
Mn	Manganese	-	*Hardens ferrite and increases the hardenability of austenite. Forms a carbide similar to cementite. In iron-carbon system lowers the rate and lowers the temperature of transformation. Lowers eutectoid carbon content and aids formation of finer pearlite lamellae.* *In cast iron, stabilises, refines and increases the hardenability of pearlite. Forms manganese sulphide in preference to iron-sulphide if present in sufficient quantities (1.7x S%); higher melting point and generally exists as separate globules.*
		1.0	Good tensile strength and ductility with 0.25%C. Improves hardenability and machinability.
		3.0	Solid solubility in α-ferrite.
		>10.0	Effectively prevents phase changes and carbide precipitation; used to keep steels austenitic after quenching.
		100.0	Unlimited solubility in γ-austenite.
Cr	Chromium	-	*Hardens ferrite slightly, moderately increases the hardenability of austenite. Restricts γ-austenite phase. Strong carbide former; in high carbon steels it increases the resistance to abrasion.* *Cr in solution increases the time required for isothermal transformation of austenite. Reduces the carbon content of eutectoid pearlite.*
		2.0	In steels with 0.3%C, prevents pearlite formation with normal cooling rates. Martensite or bainite produced instead.
		3.3-5.0	Range of Cr in high-speed steels.

		12.0	Eutectoid occurs at 0.35%C and austenite transformation temperature is raised to 800°C. With up to 2%C, steel contains free carbides that promote abrasion resistance.
		13.0	Solid solubility in α-ferrite. δ-phase exists at room temperature.
		20.0	Solid solubility in α-ferrite with 0.5%C.
		>30.0	Intermetallic compound FeCr (σ-phase) formed.
Mo	Molybdenum	-	*Hardens ferrite by solid solution and strongly increases hardenability of austenite. Very strong carbide former. By secondary hardening counteracts softening during tempering.* *Gives toughness to high tensile strength carbon steels; improved elastic properties and impact strength.* *Retards austenite transformation and increases depth of hardening.*
		0.25	Retards softening of martensite at tempering temperatures above 260°C; increases hardness of medium to high-carbon martensitic steels tempered at 400-630°C.
		1.0	Greatly enhances air-hardening in high-chromium tool steels.
		2.0-4.0	In 0.10-0.25%C steel, causes secondary hardening in both martensitic and non-martensitic structures with tempering of 535-620°C.
		3.0	Solid solubility in γ-austenite.
		8.0	Solid solubility in γ-austenite with 0.3%C.
		37.5	Solid solubility in α-ferrite.
V	Vanadium	-	*Moderately hardens ferrite by solid solution and strongly increases hardenability when dissolved in austenite. Exceptionally strong carbide former; promotes significant secondary hardening.* *Forms V_4C_3 carbide; with Fe_3C forms exceptionally fine mixture. Refines grain size in carbon and alloy steels. Produces fine carbide structures in hypereutectoid steels.* *Causes eutectoid reaction to occur at lower carbon contents.*
		0.1-0.3	Toughens ferrite and refines grain size in medium-carbon steels.
		0.2-0.5	Steels with 0.6-1.4%C and 0.25-0.50%Mn are hardened and temperered for us in cutting tools, taps, dies and hammers; higher tensile strength and impact resistance.
		1.0	Solid solubility in γ-austenite. Eutectoid in iron-carbon system occurs at 0.6%C.
		4.0	Solid solubility in γ-austenite with 0.2%C.
		100.0	Unlimited solubility in α-ferrite.
W	Tungsten	-	*Strongly increases the hardenability of austenite and mildly strengthens ferrite by solid solution. Strong affinity for carbon; tungsten carbides are extremely hard and abrasion resistant. Gives increased wear resistance and high strength at elevated temperatures.* *Effectively insoluble tungsten carbides result in fine grain size in tungsten steels.* *Raises temperature and lowers carbon content of eutectoid change; produces more free carbides in steels.* *In high-speed steel produces a matrix that does not soften on tempering with extremely hard carbides. Gives improved high temperature strength and greater toughness.*
		4.2	Solid solubility in α-ferrite at room temperature.
		6.0	Solid solubility in γ-austenite.
		11.0	Solid solubility in γ-austenite with 0.25%C.
		33.0	Solubility in α-ferrite at 1500°C.

10.3. Experimental methodologies

Determination of crater wear depth from non-plane interferometric data

As discussed in Section 3.5.2, the topographic scans made of the rake face of cutting tool inserts contained gradients in the x and y directions that could not be corrected for using simple tilt removal functions. To calculate the necessary adjustments to measured crater wear depths, additional points were identified to allow the gradients in x and y directions to be individually calculated which were then used to calculate the necessary adjustments in crater wear depths.

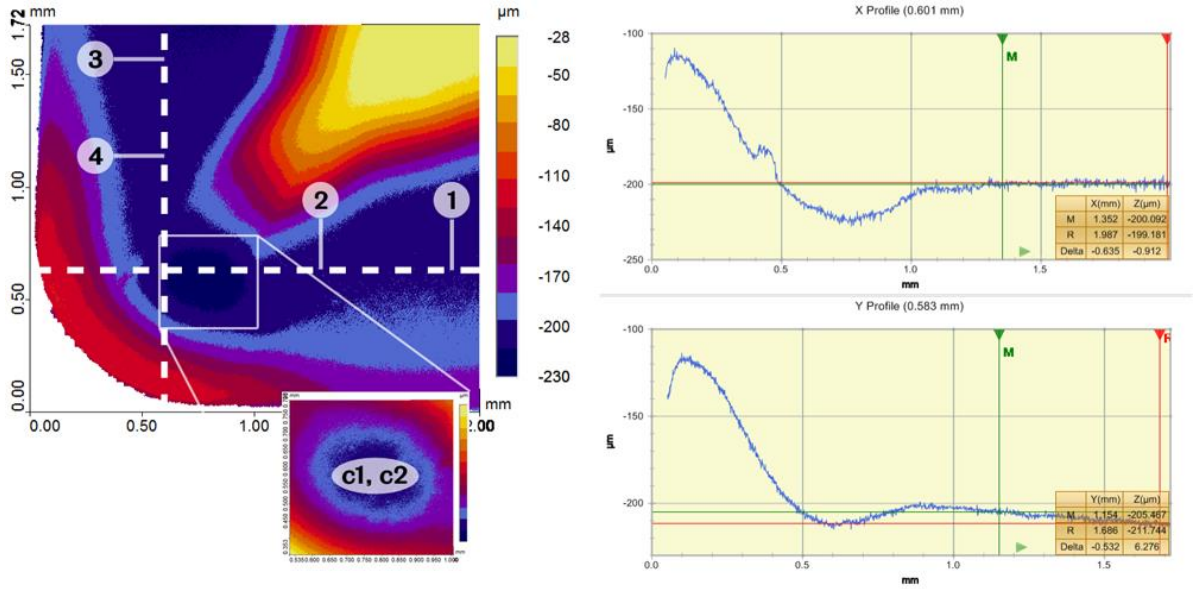

Figure 87 - Example of interferometric topograph and profiles measured from tool inserts (adapted from Figure 30).

The following steps describe the procedure taken to calculate the necessary adjustments to make accurate crater wear measurements from the collected topographic data:

Where coordinates at location i, $(x, y, z)_i$

Where the gradient in the x direction, $$k_x = \frac{z_1 - z_2}{x_1 - x_2}$$

Where the gradient in the y direction, $$k_y = \frac{z_3 - z_4}{y_1 - y_2}$$

The crater depth correction (c1) in x, $$\Delta z_{c1,x} = k_x(x_1 - x_{c1})$$

The crater depth correction (c1) in y, $$\Delta z_{c1,y} = k_y(y_1 - y_{c1})$$

The crater depth correction (c2) in x, $$\Delta z_{c2,x} = k_x(x_1 - x_{c2})$$

The crater depth correction (c2) in y, $$\Delta z_{c2,y} = k_y(y_1 - y_{c2})$$

Corrected crater depth (c1),

$$\Rightarrow z'_{c1} = z_{c1} + \frac{\Delta z_{c1,x} + \Delta z_{c1,y}}{2}$$

Corrected crater depth (c2),

$$\Rightarrow z'_{c2} = z_{c2} + \frac{\Delta z_{c2,x} + \Delta z_{c2,y}}{2}$$

Reported crater depth after pass i,

$$\therefore |KT_i| = z_1 - \frac{z'_{c1} + z'_{c2}}{2}$$

10.4. Effects of deep cryogenic treatment on the sliding wear performance

Testing parameters

Theoretical Hertzian contact stresses for each of the experimental conditions applied to EN10083 C50R, SAE J431 G10, AISI A2, D6 and M2 tool steels, illustrated in Figure 88 through to Figure 96 and presented in Section 4.2, were calculated using the established relationships given in Equations 10.1 – 10.9 [101] (including radial, tangential and axial stresses (σ_r, σ_θ, σ_z), principal shear stress (τ_1), peak Hertzian contact pressure (p_0), Poisson's ratio for indented material (v), contact half-width (a), radius from axis of centre of contact (r), depth from centre of contact (z)).

Surface stresses (within contact region):

$$\frac{\sigma_r}{p_0} = -\left(\frac{1-2v}{3}\right)\left(\frac{a}{r}\right)^2\left\{1-\left(1-\left(\frac{r}{a}\right)^2\right)^{3/2}\right\}-\left(1-\left(\frac{r}{a}\right)^2\right)^{1/2} \tag{10.1}$$

$$\frac{\sigma_\theta}{p_0} = -\left(\frac{1-2v}{3}\right)\left(\frac{a}{r}\right)^2\left\{1-\left(1-\left(\frac{r}{a}\right)^2\right)^{3/2}\right\}-2v\left(1-\left(\frac{r}{a}\right)^2\right)^{1/2} \tag{10.2}$$

$$\frac{\sigma_z}{p_0} = -\left(1-\left(\frac{r}{a}\right)^2\right)^{1/2} \tag{10.3}$$

Surface stresses (outside contact region):

$$\frac{\sigma_r}{p_0} = -\frac{\sigma_\theta}{p_0} = \left(\frac{1-2v}{3}\right)\left(\frac{a}{r}\right)^2 \tag{10.4}$$

$$\sigma_z = 0 \tag{10.5}$$

Subsurface stresses:

$$\frac{\sigma_r}{p_0} = -(1+v)\left\{1-\left(\frac{z}{a}\right)\tan^{-1}\left(\frac{a}{z}\right)\right\}+\frac{1}{2}\left(1+\left(\frac{z}{a}\right)^2\right)^{-1} \tag{10.6}$$

$$\frac{\sigma_\theta}{p_0} = -(1+v)\left\{1-\left(\frac{z}{a}\right)\tan^{-1}\left(\frac{a}{z}\right)\right\}+\frac{1}{2}\left(1+\left(\frac{z}{a}\right)^2\right)^{-1} \tag{10.7}$$

$$\frac{\sigma_z}{p_0} = -\frac{1}{2}\left(1+\left(\frac{z}{a}\right)^2\right)^{-1} \tag{10.8}$$

$$\Rightarrow \tau_1 = \frac{1}{2}|\sigma_z - \sigma_\theta| \tag{10.9}$$

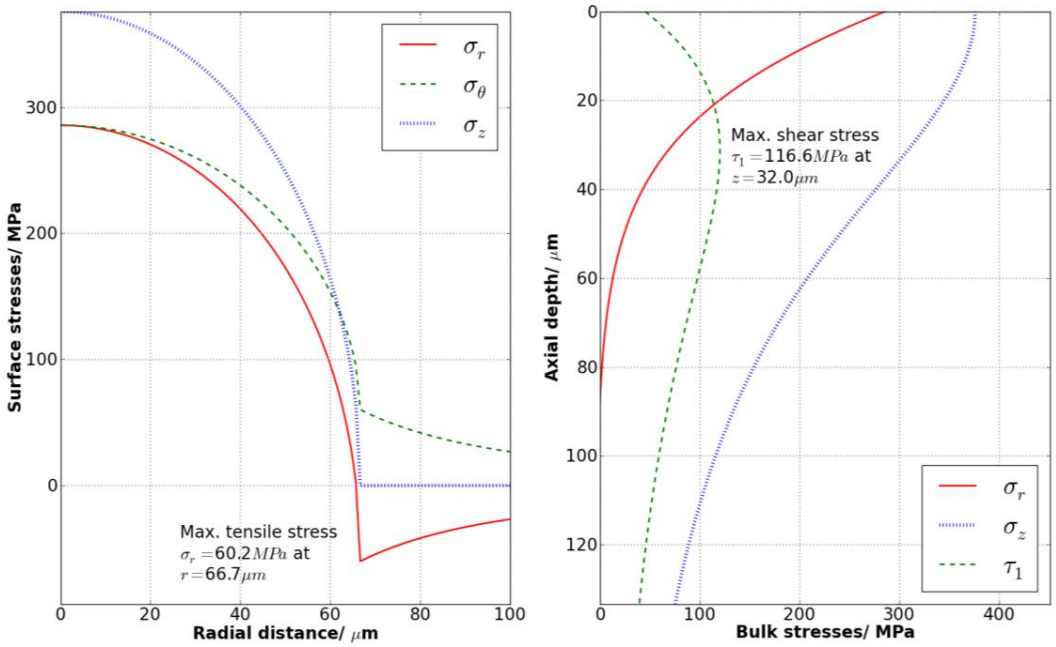

Figure 88 - Predicted initial surface and subsurface stresses for SAE J431 G10 when p_0 = 375.0MPa.

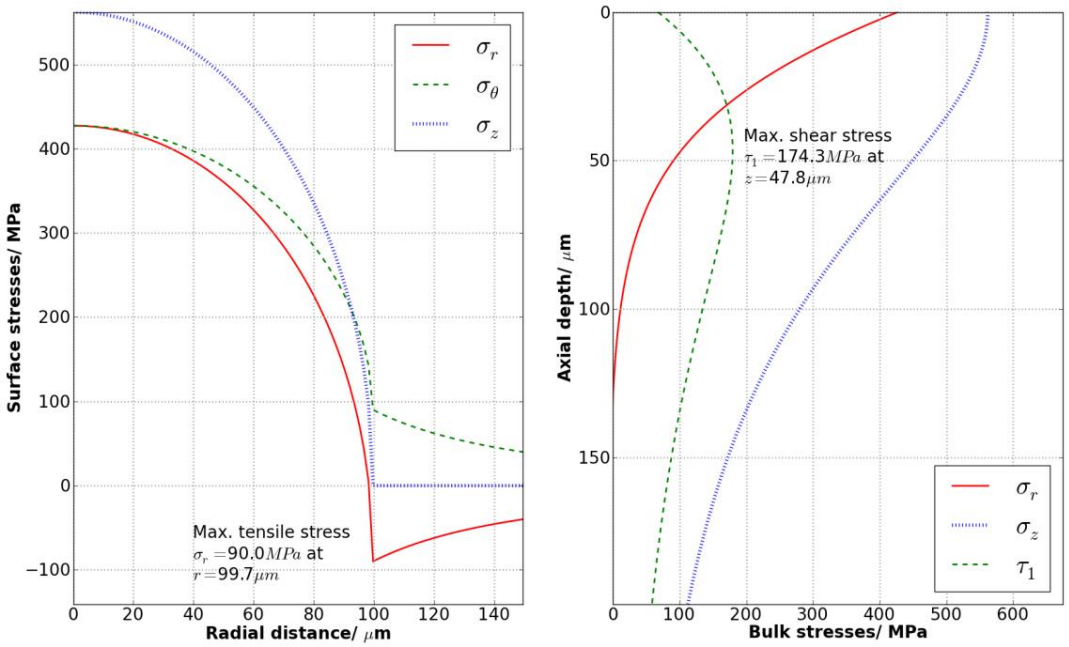

Figure 89 - Predicted initial surface and subsurface stresses for SAE J431 G10 when p_0 = 562.5MPa.

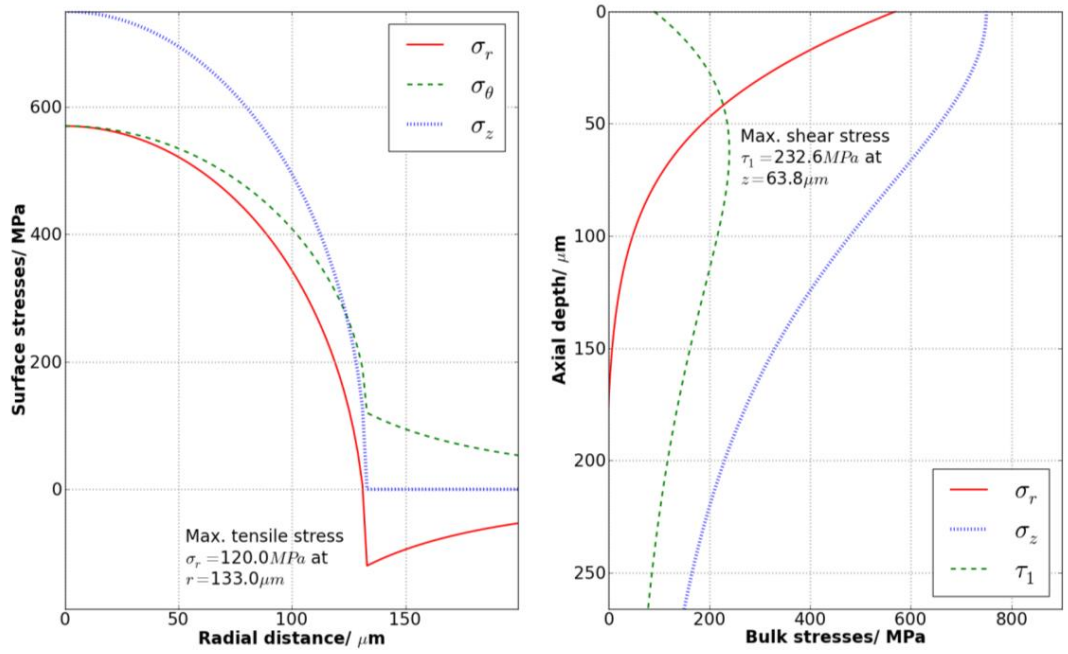

Figure 90 - Predicted initial surface and subsurface stresses for SAE J431 G10 when p_0 = 750.0MPa.

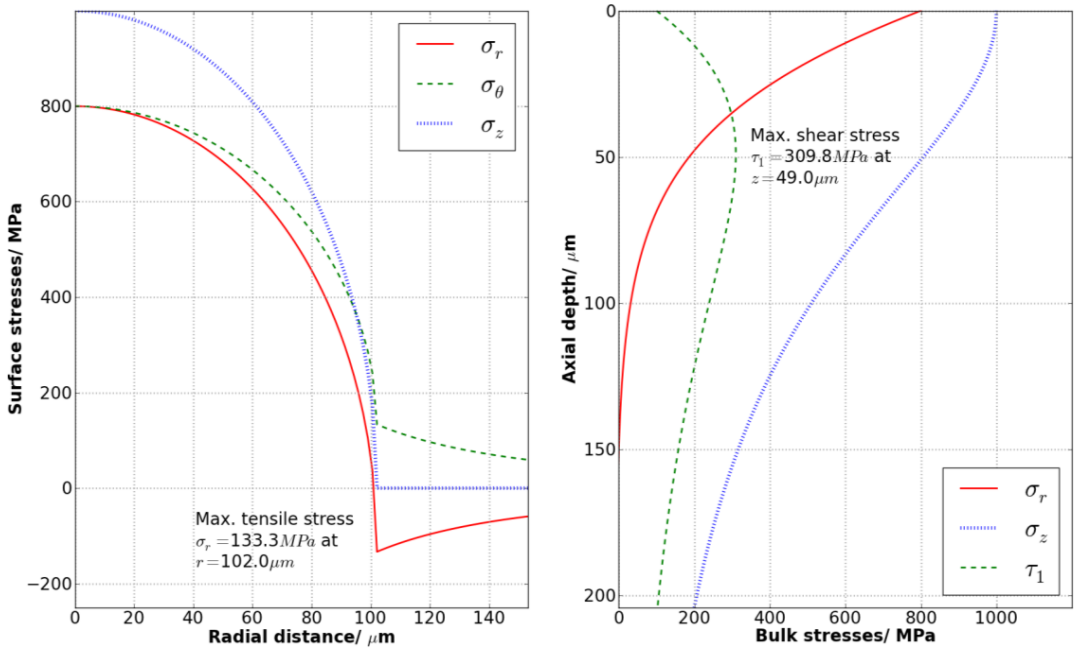

Figure 91 - Predicted initial surface and subsurface stresses for C50R when p_0 = 1000MPa.

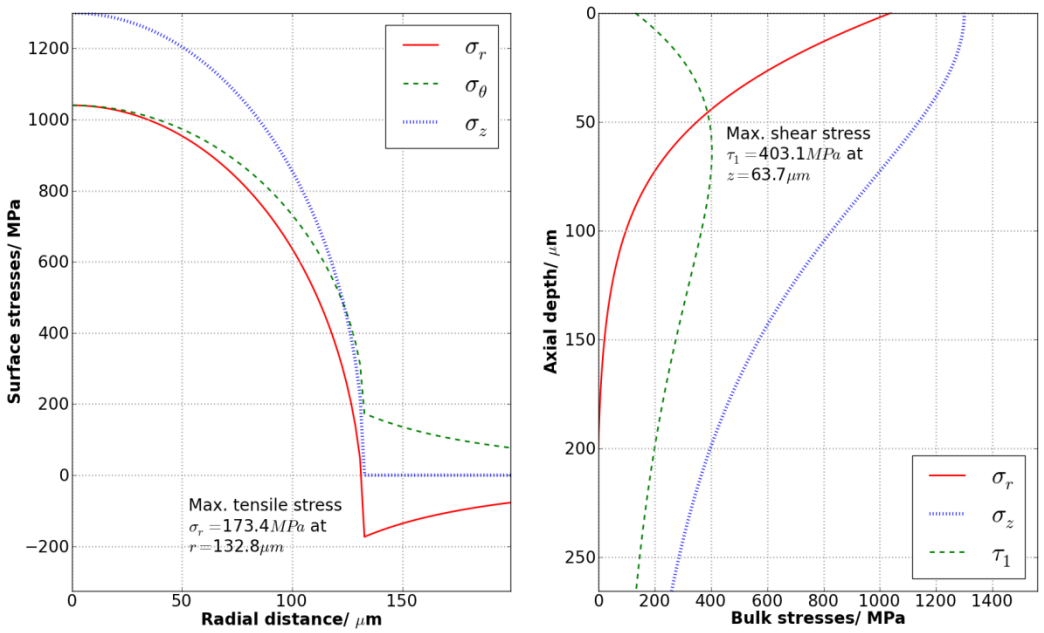

Figure 92 - Predicted initial surface and subsurface stresses for C50R when p_0 = 1300MPa.

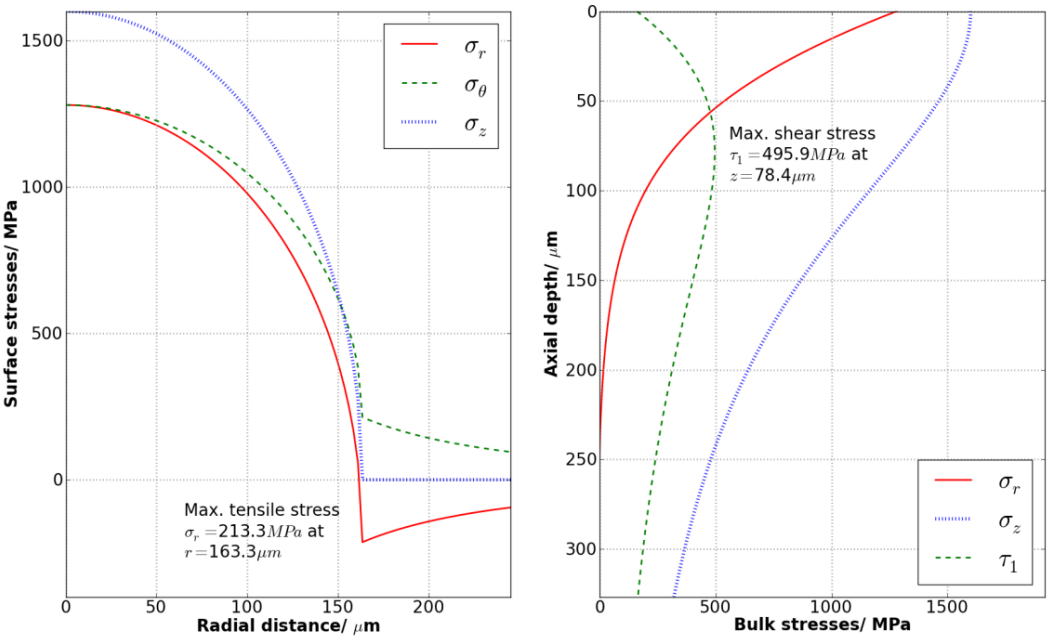

Figure 93 - Predicted initial surface and subsurface stresses for C50R when p_0 = 1600MPa.

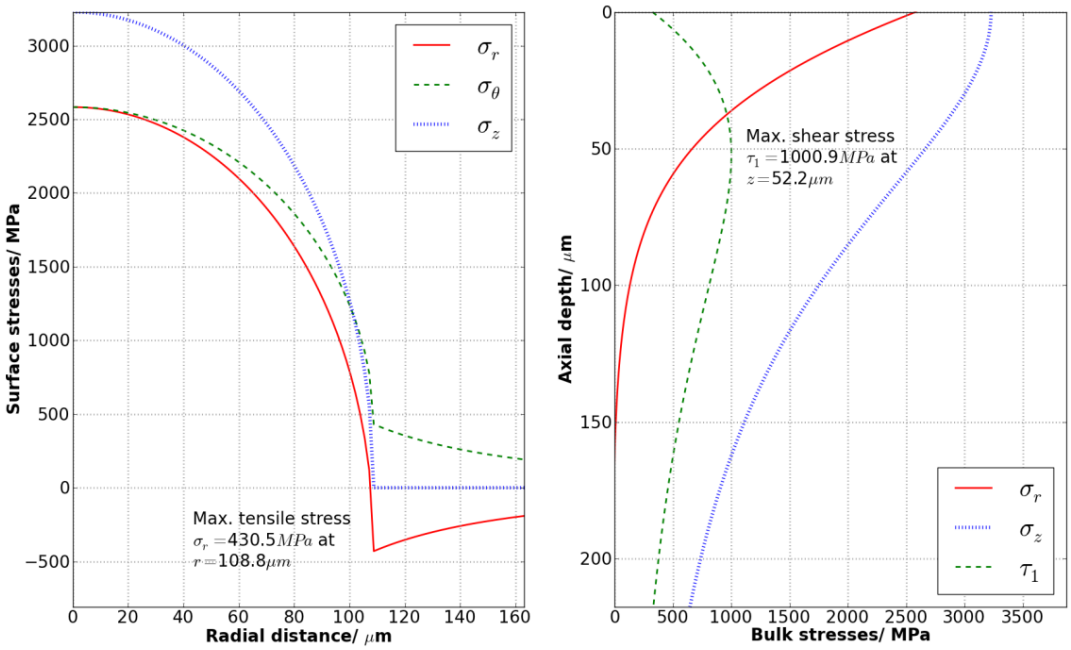

Figure 94 - Predicted initial surface and subsurface stresses for AISI A2 when p_0 = 3250MPa.

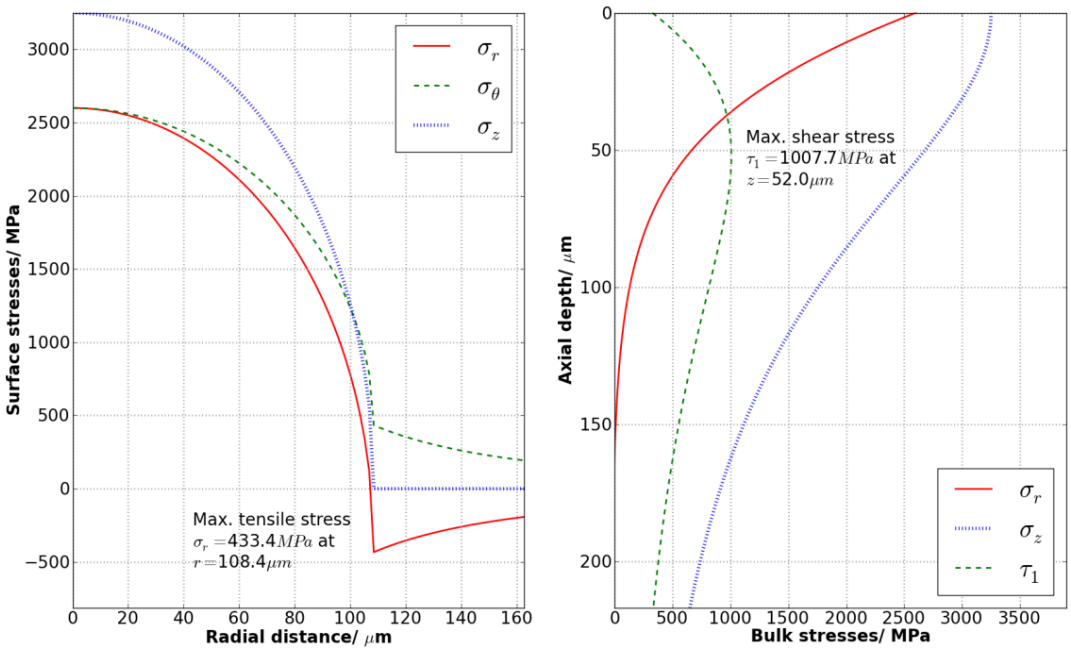

Figure 95 - Predicted initial surface and subsurface stresses for AISI D6 when p_0 = 3250MPa.

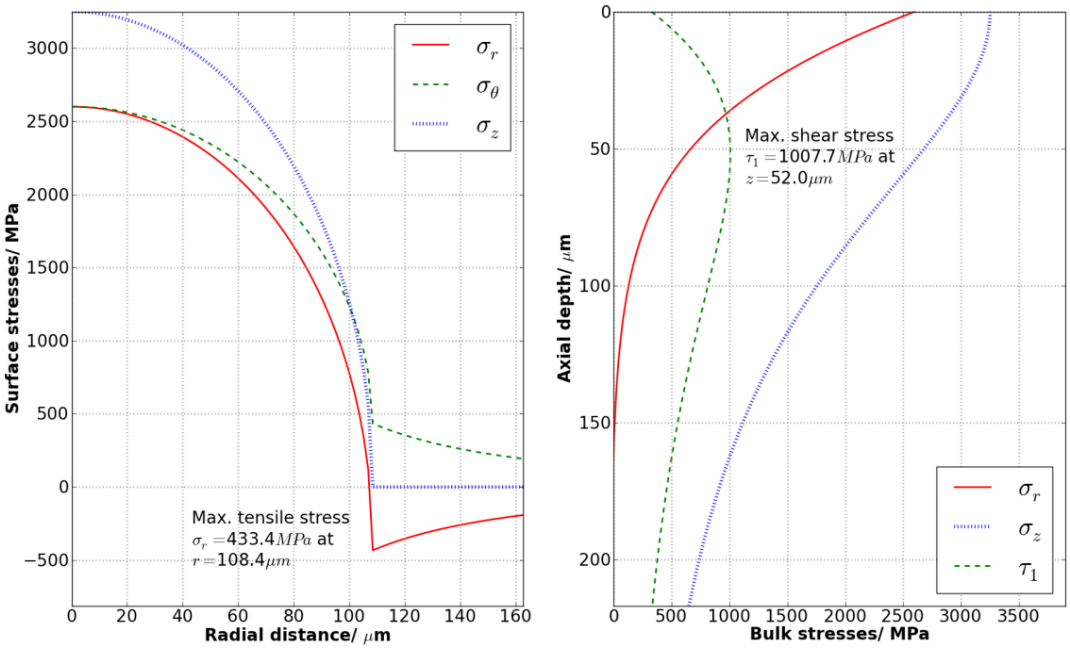

Figure 96 - Predicted initial surface and subsurface stresses for AISI M2 when p_0 = 3250MPa.